

ABSTRACT

BAEK, SEUNGHUN. High-Frequency AC-link Transformers for Medium-Voltage DC/DC Converters and Solid State Transformer Applications. (Under the direction of Subhashish Bhattacharya.)

Traditional electricity systems rely heavily on easily accessible fossil fuels, such as coal and natural gas. However, the price of these finite sources has been increasing rapidly, and the combustion of these fossil fuels have caused considerable damage to the environment. The utilization of clean local energy resources, such as solar, wind, ocean energy, etc. is no longer a viable option in preparing for the shortage of these finite natural resources or avoiding environmental pollution.

In order to efficiently link local renewable energy to the power grid, there is a critical demand for modernized and functional distribution systems. The core element of the future smart distribution system is the power electronics-based distribution transformer made using power semiconductor devices, also known as the Solid-State Transformer (SST).

State-of-the-art power electronics applications using enhanced DC technology for high-voltage, high-frequency applications have taken center stage recently for levels in the range of tens of kW to MW. Power electronic applications using developing 15kV SiC devices to directly support distribution line voltage is a challenging work and derives many related topics. Designing and implementing medium-voltage, AC-link transformers in an isolated DC/DC stage of an SST at an operating frequency of 20kHz is one of the challenging tasks in the realization this technology.

This thesis contains comprehensive design considerations for medium-voltage and medium frequency(MV-MF) AC-link transformers for SST applications under operations of different types of high-power dual-active bridge DC/DC converters. The main goal of this thesis is to understand the operation and system characteristics of the DC/DC conversion stage of SST, and design the most suitable and optimized magnetic components for these specific applications. Specifically, the inductor-integrated coaxial winding transformer (ICWT) and three winding low-profile transformer are designed for these specific applications and studied in this thesis for the first time. Detailed studies into steady-state operations for different types of MV-MF DAB DC/DC converters and transformers, including inductor integration, switching response with parasitic effects, loss characterization, and experimental verification, are carried out. Computer-aided design and finite element analysis (FEA) are intensively used for detailed study.

The laboratory prototype of the DC/DC stage of the SST application has been built at the FREEDM Systems Center of NSF's ERC headquarters. 15kV SiC devices are used to realize one stage conversion in a distribution level and tested up to an operating frequency of 20kHz and 6kVDC with optimized isolation transformers.

© Copyright 2014 by Seunghun Baek

All Rights Reserved

High-Frequency AC-link Transformers for Medium-Voltage DC/DC Converters and Solid
State Transformer Applications

by
Seunghun Baek

A dissertation submitted to the Graduate Faculty of
North Carolina State University
in partial fulfillment of the
requirements for the Degree of
Doctor of Philosophy

Electrical and Computer Engineering

Raleigh, North Carolina

2014

APPROVED BY:

Alex Huang

Jayant Baliga

Daniel Stancil

Subhashish Bhattacharya
Chair of Advisory Committee

ACKNOWLEDGEMENTS

First of all, I would like to show my sincere appreciation for the opportunities and support by Prof. subhashish bhattacharya. I couldn't have completed all the hard work without him, and my colleagues at the FREEDM System Center at North Carolina State University.

Furthermore, I want to express my gratitude to Prof. Dr. Huang, Dr. Baliga and Dr. Stancil for serving as committee members for my Ph.D. exam and for their effort to evaluate my thesis.

Many thanks go to all my friends who shared hard times and their thoughts in United States in the past year.

Finally, to my family, father, mother, elder brother and his lovely wife and kids, Hyenjin and Hyengjun, and Stephanie who have supported me with love and patience.

I love you all. Thank you.

TABLE OF CONTENTS

LIST OF TABLES	vi
LIST OF FIGURES	viii
CHAPTER 1 Introduction	1
1.1 Current state of the solid state transformer applications	1
1.2 Medium-voltage and medium-frequency AC-link transformers for SST applications	4
1.2.1 Topologies of SST applications using bidirectional isolated DAB DC/DC conversion	4
1.2.2 Chapter overview	11
1.3 Motivations and contributions	14
1.3.1 Importance of the magnetics components in AC-link section of the isolated high-power DC/DC converter	14
1.3.2 Contributions	15
CHAPTER 2 EXISTING BIDIRECTIONAL AND ISOLATED DAB DC/DC CONVERTERS	16
2.1 DAB DC/DC converter operations and scope of the study	16
2.1.1 Investigated topologies of DAB DC/DC converter	16
2.1.2 Understanding power flow and soft switching of DAB operation using fundamental frequency component	17
2.1.3 Modulation schemes of DAB DC/DC converter	18
2.2 Single-phase dual active bridge (DAB) DC/DC converter	20
2.2.1 Steady state lossless operation - Single phase DAB	20
2.2.2 Soft switching schemes - single phase DAB DC/DC converter	23
2.2.3 Influence of a finite magnetizing inductance with an asymmetric impedance matrix	25
2.3 Three-phase dual-active bridge converter topology - Yy connection	32
2.3.1 Steady state lossless operation Three phase Yy connection	32
2.3.2 Soft switching scheme - Three phase Yy connection	34
2.4 Summary	35
CHAPTER 3 MEDIUM-FREQUENCY AND MEDIUM-VOLTAGE COAXIAL WINDING TRANSFORMER	37
3.1 Summary of transformer design equations and parameters	38
3.2 Modeling coaxial winding transformer (CWT) with parasitic effects	43
3.2.1 Configuration of CWT and prototype	43
3.2.2 Geometric simplification and meshing considerations for finite element analysis	45
3.2.3 Inductance modeling and calculation for CWT	48
3.2.4 Parasitic capacitances modeling of CWT	53
3.2.5 Lumped-element equivalent circuit model and measurement results of CWT prototype	57

3.3	Skin and proximity effects on concentrically arranged windings	66
3.3.1	Skin and proximity effect	66
3.3.2	EM field distribution on an infinite tubular conductor - review of literatures	67
3.3.3	Proximity effect on conductors in concentric geometry	70
3.3.4	Computer aided FEM results in 3D for CWT prototype	72
3.4	Insulation strategy for MV-MF CWT prototype for SST application	77
3.4.1	Electric filed distribution in simple configurations of insulation	77
3.4.2	Insulation strategy and case study for MV-MF CWT	78
3.5	MV-MF CWT prototype and experimental test results	85
3.5.1	Loss and insulation test results	85
3.6	Summary	87
CHAPTER 4 PROPOSED INDUCTOR-INTEGRATED COAXIAL WIND- ING TRANSFORMER FOR DAB DC/DC CONVERTER . . .		88
4.1	Modeling concept: Inductance integration	91
4.1.1	Lumped-element equivalent inductance model of ICWT	91
4.2	Selection of materials and dimensions of cores	98
4.2.1	Selection of core material	98
4.2.2	Dimension optimization of the cores	100
4.3	Proposed loss formula for ICWT for phase-modular single phase DAB DC/DC converters	103
4.3.1	Cores properties	103
4.3.2	Loss characteristics with DAB DC/DC conversion operation	106
4.4	High frequency effect on a multi-tubular conductor with harmonics components .	109
4.5	Insulation strategies for MV-MF ICWT prototype	113
CHAPTER 5 ICWT PROTOTYPE IMPLEMENTATION AND EXPERI- MENT RESULTS		116
5.1	Loss Characteristics of the ICWT prototype	117
5.1.1	Eddy and proximity effects in real geometry and consideration on the auxiliary parts	117
5.1.2	Inner and outer core losses	125
5.1.3	Operation region of ICWT prototype with SiC-based 6kVDC/400VDC DAB DC/DC converter	126
5.2	ICWT with SiC-based 6kVDC/400VDC DAB DC/DC stage of SST	132
5.2.1	The switching response of the ICWT with 15kV SiC MOSFET under DAB operation	132
5.3	Loss and temperature measurement of ICWT under operation at 10kVA	136
5.4	Summary	139
CHAPTER 6 PROPOSED THREE-PORT AND THREE-PHASE DAB CON- VERTER IN Y_{yd} CONFIGURATION		140
6.1	Winding types and considerations on three-phase system	140
6.2	Three-phase DAB converter topology - Y _d connection	142
6.2.1	Steady state lossless operation Y _d connection	142

6.2.2	Soft switching scheme three phase Yd connection	145
6.3	Proposed three-port three-phase bidirectional and isolated dc/dc converter in Yd connection	147
6.3.1	Power flow analysis using network calculations and impedance model . . .	147
6.3.2	Steady state lossless operation - Three phase in Yd connection	149
6.3.3	Soft switching scheme Three phase Yd connection	151
6.4	Proposed inductor integrated three-winding planar transformer for the proposed topology	155
6.4.1	Modeling concept : inductance matrix of a three winding planar transformer and geometrical analysis	155
6.4.2	Winding arrangement and inductance calculation	155
6.4.3	FEM transient simulation results and comparison with analytical solution	157
6.5	Comparison and implementation of laboratory prototype	162
6.6	Prototype implementation and experiment results	167
CHAPTER 7 Conclusions		170
7.1	Summary and conclusion	170
REFERENCES		175
Appendices		180
	Appendix A	181
	Appendix B	185

LIST OF TABLES

Table 1.1	Specifications of SST Gen.1 transformer and AC-link transformer	8
Table 1.2	Specifications of the AC-link transformer prototypes	8
Table 1.3	Specifications of the Lab. prototype A	9
Table 1.4	Specifications of the Lab. prototype B	12
Table 3.1	Field distribution	44
Table 3.2	Specifications of the AC-link transformer prototype [mm]	50
Table 3.3	Leakage permeance calculated by finite element method in 2 dimension	52
Table 3.4	Permeance measurement from the prototype (The length of the body is 0.6m)	52
Table 3.5	Measurement conditions	59
Table 3.6	Calculation results	60
Table 3.7	Current density on coppers in series connection at $100kHz$	67
Table 3.8	Current density on coppers in parallel connection at $100kHz$	68
Table 3.9	Electric field intensity in simple geometry	78
Table 3.10	Rated withstand voltages	79
Table 3.11	Electric stress	80
Table 3.12	Specifications of the windings and insulation materials	81
Table 3.13	Switching condition of a half bridge configuration	82
Table 3.14	Insulation medium : Insulation oils and air	82
Table 3.15	Insulation medium : Epoxy resins	83
Table 3.16	Dielectric breakdown test results without active cooling method	85
Table 3.17	Pulse switching test results without active cooling method	85
Table 3.18	AC resistances of LV and HV winding at $20kHz$	86
Table 4.1	Operating condition	94
Table 4.2	Specification of the outer cores and inner cores	94
Table 4.3	Equations	101
Table 4.4	Coefficients of specific loss of MPP cores on datasheets	102
Table 4.5	Loss and size comparison (Sinusoidal excitation, line current = $3.33 [A_{rms}]$)	102
Table 4.6	Coefficients of specific loss of 0.0007" Nanocrystalline	103
Table 4.7	Specific loss of MPP cores at $20kHz$, 0.1T (ID: 14.7mm, OD:26.9mm, HT: 11.2mm))	105
Table 4.8	Loss coefficients of inner and outer cores	108
Table 4.9	Fourier series quantities of trapezoidal waveform with phase shift 30° at $20kHz$, 1Arms	109
Table 4.10	AC resistance [$\mu\Omega/m$] with thickness and frequency	111
Table 4.11	AC resistance [$\mu\Omega/m$] with thickness of trapezoidal current waveform with DAB DC/DC operation phase shift 30° at $20kHz$	112
Table 4.12	Rated withstand voltages IEC60076-3	113
Table 4.13	Electric stress at power frequency	114
Table 4.14	Specifications of MV-MF CWT prototype	115

Table 4.15	Specifications of the windings and insulation materials	115
Table 5.1	Specifications of LV winding [mm]	118
Table 5.2	Specifications of inner and outer cores	133
Table 5.3	Parasitic elements	134
Table 5.4	Specifications of the single phase DAB DC/DC converter for loss measurement	137
Table 5.5	ICWT with $2.7mH$ inductance integration (efficiency η)	138
Table 5.6	ICWT with $4.0mH$ inductance integration (efficiency η)	138
Table 6.1	Dimensions of the proposed planar transformer	158
Table 6.2	Specifications	159
Table 6.3	Terminal leakage inductances	159
Table 6.4	Ratings and losses	167

LIST OF FIGURES

Figure 1.1	Electric power transmission in United States	2
Figure 1.2	Current status of the MV-MF transformer with rated frequency and voltage	3
Figure 1.3	Current status of the MV-MF transformer with rated frequency and power	3
Figure 1.4	Conceptual diagram of SST applications	5
Figure 1.5	Isolated high power resonant/ non-resonant type DC/DC converters . . .	5
Figure 1.6	The first generation SST with IGBT-based cascaded DC/DC stage . . .	8
Figure 1.7	15kV SiC Mosfet based single-stage 6kVDC/400VDC DAB converter . . .	9
Figure 1.8	The transformer less Intelligent Power Substation (TIPS)	12
Figure 1.9	1200V IGBT based three-port three-phase DAB DC/DC converter in Yyd configuration	13
Figure 2.1	One line diagram and phasor diagram of DAB operation	18
Figure 2.2	Circuit mode of operation under zero voltage switching	19
Figure 2.3	One line diagram and vector notation with parasitic effects	19
Figure 2.4	Single-phase DAB converter in half bridge configuration	20
Figure 2.5	One-line diagram with square wave excitation	21
Figure 2.6	Waveforms of Single phase DAB DC/DC converter operation with phase-shift modulation and Power transfer with phase-shift modulation of a single-phase DAB DC/DC converter	22
Figure 2.7	Real and average apparent power with θ_{ps} and k (Red line : Soft switching boundaries)	24
Figure 2.8	(a) $Pi(Delta)$ network, (b) $T(Wye)$ network	26
Figure 2.9	Simplified diagram of single phase DAB converter with T network model .	27
Figure 2.10	Lossless circuit model with finite magnetizing inductance	27
Figure 2.11	$P_o L_m/P_{max}$ with 'm' and ' χ '	28
Figure 2.12	ZVS region with k , χ and m	29
Figure 2.13	Current waveforms with finite magnetizing inductance	31
Figure 2.14	Three-phase DAB DC/DC converter topology in Yy connection	32
Figure 2.15	Waveforms of a three-phase DAB DC/DC converter in Yy connection . .	33
Figure 2.16	Line current waveforms of single phase DAB converters	34
Figure 2.17	Real and average apparent power with θ_{ps} and k (Black line : Soft switching boundary)	35
Figure 3.1	Relationship between variables in Eq3.3	40
Figure 3.2	Transformer design flow chart	42
Figure 3.3	Solenoid winding transformer	43
Figure 3.4	Coaxial winding transformer	45
Figure 3.5	Assembly	46
Figure 3.6	Prototype of MV-MF coaxial winding transformer	47
Figure 3.7	Simplification of curved surface, (a)18 segments (b) 12 segments (c) 6 segments (d) Square shape based on the cross sectional area	47
Figure 3.8	Computation error with the number of segments (x-axis : f/f_δ)	48

Figure 3.9	Skin depth based mesh generation and field distribution (a)3 layers on round shape (80 elements) , (b) 2 layers on round shape(42 elements), (c) 1 layers on round shape(24 elements), (d) 1 layers on square shape based on the cross sectional area	49
Figure 3.10	Computation error with skin depth based mesh generation (a)Inductance , (b) Resistance	49
Figure 3.11	Views on $r - z$ plane (left) and $r - \phi$ plane (right)	50
Figure 3.12	Dimensions and winding arrangement	51
Figure 3.13	Leakage magnetic field distribution in CWT	53
Figure 3.14	6 capacitance equivalent circuit model	54
Figure 3.15	Simplified capacitance equivalent circuit model	58
Figure 3.16	Impedance modulus and argument [$^{\circ}$] with frequency [Hz] of the CWT prototype	62
Figure 3.17	Equivalent circuit model of CWT ($\sim 1/4\lambda$)	63
Figure 3.18	E-field distribution in connection of each measurement	63
Figure 3.19	A circuit representation from HV side by transmission line theory in the range of $1/4\lambda \sim 30\text{MHz}$	64
Figure 3.20	Z_{in} in the range of $3\text{MHz} \sim 30\text{MHz}$	64
Figure 3.21	Switching response with step voltage excitation on the LV side	65
Figure 3.22	Switching response with step voltage excitation on the HV side	65
Figure 3.23	Electric field intensity vs. normalized thickness	69
Figure 3.24	Current density and magnetic field intensity vs. normalized thickness	70
Figure 3.25	Current density in a tubular conductor, $\sqrt{2}[A]$ current excitation at 20kHz	71
Figure 3.26	Current density in a outer tubular conductor, $\sqrt{2}[A]$ current excitation in outer tubular conductor and $-\sqrt{2}[A]$ in inner tubular conductor at 20kHz	71
Figure 3.27	Normalized ac resistance vs. thickness at 20kHz ($r_i = 60\text{mm}$)	72
Figure 3.28	Field distribution	73
Figure 3.29	Multi-tubular winding	74
Figure 3.30	Current density distribution in 2D ($I_{HV\ peak} = \sqrt{2}[A]$, $I_{LV\ peak} = 30 \cdot \sqrt{2}[A]$)	74
Figure 3.31	Effective resistance on LV and HV windings	75
Figure 3.32	Field distribution	76
Figure 3.33	Concentric winding arrangement	80
Figure 3.34	E-field distribution with insulation medium (Mineral oil)	83
Figure 3.35	E-field distribution with insulation medium (air)	83
Figure 3.36	E-field distribution with insulation medium (Epoxy resin)	84
Figure 3.37	Test set-up	86
Figure 3.38	Temp. distribution after 60 minites operation of the pulse switching test	87
Figure 4.1	Assembly of ICWT	90
Figure 4.2	Prototypes of ICWT	90
Figure 4.3	Cross sectional views	91
Figure 4.4	Equivalent circuit model	92
Figure 4.5	One quarter of a simplified model for 3D FEM transient solution	95
Figure 4.6	Peak magnetic field density in single-phase DAB DC/DC converter operation ($3\text{kV}/150\text{V}$ DAB DC/DC conversion at, $\theta_{ps} = \pi/4$, $k = 0.75$)	96

Figure 4.7	Transient waveforms of an ICWT in a single-phase DAB DC/DC conversion at $\theta_{ps} = \pi/4$	97
Figure 4.8	Inductor integration in coaxial winding transformer	99
Figure 4.9	Volume, Weight, Length and loss comparison with respect to the ratio r_o/r_i	101
Figure 4.10	Outer cores	104
Figure 4.11	Specific loss measurement of MPP cores	105
Figure 4.12	Specific losses vs magnetic flux density at 20kHz	106
Figure 4.13	DAB DC/DC converter at $k = 1$ with phase-shift modulation	109
Figure 4.14	trapezoidal current waveform	110
Figure 4.15	Copper tubes	111
Figure 4.16	AC resistance of the multiple of copper tubes	112
Figure 4.17	Winding arrangement	113
Figure 4.18	E-field distribution in 2D (Excitation : $V_1=60kV, V_2=V_3=0$, insulation medium : epoxy resin)	114
Figure 5.1	ICWT prototype with aluminum case and heatsinks- Machine shop built assembly	117
Figure 5.2	Tubular copper and connecting copper for LV winding of ICWT	118
Figure 5.3	Effective resistance on LV windings	118
Figure 5.4	Current density on LV winding of the ICWT prototype in 3D	119
Figure 5.5	Current density distribution on the HV winding (Excitation : inner winding -1Arms, outer winding 1Arms)	122
Figure 5.6	H-field distribution at 10kHz	123
Figure 5.7	Effective resistance on HV windings	124
Figure 5.8	Eddy current in an aluminum case (Excitation : HV winding 3.33Arms, LV winding:51.0A with magnetizing current at 20kHz)	124
Figure 5.9	Configurations with ratio $r_{oc,o}/r_{oc,i}$, m	125
Figure 5.10	Efficiency of the ICWT laboratory prototype with m and load condition	126
Figure 5.11	Loss and real power transfer vs. load	127
Figure 5.12	Efficiency vs. load ($\eta = \frac{P_{in}-P_{loss}}{P_{in}}$)	128
Figure 5.13	Loss measurements from ICWT Prototype with C055927A2 and comparison with analytical solution (turns ratio 1:1)	128
Figure 5.14	Heat pathes from hot-spot to the case and heatsink	129
Figure 5.15	Waveforms of open-circuit tests (turns ratio 4:1)	130
Figure 5.16	B-H curve at 20kHz	130
Figure 5.17	Nominal operation region of the laboratory prototype, SiC based single-phase DAB 6kVDC/400VDC converter and ICWT with C055925A2	131
Figure 5.18	The SiC-based 6kVDC/400VDC DAB DC/DC stage of SST with an inductor ($3.8mH$) integrated coaxial winding transformer	133
Figure 5.19	Impedance plot (turns ratio 15:1)	134
Figure 5.20	Equivalent lumped circuit model of high frequency switching response	134
Figure 5.21	Waveforms of DAB 6kVDC/400VDC operation with the ICWT prototype	135
Figure 5.22	Heat distribution at 6.5kW power transfer without an active cooling method after 60 minute operation	135

Figure 5.23	The configuration of the test set-up, 1200V IGBT-based DAB DC/DC converter for load-test	136
Figure 5.24	1200V IGBT-based DAB DC/DC converter test set-up using NI Crio and LabviewFAPGA	137
Figure 5.25	Thermal images of ICWT with C055925A2 ($\mu_r = 200$) at 10.9kVA, 10.1kW and total transformer loss of 360W	138
Figure 6.1	One line diagram of a three-port three-phase bidirectional isolated DAB DC/DC converter in Yd connection	141
Figure 6.2	Three phase DAB in Yd connection	142
Figure 6.3	Waveforms in Yd connection	143
Figure 6.4	Line current waveforms ($k = 1/\sqrt{3}$)	146
Figure 6.5	Real and average apparent power with θ_{ps} and k (Red line : Soft swathing boundary)	146
Figure 6.6	Proposed three-port three-phase bidirectional and isolated dc/dc converter in Yd connection.)	148
Figure 6.7	Simplified <i>Wye</i> -type (left) and <i>Delta</i> -type (right) primary-referred equivalent circuit of three port system)	149
Figure 6.8	One line diagram of DAB operation and vector notation for voltage and current in phasor form)	150
Figure 6.9	One line diagram Proposed three-port three-phase bidirectional and isolated dc/dc converter in Yd connection)	151
Figure 6.10	Line current waveforms in winding 1	152
Figure 6.11	Current waveforms referred to the primary winding	153
Figure 6.12	Real and average apparent power with θ_{ps} and k (Red line : Soft swathing boundary)	154
Figure 6.13	Terminal leakage inductances measurements	156
Figure 6.14	Leakage magnetic field intensity distribution in planar window area	157
Figure 6.15	H-field distribution - Top view	158
Figure 6.16	Inductance integrated planar MV-MF transformer	159
Figure 6.17	Winding arrangement	159
Figure 6.18	Transient behavior during proposed three-winding planar transformer with three-phase and three port DAB DC/DC converter 3D FEM transient solution	160
Figure 6.19	Current waveforms on HV side of single-phase DAB (blue, topology 2) and phase current waveforms on HV side of three-phase DAB in Yd connection (red, topology 3) - the same DC-link voltages and line inductance are applied	161
Figure 6.20	VA rating on HV side	164
Figure 6.21	VA rating on LV side	165
Figure 6.22	Ratio between real and average apparent power (T/P)	166
Figure 6.23	Prototype of MV-HF series inductance integrated planar transformer	167
Figure 6.24	Laboratory prototype	168
Figure 6.25	Waveforms (500V Div, 5A/Div, 20 μ s/Div)	169

Chapter 1

Introduction

1.1 Current state of the solid state transformer applications

Solid-state-transformer (SST) is a power conversion system made of high power semiconductor components with control circuitry. The concept of the solid-state transformer (SST) dates back to the 1980's, but the major obstacles slowing down the development and commercialization of SST applications at distribution-line levels are the lack of high-frequency, high-power capacity power semiconductor devices, and suitable circuit components such as transformers. Like the commercialization of the IGBTs, which led to a considerable increase in capacity of the power-electronics applications in the 90's, the new materials such as a Silicon Carbide (SiC) devices, high frequency magnetic materials, and a variety of soft-switching techniques under zero-voltage or zero current conditions, allows high-power conversion at higher frequency at a medium voltage level. The operation condition of the solid-state-transformer is, literally, at the limit of commercially available power devices and passive circuit components. With that being said, the reliability of the distribution line applications cannot be compromised.

As stated previously, the limitation of the blocking voltage and power capacity of semiconductor devices have been major obstacles to the realization of this technology. The development and commercialization of wide-bandgap semiconductor power devices, such as SiC power devices, in the 2000s made solid-state-transformer applications more practical at medium-voltage levels. Currently, this technology is being studied and applied to distribution line transformer and automotive applications where the size and controllability are critical [1]~[9]. The hottest research area is in applications at the 10kV~15kV level. This is because the distribution line voltage built in the United States until the 1970s employed 11/12kV. Additionally, railroad voltage in Europe is 15kV as shown in Fig 1.2. It is obviously going to take more time to realize these SST applications as compared to the mature conventional transformer technology in terms of both efficiency and reliability. Nonetheless, the significant advantage of SST appli-

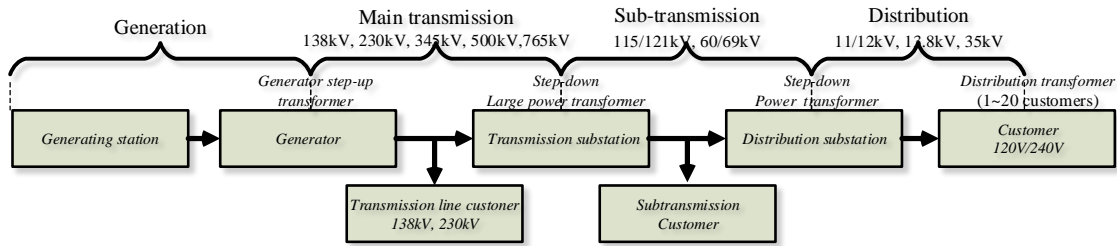


Figure 1.1: Electric power transmission in United States

cations come from its reductions in size and weight. Locomotive-traction applications can take full advantage of SST applications with respect to size and provide even more attention to this technology in Europe, where the locomotive industry is prevalent.

Even though the results and specifications of the prototypes developed in academia and industry are highly limited, the current status of the development of SST applications is plotted on the basis of published papers and reports, shown in Fig 1.2 and Fig 1.3. Most of the medium voltage-high frequency(MV-HF), or medium voltage-medium frequency(MV-MF), transformers are developed for resonant or DAB DC/DC modular converters. The clear tendency of power and voltage ratings of MV-MF transformers is seen differently in academia and industry. The applications developed in industry usually have higher power and voltage ratings, which could be related to the capability of the testing facilities. However, the switching frequency of prototypes developed in industry rarely goes up to 5 kHz even though present power devices are capable of that frequency. This is likely a result of the considerations of size, efficiency and marketability. The insulation level required at medium voltage by the international standards considerably offsets the size and cost reduction at high switching frequency. The power rating of the complete system ranges from several kW up to several MW, but it is made of several converter modules and a single module rarely exceeds 500kVA as seen in Fig 1.3. The voltage rating is typically between 10kV to 15kV which is the practical voltage level in distribution lines and railroad lines in Europe.

The prototypes built in academia typically remain lower than voltage ratings of 3kV and power ratings of 50kVA at high switching frequencies up to 100 kHz. One of the reasons for the voltage level limitations over 3kV could be the difficulty in dealing with it at the college facility level. Additionally, these limits are strictly restricted and observed by international standards. The prototypes built in academia are generally differentiated by high power density at a lower voltage and higher switching frequency than industry applications.

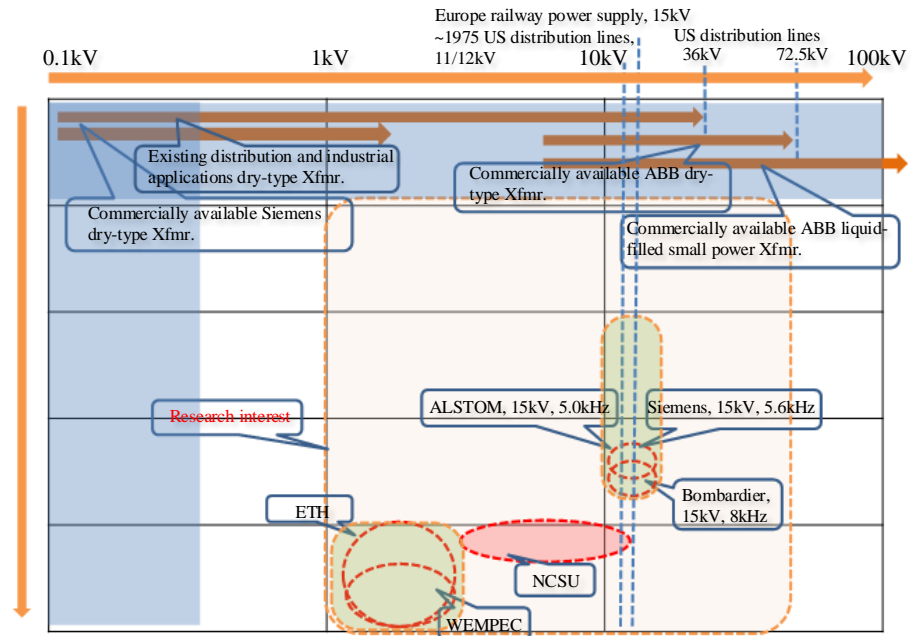


Figure 1.2: Current status of the MV-MF transformer with rated frequency and voltage

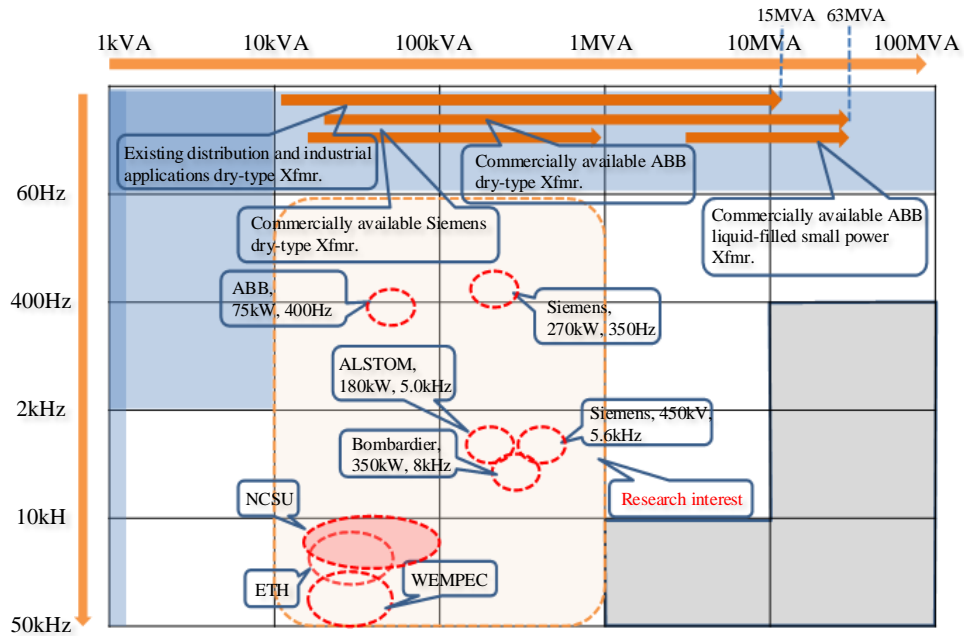


Figure 1.3: Current status of the MV-MF transformer with rated frequency and power

1.2 Medium-voltage and medium-frequency AC-link transformers for SST applications

The term, medium voltage, is typically used in the range of 1kV to 35kV (ANSI/IEEE 1585-2002, IEEE Std 1623-2004), however this term is a rather conventional working definition and varies with international standards and references (the Dept. of Energy defines medium voltage up to 138kV in transmission voltage class). It is reasonable to consider that a distribution line is in the range of medium-voltage (MV), and many next-generation switching converters are targeting for medium-voltage and medium-frequency, or high-frequency, applications. The solid-state transformer is the key element in the Future Renewable Electric Energy Delivery and Management (FREEDM) Systems. It is acting as an energy router to enable active management between distribution line and distributed energy resources with the features like instantaneous voltage regulation, voltage-sag compensation, power-factor correction and DC output. Speaking of the size of the SST applications, the isolated DC/DC stage is one of the key elements that has isolation transformers. The MV-MF transformers for high-power DC/DC converter applications at tens of kHz switching frequency, especially DAB and resonant DC/DC converters, are recently receiving a lot of attention. The MV-MF transformer is a critical element in the DC/DC conversion stage of SST applications because SST applications require galvanic isolation at medium-voltage distribution line and the high conversion ratio between distribution line and end users cannot be efficiently achieved without consideration of the turns ratio of the transformer. Additionally, the required series inductance to store energy and transfer power in the DC/DC conversion stage can be replaced by a leakage inductance of the transformer, or integrated into the transformer. This can provide a considerable improvement with respect to power density and system reliability. Optimization and series-inductance integration are one of the recent active research topics for high-power DC/DC converter applications.

1.2.1 Topologies of SST applications using bidirectional isolated DAB DC/DC conversion

SST applications developed in the FREEDM Systems Center has three conceptual stages, AC/DC, DC/DC and DC/AC as shown in Fig 1.4. A rectifier on the front-end converts the conventional AC line voltage to DC in the medium voltage range. The medium-voltage DC is then converted to low-voltage DC at the voltage level of end users through a high frequency AC-link. The LVDC can be used for DC applications or further conversion to 50/60Hz AC for existing consumer applications.

Isolated high-power DC/DC converter applications are typically categorized by resonant and DAB type, which is of a non-resonant type, and determined by the filter network at the AC-link

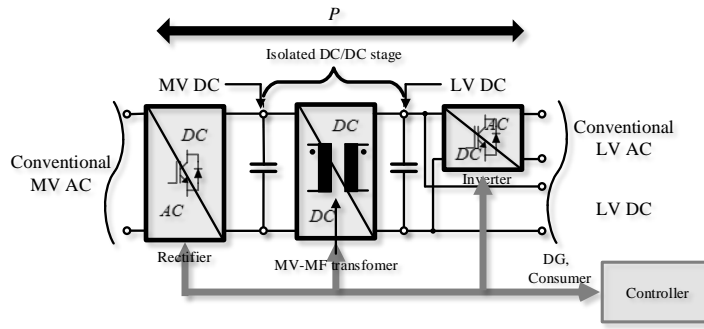


Figure 1.4: Conceptual diagram of SST applications

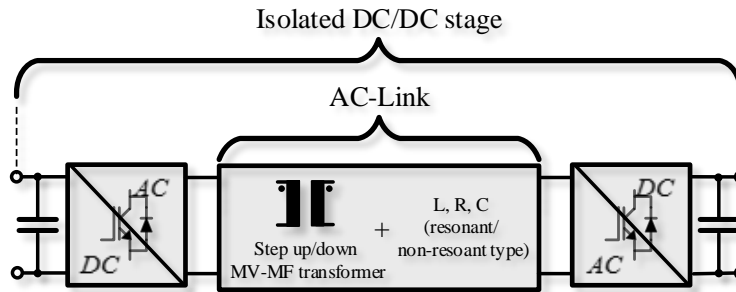


Figure 1.5: Isolated high power resonant/ non-resonant type DC/DC converters

section as in Fig 1.5. Resonant-type converters use the resonant frequency of the resonant tank with a combination of inductors and capacitors. Regardless of the types of topologies, one of the key feature of them is taking advantage of a leakage inductance of the isolation transformers as a power transfer circuit element. This is the main topic of the study in this thesis with converter operation. The comparison of both types of converters is out of scope and not discussed in this thesis. Generally speaking, the non-resonant DAB type converters, which is one of the most popular topologies for MV-HF DC/DC conversion, can be considered superior to others in terms of their simplicity and controllability. The DAB converters have very attractive features for high power applications in terms of low device and component stresses, low switching losses of zero voltage switching, bidirectional power flow, buck-boost operation, and low sensitivity to system parasitics. The DAB-type DC/DC converter is applied to the three different topologies of SST applications developed in the FREEDM Systems Center.

6.5kV IGBT based cascaded DAB DC/DC converter

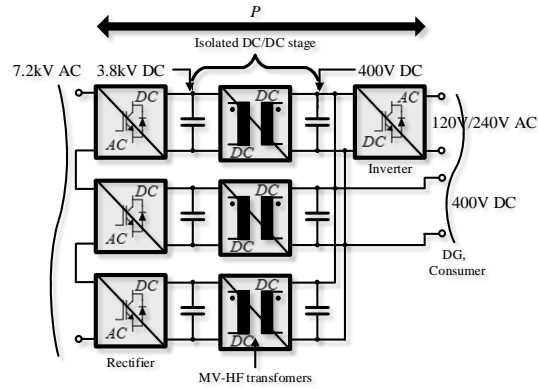
The first generation of the solid-state transformer (SST) applications developed in FREEDM Systems Center is implemented with existing 6.5kV Silicon IGBT power devices in a cascaded configuration in Fig. 1.6 [13]~[20]. The prototype is designed and implemented with an emphasis on SST concept verification. The input is single-phase 7.2 kVAC from the distribution line and single-phase DAB DC/DC converters are cascaded in the DC-link stage due to limitations of the blocking voltage of the silicon-based power devices in Fig 1.6. The voltage stress on the power devices and AC-link transformer is reduced to 3.8kVAC at the switching frequency 3 kHz. The three AC-link transformers are built in the conventional manner, with an amorphous alloy. The required series inductance for the DC/DC conversion stage is achieved through the leakage inductance of the AC-link transformer. The leakage inductance of the transformer is adjusted by changing the winding arrangement and the number of turns. The specifications of the prototypes are shown in the Table 1.1. Iterative numerical study with finite-element method simulation was conducted for optimization. The total power density of up to 1.0 kVA/cm^3 of the transformers at switching frequency 3kHz was achieved and measured by experiment, installed of an IP00 according to IEC standard.

15kV SiC Mosfet based single-stage DAB DC/DC converter

A 15kV SiC MOSFET based SST is implemented with an emphasis on efficiency improvement and size reduction. The power electronics applications at distribution voltage level has been built by series devices and multilevel configurations at today's semiconductor voltage level (6.5kV for silicon device and 10kV for SiC MOSFET). Collaboration and development of the 15kV SiC MOSFET by CREE Inc. and the FREEDM systems center allows a single stage of a DAB DC/DC converter with the minimum number of circuits at operating frequencies up to 20kHz. The single-phase DAB DC/DC converter is composed of a single HF transformer and two active bridges, which are the half-bridge circuits shown in Fig 1.7 (b). The DC/DC conversion stage is comprised of the high-voltage terminal 12kV and low-voltage terminal at 400V. The switching frequency is determined by considering device switching losses of the 15kV SiC MOSFET under development. The laboratory prototype A was built at half scale of the real application, at 6kVDC/400V, to be within a practically applicable range at the FREEDM Systems Center of NSF's ERC headquarter in Fig 1.7.

Full bridge circuits have the advantage of advanced modulation schemes, however more weight is put on the reduction of voltage stress on SiC devices on the MV side in developing phase than the mature Silicon-based low voltage devices. Hence, a standard zero-voltage switching technique with phase-shift modulation is used due to the absence of the zero voltage state of a half-bridge circuit. Reduction of the number of stages and switches considerably simplifies operation and increases system reliability. The development of the AC-link transformer

to meet system requirements of high power density at medium-voltage level was another challenging task. First, the AC-link section in between bridges must contain a certain amount of series inductance as the main energy transfer element of the DAB DC/DC converter in order to avoid adding extra circuit components. However, the series inductance value is usually not in the range of the circuit parasitics, especially the leakage inductance of the transformer, due to the relatively low power rating at medium voltage level of localized SST applications. Another fundamental difficulty of developing prototype at medium voltage is that hardware tests and measurements at medium voltage are high-risk and costly procedures. Therefore, the accurate and analyzable inductor-integrated coaxial winding transformer (ICWT) is introduced as a solution to these challenges and analytically optimized in this thesis. The ICWT prototype is built and the feasibility of the new concept is verified with the functional prototype 6kVDC/400VDC conversion stage of the SST application.



(a) Conceptual diagram



(b) Pictures with AC-link transformers (2009)

Figure 1.6: The first generation SST with IGBT-based cascaded DC/DC stage

Table 1.1: Specifications of SST Gen.1 transformer and AC-link transformer

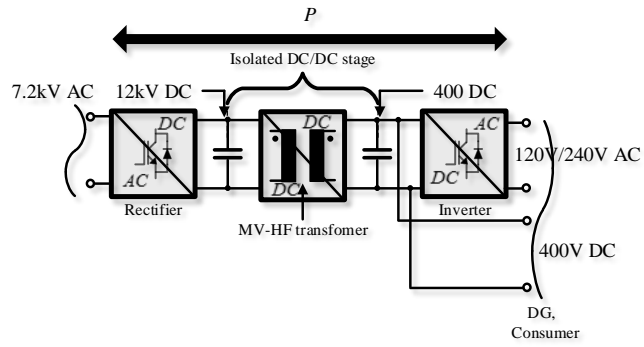
Freq.	Turns ratio	VA	MVDC : LVDC	Required series inductance	Modulation scheme
3 kHz	9.5:1	20kVA	3.8kV : 400V	~30mH	Phase-shift

Table 1.2: Specifications of the AC-link transformer prototypes

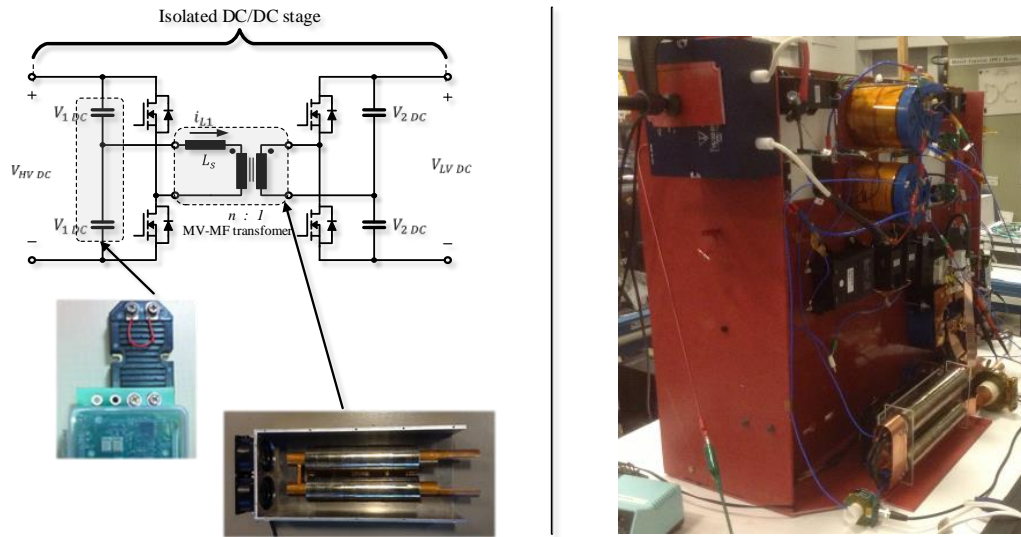
	Core Material	kVA	$L_m[mH]$	$L_l[mH]$	Total loss	Power density
Ver. 1	Metglas SA2605SA1	6.7kVA	235	36	227 W	$0.4 \text{ kVA}/dm^3$
Ver. 2			469	30	194 W	$0.8 \text{ kVA}/dm^3$
Ver. 3			341	30	199 W	$1.0 \text{ kVA}/dm^3$

Table 1.3: Specifications of the Lab. prototype A

Freq.	Connection	Type of AC-link transformer	Turns ratio	MVDC/LVDC	Modulation scheme
20 kHz	Single-phase	ICWT	15:1	6kV : 400V	Phase-shift



(a) Conceptual diagram



(b) Functional prototype model of DC/DC stage with ICWT (Lab. prototype A)

Figure 1.7: 15kV SiC Mosfet based single-stage 6kVDC/400VDC DAB converter

Proposed 12kV SiC IGBT based three-phase and three-port DAB DC/DC converter

The transformer less Intelligent Power Substation (TIPS) is a 15kV SiC-IGBT and 1200 V SiC-MOSFET based SST applications used to connect between the three-phase distribution grid and distributed resources[14], [15]. The TIPS system also follows the three-stage configuration of AC/DC, DC/DC and DC/AC in Fig 1.4 with the three-phase concept to reduce the VA rating of power devices and filter components. The 22 kVDC from the three-phase rectifier is stepped-down to 400VDC through three-phase DAB DC/DC converters with 12kV/10A SiC IGBT co-pack modules. The input stage handles 100 kVA while interfacing with the 13.8 kV utility grid in Fig 1.8. TIPS has a phase-modular three-port DC/DC converters in the isolated DC/DC stage in *Wye – Wye and Delta* (Yyd) connection. Two voltage-source inverters, VSIs, in parallel are used on the LV side to divide the high current on the LV side and reduce losses. The two VSIs are connected in a *Wye* and *Delta* connection respectively to avoid third harmonics issues in three-phase AC systems.

Since the system parameters and configuration of the application was determined on the basis of the fundamental frequency, the unnecessary circulating current generated by the mismatch of the pulse voltage excitation on each port is not completely avoidable. These high-frequency harmonic components degrade power quality and increase the power rating of the components and system loss. In order to adjust circulating power flow and improve the performance of this multi-port system, passive-components, AC-link transformer, is studied from the physical point of view rather than control strategy. An inductor-integrated three-winding shell-type planar transformer is designed and analyzed for three phase and three-port DAB DC/DC converters in Yyd connection. The steady-state operation principle of the proposed topology has also been studied and design parameters of the isolation transformer are analytically determined. The proposed geometry and design method for the ac-link transformer allows us to integrate a large number of bulky inductors required for three-phase DAB operation to the transformer without additional connections and unanticipated parasitic effects while it considerably simplifies the equivalent leakage inductance circuit model and power flow analysis. This configuration is suitable for high power and high step up/down ratio DC/DC converter applications which requires series and/or parallel combination of converters. The experimental and FEM simulation results from prototypes are presented. and validate the theoretical considerations and feasibility of the proposed approach for isolated DC/DC converter applications such as The SST.

1.2.2 Chapter overview

Chapter 1 : The current status of the existing SST applications and the scope of the study are discussed. The topologies, system specifications and design considerations of the laboratory prototypes being built in FREEDM Systems Center are introduced.

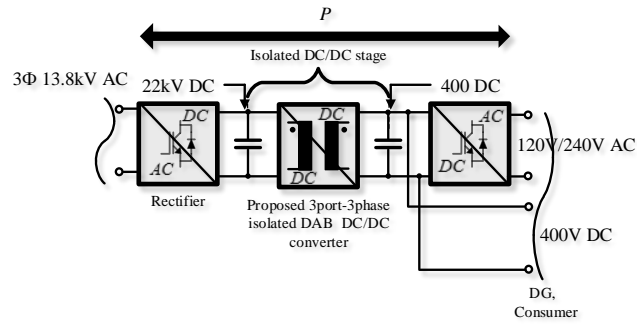
Chapter 2 : The existing DAB high- power and high-frequency DC/DC converters, single-phase and three-phase in Yy connection, are reviewed. The operation principles of both DAB converters are explained based on lossless ideal switching models. Analytical modeling approach under piece-wise linear operation is reviewed for both topologies. The power flow, RMS ratings and zero-voltage switching region with control variables are analytically calculated and shown.

Chapter 3 : The MV-MF coaxial-winding transformers (CWT) is analytically studied with parasitic effects, core and copper losses, and medium-voltage insulation perspective. The simple lumped-element equivalent circuit model is introduced to understand the high-frequency response including common-mode voltage. The switching and insulation test have been done at 20kHz and 6kVAC with the MV-MF CWT prototype. Computer aided design and finite element analysis are intensively used for detailed study of effects on high frequency electromagnetic fields.

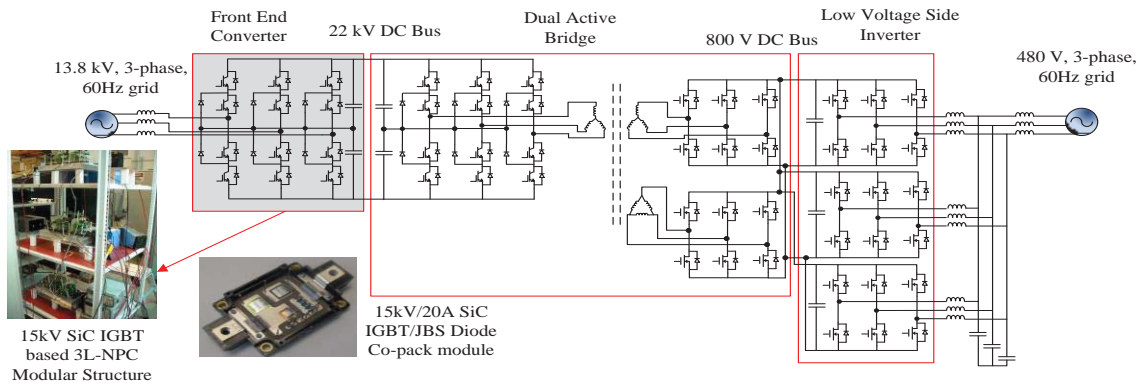
Chapter 4 : The proposed new concept of inductor-integrated coaxial winding transformer (ICWT) is analytically studied and verified. The design methodology including selection of the core material, size optimization and operational boundaries is also discussed. Loss equation with the system parameter and control variable in single-phase DAB DC/DC converter is derived and verified by measurement results. The auxiliary losses from complex geometry, such as Litz wire, case and connectors, are achieved through computer-aided finite-element analysis tools.

Chapter 5 : The ICWT prototype is built and the feasibility of the new concept is verified by experiment. 1200V IGBT-based DC/DC converter is built to collect data for detailed loss model in a wide operation range. Overall efficiency of ICWT is mapped based on the proposed loss equation to find maximum efficiency, and is compared to the loss measurement. Medium-voltage switching and operation tests are implemented by 15kV SiC-based single-phase 6kVDC/400VDC conversion stage of the SST application at power transfer of 7kVA.

Chapter 6 : The proposed three-phase three-port DAB DC/DC converter is introduced and demonstrated in steady-state operation with its soft-switching characteristics. The series inductance-integrated planar three winding transformer is designed for the proposed new three-phase DAB-based SST application. A hardware prototype of the three-phase three-port DAB DC/DC converter and inductor integrated three winding planar transformer are built and tested. The series inductors required on each winding in three phase are combined in transformers and the derived equations for steady-state operation are verified.



(a) Conceptual diagram

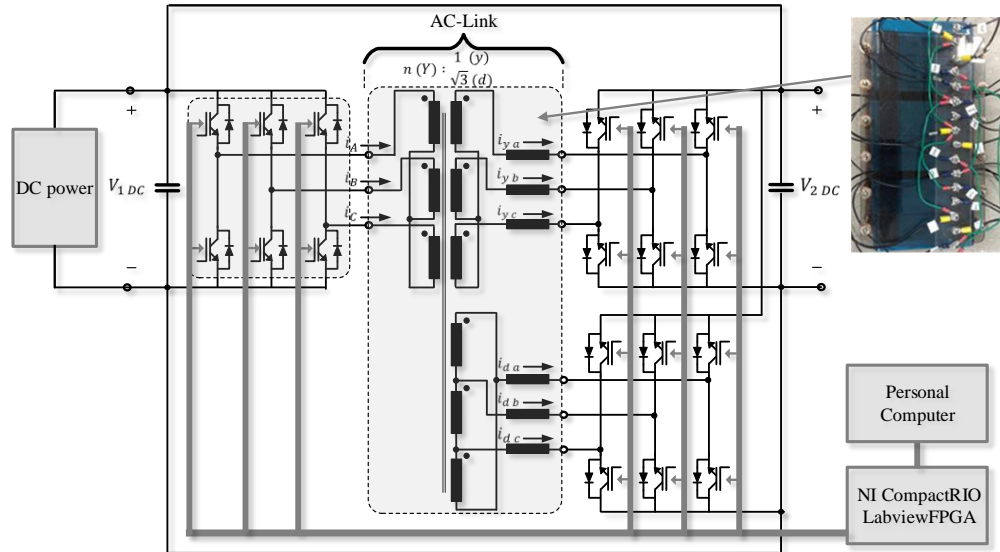


(b) Topology

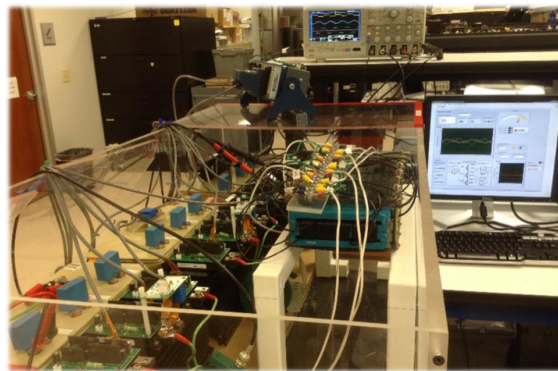
Figure 1.8: The transformer less Intelligent Power Substation (TIPS)

Table 1.4: Specifications of the Lab. prototype B

Freq.	Connection	Type of AC-link transformer	Turns ratio	DC/DC	Modulation scheme
10 kHz	Three pahse in Yyd	Three winding planar	55:4:7	400V : 400V	Phase-shift



(a) Configuration of proposed three-port three-phase DAB DC/DC converter with three-winding planar transformers



(b) Functional prototype model of DC/DC stage with NI Compact Rio and LabviewFPGA (Lab. prototype B)

Figure 1.9: 1200V IGBT based three-port three-phase DAB DC/DC converter in Yyd configuration

1.3 Motivations and contributions

1.3.1 Importance of the magnetics components in AC-link section of the isolated high-power DC/DC converter

Size and efficiency are the essential desirable characteristics and results of the design and implementation of power-conversion system. The magnetics design is therefore of great importance in the design of power electronics applications. It is well known that the size, weight and cost of magnetic components are a strong function of operating frequency. Without considering thermal limits and efficiency requirements, increasing operating frequency by high-frequency switching provides inversely-proportional size reduction of magnetic cores, however, leads to nearly proportional increase in switching losses on the power device. The high-power DC/DC converters, typically resonant and DAB-type DC/DC converters, in AC-link section is fully operating in AC operation without DC components; this is especially true for high-power DC/DC converters. The AC component of the current, which is the source of the magnetic flux variation and loss in magnetic material, has an even stronger relationship with the loss and size. Hence, the magnetic components and resonant and DAB type high power DC/DC converters are even more connected through switching frequency and system parameters. The transformer design has to take many design constraints into account, such as material properties, efficiency, thermal limits, and parasitic effects while considering material properties. The optimization process necessarily requires a good understanding of circuit operation.

Isolation protection is necessary for a grid voltage level to protect against electric shock and comply with strictly observed international standards. The advent of solid state transformer applications does not mean that electromagnetic induction-based transformers will be eliminated by solid-state circuit elements. The galvanic isolation by electromagnetic induction of transformers will not be replaced by electronic circuit components at the medium voltage level as of yet. Besides that, the high conversion ratio between grid and end users is still hard achieve with only switching operation at an acceptable efficiency. Therefore, a high frequency isolation transformer is still a critical part in solid-state transformer applications, and increasing the operating frequency of isolation transformers in medium-voltage level is an emerging research area.

There are two essential issues of the MV-MF/HF transformer in the DAB DC/DC conversion stage of the SST applications. As stated, the AC-link section in between bridges requires a certain amount of series inductance as a main energy transfer element of DAB DC/DC converter operation. However, the series inductance value is usually not in the range of the circuit parasitics, especially leakage inductance of the transformer, due to relatively low-power rating at medium-voltage levels of localized SST applications. A fundamental difficulty of developing a prototype at medium voltage level is that hardware tests and measurements at medium voltage

are difficult, high-risk and requires costly procedures. Therefore, predicting and planning the performance of the transformer under a wide range of operation conditions with accuracy is another significant advantage for minimizing the cost and risks. The design of the magnetics components is always one of the main issues and objectives of high-power and high-frequency DC/DC converters. The key feature in the operation of resonant and DAB type DC/DC converters is fully predicting and utilizing the transformer without external inductors to transfer power and achieve zero-voltage switching. Therefore, the main goal of this thesis is understanding the operation and system characteristics of the MV-MF DC/DC conversion stage and designing suitable and optimized magnetic components for these specific applications.

1.3.2 Contributions

1. Propose a unique design of an inductor-integrated coaxial winding transformer(ICWT) and analytical design methodology including operating mechanism and size optimization.
2. Implement a prototype of the ICWT for 6kVDC/400DC stage of a SST application and verify the new concepts.
3. Conduct computer aided design and finite element analysis(FEA) for detailed study of effects on high frequency electromagnetic fields.
4. Propose and analyze the steady-state operation of the new phase-modular three-port three-phase DAB DC/DC converter.
5. Propose unique design of inductor-integrated three winding planar transformer suitable for three-port three-phase DAB DC/DC converter.
6. Build and test hardware prototypes of scaled-down prototypes of 1200V IGBT-based three-port three-phase DAB DC/DC converter using NI CompactRio and LabviewFPGA .
7. Comprehensive study on DAB DC/DC converters with respect to the proposed inductor-integrated AC-link transformers including optimal operating conditions, efficiency and thermal aspects.

Chapter 2

EXISTING BIDIRECTIONAL AND ISOLATED DAB DC/DC CONVERTERS

2.1 DAB DC/DC converter operations and scope of the study

2.1.1 Investigated topologies of DAB DC/DC converter

The dual-active-bridge DC/DC converter is one of the most prominent non-resonant type converters featuring bidirectional power flow and galvanic isolation for high frequency and high power DC/DC conversion. It consists of one series inductance, used as a filter, at the high frequency AC-link section. The filter element does not necessarily exist as separate element, and can be replaced by parasitic elements of the system such as leakage inductance of the transformer. Both converters at the front and end stages convert DC to high frequency AC for the high frequency isolation transformer at the AC-link section.

Typically, full-bridge or half-bridge circuits are used for single-phase DAB DC/DC operation, while three-leg bridges are used for three phase DAB DC/DC operation. The isolation by AC-link transformers and soft-switching techniques are essential aspects to making DAB DC/DC conversion suitable for MV-MF/HF applications. The symmetric circuit structure with actively controlled power devices provides the bidirectional power transfer, and ensures the VA rating and stress on each component is evenly shared. The buck-boost operation with switching converters provides another degree of freedom in control.

In this thesis, the following different topologies are investigated, including the newly proposed three-port three-phase DAB converter in Yyd connection for SST applications :

1. Single-phase DAB DC/DC converter (Lab. prototype A)

2. Three-phase DAB DC/DC converter in Yy connection
3. Three-phase DAB DC/DC in Yd connection
4. Proposed three-port three-phase DAB DC/DC in Yyd connection (Lab. prototype B)

For comparison, the VA rating of the AC-link transformer on both the LV and HV sides, and the soft-switching region during lossless steady-state operation are studied for each topology. These characteristics are the essence of DAB DC/DC operation and critical design parameters for the power conversion system.

2.1.2 Understanding power flow and soft switching of DAB operation using fundamental frequency component

Power flow of the two port inductance model in harmonic form

It is useful to understand the system's behavior with fundamental frequency components, which has a major impact on system performance. Conceptually, the operation of DAB converter can be seen as an inductor excited by two voltage sources, $v_1 \angle 0$ and $v_2 \angle \theta_{12}$, with a phase difference of θ_{12} , such as the synchronous machine shown in Fig 2.1. Provided that all circuit quantities are sinusoidal at a single fundamental frequency, the steady-state current flow is represented in phasor notation in Eq 2.1.

$$i_{L_s} = \frac{v_2 \angle 0 - v_1 \angle \theta_{12}}{j\omega L_s} \quad (2.1)$$

Hence, the real power is represented in harmonic form by :

$$P = \frac{v_1 v_2 \sin \theta_{12}}{\omega L_s} \quad (2.2)$$

Two important concepts in dual-active bridge operation are easily perceived by the phasor diagram. The bidirectional power flow between any two ports is equally possible, and the direction is only determined by the phase shift.

This calculation results from using the fundamental frequency components by phasor notation in Eq 2.2 and actual models during piece-wise linear operation in Eq. 2.7, and shows good agreement between the two. Note that $v_1 \angle 0$ and $v_2 \angle \theta_{12}$ in Eq 2.2 are the rms value, which is $2\sqrt{2}/\pi$ times of the peak value of the square waveform.

Soft switching region of the two port inductance model in harmonic form

The fundamental frequency in phasor notation also gives an insight to the soft switching technique. An example of the circuit mode of operation under zero voltage switching is shown in

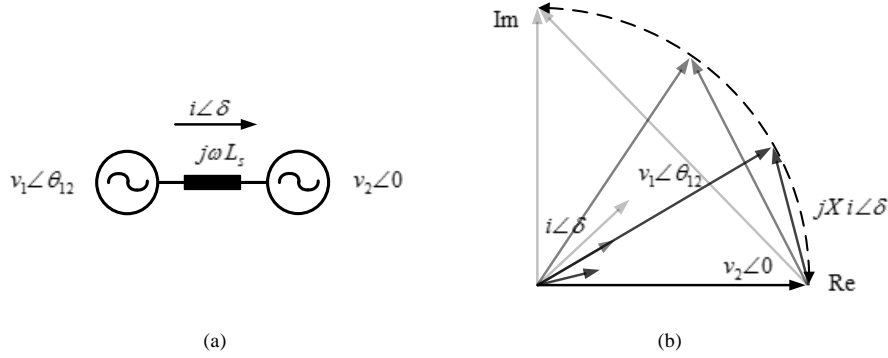


Figure 2.1: One line diagram and phasor diagram of DAB operation

Fig 2.2. Zero-voltage switching (ZVS) is achieved when a turn-on signal is applied to the switch while the anti-parallel diode is on. This switching process of a leading bridge of DAB converter can be represented in a phasor diagram as the line current $i_{L_s} \angle \delta$ lags $v_1 \angle \theta_{12}$ in Fig 2.1. We learn that the line current always lags $v_1 \angle \theta_{12}$ and leads $v_2 \angle 0$ when the magnitude of the voltage vectors are the same. This is an important design parameter for determining the soft switching region of DAB operation for high frequency switching. In the case where the step-up down isolation transformer is used, full controllability over the entire switching region is achieved when the turns ratio of the transformer is the same as the conversion ratio of the DC/DC stage.

The influence of the parasitic elements in the circuitry can simply be estimated with the phasor notation. The dominant parasitics of DAB converters, such as parasitic capacitances of devices and transformer windings and magnetizing inductance of isolation transformers, influence the soft switching region as shown in Fig 2.3. Soft switching is lost at lightly loaded conditions because parasitic capacitances always exist in real circuitry. There are existing studies about utilizing the magnetizing inductance of the isolation transformer to compensate the leading current through the parasitic capacitances with lagging current through the magnetizing inductance. By decreasing the magnetizing inductance, the load appears to lag more and the soft switching region is extended [20].

2.1.3 Modulation schemes of DAB DC/DC converter

A variety of modulation schemes, such as phase-shift, triangular, and trapezoidal, have been introduced and used for DAB DC/DC converter operation [16]~[19]. Among them, the phase-shift modulation (PSM) is the simplest and most common approach for DAB DC/DC converter

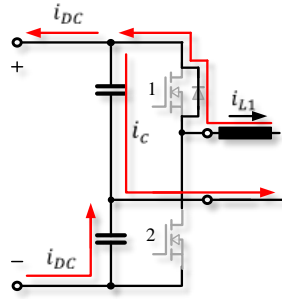


Figure 2.2: Circuit mode of operation under zero voltage switching

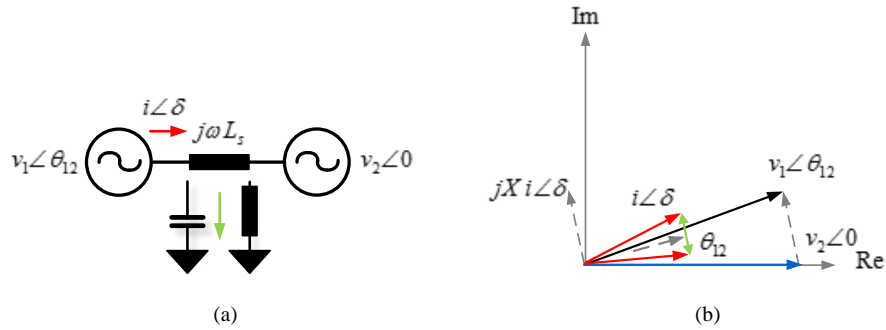


Figure 2.3: One line diagram and vector notation with parasitic effects

operation. The main reason for the wide use of the PSM is the simple control scheme, with phase-shift being the only control variable. On the other hand, the advanced modulation schemes, with additional control variables and switching strategies are used to reduce switching loss and expand the soft-switching region under different load conditions. Nonetheless, the half bridge configuration has an advantage in its low number of parts, cost, and simplicity. As mentioned in the previous chapter, more emphasis is put on the reduction of voltage stress on SiC devices on the MV side in the development phase than the mature Silicon-based low voltage devices. Therefore, laboratory prototype A is built with half-bridge circuit, where only phase-shift modulation is applicable with two voltage levels, V_{dc} and $-V_{dc}$. In this thesis, the scope of the study, with respect to the modulation scheme, is limited to the standard phase-shift modulation scheme.

2.2 Single-phase dual active bridge (DAB) DC/DC converter

The single phase DAB converter consists of two voltage sourced full bridge or half bridge circuits. Both active bridge circuits are connected through an AC-link which consists of a high frequency isolation transformer and series inductance.

The circuit model of the laboratory prototype A is shown in Fig 2.4, which was comprised of half-bridge circuits. Regardless of the topology of the bridges, the DAB converter model can be simplified with a one line diagram with one series inductance L_s as a power transfer element, and two time varying voltage sources v_{1AC} and v_{2AC} in Fig 2.5. The direction of the power flow is determined by the phase shift between two bridges θ_{ps} , and the amount of power flow is controlled by both θ_{ps} and the series inductance L_s .

The analysis for the steady state operation of the DAB DC/DC converters is based on the following assumptions:

1. DC capacitors are infinitely large and the supplied DC voltage is constant.
2. The AC-link stage is comprised of an ideal transformer and series inductance without parasitic effects.
3. The power devices operate as a lossless ideal on-off switch, without parasitic effects.

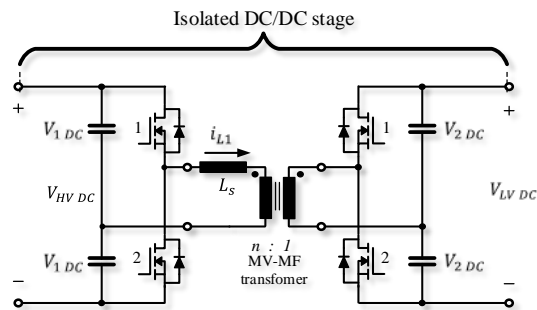


Figure 2.4: Single-phase DAB converter in half bridge configuration

2.2.1 Steady state lossless operation - Single phase DAB

The duty ratio of both converters remains 0.5, with a constant switching frequency and phase-shift modulation scheme. The inductance line current, referred to the HV side i_{L1} , is a function

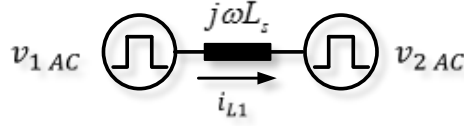


Figure 2.5: One-line diagram with square wave excitation

of $\theta = \omega t$, where ω is the switching frequency. The following calculations are based on the positive power flow from the HV side to the LV side in the range of $0 \leq \theta_{ps} < \pi$.

Two modes of operation are identified for a half switching cycle, and for the rest a half cycle is mirrored. Each side of the half bridge configuration has two different voltage levels $+V_{1DC}$ and $-V_{1DC}$, and $+V_{2DC}$ and $-V_{2DC}$ respectively. The line inductance current repeats every half cycle with reversed sign during steady-state operation, and represented by piecewise linear functions. The general equation of the line inductance current i_{L1} is represented by:

$$i_{L1}[\theta] = \frac{v_{1AC} - n \cdot v_{2AC}}{L_s \omega} \cdot (\theta - \theta_i) + i_{L1}[\theta_i] \quad (2.3)$$

where $i_{L1}[\theta_i]$ is the initial current of each mode.

The line current in each mode is represented with the voltage state of both bridges in Eq 2.4

Mode 1: $0 \leq \theta < \theta_{ps}$, ($v_{1AC} = V_{1DC}$, $v_{2AC} = -kV_{1DC}$)

$$i_{L1\ 1}[\theta] = \frac{v_{1DC}(1+k)}{\omega L_s} \cdot \theta + i_{L1\ 1}[0] \quad (2.4)$$

Mode 2: $\theta_{ps} \leq \theta < \pi$, ($v_{1AC} = V_{1DC}$, $v_{2AC} = kV_{1DC}$)

$$i_{L1\ 2}[\theta] = \frac{v_{1DC}(1-k)}{\omega L_s} \cdot (\theta - \theta_{ps}) + i_{L1\ 2}[\theta_{ps}] \quad (2.5)$$

With system conversion ratio $G = \frac{V_{2DC}}{V_{1DC}}$ and buck-boost conversion ratio $k = n \cdot G$

From the symmetry condition, $i_{L1\ 1}[0] = -i_{L1\ 2}[\pi]$ and $i_{L1\ 1}[\theta_{ps}] = i_{L1\ 2}[\theta_{ps}]$, the initial inductance current values are obtained in Eq 2.6.

$$i_{L1\ 1}[0] = -\frac{V_{1DC}}{\omega L_s} \left(\frac{\pi(1-k)}{2} + d\theta_{ps} \right), \quad i_{L1\ 1}[\theta_{ps}] = i_{L1\ 2}[\theta_{ps}] = -\frac{V_{1DC}}{\omega L_s} \left(\frac{\pi(1-k)}{2} - \theta_{ps} \right) \quad (2.6)$$

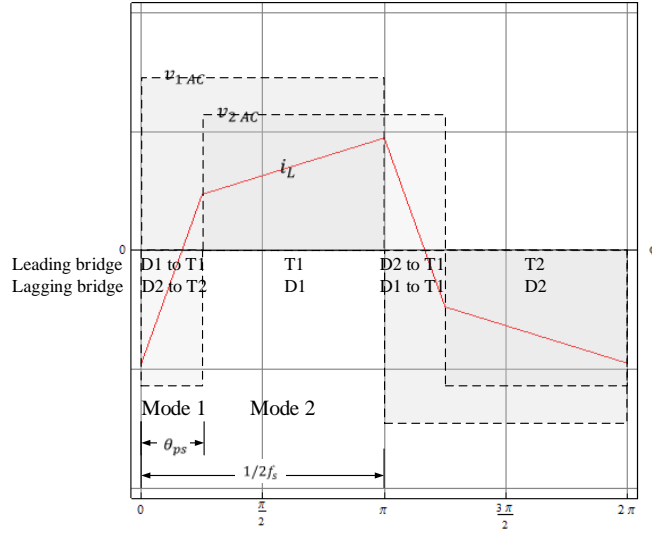


Figure 2.6: Waveforms of Single phase DAB DC/DC converter operation with phase-shift modulation and Power transfer with phase-shift modulation of a single-phase DAB DC/DC converter

The amount of power transfer in the DAB DC/DC converter is represented by the function of θ_{ps} and L_s between two bridges is:

$$P_o = \frac{1}{T_s} \int_0^{T_s} v_{1ac}[t] \cdot i_{L1}[t] dt = \frac{kV_{1DC}^2(\pi - \theta_{ps})\theta_{ps}}{\omega L_s \pi} \quad (2.7)$$

θ_{ps} is controlled by circuit control during operation and L_s is a fixed design parameter which has to be planned when it is designed according to the requirements of the system. The power flow is bidirectional and the maximum power transfer occurs at $\theta_{ps} = \frac{\pi}{2}$ under the given condition in Eq 2.8

$$\frac{dP_o}{d\theta_{ps}} = \frac{kV_{1DC}^2(\pi - 2\theta_{ps})}{\omega L_s \pi} = 0 \quad (2.8)$$

Thus, the maximum power transfer of the single-phase DAB DC/DC converter for any given k is :

$$P_{o\ max} = \frac{k\pi V_{1DC}^2}{4\omega L_s \pi} \quad (2.9)$$

On the basis of the aforementioned assumption, the voltage gain k theoretically varies with θ_{ps} from the minimum value, when $\theta_{ps} = \frac{\pi}{2}$, to infinity. However, k is limited by losses, and the

applicable operating range, in practice, is approximately 0.5 to 1.5.

The root mean square (RMS) values of the voltage and current is of importance when choosing the rating of components and design of the isolation transformer. The rating of the transformer is determined by apparent power on the basis of the rms values, which determines the dimensions of the magnetic core and windings, rather than real power transfer. Assuming the magnetizing current does not exist, the rms value of the line current $i_{L1\ rms}$ with PSM is given by:

$$i_{L1\ rms} = \frac{1}{n} i_{2\ rms} = \frac{1}{T} \int_0^{T_s} i_{L1}^2[t] dt = \frac{V_{1DC} \sqrt{((d-1)^2 \pi^3 + 12k\pi \theta_{ps}^2 - 8k\theta_{ps}^3)}}{\omega L_s 2\sqrt{3}\pi} \quad (2.10)$$

The square wave with a duty ratio of 0.5, $v_{1\ rms}$ and $v_{2\ rms}$ respectively are represented by:

$$v_{1\ rms} = V_{1DC}, \quad v_{2\ rms} = n \cdot V_{2DC} \quad (2.11)$$

Hence, the power rating of the transformer is:

$$T_{VA} = \frac{v_{1\ rms} \cdot i_{1\ rms} + v_{2\ rms} \cdot i_{2\ rms}}{2} = \frac{(1+d)v_{1\ rms} \cdot i_{1\ rms}}{2} \quad (2.12)$$

2.2.2 Soft switching schemes - single phase DAB DC/DC converter

Zero-voltage switching is one of the essential properties of DAB DC/DC converter operation in making this topology suitable for high-power and high frequency operation. The power devices are turned on while the anti-parallel diode is conducting, so the voltage seen from the power device is nearly zero during switch-on transition. The calculation results are in per unit with base numbers:

$$V_b = V_{1DC}, \quad I_b = \frac{V_b}{\omega L}, \quad P_b = V_b I_b. \quad (2.13)$$

To meet this operating condition for each bridge,

For the leading bridge : $i_{L1}[0] \leq 0$,

$$i_{L1}[0] \leq 0, \quad k \leq \frac{1}{1 - 2\theta_{ps}/\pi} \quad (2.14)$$

For the lagging bridge : $i_{L1}[\theta_{ps}] \geq 0$,

$$i_{L1}[\theta_{ps}] \geq 0, \quad k \geq \frac{\pi - \theta_{ps}}{\pi} \quad (2.15)$$

Fig 2.7 (a) shows theoretically achievable real power transfer and soft switching boundaries for the leading and lagging bridges with the phase shift θ_{ps} and k under steady-state operation. The average value of the VA ratings on both sides, which is typically considered VA rating of the transformer, is shown in Fig 2.7 (b). The design parameters can be chosen based on the required power rating of the application, and controllability under soft-switching.

The soft-switching region is defined between the boundaries on both bridges. It should be noted that full control through the entire operation range can be achieved when k is unity. However, reduction of the soft switching region due to parasitic capacitances has to be considered in practice. As the variable k is increased, meaning the transformer's turns ratio is decreased for the same system conversion ratio, the maximum power transfer is also increased with the same inductance value. The same power transfer can be achieved with a lower inductance value, size, and cost with respect to the magnetics components, however, the soft-switching region is also reduced under low load conditions. Losing soft-switching at high-power and high-frequency applications can not only considerably increase the switching losses of the power devices, but also damage the power devices and lead to system failure. Therefore, k is typically limited near unity value unless different modulation schemes are considered for low load condition. This is only applicable with a full-bridge circuit configuration, or if the power converter is designed for very constant load conditions.

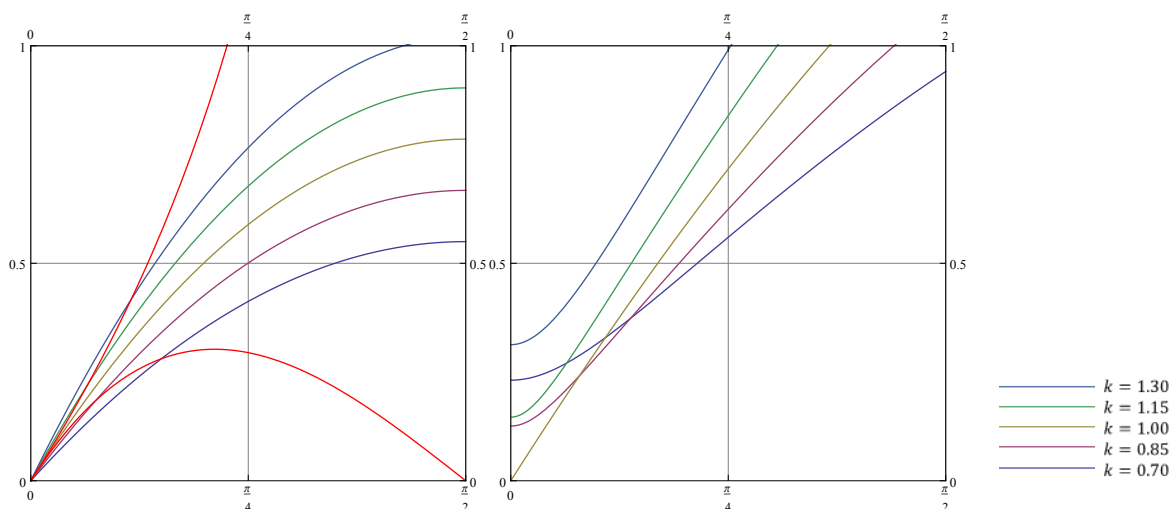


Figure 2.7: Real and average apparent power with θ_{ps} and k (Red line : Soft switching boundaries)

2.2.3 Influence of a finite magnetizing inductance with an asymmetric impedance matrix

Utilization of the finite magnetizing inductance for DAB operation

In more practical approach, the magnetizing current of the isolation transformer is taken into account. The magnetizing inductance of a transformer is usually considered as an infinite number for simplicity but, as matter a of fact, there is always a finite number for the magnetizing inductance in the magnetic components.

Even though the influence of the magnetizing inductance on DAB DC/DC converters has been studied in literature, only a few put weight on the influence of an asymmetrical configuration of the AC-link section. It is customary to assume that the impedance matrix of isolation transformers is diagonally symmetric, and the leakage inductance on each winding is fairly similar. Conventional transformers are generally built in a symmetric manner in symmetric structure, which is a mostly solenoidal structure, hence the leakage magnetic flux of each winding shares space under a balanced condition. However, the coaxial winding transformer (CWT) or the ICWT introduced in this thesis has a considerably different structure and asymmetric impedance matrix in concentric geometry. Therefore, it is worth recognizing the effect of the asymmetric structure and impedance matrix in case where the magnetizing inductance is considerable when compared to the series inductance, L_s .

There is no such difference between transformers and inductors, physically, besides the design purpose and functionality. The magnetizing inductance of transformers has not been a design parameter because it does not play a role as a circuit element. However, it can also be adjusted using the gap between cores, such as inductors or material change. As stated in the previous chapter, it is possible to utilize the effect of the magnetizing inductance to extend the soft switching region of a DAB DC/DC converter by purposefully increasing the lagging current.

A port network is used for circuit analysis with pairs of terminals through which current enters and leaves as a port. The four terminal or two port system is represented by an 2×2 impedance or admittance matrix when the system is a lossless and linear electrical circuit. Hence, two winding transformers can be seen as a 2-port system of the 2×2 impedance matrix with pure inductance elements, without considering the parasitic effects of the capacitances and resistances in Eq 2.16.

$$\begin{bmatrix} Z_{11} & Z_{12} \\ Z_{21} & Z_{22} \end{bmatrix} d/dt \begin{bmatrix} i_1 \\ i_2 \end{bmatrix} = \begin{bmatrix} v_1 \\ v_2 \end{bmatrix} \quad (2.16)$$

The 2-port network can be seen as *Pi* and *T* networks, also known as *Wye*(Y) and *Delta*(D) equivalent circuit models, with lumped elements as in Fig 2.8. Both circuit models are theoretic-

cally identical in different circuit configuration. In this analysis, a *Wye* equivalent circuit model with lumped elements is used, which considerably reduce the complexity of the calculation with respect to circuit analysis.

Considering the inductances of the transformer are referred to as the one side for simplicity, the lumped elements of the *T* network can be seen as leakage inductance on winding 1 ' L_1 ', leakage inductance on winding 2 ' L_2 ', and the magnetizing inductance ' L_m '. Hence, the lossless circuit representation is depicted without the parasitic effects of winding capacitances in Fig 2.10

$$L_m = L_{12} \approx Z_{12} \quad (2.17)$$

$$L_1 = L_{11} - L_{12} \approx Z_{11} - Z_{12} \quad (2.18)$$

$$L_2 = L_{22} - L_{12} \approx Z_{11} - Z_{12} \quad (2.19)$$

L_1 and L_2 does not have to be the leakage inductance of the transformer itself, and they can be external or integrated inductors. The series inductance L_s for power transfer, which is the sum of L_1 and L_2 , is the major factor of power transfer for DAB operation. We are going to give a weight factor to the system symmetry of ' χ ' and an impact of magnetizing inductance ' m '.

$$L_1 = \chi \cdot L_s, \quad (0 < \chi < 1) \quad (2.20)$$

$$L_2 = L_s - \chi \cdot L_1 \quad (2.21)$$

$$L_m = (L_p + L_s) \cdot m \quad (2.22)$$

Hence, the general equations of i_{L1} and i_{L2} referring to the V_1 *DC* side is represented by:

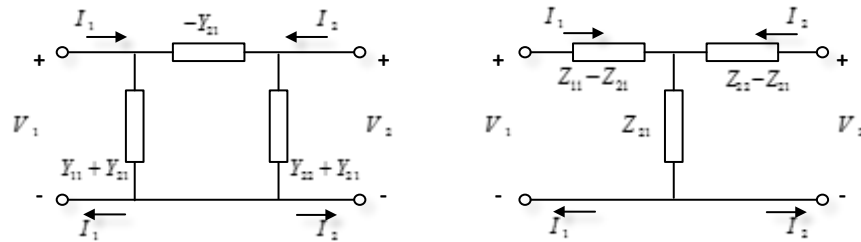


Figure 2.8: (a) *Pi(Delta)* network, (b) *T(Wye)* network

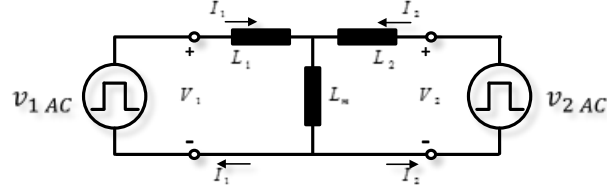


Figure 2.9: Simplified diagram of single phase DAB converter with T network model

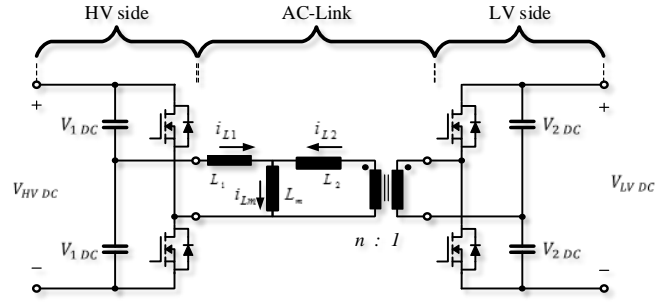


Figure 2.10: Lossless circuit model with finite magnetizing inductance

$$i_{L1}[\theta] = \left(\frac{V_{1DC}}{\omega(L_1 + L_2 \parallel L_m)} - \frac{n \cdot V_{2DC}}{\omega(L_2 + L_1 \parallel L_m)} \right) \cdot \frac{L_m}{L_m + L_1} \cdot (\theta - \theta_i) + i_{L1}[\theta_i] \quad (2.23)$$

$$i_{L2}[\theta] = - \left(\frac{V_{1DC}}{\omega(L_2 + L_1 \parallel L_m)} - \frac{n \cdot V_{2DC}}{\omega(L_1 + L_2 \parallel L_m)} \right) \cdot \frac{L_m}{L_m + L_2} \cdot (\theta - \theta_i) + i_{L2}[\theta_i] \quad (2.24)$$

where $i_{L1}[\theta_i]$ and $i_{L2}[\theta_i]$ are the initial currents of the each mode. If the magnetizing current L_m is not large enough, it may considerably influence the line currents i_{AC1} and i_{AC2} . The amount of power flow in DAB converter operation with phase-shift modulation is revised with finite magnetizing inductance and system symmetry in Eq 2.25.

$$P_o L_m = \frac{k m V_{1DC}^2 \phi(\pi - \phi)}{\pi \omega L_s (m + \chi - \chi^2)} \quad (2.25)$$

Hence, the equation can be simplified with using the scale factor and Eq 2.7

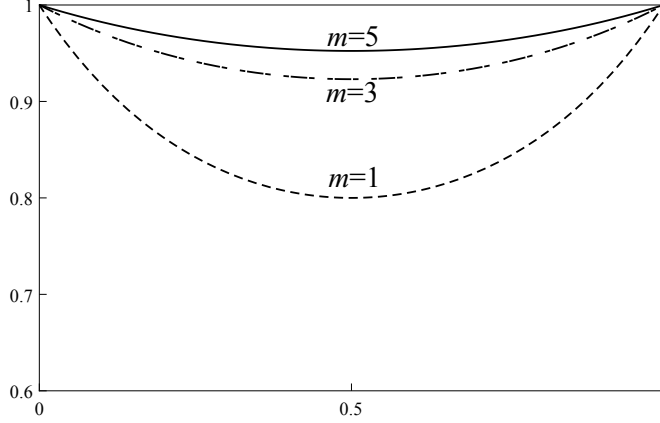


Figure 2.11: $P_o L_m / P_{max}$ with 'm' and ' χ '

$$P_o L_m = \frac{m}{m + \chi - \chi^2} \cdot P_o \quad (2.26)$$

The equations of line current and the amount of power transfer with a finite magnetizing inductance are a function of χ and m . As can be expected intuitively, the derived equations in Eq 2.23 ~ Eq 2.26 become the same as equations Eq 2.3 ~ Eq 2.7 with m going to infinity. Additionally, $P_o L_m$ becomes the same as P_o when χ is zero or unity as seen in the scaling factor and Fig 2.26. When the system is symmetric ($\chi=0.5$), the effect of magnetizing inductance is maximized as shown in Fig. 2.11. Theoretically, there is no impact on power transfer by the magnetizing inductance, regardless of its value, when any of the ports does not have a series inductance value.

Conventional transformers are generally built in a symmetric manner so that the case when $\chi=0.5$ has been considered in order to understand the impact of the magnetizing inductance of the transformers. However, the coaxial winding transformer (CWT) or ICWT have a considerably different structure and impedance matrix, so it is worth recognizing the effect of the magnetizing inductance with system symmetry in the case where the magnetizing inductance is considerable compared to the series inductance L_s .

The influence on the soft switching region with an asymmetric impedance matrix

The total series inductance value L_s , which is the sum of L_1 and L_2 , has to be in a certain range to achieve the required power transfer of the DAB converters. If the magnetizing inductance value is competitive with the leakage inductance values, the purposefully designed asymmetric impedance matrix of the AC-link section of the DAB converter affects the ZVS region of each bridge to different degrees. The initial current at switching under no load conditions on the

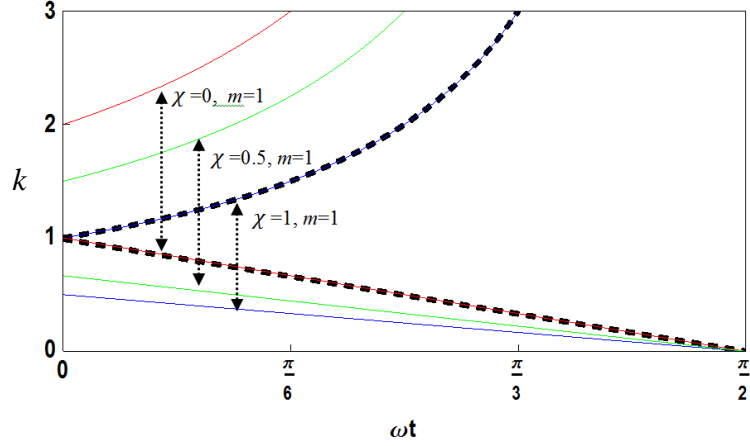


Figure 2.12: ZVS region with k , χ and m

primary and the secondary sides is derived in the same manner from the mirrored waveform of steady state operation . The initial inductance current values are obtained in Eq 2.27.

$$i_{L11}(0) = \frac{\pi V_i(\chi - 1 + (k - 1)m)}{2\omega L_s(m + \chi - \chi^2)}, \quad i_{L12}(\phi) = \frac{\pi V_i(k\chi + (k - 1)m)}{2\omega L_s(m + \chi - \chi^2)} \quad (2.27)$$

The condition for the devices to stay in the ZVS region with phase shift modulation is:

For leading bridge : $i_{L1}[0] \leq 0$,

$$\frac{\chi - 1 + (k - 1)m}{(m + \chi - \chi^2)} < 0 \quad (2.28)$$

For lagging bridge : $i_{L1}[\theta_{ps}] \geq 0$,

$$\frac{k\chi + (k - 1)m}{(m + \chi - \chi^2)} > 0 \quad (2.29)$$

As shown with single fundamental frequency operation, the finite magnetizing inductance adds a lagging current and extends the ZVS region as seen in Fig 2.12. The line current waveforms on both bridges and the magnetizing currents are shown in different operating conditions in Fig 2.13. As seen in the case of $\chi = 0$, the lagging current generated by magnetizing inductance is fully added to the line current on the leading bridge, which is clearly shown in the waveform under no load conditions with $\theta_{ps}=0$. The lagging current on the leading bridge provides an additional margin for ZVS turn-on for the leading bridge while having no impact on the lagging bridge. The series inductances shared on each side have different effects on the ZVS region of each bridge. Parasitic effects are not considered and the devices are assumed to

be ideal switches.

In the case of transformers, a winding that has a lower self inductance value has greater benefit in soft switching. The investigated coaxial winding transformer, which has a considerable asymmetric impedance matrix, needs to take this into account for system configuration. In the case where the leakage inductance of the transformer is not in the specific range required for power transfer, which is often the case, the location of the external inductors can also be considered.

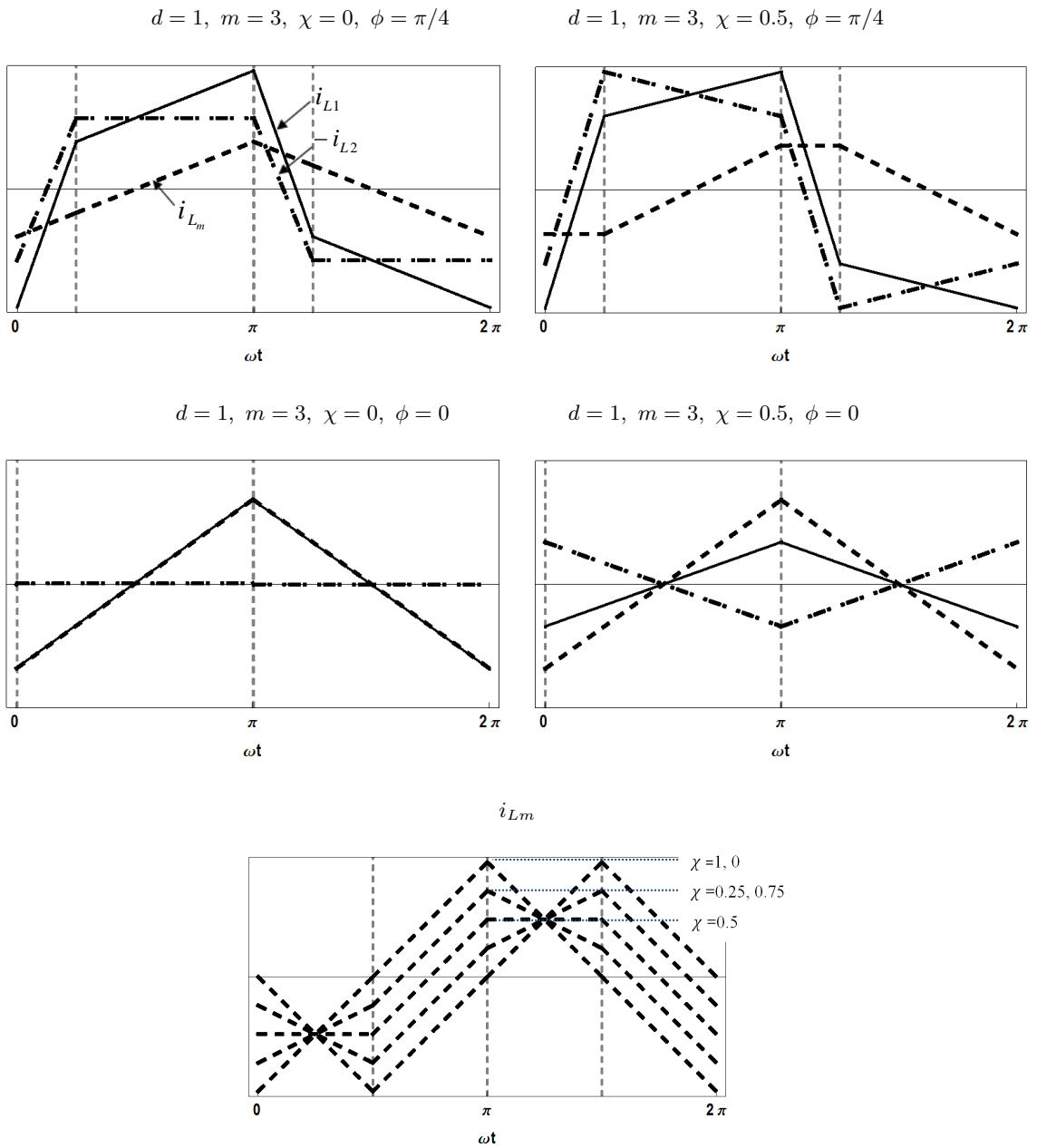


Figure 2.13: Current waveforms with finite magnetizing inductance

2.3 Three-phase dual-active bridge converter topology - Yy connection

The three-phase DAB DC/DC converters previously introduced are conventionally configured in a three-phase Yy connection as shown in Fig 2.14. The three-phase DAB DC/DC converters have the advantage with a lower VA rating and stress on circuit components, in exchange for requiring a high number of power devices when compared to single-phase DAB DC/DC converter topology.

2.3.1 Steady state lossless operation Three phase Yy connection

The approach to deriving inductance current and design parameters is the same as with single-phase DAB DC/DC converter applications. There are a total of six modes for two distinct regions of operation between $0 \leq \theta_{ps} < \pi/3$ and $\pi/3 \leq \theta_{ps} < \pi/2$. The transition of the line current between modes is more sinusoidal than that of the single phase DAB operation.

Six modes of operation with phase-shift modulation are identified for each operating regions, and equations are derived in Appendix B. The amount of power transfer with phase-shift modulation in a three-phase DAB DC/DC converter in Yy connection is shown in Eq 2.30.

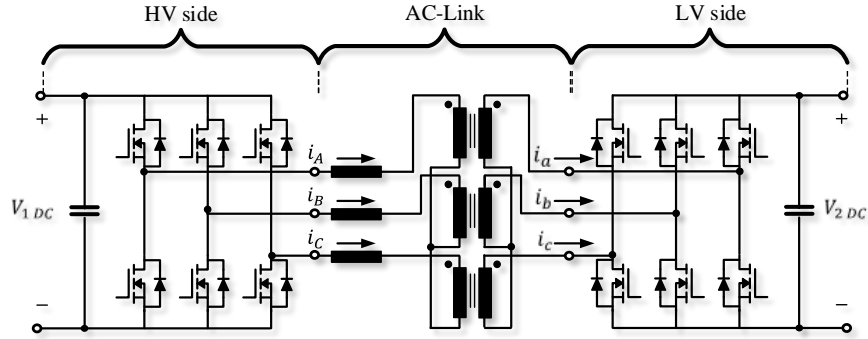


Figure 2.14: Three-phase DAB DC/DC converter topology in Yy connection

$$\begin{cases} P_o Yy = \frac{kV_{1DC}^2(4\pi - 3\theta_{ps})\theta_{ps}}{6\omega L_s \pi}, & \text{for } 0 \leq \theta_{ps} < \frac{\pi}{3} \\ = \frac{kV_{1DC}^2(\pi^2 - 18\pi + 18\theta_{ps}^2)}{18\omega L_s \pi}, & \text{for } \frac{\pi}{3} \leq \theta_{ps} < \frac{\pi}{2} \end{cases} \quad (2.30)$$

the line inductance current $i_{L1 rms}$ is given by:

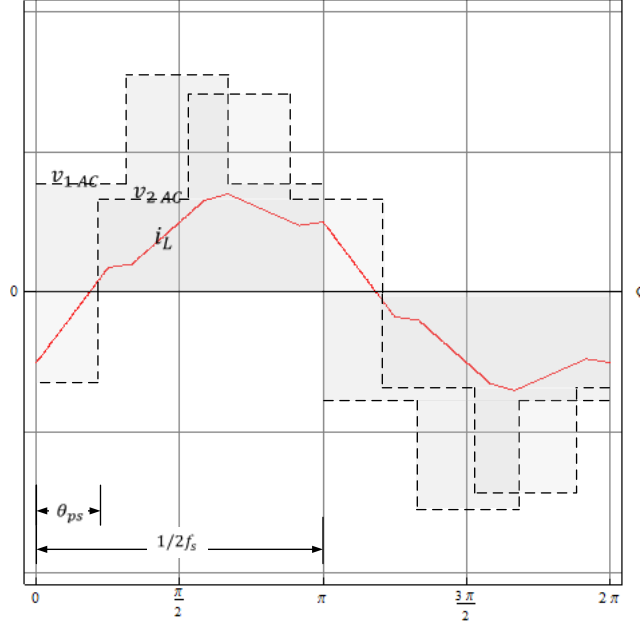


Figure 2.15: Waveforms of a three-phase DAB DC/DC converter in Yy connection

$$\begin{cases} i_{L1 Yy rms} = \frac{V_{1DC} \sqrt{5(k-1)^2 \pi^3 + 54k\pi\theta_{ps}^2 - 27k\theta_{ps}^3}}{9\sqrt{3}\pi\omega L_s}, & \text{for } 0 \leq \theta_{ps} < \frac{\pi}{3} \\ = \frac{V_{1DC} \sqrt{(5-9k+5k^2)\pi^3 - 9k\pi^2\theta_{ps} + 81k\pi\theta_{ps}^2 - 54k\theta_{ps}^3}}{9\sqrt{3}\pi\omega L_s}, & \text{for } \frac{\pi}{3} \leq \theta_{ps} < \frac{\pi}{2} \end{cases} \quad (2.31)$$

where $i_{L1 rms} = i_{A rms} = n i_a rms$

$v_{1 Yy rms}$ and $v_{2 Yy rms}$ of the three-phase converter are represented by:

$$v_{1 Yy rms} = \frac{\sqrt{2}}{3} V_{1DC}, \quad v_{2 rms} = n \frac{\sqrt{2}}{3} V_{2DC} \quad (2.32)$$

Hence, the VA rating of the transformer is shown in Eq 2.33.

$$T_{VA Yy} = \frac{v_{1 rms} \cdot i_{1 rms} + v_{2 rms} \cdot i_{2 rms}}{2} = \frac{(1+k)v_{1 rms} \cdot i_{1 rms}}{2} \quad (2.33)$$

In order to generalize and compare converter topologies under the same load condition, different base values are used based on the maximum power transfer. The scaling factor for the three-phase DAB DC/DC converter in a Yy connection that matches the maximum power transfer in both cases is 9/7:

$$\frac{P_o \text{ single phase} |_{\theta_{ps}=\frac{\pi}{2}}}{P_o Yy |_{\theta_{ps}=\frac{\pi}{2}}} = \frac{9}{7} \quad (2.34)$$

The inductance value per phase of a three-phase transformer in Yy connection should be scaled down by a factor of $\frac{7}{9}$ to achieve the same amount of maximum power transfer with a single-phase DAB DC/DC converter. Hence, the base numbers for a three-phase DAB DC/DC converter in Yy connection are:

$$V_b Yy = V_{1DC}, I_b Yy = \frac{9}{7} \frac{V_b}{\omega L}, P_b Yy = V_b I_b. \quad (2.35)$$

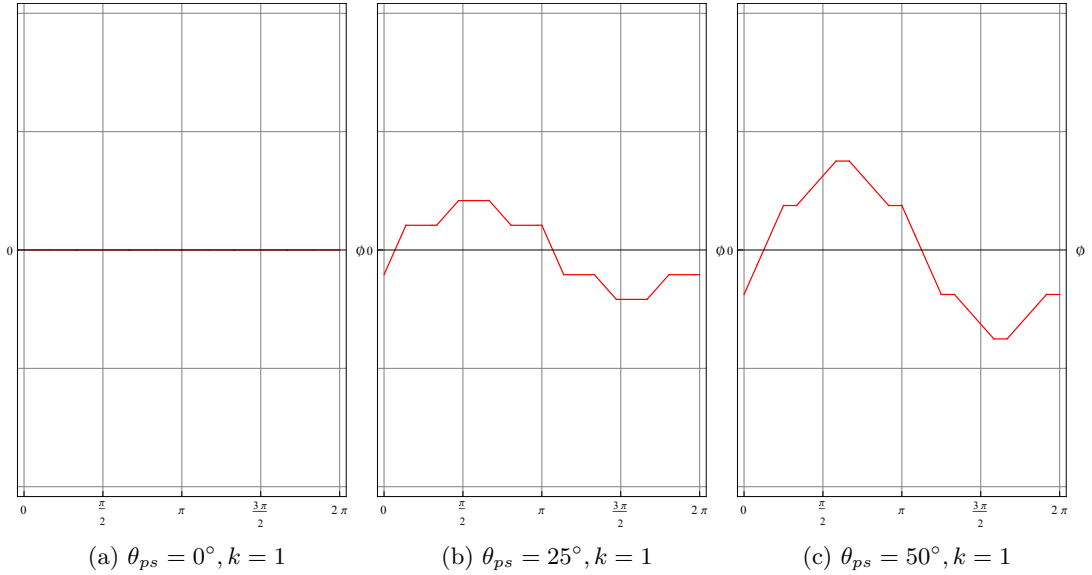


Figure 2.16: Line current waveforms of single phase DAB converters

2.3.2 Soft switching scheme - Three phase Yy connection

The same approach used for single phase DAB converters is applied for six modes with two distinct regions of operation between $0 \leq \theta_{ps} < \pi/3$ and $\pi/3 \leq \theta_{ps} < \pi/2$. In order to meet the given conditions for each bridge four equations are derived.

For the leading bridge : $i_{L1}[0] \leq 0$,

$$\begin{cases} k \leq \frac{18\pi}{7(2\pi-3\theta_{ps})}, & \text{for } 0 \leq \theta_{ps} < \frac{\pi}{3} \\ k \leq \frac{9(2\pi-3\theta_{ps})}{14\pi}, & \text{for } \frac{\pi}{3} \leq \theta_{ps} < \frac{\pi}{2} \end{cases} \quad (2.36)$$

For the lagging bridge : $i_{L1}[\theta_{ps}] \geq 0$,

$$\begin{cases} k \leq \frac{6\pi}{7(\pi-2\theta_{ps})}, & \text{for } 0 \leq \theta_{ps} < \frac{\pi}{3} \\ k \leq \frac{27(\pi-2\theta_{ps})}{14\pi}, & \text{for } \frac{\pi}{3} \leq \theta_{ps} < \frac{\pi}{2} \end{cases} \quad (2.37)$$

The real and apparent power transfer, with soft switching boundaries, of the three-phase DAB DC/DC converter in a Yy connection is shown in Fig 2.17 in the same manner as it was for single-phase DAB applications.

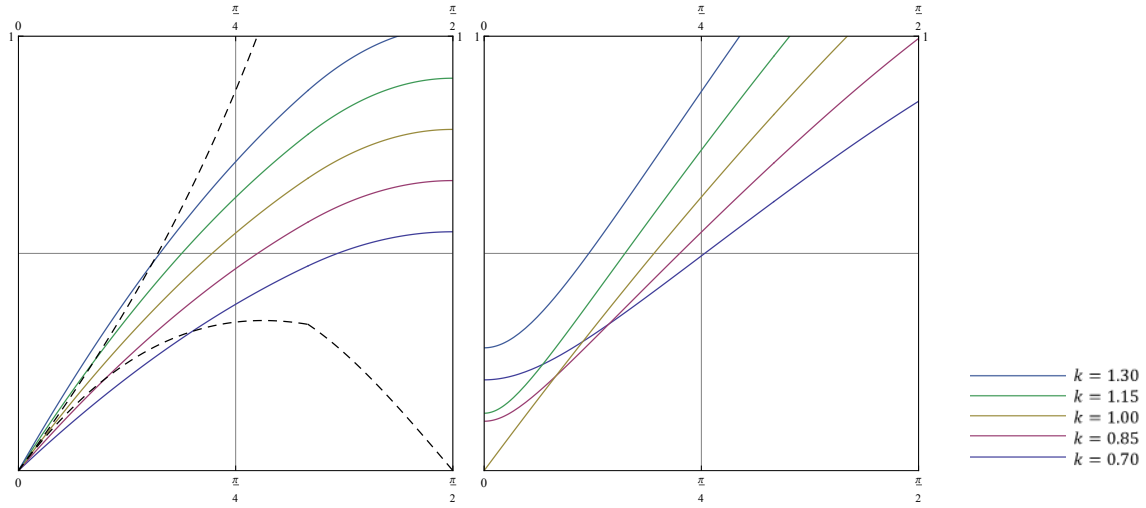


Figure 2.17: Real and average apparent power with θ_{ps} and k (Black line : Soft switching boundary)

2.4 Summary

The lossless steady state operation of the two existing DAB DC/DC converter topologies, single phase and three-phase, has been analytically derived in a linear piece-wise fashion. The VA ratings on each side of the AC-link section during operating conditions is investigated, and soft-switching regions are also defined. Specifically, detailed study with the weight factor

on the symmetry of the impedance matrix of the AC-link section including effects of magnetizing inductance have been conducted to investigate the influence on the power transfer and soft switching regions. The single-phase DAB DC/DC converter with phase-shift modulation is applied to the 15kV SiC-based Lab. prototype A. A comparison between the investigated topologies will be discussed in chapter 6. The detailed process for the calculations is shown in Appendix B.

Chapter 3

MEDIUM-FREQUENCY AND MEDIUM-VOLTAGE COAXIAL WINDING TRANSFORMER

There are many high frequency transformers used commercially in the range of several hundreds of kHz for low voltage switching mode power electronics applications. However, grid connected transformers are the same physical transformers, based on electromagnetic induction at 60Hz line frequency, that have been used since the 1900's. As solid-state transformers and a variety of high frequency materials are introduced, a lot of attention has been drawn to MF/MV transformers to replace conventional line transformers for power electronics applications.

The advent of solid state transformer applications does not mean that electromagnetic induction-based transformers will be eliminated by solid-state circuit elements. The galvanic isolation by electromagnetic induction of transformers cannot be replaced by electronic circuit components at the medium voltage level as of yet. Isolation protection is necessary for a grid voltage level to protect against electric shock and comply with strictly observed international standards. Besides that, the high conversion ratio between grid and end users is still hard to achieve with only switching operation at an acceptable efficiency. Therefore, a high frequency isolation transformer is still a critical part in solid-state transformer applications, and increasing the operating frequency of isolation transformers in medium-voltage level is an emerging research area.

In practice, development and testing of MV/MF transformers in the range of several kV at several tens's of kHz in a college facility is a truly challenging task. Designing transformers at a medium-voltage level not only requires strong technical knowledge and experience, but also elaborate manufacturing facilities that include winding, insulation and packaging capabilities.

A dry-type coaxial winding structure has been used in prototypes for several reasons. First, a

dry-type configuration reduces environmental effects and manufacturing difficulty. In the case of conventional methods for designing medium-voltage transformers, a large number of turns and multiple sections are used with insulation materials, usually submerged in liquid insulation oil or casted. The permittivity of insulation materials are typically 2~4 times higher than air and simply scales up parasitic capacitance of transformer windings at the same rate. The distance between windings can be shortened with high dielectric strength of the insulation ; however, this is another factor that will increase parasitic capacitances by increasing the electric energy stored in the space with a high electric field. The parasitic capacitances of the transformer are undesirable because intensive voltage ringing could be generated during high dV/dt pulse switching transitions which could damage power devices and circuit elements. Also, the soft switching region of the DAB converter is narrowed down by adding leakage leading current. The increase in switching losses by losing ZVS during lightly loaded conditions is another important concern for DAB converter design. Additionally, the performance of the coaxial winding transformer is more predictable in simple geometry with a very low number of turns.

The design procedures are studied with an analytical approach, and verified with numerical methods using computer-aided finite-element simulation for an accurate results of parasitic effects and electric stress level. The important features and requirements of the MF-MV transformer are:

1. Minimization and optimization of transformer volume and losses.
2. Limitation of hot-spot temperature under $180^{\circ}C$, targeting class H according to international standard.
3. Integration of the required series inductor in the transformer for high-power DAB DC/DC operation.
4. Accurate prediction of parasitic effects and strategies for reliable insulation in medium voltage level switched mode operation.
5. Verification and revision with FEM Computer-aided simulation in three dimensional geometry.
6. Implementation of the prototype, and verification of the design by experimentation.

3.1 Summary of transformer design equations and parameters

Regardless of the geometry, the fundamental principles used to explain the operation of the transformer are *Faraday's law of induction* and *Ampere's law*.

One dimensional electric and magnetic circuit analysis is simply understood with electromotive force and magnetomotive force, shown in Eq 3.1 and Eq 3.2. Analysis for transformer design using a magnetic circuit is based on the dimensional approximation.

$$\text{Electromotive force}(EMF) = \oint E \cdot dl \quad (3.1)$$

$$\text{Magnetomotive force}(MMF) = I_{enc} = NI = \oint H \cdot dl \quad (3.2)$$

In practice, transformer design involves in numerous factors, not only from electrical aspects, but from mechanical and thermal aspects as well. All of these requirements have to be met for reliable and efficient transformer design, and it is almost impossible to formulate with one equation in a closed form. Therefore, transformer design requires an iterative procedure with several fundamental equations and a detailed study on auxiliary effects.

The fundamental equations for preliminary transformer design:

1. Excitation voltage related equation by *Faraday's law of induction*:

$$V = K_f f N B_{ac} A_c \quad (3.3)$$

2. Volume and power capacity related equation:

$$A_p = W_a A_c = \frac{V_p I_p + V_s I_s}{B_{ac} f J K_f K_u} \quad (3.4)$$

- The area product A_p is the product of the effective cross section area of the magnetic core A_c and the window area W_a . A_p is a customary technical term used to estimate transformer size with relation to power rating. These equations can be analytically derived in a closed form.

3. Copper loss related equation:

$$P_{Cu} = Volume_{cu} \cdot \rho_{cu} J^2 \quad (3.5)$$

- The starting value of the current density, J , is determined according to copper loss requirements before considering high frequency effects. The current density is assumed to be uniform in the entire copper area.

4. Core loss related equation *Steinmetz's equation*:

$$P_{Co} = Volume_{Co} \cdot C B_{ac}^\alpha f^b \quad (3.6)$$

- *Steinmetz's equation* is a function of the maximum value of the magnetic flux density B_{ac} and the operating frequency. The excitation voltage is assumed to be purely sinusoidal, without DC components, and the coefficients are extracted empirically. The starting value of B_{ac} is determined according to material characteristics and core loss requirements.

The most fundamental equation for preliminary determination of the configurations of transformers with given ratings is Eq 3.3. The relationship between the variables is shown in Fig 3.1.

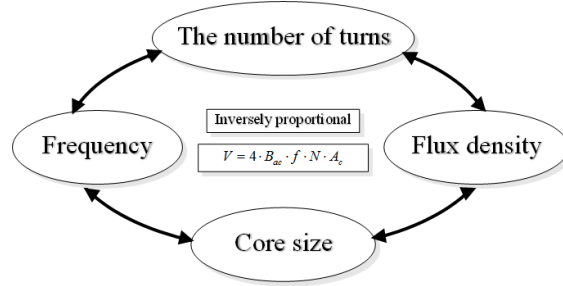


Figure 3.1: Relationship between variables in Eq3.3

Starting variables : B_{ac} , J , A_c

The selection of starting point is important in reducing the number of iterations, and can be used as is for a preliminary design. The starting parameters: power rating, voltage rating, current rating, and operating frequency, are typically given as constant numbers. The variables B_{ac} , J , A_c have to be determined by reasonable estimation and material characteristics at the designer's discretion.

B_{ac} is the source of the specific magnetic loss and J is the source of the specific electric source. These two values are a direct indication of transformer losses. B_{ac}^α ($\alpha \cong 2$) is proportional to the specific core loss ($[W/kg]$ or $[W/dm^2]$), and J^2 is proportional to the specific copper loss under pure sinusoidal operation without considering parasitic effects. The even distribution of the loss in space is one of the most important design factors. System degradation and failure is more closely related to the congested heat at hot-spot rather than the total loss of the transformer.

It is noted that power density and efficiency are in Pareto optimum and are always a trade-off unless the material characteristics are changed. Size and cost reduction of the cores can be achieved with a high B_{ac} , however it is restrained by thermal and efficiency requirements.

Another constraint of B_{ac} is the saturation flux density of the magnetic materials, and it depends on material characteristics and operating conditions. Therefore, proper selection of magnetic material is also an important part of the design process. Similarly, the amount of copper used can be reduced with high the current density, however it is limited by the hot-spot temperature.

Current density of the copper wires is typically in the range of $230A/cm^2$ to $550A/cm^2$ with forced cooling. The insulation material and cooling method could be another factor in determining current density and high frequency effects, such as eddy and proximity effects, and become important design concerns for high frequency applications. On the other hand, the saturation flux density of the magnetic material is highly material dependent and typically ranges from 0.3 T of ferrite material to 2.0 T silicon-iron material among commercially popular materials..

Cross sectional area of the magnetic cores A_c is the most flexible value depending on the core type and winding arrangement. The starting point can be estimated by the approximate ratio between copper area in the window area A_{Cu} and the cross sectional area of the core A_c according to the type of the transformer.

$$A_c = \frac{s_{in} + s_{out}}{K_f \cdot f \cdot B_{ac} \cdot J \cdot A_{Cu}} = \left(\frac{s_{in} + s_{out}}{K_f \cdot f \cdot B_{ac} \cdot J \cdot (A_{Cu}/A_{Co})} \right)^{1/2} \quad (3.7)$$

A detailed study of design procedures has been introduced in many other works; therefore, it is simply shown in the flow chart with equations in Fig 3.2.

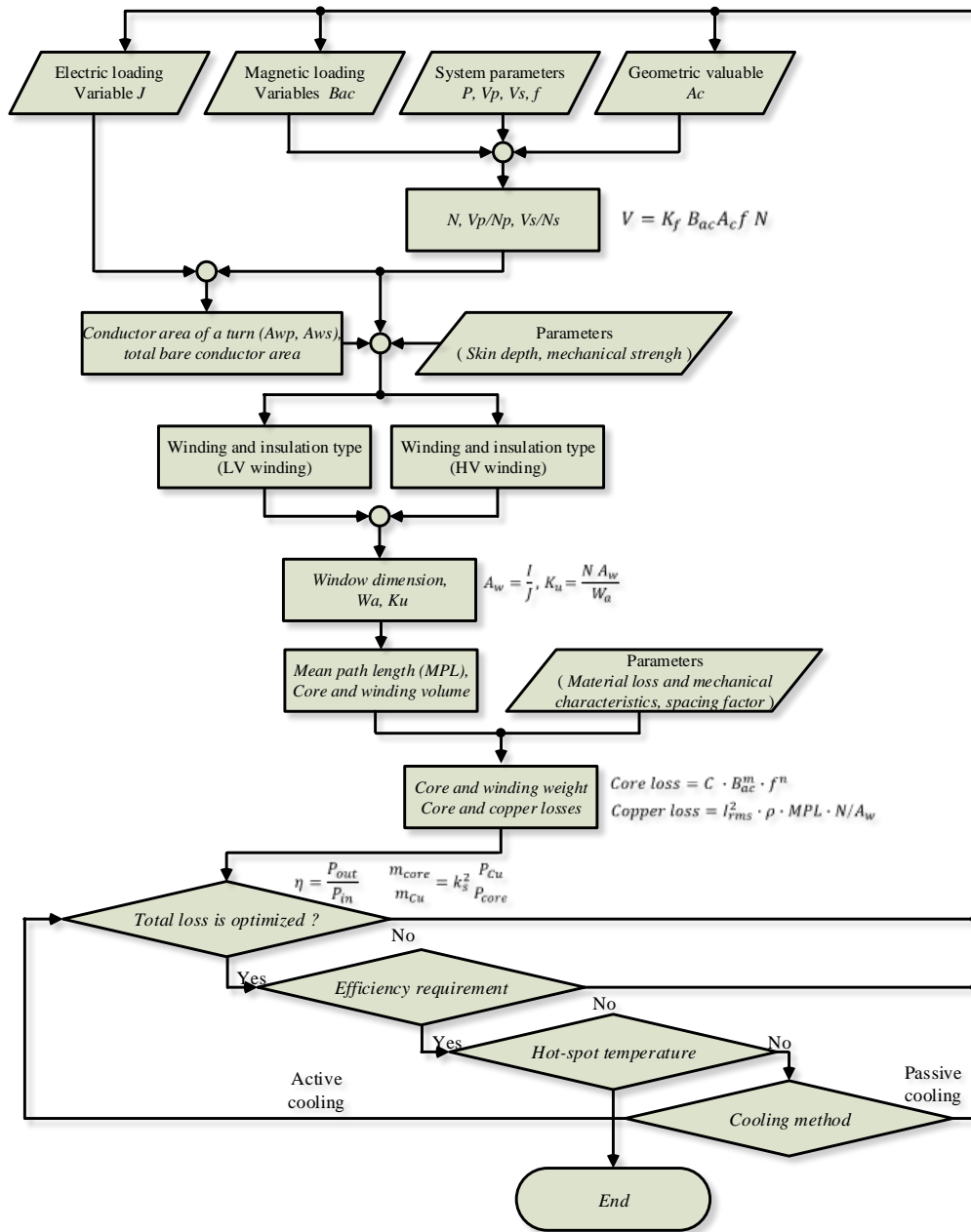


Figure 3.2: Transformer design flow chart

3.2 Modeling coaxial winding transformer (CWT) with parasitic effects

3.2.1 Configuration of CWT and prototype

The long loop of wire, also known as the solenoid, plays an important role in engineering. The magnetic field inside an infinitely long solenoid is homogeneous and its strength does not depend on the distance from the axis. Conventional power transformers have been designed on the basis of the winding arrangement of a solenoid with a large number of turns. The solenoidal winding structure and coaxial winding structure are the opposite of one another. In the case of the solenoidal winding structure, the magnetic flux flows parallel to the cylindrical axis while the current encircles the cylindrical axis. The magnetic flux becomes more uniform and more accurately predicted with a highly packed, large number of turns as shown in Fig 3.3.

This structure of wiring, with cut-cores, has another great advantage in its simple assembly, which is a critical aspect of mass production and commercialization. However, there is typically a high parasitic inductance and capacitance with this winding arrangement, and there are flux congestions and fringing effects in close proximity to the gaps and edges of cores.

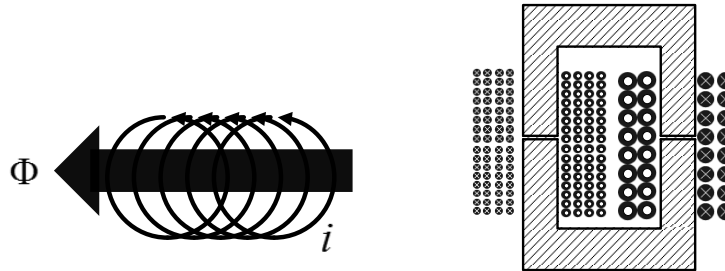
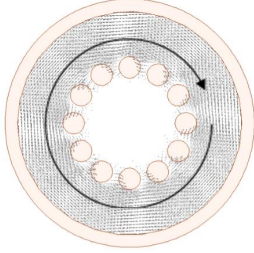
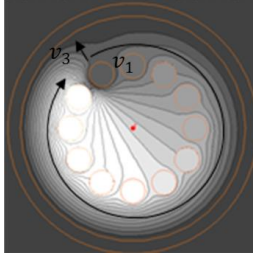
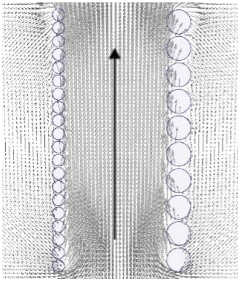
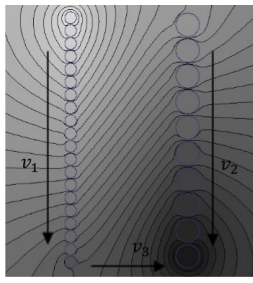


Figure 3.3: Solenoid winding transformer

The coaxial winding power transformer consists of a conducting tube on the low voltage side, and another winding is placed inside the tube in a concentric manner. The current of the coaxial winding structure flows parallel to the cylindrical axis and the magnetic flux encircles the current. Assuming the infinitely long outer winding covers the inner winding concentrically, the magnetic flux of the outer winding is entirely linked to the inner winding, so that the outer winding does not have leakage inductance. The coaxial structure has been more popular in radio frequency applications due to its simple geometry and predictability.

Each method has its pros and cons. The effect of the skin and proximity effects on the

Table 3.1: Field distribution

Magnetic field distribution	Voltage distribution
	
	

copper wire, and the parasitic inductances and capacitances are increased considerably at high frequency operation. Those high frequency effects are of the utmost concern for transformer design at increased frequencies. The conventional design method, using a solenoid structure, has a limitation of predictability in complex geometry while the parasitic elements are typically high. High frequency phenomena in coaxial geometry are more accurately observed and resolved in simple geometry.

In order to derive equations in an analytical expression, a two dimensional approximation is used for simplicity. For the two dimensional approximation, a large number of turns is desired for the solenoid winding structure and vice versa for coaxial winding transformers. The magnetic field and voltage distribution on each structure is shown in Fig 3.4. There is only magnetic flux in the Φ direction and electric flux in the z direction with a two dimensional approximation. Because of this all magnetic flux induced by the outer winding is mutually connected by the inner winding. The magnetic flux between both windings is a leakage flux, which is only dependent on the inner winding.

Prototype

The complete 3D CAD sketch of the prototype is shown in Fig 3.5. The HV winding is arranged in order to minimize the electric stress through each hole of the Teflon bobbin and the LV winding is made of a single copper tube with a thickness of 1.5mm. At 20kHz, a copper tube

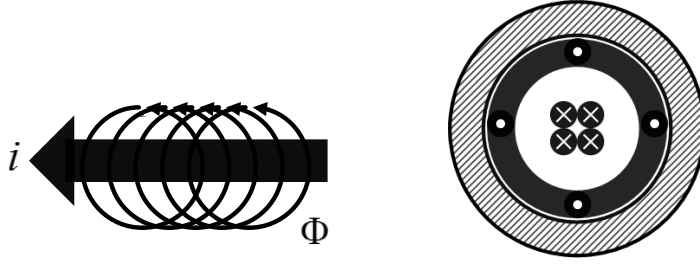


Figure 3.4: Coaxial winding transformer

with a thickness 0.7mm is an optimal value with the lowest resistance. However, the mechanical strength of the tube is another concern, as a frame to hold the weight of the cores. The whole body has to be placed inside a case that is grounded to the earth. The commercially available Fe-based nanocrystalline tape-wound cores (VAC Vitroperm 500F, T60004-L2080-W628) are used along with PFA wire insulation. The prototype is a dry-type with an insulation medium of air in the preliminary design.

3.2.2 Geometric simplification and meshing considerations for finite element analysis

The finite element method is a numerical technique used to find approximate solutions to boundary value problems for differential equations. Mesh generation is a part of the techniques for discretizing a complex geometry into small pieces called finite elements, e.g. an equilateral triangle in 2D and a tetrahedra in 3D.

Mesh plays important role in the accuracy of the computed results. A higher resolution of meshes yields more accurate result, however the used of unnecessary meshes increases computation time without showing considerable influence on the results. Meshing consideration is another aspect that must be considered for numerical FEM simulation. Ansys Maxwell 3D Eddy current solution is used for this test, and simplification of the geometry has been studied based on the accuracy of the inductance and resistance results from eddy solution type.

Simplification of round shape object and mesh generation

Curved surfaces of geometry generate a high number of meshes and are a large source of the computational load in finite element analysis. By segmenting the curved surface with straight lines, considerable computational load and time can be saved. Four different shapes are considered with a different number of segments and cross sectional area. The number of meshes and the accuracy of the inductance and resistance values are compared using a frequency sweep.

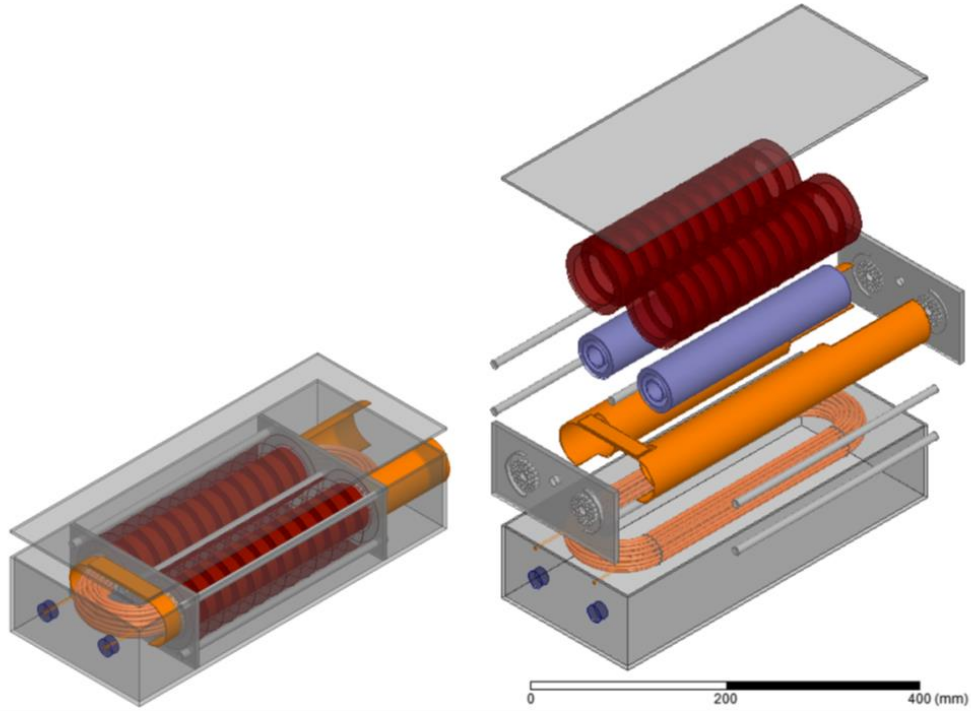


Figure 3.5: Assembly

The first three conductors are segmented with 18, 12 and 6 straight lines respectively and the last square shape is converted based on the same cross sectional area shown in Eq 3.8.

$$d = D_c \frac{\sqrt{\phi}}{2} \quad (3.8)$$

The investigated objects are set up as copper with finite conductivity $\sigma = 5.8 \cdot 10^7$. The radius $D/2$ of the round copper is the skin depth δ at the skin depth corner frequency f_δ . Regardless, the curved surface has to be segmented with finite elements for calculation, so a shape consisting of 24 segments is considered a round shape in this investigation. The simulation results are collected at operating frequencies in range between $0.1f_\delta$ to $10.0f_\delta$. The x -axis value of the plot is generalized with respect to skin depth, and y -axis values are generalized with the calculation results from the shape with 24 segments.

As long as mesh is of high enough quality, the difference in accuracy among the given geometries comes from the cross sectional area and surface area. The inductance values are mainly determined by the length of closed path of magnetic fields. The magnetic flux is distributed in a concentric manner in the given geometries, therefore the variation of the accuracy is within 4%.



Figure 3.6: Prototype of MV-MF coaxial winding transformer

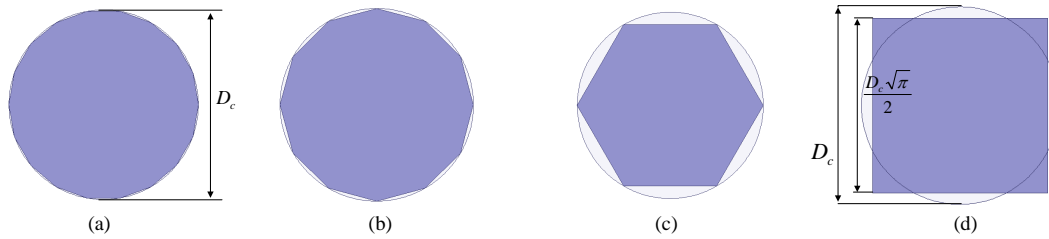


Figure 3.7: Simplification of curved surface, (a)18 segments (b) 12 segments (c) 6 segments (d) Square shape based on the cross sectional area

In any case, it is a reasonable result. In the case of effective resistance, total cross sectional area is the dominant factor below the frequency at skin depth f_δ , however the surface area takes over above f_δ due to the skin effect, which is the usual tendency of an AC current congested near surface of a conductor. The simplified geometry with 6 segments has the smallest cross section and surface area, hence it has the highest resistance value of up to 120% compared to that of the round shape. A square shape with the same cross sectional area of the round shape shows good agreement below f_δ because the current density is well distributed in the entire cross sectional area. However, the effective resistance increases slightly at $10.0f_\delta$ due to the smaller surface when compared to the round shape. Nonetheless, it shows good agreement with an acceptable error even though the computational load is the smallest. Meshing is another factor in the accuracy and computational load of finite element analysis. The field distribution under

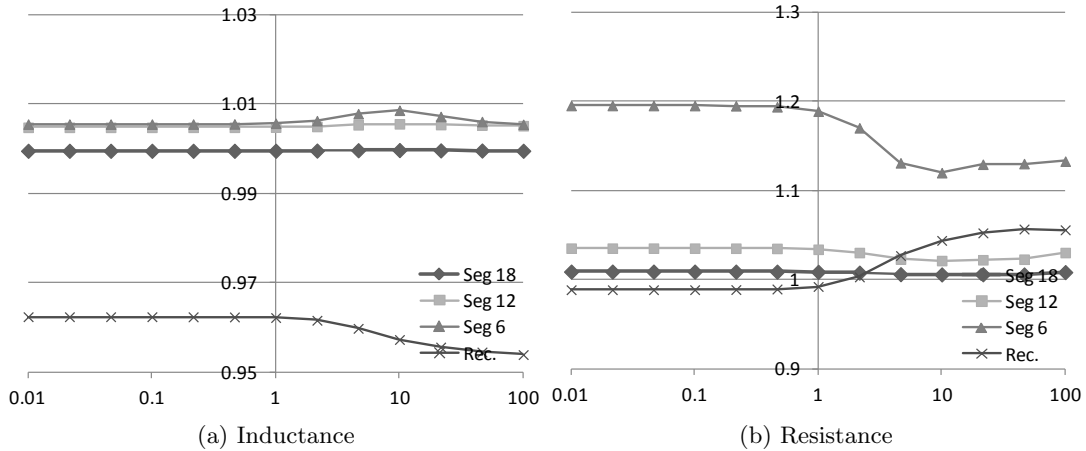


Figure 3.8: Computation error with the number of segments (x-axis : f/f_δ)

different mesh configurations is shown in Fig 3.9. The radius of the round copper is skin depth δ and frequency is ten times higher, $10.0f_\delta$. Meshes are generated based on the skin depth, and 3 different cases with a different number of layer of meshes are investigated in Fig 3.9. One layer of meshes results in a significant distortion of field distribution. The low resolution of meshes combined with high aspect ratio lowers the quality of the mesh, and the effective resistance at $10f_\delta$ is not in an acceptable range. The inductance values are mainly determined by the magnetic flux in the region, rather than the internal inductance inside the conductors. Hence, the error of the inductance value is not as bad as that of the effective resistance. The geometry with 2 layers of meshes also shows around 4% error at $10f_\delta$. At least 3 layers of meshes are required to investigate the eddy effect in the interest of the tenth harmonic component. In transformer design, cross sectional area is a meaningful value, because the current density on the copper and magnetic flux density of magnetic cores are determined by the cross sectional area of copper and the magnetic core. The approximation based on the cross sectional area shows good agreement with a low computational load.

3.2.3 Inductance modeling and calculation for CWT

The most accurate results are extracted in real geometry in three dimension; however, they are not analytically calculable in most cases. Therefore it is reasonable to estimate the results with a two dimensional approximation first. Accurate values can be revised using a computer-aided 3D FEM tool when detailed work is required. In most cases, the results from well-approximated geometry in two dimensions is accurate enough.

In order to understand the configuration of a CWT, the cross sectional views are shown in

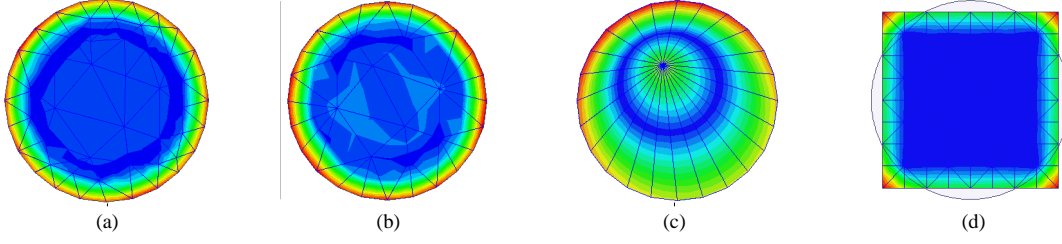


Figure 3.9: Skin depth based mesh generation and field distribution (a)3 layers on round shape (80 elements) , (b) 2 layers on round shape(42 elements), (c) 1 layers on round shape(24 elements), (d) 1 layers on square shape based on the cross sectional area

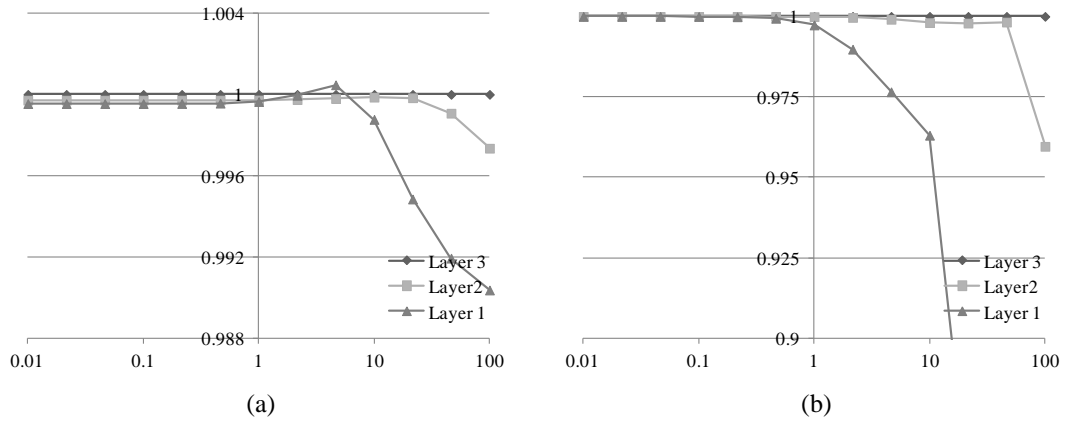


Figure 3.10: Computation error with skin depth based mesh generation (a)Inductance , (b) Resistance

Fig 3.11. The low voltage side is made of a copper tube, which can be considered as a single turn of LV winding. Multiple turns of high voltage winding are placed inside the tube in a concentric manner. Hence, the analysis can be approximated in cylindrical coordinates on the $r - \pi$ plane in two dimensions.

The inner winding on the HV side consists of many round wires arranged in a layered concentric configuration, shown in Fig 3.12. The $i - th$ layer of the wires is converted to a copper tube based on the same amount of copper area as in Eq 3.9.

$$d_1 = \frac{N_i A_W^2}{2r_i} \quad (3.9)$$

Magnetizing inductance calculation: The Flux distribution in a symmetrically concentric coaxial winding structure in two dimensions is a simple function of radius with a constant

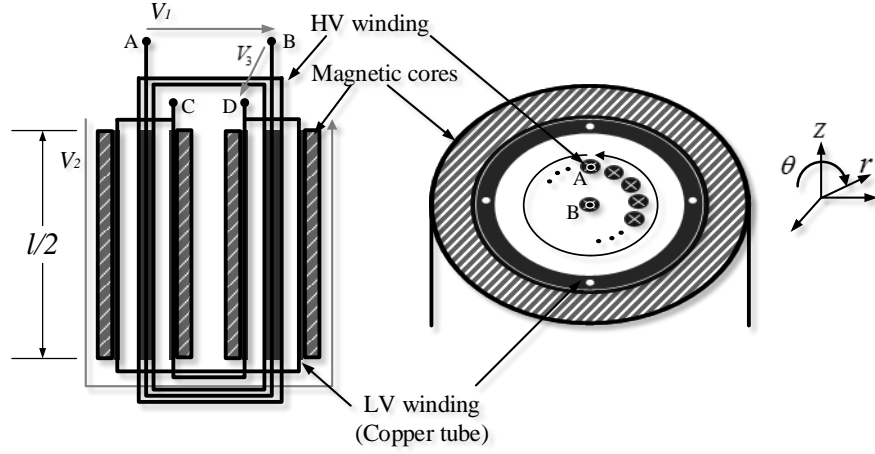


Figure 3.11: Views on $r - z$ plane (left) and $r - \phi$ plane (right)

relative permeability μ_r by *Ampere's law*.

$$B = \frac{\mu_o \mu_r I}{2\pi r} \quad (3.10)$$

Typically, the permeability of the transformer's magnetic cores are significantly higher than that of air or conducting materials $\mu_{r \text{ core}} \gg \mu_o$. It can be assumed that all mutual flux is constrained within the transformer cores. The magnetic flux in the cores is derived by integrating magnetic flux density on the cross sectional area of the flux path

$$\Phi_m = \int_{r_{ci}}^{r_{co}} \frac{\mu_o \mu_r N_{in} I_m}{2\pi r} = N_o \frac{\mu_o \mu_r I_m}{2\pi} \ln \frac{r_{co}}{r_{ci}} \quad (3.11)$$

by *Faraday's law of induction*

$$v(t) = V_{in} \frac{d\Phi}{dt} = N_{in}^2 \frac{\mu_o \mu_r}{2\pi} \ln \frac{r_{co}}{r_{ci}} \cdot \frac{dI_m}{dt} = N_{in}^2 P_m \cdot \frac{dI_m}{dt} \quad (3.12)$$

Hence the magnetizing inductance is achieved in Eq 3.13.

Table 3.2: Specifications of the AC-link transformer prototype [mm]

r_1	r_2	r_3	N_1	N_2	N_3	$r_{tube \ i}$	$r_{tube \ o}$	$r_{c \ i}$	$r_{c \ o}$	r_w
3.2	8.5	15.5	4	9	17	25.5	27.0	9.8	40.5	2.24

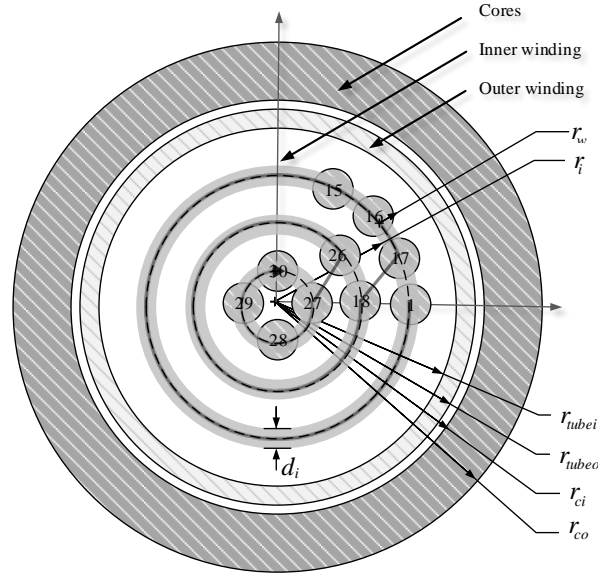


Figure 3.12: Dimensions and winding arrangement

$$L_m = N_{in}^2 \frac{\mu_o \mu_r}{2\pi} \ln \frac{r_{co}}{r_{ci}} [H/m] \quad (3.13)$$

The results are based on the isotropic constant μ_r . However, the relative permeability of the magnetic material is nonlinear with a variety of factors. Hence, the magnetizing inductance of the transformer without air gap is directly dependent on the material characteristics μ_r , and not a constant value. Nonetheless, the magnetizing inductance is typically not a circuit element and can be ignored as long as the magnetizing current is small when compared to the rated line current, in most cases.

Leakage inductance calculation in a layered winding As discussed in previous chapters, the entire leakage flux of the coaxial transformer is constrained between inner winding and outer winding in two dimension approximation. The magnetic flux density is determined by the closed magnetic path with the current enclosed inside its surface. Therefore, the magnetic flux density, B , is represented by the turns enclosed in the magnetic flux path in concentric geometry.

$$B = \frac{\mu_o \mu_r N_{enclosed} I}{2\pi r} \quad (3.14)$$

The partial leakage inductance of each section between layers is calculated by:

$$L_{i \text{ to } i+1} \cong N_{enclosed}^2 \frac{\mu_o \mu_r}{2\pi} \ln \frac{r_{i+1}}{r_i} \quad (3.15)$$

Then, the total leakage inductance on the inner winding side is given by:

$$L_{leak} = \frac{\mu_o \mu_r}{2\pi} \sum_{i=1}^n N_{enclosed}^2 \ln \frac{r_{i+1}}{r_i} \quad (3.16)$$

The magnetic field distribution of the prototype is shown as an example in Fig 3.13. Calculations and FEM results in two dimensions show good agreement with both the round wires and simplified tubes in Table 3.3. Analytical solutions in a closed form are available by geometric simplification based on the cross sectional area and also show good agreement.

In the real world, the magnetic energy stored by leakage flux in the air inside transformer is usually smaller than the that of the edges and accessories. Even though the leakage inductance within the coaxial body is properly estimated, the total leakage inductance measured often shows difference as in case 3.4. On the other hand, the accuracy of the measurement of magnetizing inductance depends on the linearity of the $B - H$ curve of the magnetic material without an airgap.

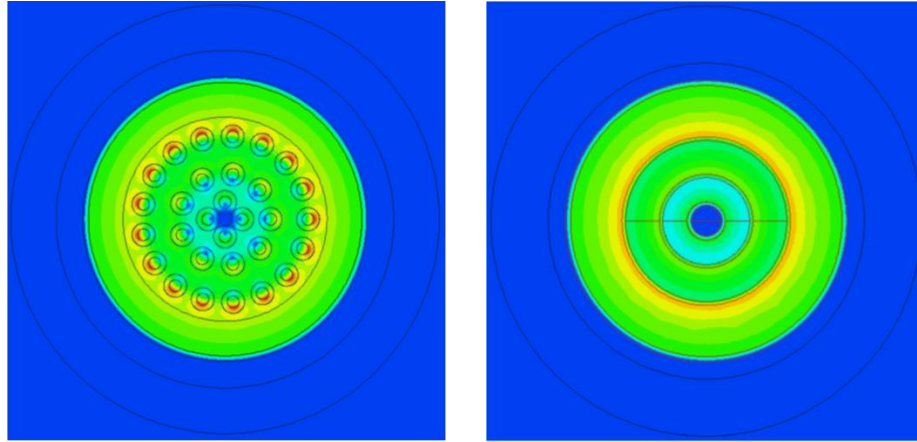
Even though the calculation for leakage inductance is a more conceptual approach and the results are not practical in three dimension for conventional CWT applications, this concept is improved to configure inductor-integrated coaxial winding transformers (ICWT) by locating magnetic material in the space where the predictable leakage flux exits as dicussed in chapter 4.

Table 3.3: Leakage permeance calculated by finite element method in 2 dimension

Calculation in simplified geometry	2D FEM results in exact geometry	2D FEM results in Simplified geometry
118 [nH/m]	108 [nH/m]	117 [nH/m]

Table 3.4: Permeance measurement from the prototype (The length of the body is 0.6m)

	P_{sc}	P_{oc}
Calculation in 2D	118 [nH/m]	1.38[mH/m]
Measurement	715 [nH]	519 [uH]



(a) The prototype in symmetric 2D configuration

(b) Simplified geometry

Figure 3.13: Leakage magnetic field distribution in CWT

3.2.4 Parasitic capacitances modeling of CWT

Calculating the parasitic capacitances of transformer windings is a complex task, because the parasitic capacitances on wires are physically distributed with voltage distribution induced by electromagnetic induction. The general derivation for a three-port electrostatic system with six equivalent capacitances is briefly explained in this section, including the impact of common-mode voltage between two isolated circuits [21] ~ [24].

As long as the elements are small enough in comparison to wavelength,

$$\lambda = \frac{v}{f} \quad (3.17)$$

The EM field is well represented by static field equations. Hence, the electrostatic and magnetostatic behaviors can be considered independently under the practical working conditions of a medium-frequency, medium-voltage power conversion system. Generally, the magnetically coupled two winding transformer can be represented by a two-port network, and the electrically coupled two winding transformer is shown as a three port network with considerations to the common-mode voltage.

The three-port electrostatic circuit model is represented by the three independent voltages and six capacitances of the equivalent circuit model from an energy-based approach regardless of circuit topology, as seen in Fig 3.14. The total electrostatic energy in the space W_{EC} of a three-port equivalent model is calculated by circuit analysis.

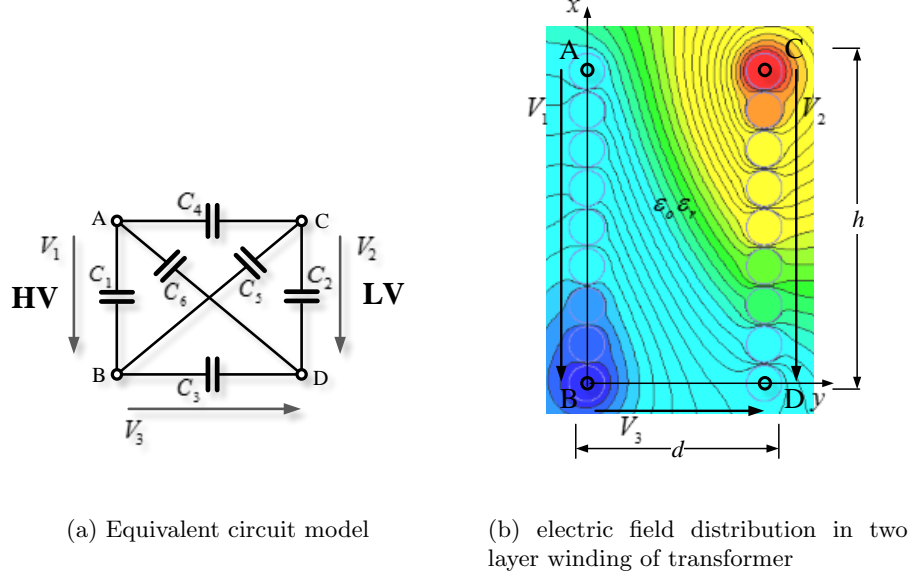


Figure 3.14: 6 capacitance equivalent circuit model

$$W_{EC} = \frac{C_1 V_1^2}{2} + \frac{C_2 V_2^2}{2} + \frac{C_3 V_3^2}{2} + \frac{C_4 (V_1 - V_2 - V_3)^2}{2} + \frac{C_5 (V_2 + V_3)^2}{2} + \frac{C_6 (V_1 - V_3)^2}{2} \quad (3.18)$$

Capacitance modeling in linear voltage distribution between two layer windings

If the number of wires is large enough and placed evenly in order, the voltage distribution along the layer can be considered as linear. The turn-to-turn capacitances caused by the leakage flux on a single turn are ignored, because it is very small and edge effects are not considered in the following calculation. Then, the six effective capacitance values for circuit analysis can be geometrically calculated with electric field calculation using Laplace's equation.

$$\nabla^2 V = 0 \quad (3.19)$$

The coefficients of the total energy calculated by integrating electric field intensity in the space between two layers are compared to the coefficients of the total energy stored in the six capacitance equivalent circuit model. The details of the work for the calculation is shown in reference [23]

$$length \cdot \int_0^h \int_0^d \frac{\epsilon_o \epsilon_r |E|^2}{2} dx dy = W_{EC} \quad (3.20)$$

An even simpler approach is calculation using the voltage distribution on a winding, which is a function of x and the static capacitance C_o . This is the capacitance between two sheets at a constant potential [24].

$$length \cdot \frac{1}{2} C_o V(x)^2 dx = W_{EC} \quad (3.21)$$

Where $V(x) = V_3 + \frac{(V_2 - V_1)x}{h}$,

The static capacitance can be used conveniently by knowing the voltage distribution in the winding, which is dependent upon the winding arrangement. The equations for the six capacitances of the equivalent circuit model are extracted by either method as a function of static capacitance C_o in Eq 3.22. The energy-based approach is a mathematical manipulation to represent the total electrostatic energy in the given space with lumped circuit elements of the equivalent circuit model. Hence, negative capacitance values can occur, and the lumped element capacitance C_1 is usually a negative value in a two layer configuration.

$$\begin{cases} C_1 = C_2 = -\frac{C_o}{6} \\ C_3 = C_4 = \frac{C_o}{3} \\ C_5 = C_6 \end{cases} \quad [F/m], (C_o = \frac{\epsilon_o \epsilon_r h}{d}, d \ll h) \quad (3.22)$$

Equivalent capacitance modeling for two layer windings in an arbitrary arrangement using FEM

The parasitic capacitance calculation of the transformer windings has been based on the layer-to-layer capacitance C_o for simplicity. This means that all turns in one winding are assumed to be shorted, and the edge effects are neglected. However, this assumption is only valid when the number of turns is large and the field distribution is linear. The six capacitance model in complex geometry, any arbitrary geometry, can be achieved by using FEM computer-aid simulation.

The $N \times N$ capacitance matrix is comprised of node-to-node capacitance elements C_{ij}

$$\begin{bmatrix} C_{11} & \cdots & C_{1n} \\ \vdots & \ddots & \vdots \\ C_{n1} & \cdots & C_{nn} \end{bmatrix} \begin{bmatrix} U_1 \\ \vdots \\ U_n \end{bmatrix} = \begin{bmatrix} Q_1 \\ \vdots \\ Q_n \end{bmatrix} \quad (3.23)$$

This capacitance matrix can be formed by dividing both windings into p and q number of distributed nodes respectively, the voltage matrix is then transformed to apply this matrix to a three-port electrostatic system.

$$\begin{bmatrix} C_{pp} & C_{pq} \\ C_{qp} & C_{qq} \end{bmatrix} \begin{bmatrix} U_p \\ U_q \end{bmatrix} = \begin{bmatrix} Q_p \\ Q_q \end{bmatrix}, \quad (p + q = n) \quad (3.24)$$

$$\text{Where } C_{pp} = \begin{bmatrix} C_{11} & \cdots & C_{1p} \\ \vdots & \ddots & \vdots \\ C_{p1} & \cdots & C_{pp} \end{bmatrix}, C_{pq} = \begin{bmatrix} C_{1p+1} & \cdots & C_{1n} \\ \vdots & \ddots & \vdots \\ C_{pp+1} & \cdots & C_{pp+1} \end{bmatrix},$$

$$C_{qp} = \begin{bmatrix} C_{p+11} & \cdots & C_{p+1p} \\ \vdots & \ddots & \vdots \\ C_{n1} & \cdots & C_{np} \end{bmatrix}, C_{qq} = \begin{bmatrix} C_{p+1p+1} & \cdots & C_{p+1n} \\ \vdots & \ddots & \vdots \\ C_{np+1} & \cdots & C_{nn} \end{bmatrix}, \quad (3.25)$$

$$\text{and } U_p = \left[\frac{V_1}{p} \times 1 \quad \frac{V_1}{p} \times 1 \quad \dots \quad V_1 \right]^T,$$

$$U_q = \left[V_3 + \frac{V_2}{q} \times 1 \quad V_3 + \frac{V_2}{q} \times 2 \quad \dots \quad V_3 + V_2 \right]^T \quad (3.26)$$

Once the capacitance matrix is achieved by finite element analysis, the parasitic capacitances of the equivalent circuit are calculated by comparing the coefficients of the numerical solution and W_{EC} of a three port equivalent capacitance model using the same approach. The accuracy of this result is improved by increasing the number of nodes.

$$W_{\text{Numerical solution}} = \frac{1}{2} \sum_{i=1}^n \sum_{j=1}^n U_i C_{ij} U_j = W_{EC} \quad (3.27)$$

Capacitance modeling of coaxial winding transformer

The parasitic capacitance of the CWT prototype can be calculated in Cartesian coordinates in two dimensions with a reasonable error. Accuracy will be improved by using calculations based on cylindrical coordinates; however, the difference between the two methods is typically not significant with a layered geometry, and the details can be revised by simulation tools. The equivalent capacitance of each layer is calculated by Eq 3.28 with a static capacitance value.

$$W_{i \text{ layer}} = \frac{1}{2} C_{\text{layer}} V_{\text{layer}}^2 = \int_{x=0}^h \frac{1}{2} C_o V(x)_{\text{layer}}^2 dx \quad (3.28)$$

Hence, the total effective capacitance is derived by:

$$\begin{aligned} W_E &= \sum_{i=1}^n \int_0^{2\pi \frac{r_{i+1} + r_i}{2}} \frac{1}{2} C_{0,i} (V_{i+1}(x) - V_i(x))^2 dx \\ &= \frac{1}{2} C_{eff} V_{HV}^2, \quad (C_{0,i} = \frac{\epsilon_o \epsilon_r}{r_{i+1} - r_i - d_{i+1} - d_i}) \end{aligned} \quad (3.29)$$

3.2.5 Lumped-element equivalent circuit model and measurement results of CWT prototype

In this chapter, three capacitance equivalent circuit model for a coaxial winding transformer with a large turns ratio is discussed. The frequency response of the CWT prototype with a large turns ratio shows a different, but clearer, pattern. The lumped-element equivalent circuit model is valid up to frequencies of approximately $f_{1/4\lambda}$ and transmission line theory can be applied to the frequencies over $f_{1/4\lambda}$. The results of the proposed equivalent circuit model represents the electromagnetic behavior of the two winding CWT with a large turns ratio within $f_{1/4\lambda}$.

Characteristics of frequency response on windings of CWT and measurements at 30MHz

The electric potentials on the HV and LV sides are between nodes A-B and C-D, respectively. The electric energy stored within the transformer by V_2 on the LV side is relatively small, and the contribution on the effective capacitance is significantly mitigated by a factor of $1/n^2$. Therefore, V_2 on the low voltage winding, which has a single turn of copper tubes in the z direction, can be ignored as if shorted from an electrostatic point of view. This assumption allows for simple analysis without causing significant error in the calculation in two dimensions. Also, it is consistent with the conventional method of calculating the parasitic capacitances of windings, which considers one turn as an equipotential body for calculation in two dimensions.

Under this assumption, where the low voltage winding can be seen as shorted, the electric energy stored within the six capacitor notation is represented by:

$$\begin{aligned} W_{E, V_2=0} &= \frac{C_1 V_1^2}{2} + \frac{(C_3 + C_5) V_3^2}{2} + \frac{(C_4 + C_6)(V_1 + V_3)^2}{2} \\ &= \frac{c_a V_1^2}{2} + \frac{c_b V_3^2}{2} + \frac{c_c (V_1 + V_2)^2}{2} \end{aligned} \quad (3.30)$$

Hence, the six capacitance values are simplified with three capacitances as

$$C_1 = C_a, \quad C_3 + C_5 = C_b, \quad C_4 + C_6 = C_c \quad (3.31)$$

For the measurement, the frequencies of the series and parallel resonant peaks [21], or simple capacitance measurements in six different connections, can be used [24]. In either fashion, there are only three capacitance values that are achievable with a large turns ratio n based on either the impedance plot or capacitance measurements for each of the six different connections. Hence, the three capacitance values are simply achieved by three measurements when $V_1 = 0$, $V_3 = 0$ and $V_1 = -V_3$ by shorting two nodes at a time.

The equivalent circuit model is simplified with three capacitances, C_a , C_b and C_c in Fig 3.18. It can be also recognized that the capacitance related switching on high voltage side is not only ' C_a ', but it also the common-mode capacitance ' $C_b + C_c$ '.

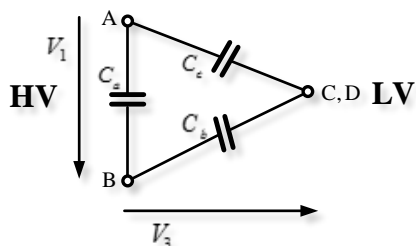


Figure 3.15: Simplified capacitance equivalent circuit model

Because the electric and magnetic field distributions within the transformer, with connections from the HV side to the 'C' or 'D' nodes, are symmetric, the frequency responses of this connection should be the same. It can be seen that one turn in the z direction is equipotential, under the aforementioned assumption. Therefore, the input impedance measurements from connections B-C and B-D, and the measurements from connections A-C and A-D are always identical. The first parallel resonance frequencies caused by L_{oc} and C_{eff} from open circuit measurements are the same from either side. The first parallel resonance frequency of the short circuit measurements from the HV side, and the series resonance frequency of the short circuit measurements from the LV side are caused by L_{sc} and C_{eff} . They are almost the same as shown in Fig 6.9.

Low voltage winding side : The electrical energy stored within the transformer depends not on the voltage on LV winding, but on the voltage on the HV winding. The effective capacitance that interacts with L_{sc} and L_{oc} on the LV side is the effective capacitance seen from the HV side by magnetic coupling. Hence, there is series and parallel resonance between L_{sc} , L_{oc} and C_{eff} transformed from the HV side in the case of open circuit measurements. However, only inductance is measured on the LV side when shorting the HV winding terminals within 30MHz.

High voltage winding side : The magnetizing inductance resonates with the effective capacitance between node A and B at the same frequency when measured from the LV side. After the magnetizing inductance is nulled by the capacitance between node A and B, the response is only capacitive until the multi-resonance occurs with distributed inductances L_d

and capacitances C_d from transmission line theory.

It is tricky to represent electromagnetic behavior in three dimensions with circuit theory in one dimension and over a wide range of frequencies. However, a simple equivalent circuit model can be developed in the frequency range of interest, approximately up to the frequency where the length of the coaxial geometry is one quarter of wavelength.

Frequency response up to $f_{1/4\lambda}$: The capacitance and combined equivalent circuit models are shown in Fig 3.17. This equivalent circuit can represent the resonant peaks in different connections for CWT configurations with a large turns ratio n . Note that the approximation is based on the assumption of a large turns ratio of n . One quarter of the wavelength of the CWT prototype for SST applications is around 4MHz, which is around several hundred times of the operating switching frequency of 20kHz. Therefore, the proposed equivalent circuit is sufficient to represent the frequency response of a high step up-down coaxial winding power transformer. If the conventional six capacitances notation is used, the capacitance values calculated through circuit theory are also approximated with only three values, ' C_1 ', ' $C_3 + C_5$ ' and ' $C_4 + C_6$ ' with a large n as shown in Table 3.5. The frequency response of the prototype with a large turns ratio was measured with an Agilent 4294A precision impedance analyzer in Fig 6.9. The lumped-elements values can be extracted by the measured frequencies in Eq 3.32. All values refer to the high voltage side.

$$\begin{aligned} f_1 &= \frac{1}{2\pi\sqrt{L_{ocHV}C_{eff2HV}}}, f_2 = \frac{1}{2\pi\sqrt{L_{ocHV}C_{eff1HV}}}, \\ f_3 &= \frac{1}{2\pi\sqrt{L_{scHV}C_{eff2HV}}}, f_4 = \frac{1}{2\pi\sqrt{L_{scHV}C_{eff1HV}}}, \end{aligned} \quad (3.32)$$

Table 3.5: Measurement conditions

Connection	C_{eff}	Large 'n' approximation
A-B and C-D	$C_3 + C_4 + C_5 + C_6$	$C_3 + C_4 + C_5 + C_6$ $= C_b + C_c(C_{eff1})$
B-D	$C_1 + C_6 + \frac{(n-1)^2}{n^2}C_4 + \frac{1}{n^2}(C_5 + C_6)$	$C_1 + C_6 + C_4 = C_a + C_c$
B-C	$C_1 + C_4 + \frac{(n-1)^2}{n^2}C_6 + \frac{1}{n^2}(C_3 + C_2)$	(C_{eff2})
A-D	$C_1 + C_3 + \frac{(n-1)^2}{n^2}C_5 + \frac{1}{n^2}(C_6 + C_2)$	$C_1 + C_5 + C_3 = C_a + C_b$
A-C	$C_1 + C_5 + \frac{(n-1)^2}{n^2}C_3 + \frac{1}{n^2}(C_6 + C_2)$	(C_{eff3})

The method in the previous chapter can also be applied to the computer-aided FEM tool. The electric field distribution on $r - \phi$ in two dimensions is shown in three different connections

in Fig 3.18. The effective capacitances can be extracted by the total electrostatic energy stored in the space under different conditions of voltage distribution. The measurement from the prototype, calculation, and FEM simulation show all good agreement in Table 3.6.

Table 3.6: Calculation results

	C_{eff1}	C_{eff2}	C_{eff3}	C_{CM}	C_a	C_b	C_c
Calculation in 2D	196pF/m	93pF/m	143pf/m	125pF	13pF	79pF	47pF
2D FEM	200pF/m	64pF/m	143pf/m	128pF	2pF	89pF	39pF
3D FEM	137pF	55pF	112pf	137pF	15pF	97pF	40pF
Measurements	138pF	60.8pF	109pf	138pF	16pF	93pF	45pF

Frequency response in the range $f_{1/4\lambda}$ - 30MHz: Further study can be done to better understand higher frequency response, up to 30MHz. From the frequency at which the length of the coaxial geometry is longer than a quarter of the wavelength, the lumped-element model of a transmission line can be applied using distributed series inductance L_d and shunt capacitance C_d per unit length under lossless conditions. The effect of the magnetic coupling can be neglected in the given frequency range, and represented with respect to the infinitesimal length dz over the transmission line. In the case where nodes ‘B’ and ‘D’ are shorted, the change in voltage and current per unit length are given as:

$$V(z) = V_1(z) - V_2(z), \quad V_2(z) \cong 0, \quad (3.33)$$

$$-\frac{\partial}{\partial z}V_1(z, t) = L_d \cdot \frac{\partial}{\partial t}I_1(z, t), \quad \frac{\partial}{\partial z}I_1(z, t) = C_d \cdot \frac{\partial}{\partial t}V_1(z, t). \quad (3.34)$$

The voltage and current at ‘z’ in phasor notation are:

$$\bar{V}_1(z) = V_a \cdot e^{-i\beta z} + V_b \cdot e^{i\beta z}, \quad \bar{I}_1(z) = I_a \cdot e^{-i\beta z} + I_b \cdot e^{i\beta z} \quad (3.35)$$

with the phase constant, $\beta = \omega\sqrt{L_d C_d}$, and characteristic impedance, $Z_0 = \sqrt{\frac{L_d}{C_d}}$.

Then, the input impedance is given by:

$$Z_{in} = \frac{V_{HV}}{I_{HV}} = \frac{V_1(-l)}{I_1(-l)} = -iZ_0 \frac{1}{\tan(\omega\sqrt{L_d C_d}l)} \quad (3.36)$$

The frequency where a length of the coaxial geometry is one quarter of the wavelength of the A-D and B-D connections is 3.2MHz and 4.2MHz respectively. This is found by calculating using the inductance and capacitance per unit length from the 2D FEM results without considering

the effect on the edges.

The switching response under open-circuit conditions has been measured and compared with the circuit simulation result with the proposed equivalent circuit model. Parasitic line inductance $1\mu H$ and resistance 0.2Ω is considered on the power converter and connections. The switching response, measured by switching test with CWT prototype, and the simulation shows good agreement in Fig 3.21 and Fig 3.22.

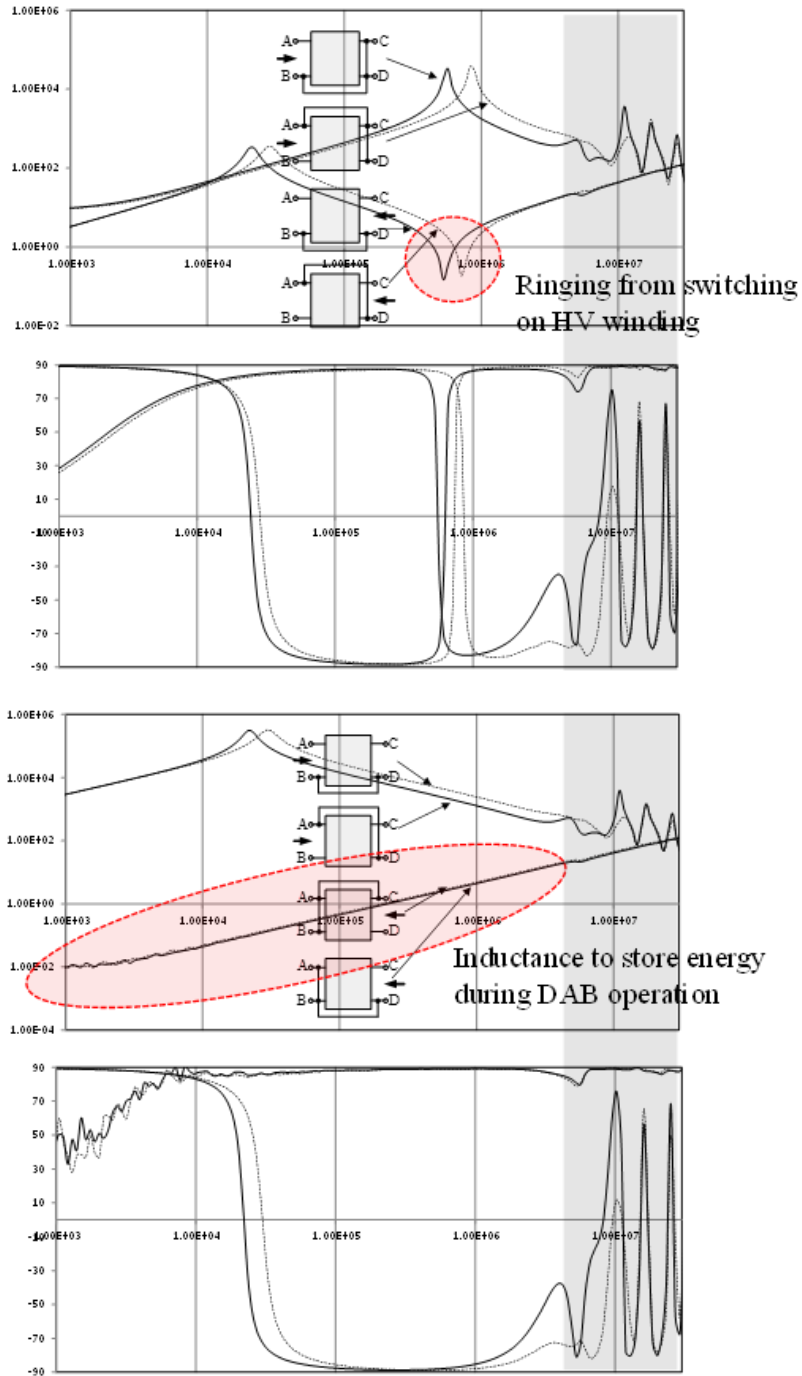
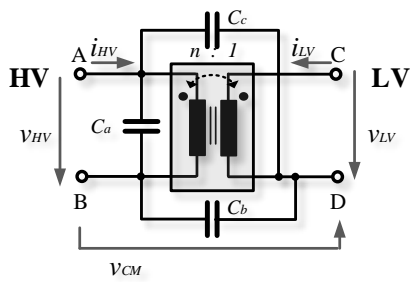
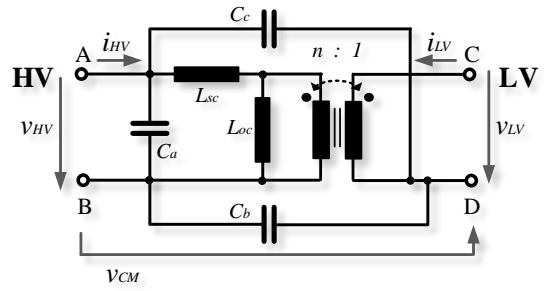


Figure 3.16: Impedance modulus and argument [°] with frequency [Hz] of the CWT prototype



(a) Capacitance model



(b) Combined eq. circuit model

Figure 3.17: Equivalent circuit model of CWT ($\sim 1/4\lambda$)

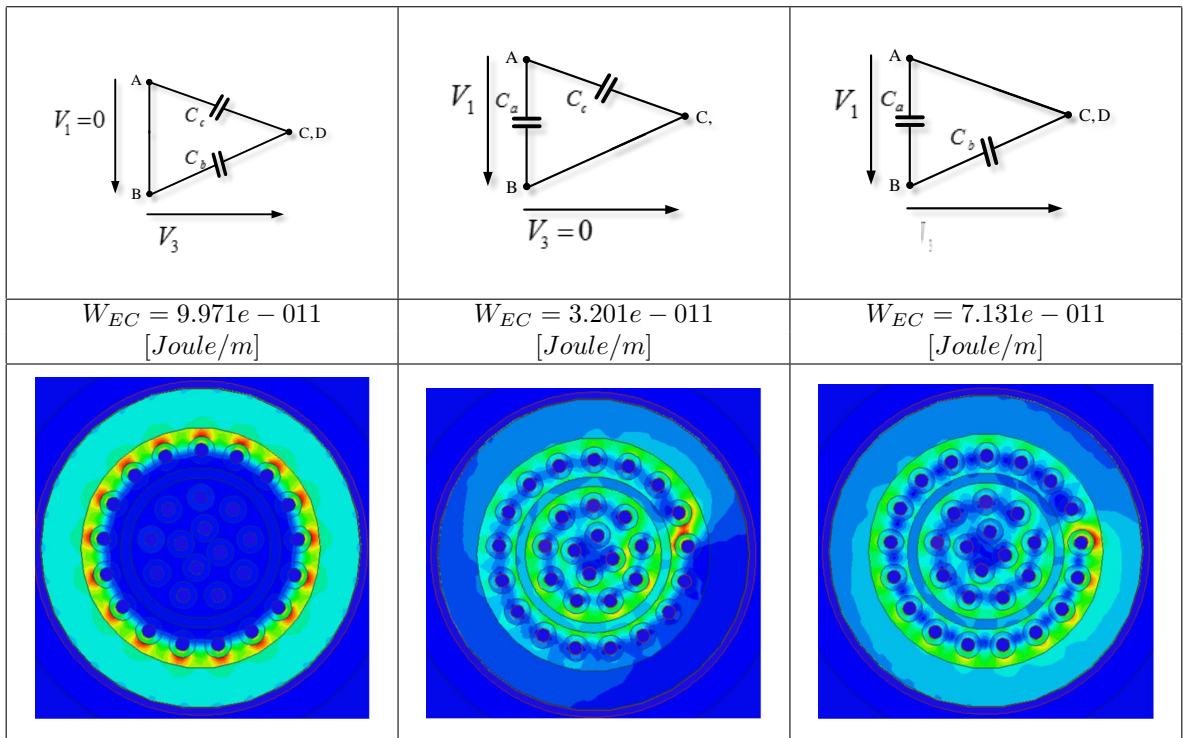


Figure 3.18: E-field distribution in connection of each measurement

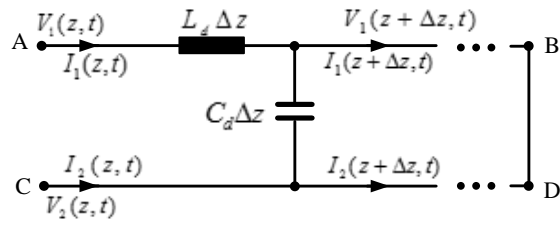


Figure 3.19: A circuit representation from HV side by transmission line theory in the range of $1/4\lambda \sim 30\text{MHz}$

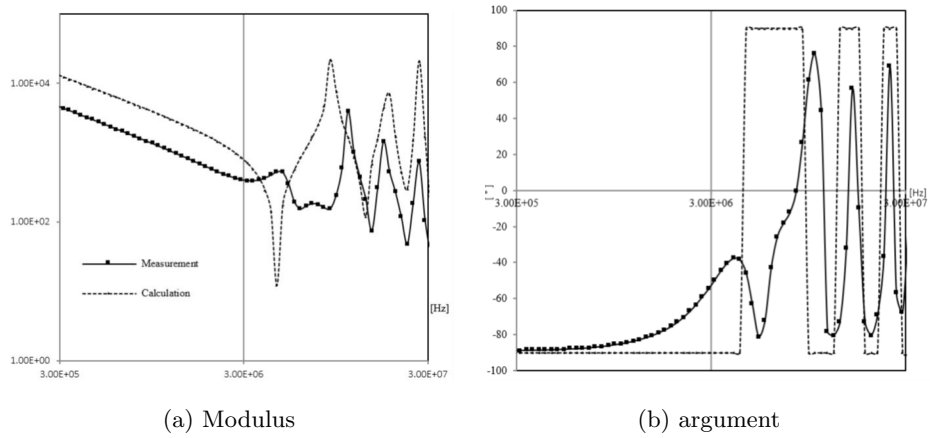
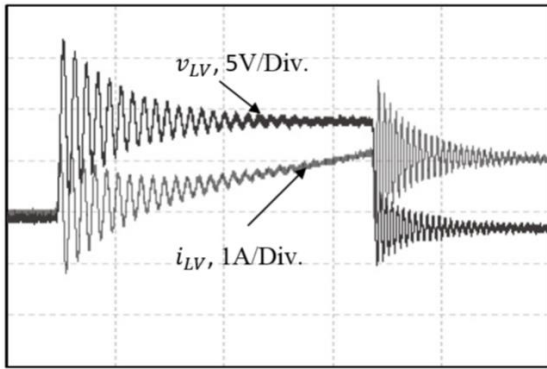
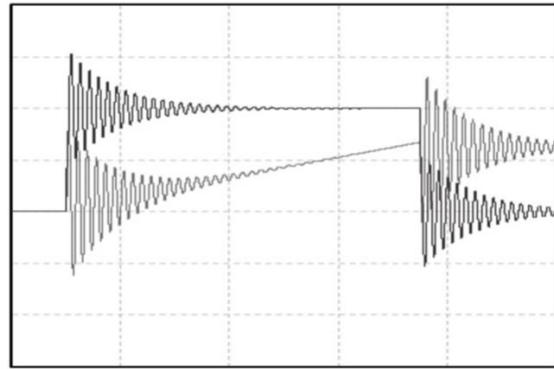


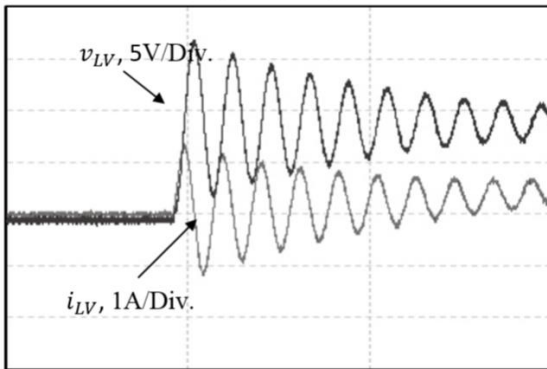
Figure 3.20: Z_{in} in the range of $3\text{MHz} \sim 30\text{MHz}$



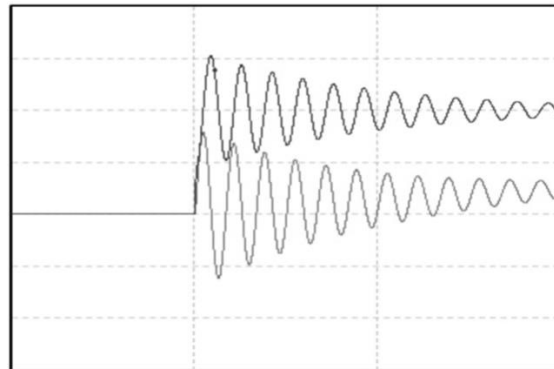
(a) Measurement



(b) Simulation results based on the proposed Eq. model

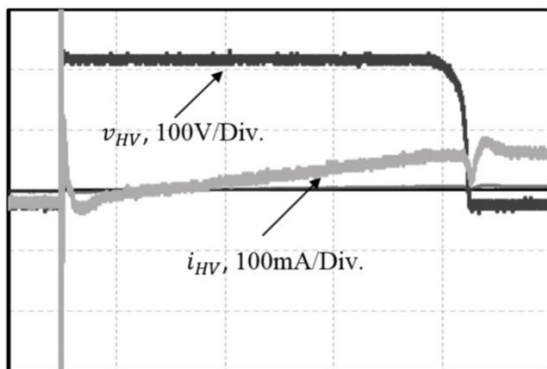


(c) Measurement

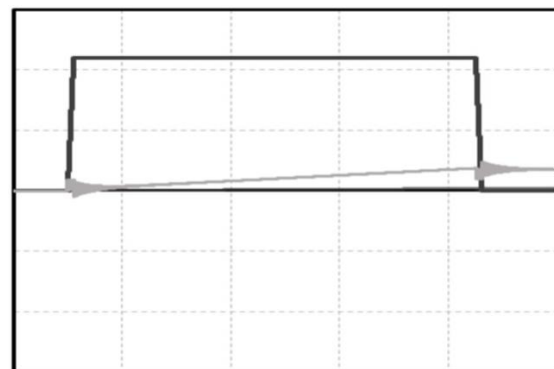


(d) Simulation results based on the proposed Eq. model

Figure 3.21: Switching response with step voltage excitation on the LV side



(a) Measurement



(b) Simulation results based on the proposed Eq. model

Figure 3.22: Switching response with step voltage excitation on the HV side

3.3 Skin and proximity effects on concentrically arranged windings

3.3.1 Skin and proximity effect

The resistance of a direct current with uniform current density distribution on the cross sectional area, A_c , of the copper is represented with the electrical conductivity ρ ($\rho_{Cu} \sim 5.96 \cdot 10^7$ [S/m] at 20°) in Eq 3.37.

$$R = \frac{l}{\sigma A_c} \quad (3.37)$$

According to *Lenz'law*, time-varying current generates electromotive force (*emf*) which induces a current whose magnetic field opposes the original change in magnetic flux. The mechanism is also applied to current flow in a solid conductor. The current distribution of the conducting material has a tendency where the current density decreases as a function of distance from the surface.

From an EM field analysis point of view, the resistance of the conducting material for alternating currents is revised due to the attenuation of the EM field. The plane wave for good conductors with propagation constant γ is shown in Eq 3.38

$$E_z(z, t) = E_o e^{-\alpha t} \cos(\omega t - \beta z) \hat{a}_z, \quad \gamma = \alpha + j\beta \quad (3.38)$$

$$\text{Where } \alpha = \omega \sqrt{\frac{\mu\epsilon}{2} \left[\sqrt{1 + \left(\frac{\sigma}{\omega\epsilon}\right)^2} \right]} - 1, \quad \beta = \omega \sqrt{\frac{\mu\epsilon}{2} \left[\sqrt{1 + \left(\frac{\sigma}{\omega\epsilon}\right)^2} \right]} + 1.$$

The distance δ with which the wave amplitudes decrease by a factor e^{-1} is the penetration depth, which is also known as skin depth, of the medium where:

$$\delta = \sqrt{1/\pi f \mu \sigma} \quad (3.39)$$

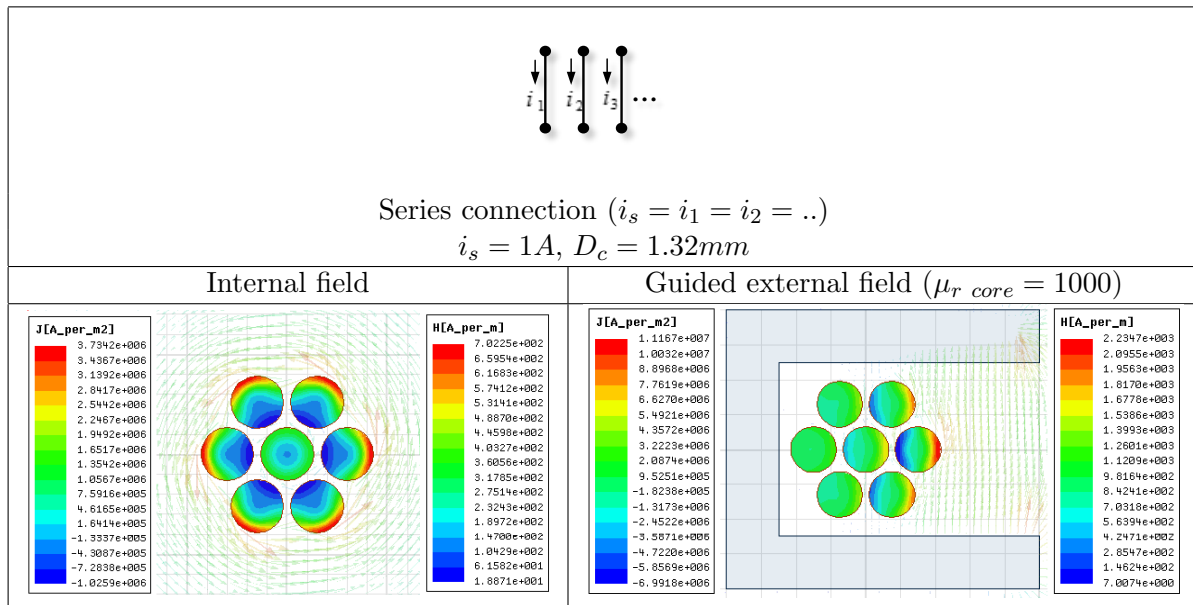
The time-varying magnetic field induces eddy currents in adjacent conductors as well which is known as the proximity effect. The conductor furthest from the conductors carrying current in the same direction has the highest current density. The proximity effect significantly influences the AC effective resistance of adjacent conductors, and is one of the most critical factors of copper loss at high frequency operation. Four different cases are considered with connections, or boundary conditions, and the presence of guided external fields to represent the skin and proximity effects on multiple conductors.

In the case of the turns of the transformer winding shown in Table 3.7, the series connection of conductors which has the same amount of current in the same direction. The radius of each copper is 0.66mm, which is the skin depth at 10kHz, and the magnetic material guiding the

external field has a relative permeability $\mu_r = 1000$. The effective resistance of the conductors in the n th layer increases by a factor of $(n - 1)^2 + n^2$. The tendency of the field variation is perpendicular to the magnetic flux line, hence concentric configuration of the conductors without a guided external field has a field variation in a radial direction. The conductors with guided external fields depends on the direction of the guided fields. The example with magnetic core shown in Table 3.7 is a common configuration of the winding of solenoidal type transformers.

Multiple conductors in a parallel connection are also considered. This shares total current with same nodes in Table 3.8. Note that there is no effective difference between multi-conductors in parallel connection and one solid conductor when the cross sectional areas of the two are the same. The multi-strands wire benefits at high frequencies only when each strand switches their location such as with twisted multi-strands wires.

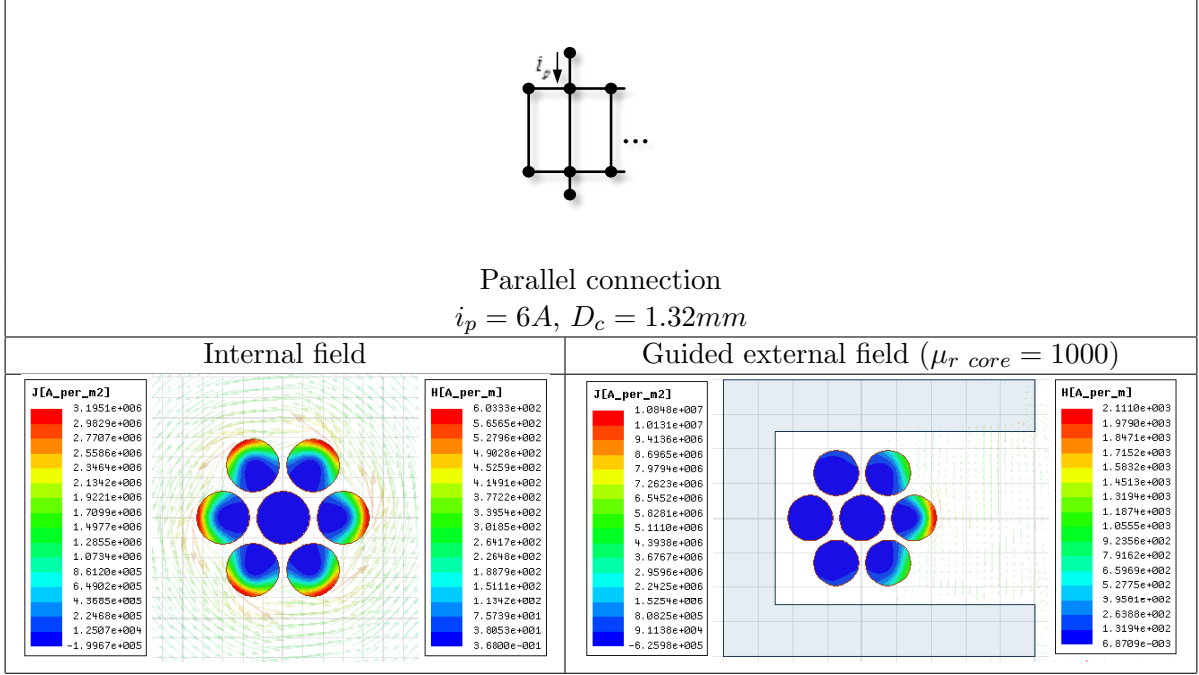
Table 3.7: Current density on coppers in series connection at $100kHz$



3.3.2 EM field distribution on an infinite tubular conductor - review of literatures

The current density in concentric geometry is described by Bessel's differential equation of order zero in cylindrical coordinates in Eq 3.40. The overline indicates a phasor in rms. The electric and magnetic fields have only tangential components on the surface under the assumption of infinite tubular conductors. The displacement current is negligible when considering the

Table 3.8: Current density on coppers in parallel connection at $100kHz$



wavelength on the basis of practical operating frequency of the power electronics applications. $\bar{J}_z(r)$ is the current density in the z direction as a function of the radius r .

$$\bar{J}_z(r) = AJ_0(T_r) + BY_0(T_r), \quad T = \frac{i^{-1/2}\sqrt{2}}{\delta} \quad (3.40)$$

The two boundary conditions are determined by the enclosed current at boundaries, $r = r_{tube\ i}$ and $r = r_{tube\ o}$ in Fig 3.12. In this calculation, $r_i = r_{tube\ i}$ and $r_o = r_{tube\ o}$ are used as abbreviations.

$$\begin{aligned} T \cdot (AJ_1(T_{r_i}) + BY_1(T_{r_i})) &= -i\omega\mu\sigma \frac{I_{enclosed=r_i}}{2\pi r_i}, \\ T \cdot (AJ_1(T_{r_o}) + BY_1(T_{r_o})) &= -i\omega\mu\sigma \frac{I_{enclosed=r_o}}{2\pi r_o}. \end{aligned} \quad (3.41)$$

In the case of a single tubular conductor with perfect magnetic coupling $I_{enclosed\ r=r_i} = I_p$ and $I_{enclosed\ r=r_o} = 0$. This means the current flow in the inner winding is I_p [A] and the current flow in the copper tube is I_p [A] in the opposite direction. The coefficients under the given conditions are shown in Eq 3.42.

$$\begin{aligned}
A &= -I_p \frac{iY_1(Tr_o)}{\pi r_i T \delta^2 (J_1(Tr_o)Y_1(Tr_o) - J_1(Tr_o)Y_1(Tr_o))}, \\
B &= I_p \frac{iJ_1(Tr_o)}{\pi r_i T \delta^2 (J_1(Tr_o)Y_1(Tr_o) - J_1(Tr_o)Y_1(Tr_o))}.
\end{aligned} \tag{3.42}$$

The effective resistance of each tubular conductors is achieved on the basis of complex Poynting theorem in phasor form in Eq 3.43.

$$P_{avg\ r=r_i} [W/m] = 2\pi r_i \cdot Re(\bar{E}_z(r_i) \cdot \bar{H}_\theta(r_i)) = \frac{1}{2} I_p \cdot Re(\bar{E}_z(r_i)) \tag{3.43}$$

The particular solution of the effective resistance of a tubular conductor winding in the case of the perfect magnetic coupling is in Eq 3.44.

$$R_{ac} [\Omega/m] = Re\left(\frac{i(J_1(Tr_o)Y_o(Tr_i) - J_o(Tr_i)Y_1(Tr_o))}{\pi T \delta^2 r_i \sigma (J_1(Tr_o)Y_1(Tr_i) - J_1(Tr_i)Y_1(Tr_o))}\right) \tag{3.44}$$

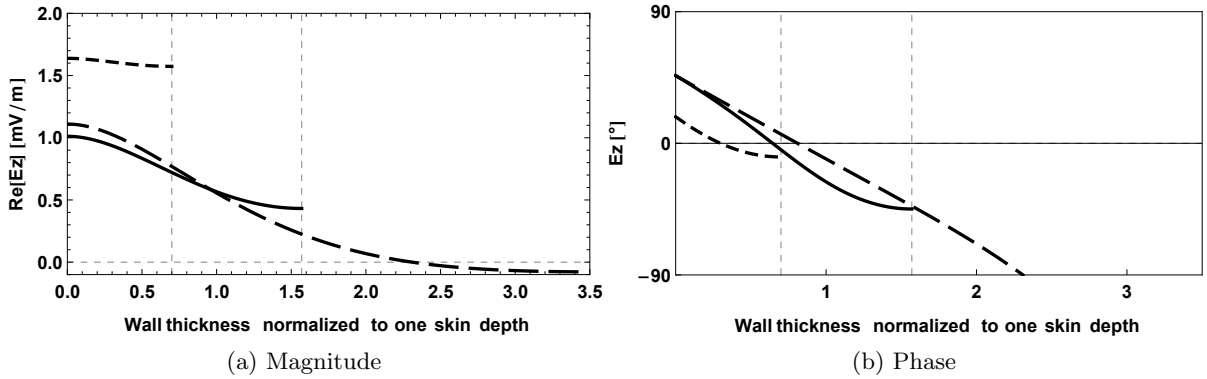


Figure 3.23: Electric field intensity vs. normalized thickness

The total current flowing through the conductor is fixed by a boundary condition with zero degrees of phase. Therefore, the real part of the electric field intensity at the source side, the inner surface of the conductor in this case, is directly proportional to the dissipated power in the conductor. The real part of the electric field intensity decreases as the thickness of the cylinder increases, but it will slightly bounce up again from 1.57δ as seen in Fig 3.23 [25].

The real part and argument of the current density, and magnetic field intensity in a solid copper tube at 20kHz, are plotted to investigate the characteristics of electromagnetic wave propagation in the conductor in Figure 3.24. The wall thickness is normalized to the skin depth

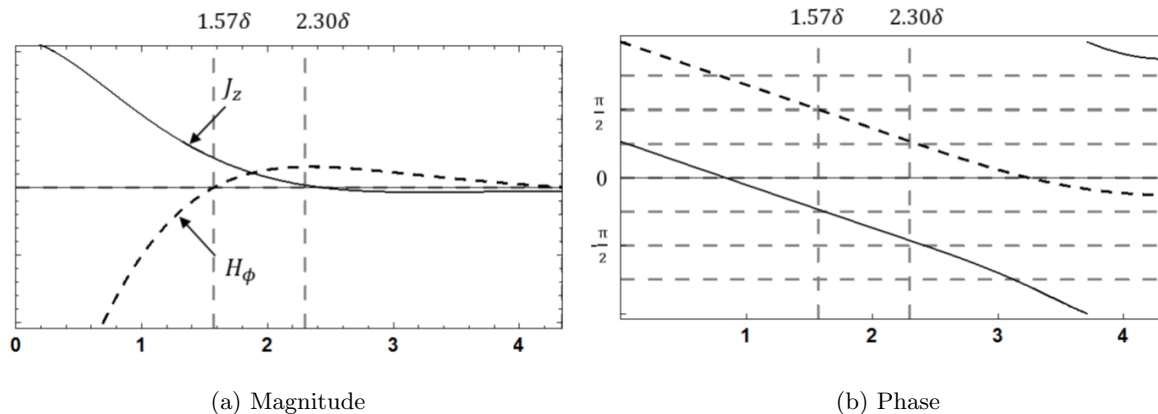


Figure 3.24: Current density and magnetic field intensity vs. normalized thickness

δ . The effective resistance slightly increases again at the thickness 1.57δ at phase difference $\pi/2$ from the boundary because the current density at phase differences from $\pi/2$ to $3\pi/2$ has a negative contribution to the net current flow. Note that the solution in Eq 3.44 is valid in the case of good magnetic coupling, which has the same amount of current inside in the opposite direction. The effective resistance changes with the location of the current congestion based on boundary conditions.

For example, the current congestion in a single conducting tube is on the outer boundary as shown in Fig 3.25. On the other hand, the current congestion on the outer tubular conductor with a magnetically coupled conductor inside, which is the case of CWT, is on the inner boundary as in Fig 3.26. Therefore, the effective resistance for both cases differs with the amount of the surface area on inner radius and outer radius in the case of a thick tubular conductor, $r_o \gg r_i$.

Fig 3.27 illustrates the different cases of the inner radius of the copper cylinder. The AC resistance is normalized to the DC resistance and the wall thickness is normalized to one skin depth δ . The ac resistance converges to a certain value regardless of increasing the thickness of the conductor.

3.3.3 Proximity effect on conductors in concentric geometry

As stated in the previous section, the effective resistance of the conducting material in multiple layers increases per layer by a factor of $(n - 1)^2 + n^2$. The proximity effect in conducting material in high frequency is one of the major concerns at high frequency applications. Specifically, the current waveform of the switched-mode power electronics application, such as DAB DC/DC operation of the applications, is highly contaminated by high-harmonic components. There-

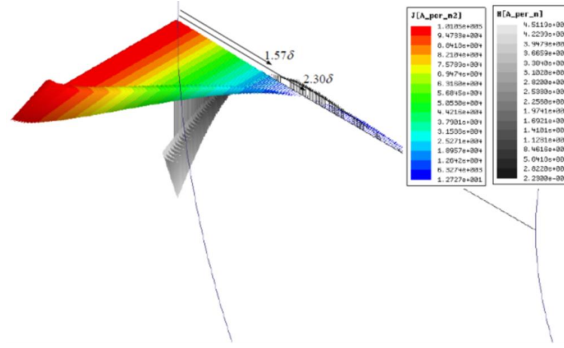


Figure 3.25: Current density in a tubular conductor, $\sqrt{2}[A]$ current excitation at 20kHz

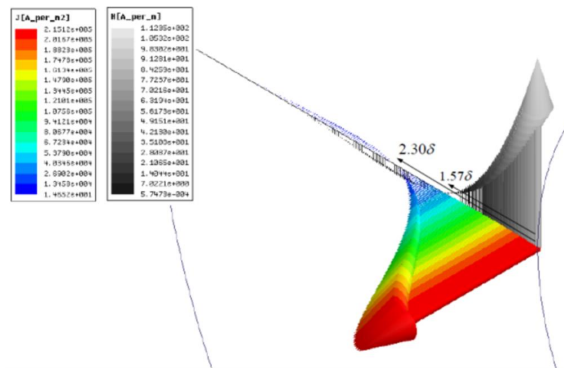


Figure 3.26: Current density in a outer tubular conductor, $\sqrt{2}[A]$ current excitation in outer tubular conductor and $-\sqrt{2}[A]$ in inner tubular conductor at 20kHz

fore, sizing the conductor materials in transformer on the basis of skin depth at the switching frequency is not the proper approach.

In the case of core-type transformers, the magnetic field makes a closed-path through the high permeability magnetic core and across the conducting materials, dominantly in a perpendicular direction in the window area in Fig ?? . On the other hand, the closed-path of magnetic field in the coaxial winding configuration is in a concentric manner and field attenuation is in a radial direction perpendicular to the magnetic field in the ϕ direction in Fig ?? . Another considerable advantage of coaxial winding structure for high frequency operation is that windings are not affected by the guided external field. As shown in in Fig ?? and Fig ?? , the highest current density on conductors in a core-type transformer is almost three times of that of coaxial winding transformer. We can see it comes from the number of layers due to the direction of external field. The number of layers in CWT can be seen 2 layers in radial direction and the number of layer in the core-type transformer can be seen as 3 layers with width of the window

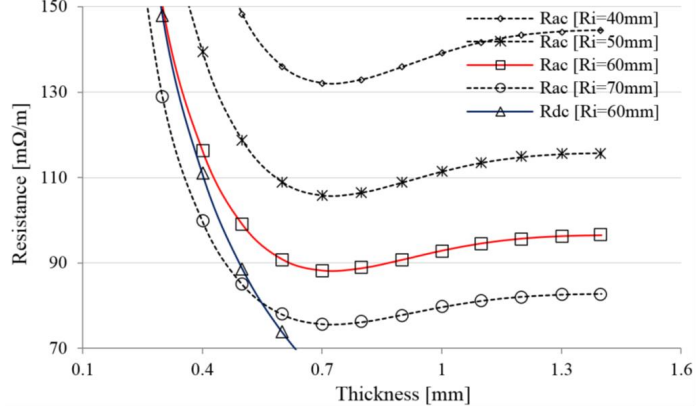


Figure 3.27: Normalized ac resistance vs. thickness at 20kHz ($r_i = 60mm$)

area.

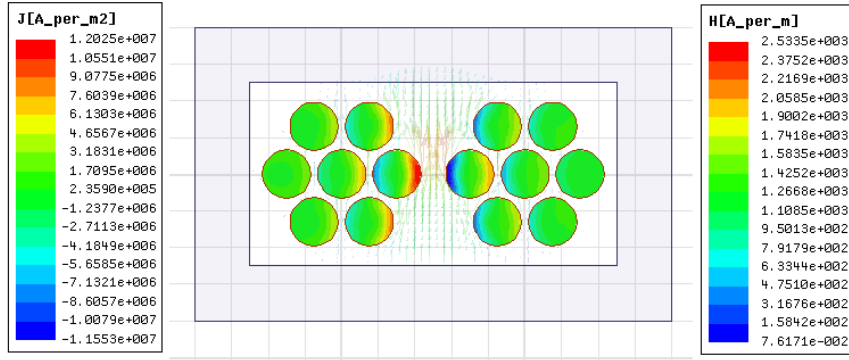
The effective resistance can be calculated by the general solution with different boundary conditions. The skin and proximity effects are comprehensively taken care of with the same approach in Chapter 3.3.2 under specific boundary conditions, which is the amount of current inside the closed path of the magnetic fields.

$$R_{ac}[\Omega/m] = \frac{\sum_1^i p_{avg i}}{I_{rms}^2} \quad (3.45)$$

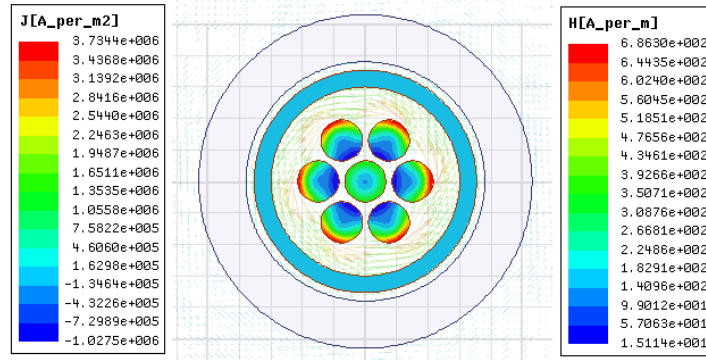
From a transformer design point of view, the conversion ratio is limited to an integer number because the number of turns of the outer winding is typically fixed at one due to the mechanical difficulties of assembly. When multiple tubular conductors are connected in series as in Fig 3.29, there is greater flexibility in the turns ratio so that it is no longer limited to an integer number. In the case of copper tube with multi-turns in a series connection, the calculation is clear with the same amount of current on each tube. However, in the case of copper tube with multi-layer in a parallel connection, the parasitic resistances, such as the connection part, are more comparable with the resistance of the copper tube section. Hence, current sharing, which is the boundary condition between conductors in a parallel connection, is not clearly defined.

3.3.4 Computer aided FEM results in 3D for CWT prototype

The configuration of the CWT prototype and its specifications are in chapter 3.2.1 and chapter 3.2.2. The effective resistance of the LV and HV windings at 20kHz are investigated in 2D in Fig ???. The winding arrangement and distance between conductors are determined with consideration given to insulation in chapter 3.4, hence only the size of the wire on HV side and



(a) core-type transformer



(b) coaxial winding transformer

Figure 3.28: Field distribution

thickness of LV winding are considered at fixed location. As analytically derived in Chapter 2.3.2, the lowest effective resistance of the tubular copper is at $0.7mm$, 1.58δ where it converges. The current density at DC is a fairly good approximation up to skin depth and the $150A/cm^2$ at $0.7mm$ is an acceptable value. The effective resistance of HV wires is for 30 turns per unit thickness of the CWT. The effective resistance after skin depth also converges, however the current density is relatively high. Considering the high frequency harmonics components and that the location of the HV winding is inside the copper tube and magnetic cores, it was decided to use Litz wire instead of solid copper.

The effective resistance of the LV winding is revised in real geometry in 3 dimension in Fig 3.32. The current density is congested in the narrow connection area, that links the two copper tubes for rerunning wires. However, the connection part is located separately outside and exposed to the air. The effective resistance of the LV winding in real geometry is plotted in Fig 3.31. The current rating on the LV winding is less than $200A$, the given specification should meet the requirements within an acceptable margin.

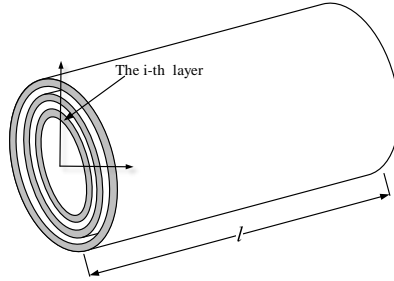


Figure 3.29: Multi-tubular winding

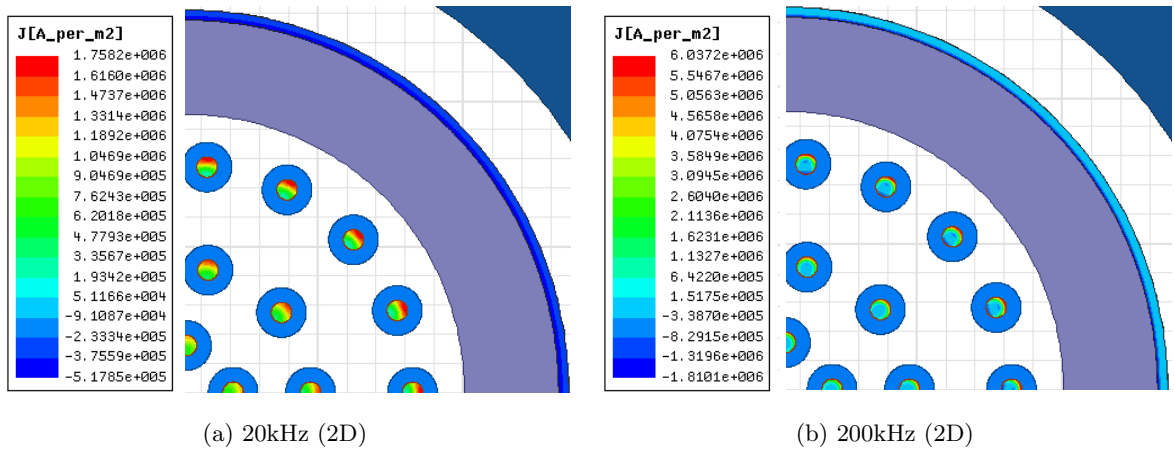
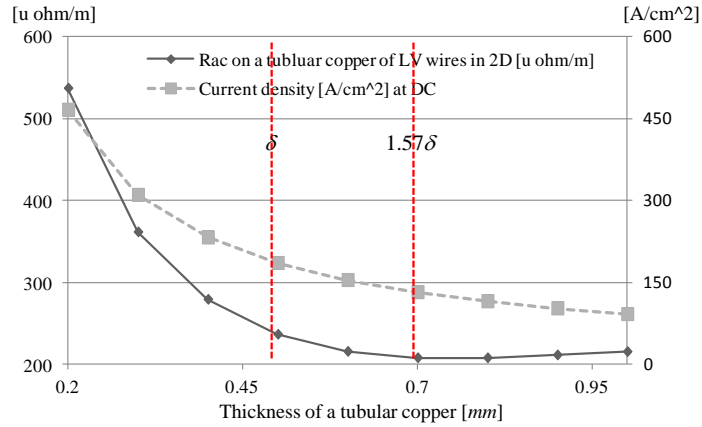
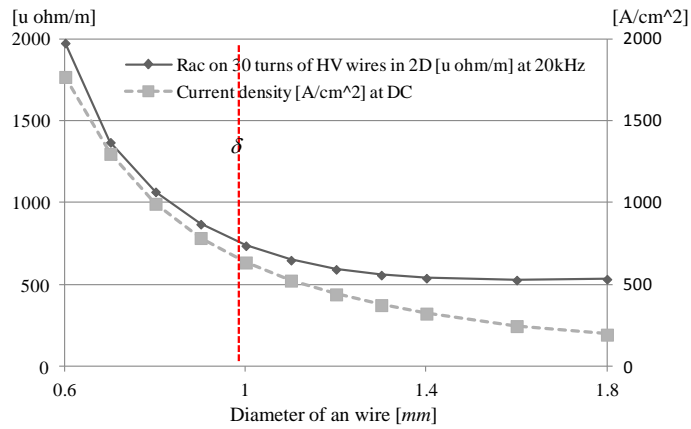


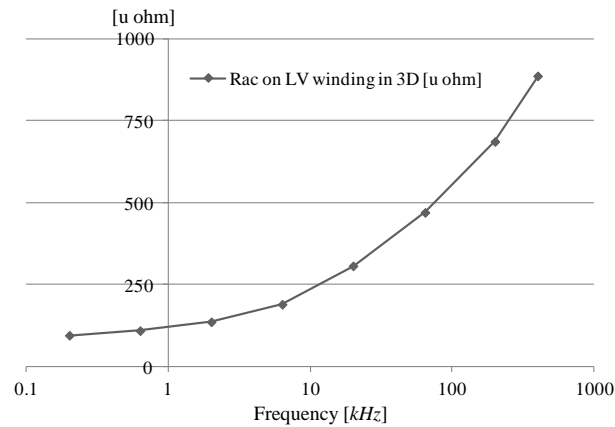
Figure 3.30: Current density distribution in 2D ($I_{HV\ peak} = \sqrt{2}[A]$, $I_{LV\ peak} = 30 \cdot \sqrt{2}[A]$)



(a) Rac on LV winding at 20kHz in 2D

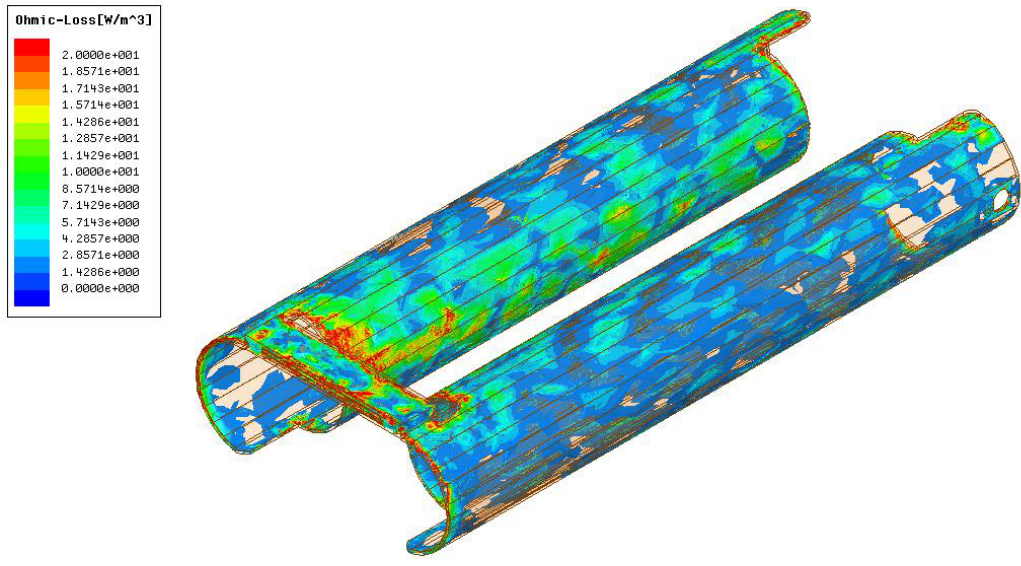


(b) Rac on 30 turns of HV winding at 20kHz in 2D

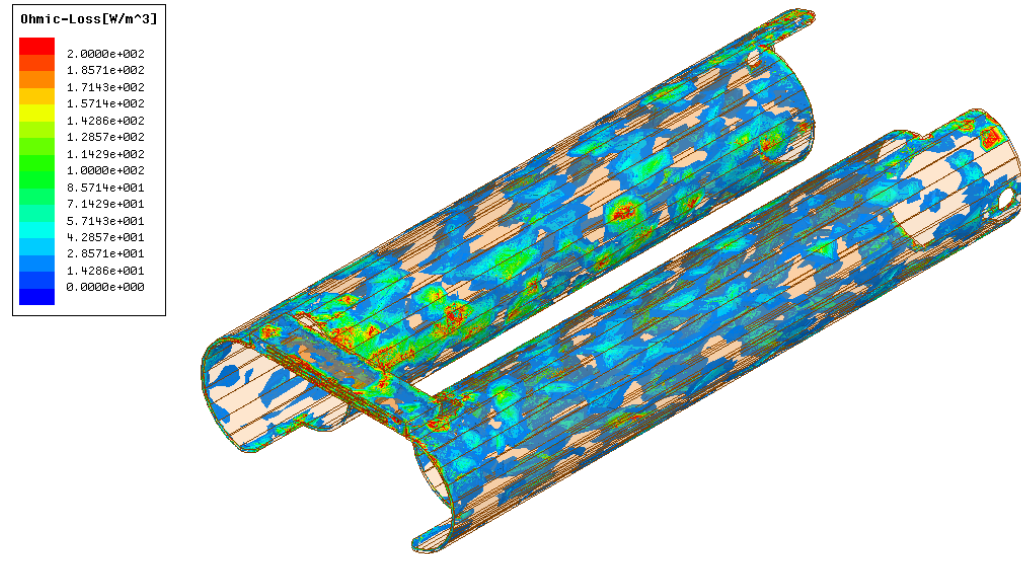


(c) Rac on LV winding of prototype in 3D

Figure 3.31: Effective resistance on LV and HV windings



(a) 20kHz



(b) 200kHz

Figure 3.32: Field distribution

3.4 Insulation strategy for MV-MF CWT prototype for SST application

The insulation is one of the main concerns of designing transformers in a medium voltage level and is strictly observed by international standard. However, it is difficult to predict with calculation or simulation results because the strength of insulation is considerably influenced by the manufacturing process and the precision of production. This is not taken care of calculation or simulation. The complete design has to be verified by experimental tests and the final results can only be achieved statistically by iterative tests due to the variations of the insulation characteristics in practice. In order to reduce the risk and cost for the transformer and tests, we have to predict and plan using properly designed construction and correct settings of voltage distribution.

3.4.1 Electric field distribution in simple configurations of insulation

The main references of insulating materials are permittivity, resistivity, dielectric dissipation factor, and partial discharge characteristics. There are two major phenomenon causing the danger of electric shock by contact or proximity.

Electrical breakdown: Rapid reduction in the resistance of the insulator that can cause a spark jumping around or through the insulator. This insulation breakdown occurs at the breakdown voltage and results in a short circuit.

Partial (Corona) discharge: Localized electrical dielectric breakdown of a small portion of a solid or liquid insulation system between conductors. The partial discharge occurs when the local electric field intensity exceeds the dielectric strength of the material surrounding the conductor. The pulse discharge occurs in a short time, less than 1 μ s. The intensity is represented by the charge level in picocoulombs or nanocoulombs. It is also affected by geometry, because a sharp point has much higher gradient. The breakdown can be initiated from the location of the highest electric stress and is subjective to the physical and chemical properties of the dielectric material and its impurities.

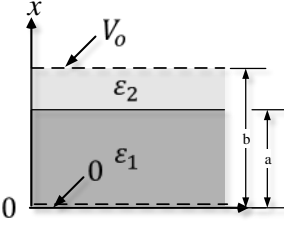
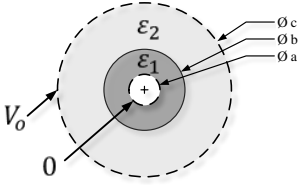
Electric field distribution: Even though the geometry of a transformer is complicated, the design and selection of insulation can be estimated with a prior knowledge of electric field distribution. Analysis and testing in simple geometry can be used to gain an insight to the preliminary choice of insulation materials and determination of the clearance distance. The insulation level can be revised based on the results of experiments carried out with the preliminarily design prototype.

The electric stress is subjected to the numerical voltage gradient, electric field intensity. The dielectric strength of an insulation material can be defined as the maximum dielectric strength

the material can withstand. The electric field intensity is analytically calculated by Poisson's equation and the results can be an indication of how much distance is required to withstand the potential difference.

Since the relative permittivity of insulation mineral oil ($\epsilon_r = 2.2$) or air ($\epsilon_r = 1$) is lower than that of solid materials, such as paper-based phenol ($\epsilon_r = 5 \sim 6$) or pressboard ($\epsilon_r = 4 \sim 5$), the field strength in the oil or air have a higher electric stress. In the case of a dry-type transformer, the air between conductors always has the highest electric field, despite the lower dielectric strength compared to typical insulation materials due to its low permittivity. Therefore, the clearance distance between conductors is a critical factor when determining the insulation level of the transformer, unless whole transformer is potted and encapsulated under vacuum conditions.

Table 3.9: Electric field intensity in simple geometry

Parallel plates	Concentric plates
$\begin{cases} E_{x1} = \frac{V_o}{a\left(1-\frac{\epsilon_1}{\epsilon_2}\right)+b\frac{\epsilon_1}{\epsilon_2}} & a \leq y \\ E_{x2} = \frac{V_o}{a\left(\frac{\epsilon_1}{\epsilon_2}-1\right)+b\frac{\epsilon_1}{\epsilon_2}} & 0 \leq y < a \end{cases}$	$\begin{cases} E_{r1} = \frac{-V_o}{\ln\frac{b}{a}-\frac{\epsilon_1}{\epsilon_2}\cdot\ln\frac{b}{c}} \cdot \frac{1}{r}a_r & a \leq r \leq b \\ E_{r2} = \frac{-V_o}{\ln\frac{b}{a}-\frac{\epsilon_1}{\epsilon_2}\cdot\ln\frac{b}{c}} \cdot \frac{1}{r}a_r & b \leq r \leq c \end{cases}$
	

3.4.2 Insulation strategy and case study for MV-MF CWT

The primary requirement of the transformer's insulation is to make it capable of withstanding the power frequency, lighting impulse, and switching impulse stresses. Transformer voltage ratings below 250kV are only subject to impulse and power frequency voltages. They are rated to withstand specific levels according to IEC standards, because properly designed transformers that can withstand a lightning impulse voltage are generally capable of passing switching impulse tests. The rated withstand voltages for transformer windings with 12kV medium voltage, as set by international standards, are shown in Table 3.10.

Table 3.10: Rated withstand voltages

Highest voltage for equipment	Rated short duration power frequency withstand voltage	Rated lightning withstand voltage
12kV	28kV	75kV

The operating frequency of 20kHz is around 400 times that of a conventional distribution line frequency of 50/60Hz in a medium voltage level and the excitation voltage is not a sinusoidal waveform, but a pulse switching waveform. The international standard, and a variety of principles introduced to design the insulation of transformers, in a medium voltage level, is set on the basis of conventional systems and applications. It may not be proper to directly apply them to power electronics-based SST applications; however, they provide a good starting point from a design standpoint. The preliminary insulation design of the prototype in this thesis relies on knowledge from the principles for conventional transformers and the results found under static conditions.

The major differences in the MV-MF transformer for SST applications are the operating frequency and the pulse voltage excitation. It is known that an increase in frequency generally results in a reduction of insulation strength, such as $\propto \frac{1}{f^{0.137}}$. However, this relationship cannot be properly applied to SST applications with conventional applications. Dielectric strength is a strong function of temperature. The reduction of insulation strength seen with the increase of frequency in the equation could rather be due to a relationship of dielectric loss and temperature increase caused by the increase in operating frequency. Dielectric breakdown requires a certain amount of energy, and the volt-time characteristics in short-time tests show the reciprocal relationship required to reach electric breakdown.

Winding method of MV-MF transformer for SST applications: The configuration and winding methods are significant factors with respect to insulation and parasitic capacitance. Hence, reduction of the electric field intensity in the transformer using an appropriate winding arrangement can not only reduce the insulation level and cost, but also lower the equivalent capacitances of the system. The proposed winding method for a coaxial type transformer is shown in Fig 3.34. The winding method can be more specific due to the low number of turns for the CWT. Each turn of the high voltage winding is arranged in order to the lower electric potential between layers. Each layer of turns also acts as an electrical shield to each the others. The highest electric potential is located in the innermost layer to be electrically screened by the other layers. This winding configuration reduces the electric stress and insulation level by a factor of the number of layers. The highest electric stress between interturn, interlayer and winding to winding are shown in Table 3.11. The specification of the wire used is listed in Table 4.15.

Table 3.11: Electric stress

Interterm insulation		Interlayer insulation		Main insulation (Inter winding insulation)
Turn 1 and 2	Turn 1 and 17	layer 1-2	layer 2-3	Turn 17 and copper tube
200V	3.4kV	3.4kV	2.4kV	6kVDC+3.4kVAC

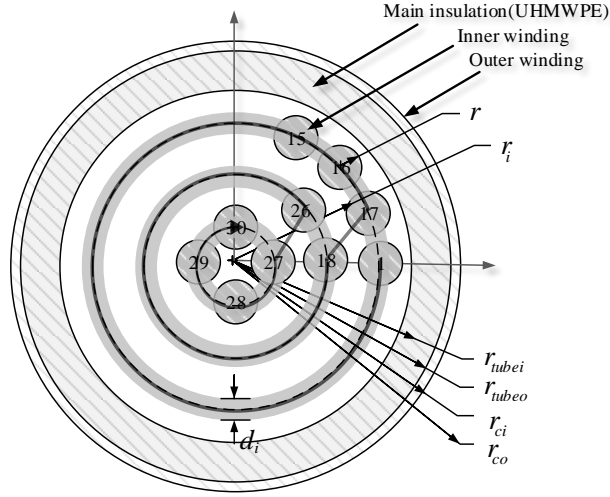


Figure 3.33: Concentric winding arrangement

Electrostatic field distributions in two dimensions are investigated with FEM simulation for two switching condition of a 12kV-400V half bridge configuration for single-phase DAB operation in Table 3.13. The low voltage terminal of the each half bridge is assumed to be grounded.

Liquid immersion-type: Assuming the electric potential is evenly distributed on the turns in a HV winding, the highest electric stress is located between the secondary winding and the 17th turn. The highest electric field is found on the surface of the copper of the 17th turn. This is because the permittivity of mineral oil is 2.2, which is almost same as the Teflon insulation of the wires ($\epsilon_r = 2.1$). The properties of insulation oils are shown in Table 3.14. The relative permittivity of the insulation oils is typically close to, or higher than, that of PFA wire insulation. Hence, the highest electric field is always on the wire insulation. The recommended distance between the windings of a liquid-immersed transformer at 10kV rated voltage is 8mm. The maximum electric field is 1.7MV/m under switching condition 1

Table 3.12: Specifications of the windings and insulation materials

HV Side	Type	Type 2 litz 5*70/40	
	Guage	15AWG	
	Strands	MW77-C (Thermal class H 180°C)	
	Insulation material and thickness	0.04" PFA JACKET	
		Relative permittivity	$\epsilon_r = 2.1$
		Dielectric strength	$\sim 80\text{MV/m}$
		Continuous service temperature	260C°
	Outer diameter	0.17"	
DC resistance	$9.9 \cdot 10^{-3}\Omega/m$		
LV Side	Type	Two copper tubes connected by plates	
	Dimenstion	Length of body 500mm each	
Main insulation (winding-winding)	Insulations material and thickness	0.25" UHMWPE	
		Relative permittivity	$\epsilon_r = 2.3$
		Dielectric strength	$\sim 28\text{MV/m}$
		Continuous service temperature	80C°

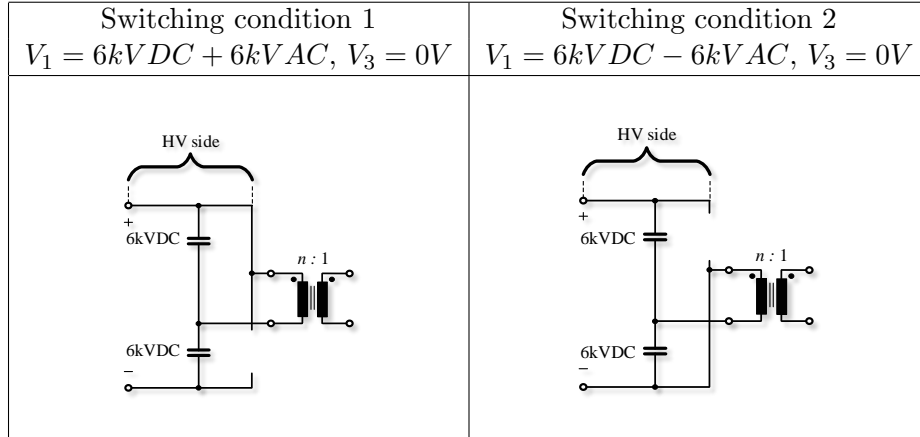
$(V_1 = 6\text{kVDC} + 6\text{kVAC}, V_3 = 0\text{V})$.

At 75kV, under static conditions, the maximum electric field is 18.5MV/m on the PFA insulation jacket of the 17th turn, which is around 65% of the typical breakdown voltage. Considering that dielectric strength decreases with time, the insulation is in a safe region and meets the IEC international standard: 28kV of power frequency tests and 75kV of lightning impulse tests.

Dry-type (Insulation medium : Air): When air is used as insulation medium, the maximum electric field is 2.8MV/m. It should be noted that the permeability of air is always lower than that of insulation materials. The highest electric field is in the air-gap, which has a lower dielectric strength than other insulation materials. Thermal issues due to the low thermal conductivity of air degrade the insulation during operation. 2.8MV/m is below the typical breakdown voltage of air; however, additional insulation or other methods have to be considered in order to withstand the voltage ringing of the switching transition, overvoltage, lightning impulse conditions, etc. A dry-type using an insulation medium of air is typically not used in medium voltage levels due to the large clearance distance required and insulation concerns. The large size also leads to an increase in cost.

Dry-type, (Insulation medium : Epoxy potting and encapsulating resin): Potting and encapsulation is the preferred insulation method for dry-type transformers due to size reduction and insulation reliability. The maximum electric field is only 1.8MV/m on the PFA

Table 3.13: Switching condition of a half bridge configuration



insulation of the wire due to the high permittivity of the epoxy resin, and the much lower breakdown voltage of 80MV/m for the PFA insulation. Any air bubbles or voids inside the transformer could possibly cause a partial discharge or corona. Hence, the encapsulation has to be processed without air or contaminants. The high thermal conductivity helps to dissipate the heat congested in the center of the concentric configuration. The strength of the insulation is considerably influenced by the manufacturing technology of drying-out and impregnation, and the precision of production.

The insulation level with epoxy encapsulation in this size is excessive and further size reduction is possible with further revision. However, the high permittivity of the insulation medium increases the parasitic capacitance on the transformer and causes high leakage current during high dv/dt switching.

Table 3.14: Insulation medium : Insulation oils and air

Material	Relative permittivity	Dielectric strength	Flash point	Thermal conductivity
Mineral oil	2.2	70MV/m	$160C^\circ$	0.126 [W/m/K] @ $20C^\circ$
Synthetic oil	3.2	75MV/m	$275C^\circ$	0.144 [W/m/K] @ $20C^\circ$
Silicon oil	2.7	50MV/m	$300C^\circ$	0.15 [W/m/K] @ $20C^\circ$
Air	1.0	3MV/m	N/A	0.024 [W/m/K] @ $20C^\circ$

Table 3.15: Insulation medium : Epoxy resins

Material	Relative permittivity	Dielectric strength	Operating temperature	Thermal conductivity
Epoxy potting and encapsulating resin	4.7	230MV/m	-50C° ~ 160C°	3 [W/m/K] @20C°

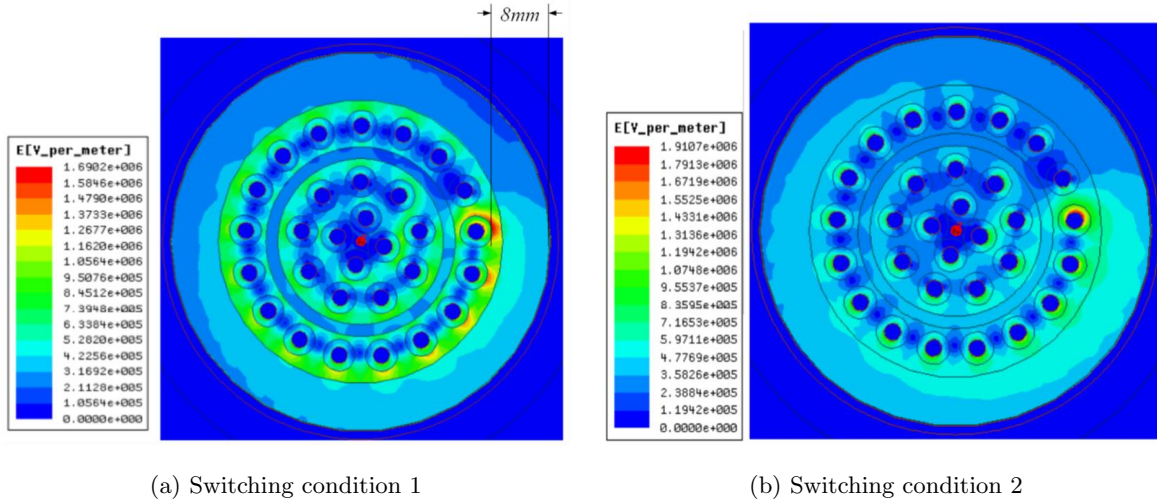


Figure 3.34: E-field distribution with insulation medium (Mineral oil)

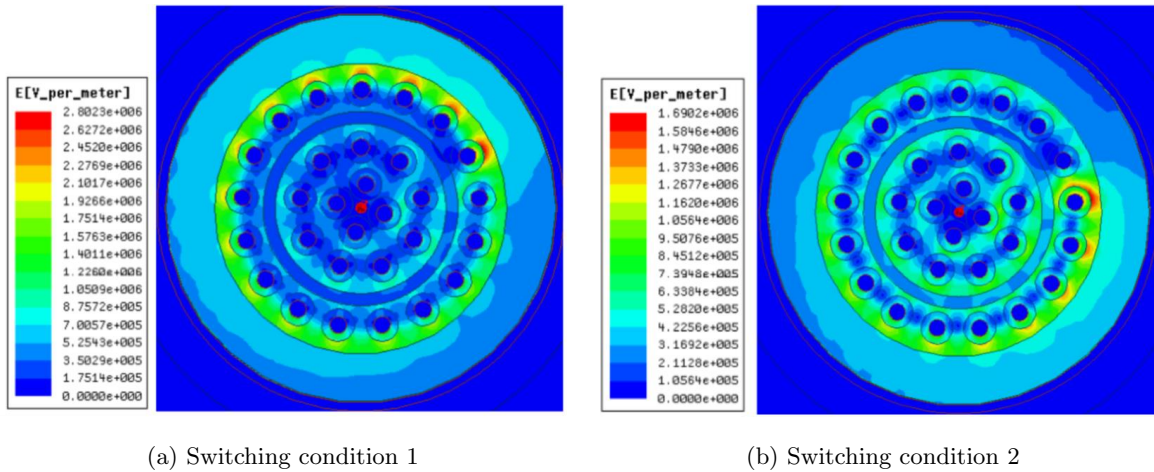
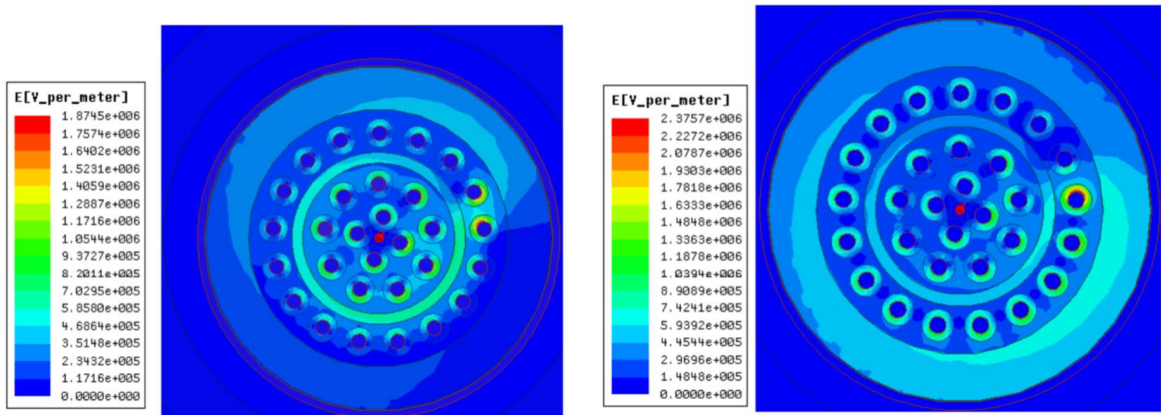


Figure 3.35: E-field distribution with insulation medium (air)



(a) Switching condition 1

(b) Switching condition 2

Figure 3.36: E-field distribution with insulation medium (Epoxy resin)

3.5 MV-MF CWT prototype and experimental test results

3.5.1 Loss and insulation test results

Insulation tests: A DC dielectric breakdown Test was conducted on the prototype at 9.5kVDC between both windings for 60 seconds. There was no air breakdown or dielectric failure while retaining a leakage current of 0.7mA. A pulse switching frequency test was done by exciting a 200V square wave from the LV winding and inducing 6kV on the HV winding under a no load condition. There was no sign of electrical failure or heat problems without the use of cooling methods over a period of 60 minutes. The pulse switching frequency test under open circuit condition was conducted without an active cooling method at an ambient temperature of 23°C. Core loss and hot spot temperatures were stabilized at 150W and 84°C respectively after 60 minutes of operation and heat is uniformly distributed on the wide and round surface without air-gap as shown in Fig 3.38. There were no additional losses or heat issues without an active cooling method, as planned.

Table 3.16: Dielectric breakdown test results without active cooling method

DC Dielectric breakdown test			
Excitation	Duration	Leakage current	Freq
9.5kVDC between winding	60 sec.	0.7mA	20kHz

Table 3.17: Pulse switching test results without active cooling method

Pulse switching frequency dielectric breakdown test			
Excitation	Duration	Ambient temp.	Hop spot
200Vrms and 7kVrms square wave	60 min.	23°C	84°C

Power rating and loss estimation: The copper loss and full-load rating are estimated by FEM simulation. The estimated ac resistance of the LV and HV winding are 193[$\mu\Omega$] and 0.62[Ω] respectively at 20kHz. Considering the high harmonic components of the trapezoidal waveform, the loss could be as high as twice that of the results from the sinusoidal waveform,

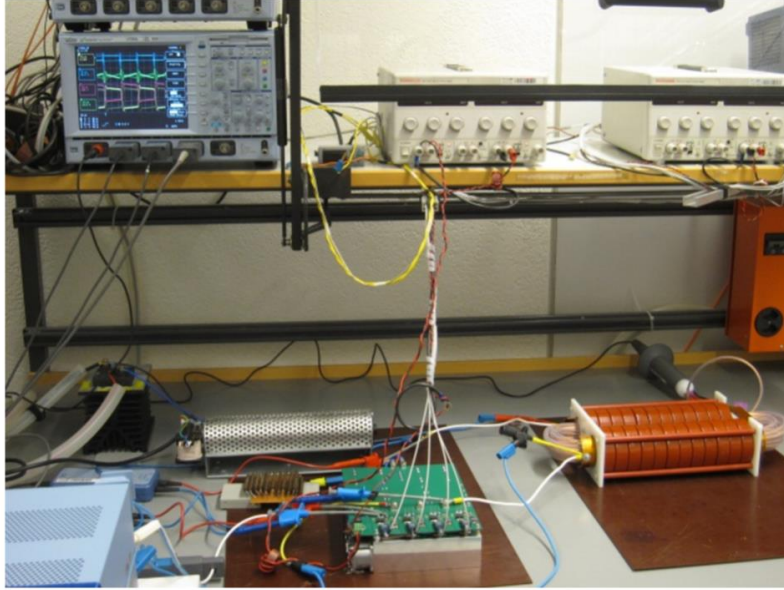


Figure 3.37: Test set-up

which will be discussed in Chapter 4. The current rating could be $250A$ with an approximated loss of $110W$ from the windings. The full rating of the transformer could be up to $50kVA$ with a $260W$ loss based on open-circuit measurement and the simulation results. In order to define the power rating of the transformer, the hot spot temperature has to be examined by load tests, however the full-load test is not yet possible due to the limitation of capacity at the converter stage.

Table 3.18: AC resistances of LV and HV winding at 20kHz

Outer winding (LV winding)		Inner winding (HV winding)
Copper tubes, Length of body = $0.51m$		30 turns of round solid copper wires Length(body) = $0.51m$, Edges $0.3m$
Calculation	$115 [u\Omega](226[u\Omega/m])$.
2D FEM	$124 [u\Omega](243[u\Omega/m])$	$521 [u\Omega/m]$
3D FEM with connections	$193 [u\Omega]$.

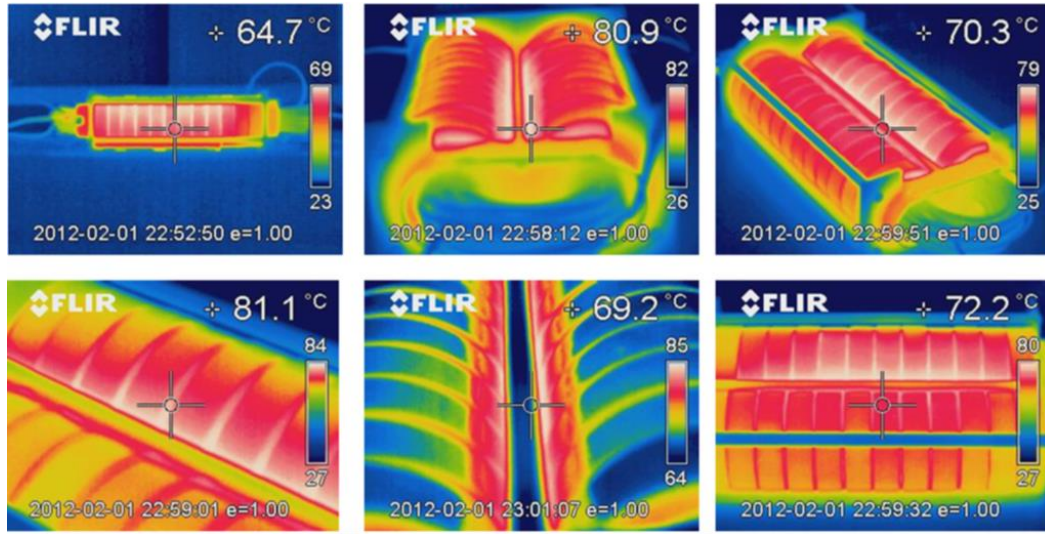


Figure 3.38: Temp. distribution after 60 minutes operation of the pulse switching test

3.6 Summary

This chapter reviewed existing literature and analytical design approaches, and verified using computer aided finite-element analysis. The parasitic inductance and capacitance elements for CWT are derive by analytical calculation and verified by FEM simulation and measurement results. The equivalent circuit model for a coaxial winding transformer with a high turns ratio was proposed to expect the response from the high dV/dt pulse switching in the circuit model. The first CWT prototype is built with an emphasis on verication of the feasibility to operate with 15kV SiC based DAB DC/DC converter(Laboratory prototype A). The insulation of the CWT prototype was designed by investigating electric stress using FEM and tested up to 10kVDC and 6kVAC pulse switching condition using air as an insulation medium. There is no sign of insulation failure in laboratory tests; however, insulation oil may have to be considered to meet the international standards at 12kV. With respect to the insulation level, further study and tests in qualified facilities will be required. Even though the load test was not available due to the limitation of the laboratory capacity, the CWT prototype is expected to achieve an overall efficiency 99.5% at 50kVA based on open-circuit tests and computer-aided analysis. The coaxial winding power transformer is suitable for high frequency applications with good electric and magnetic shielding. The concentric configuration generates low parasitics and strong against skin and proximity effects. The evenly distributed magnetic field and losses help to avoid heat congestion and high hot-spot temperatures. The highly predictable leakage inductance inside the transformer can be utilized for special purposes, such as inductor integration in Chapter 4.

Chapter 4

PROPOSED INDUCTOR-INTEGRATED COAXIAL WINDING TRANSFORMER FOR DAB DC/DC CONVERTER

One of the key advantages of resonant/non-resonant high power DC/DC converters comes from utilizing the transformer without external inductors to transfer power and achieve zero-voltage switching. However, the leakage inductance of the transformer is generally not in the desirable range and is difficult to adjust to arbitrary values. In many cases, the series inductance required for power transfer can be realized by adding external inductors to make up the rest of the required series inductance when added to the leakage inductance of the transformer.

As one solution, the leakage inductance of the transformer can be intentionally guided and amplified using geometry and turns. However, one should keep in mind that the leakage inductance of the transformer is not a free source either. The leakage magnetic flux needs more guidance by a magnetic material in order to amplify and predict the leakage inductance of a transformer. The guided flux also flows through the magnetic material and generates additional losses. Additionally, the guided magnetic field causes significant skin and proximity effects in the conductors and increases copper losses considerably as discussed in chapter 3. Generally, when more accurately predicted and amplified leakage magnetic flux is used in the transformer, higher core and copper loss results.

As another proposed solution in this thesis, a highly accurate and analyzable inductor-

integrated coaxial winding transformer is introduced. The main advantage of this configuration is that the inductor and transformer body are integrated together and the inductor values are selected arbitrarily by changing the commercially available magnetic cores. In this configuration, it has several considerable advantages along with the benefits of conventional CWT, such as predictability, and low sensitivity on skin and proximity effect. ICWT uses less amount of copper by integrating the inductor core within the transformer by sharing the winding without compromising the two different functionalities of transformer and inductor. The auxiliary accessories, such as connectors and wires, which causes additional space, loss, and parasitics, are also eliminated. We are fully utilizing the predictable leakage magnetic flux inside transformer while any external field does not affect the copper wires. The characteristics are still analyzed separately in an integrated body and expressed in closed form. This is one of the most desirable configurations for high frequency applications that are considerably affected by parasitic effects.

ICWT has typically the minimum number of turns due to the mechanical difficulty of changing the number of turns. The laboratory prototype is also built with a single turn on the LV side at turns ratio 15:1. The distance and area between windings to withstand medium voltage 6kV is dominant in the window area compared to the copper area of ICWT windings. Hence, the copper area is not sensitive with system size and performance and designed for very low copper loss, without a considerable compromise of size of the transformer. Therefore, the portion of the copper loss out of total load-loss of the ICWT is relatively low at the given power rating 20kVA 30kVA 20kHz at 6kVDC.

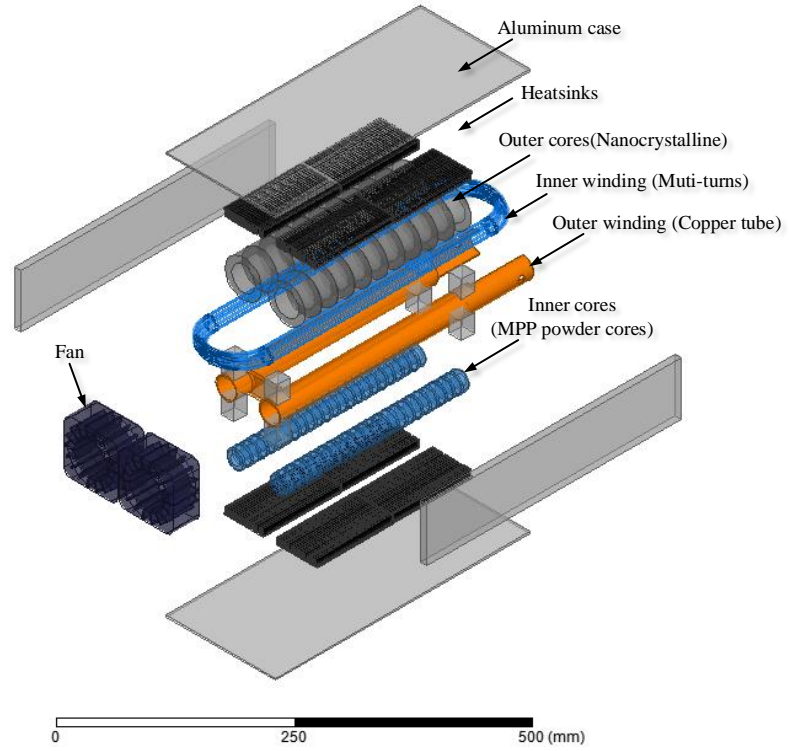
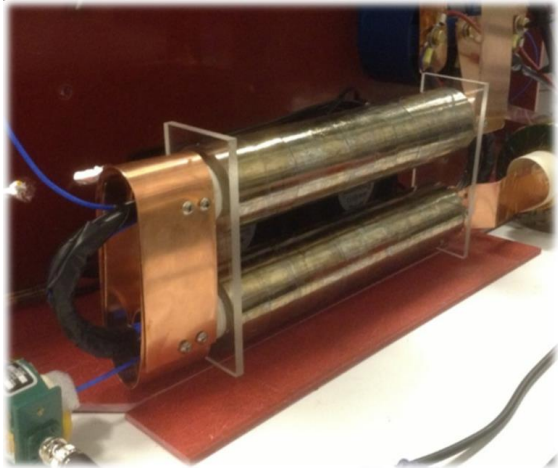
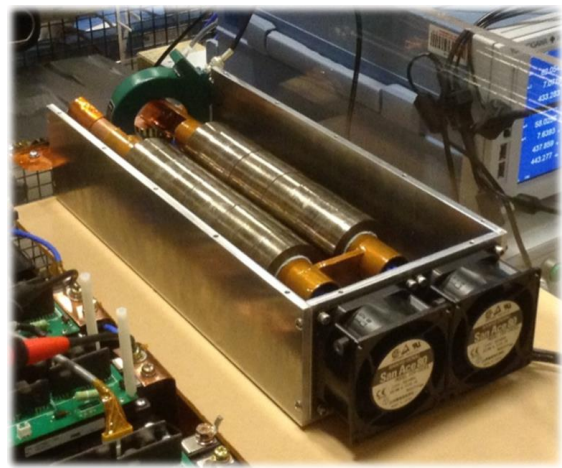


Figure 4.1: Assembly of ICWT



(a) preliminary ICWT prototype



(b) Machine shop built ICWT prototype with aluminum case and heatsinks

Figure 4.2: Prototypes of ICWT

4.1 Modeling concept: Inductance integration

4.1.1 Lumped-element equivalent inductance model of ICWT

An easy and highly predictable method used to integrate arbitrary values of series inductors on the CWT geometry is to place another magnetic material, toroid cores, in the aligned leakage magnetic flux in the concentric geometry of the CWT as shown in Fig 4.3. As with conventional coaxial winding power transformers, a thin concentric conducting cylinder passes through the outer cores while an outer winding with multi-turns of wires is placed in the center of the outer winding to function as an inner winding. Another magnetic core can be placed between the inner and outer windings to amplify the leakage magnetic flux density. This additional core functions as a series inductance, which is an element used to determine the amount of power transfer for the DAB converter.

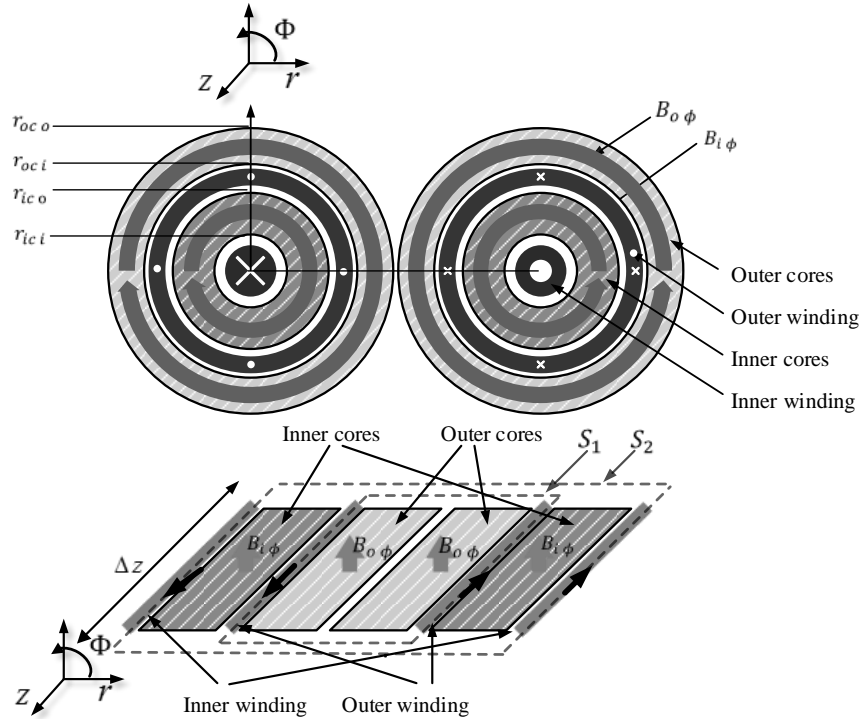


Figure 4.3: Cross sectional views

The permeability of the magnetic material is much higher than that of air, so only magnetic

flux inside the inner and outer cores is considered as a lumped-element circuit element. The magnetic field density in the both cores is calculated in Eq 60

$$B_{i\Phi} = \frac{\mu_o\mu_{ri}N_i i_i}{2\pi r} \quad B_{o\Phi} = \frac{\mu_o\mu_{ro}(N_i i_i - N_o i_o)}{2\pi r} \quad (4.1)$$

By the integral form of Maxwells equations

$$\oint E \cdot dl = - \int_s \frac{d}{dt} B \cdot dS \quad (4.2)$$

Hence, the electric field intensity and the voltage on the inner and outer winding are:

$$E_{oz} = \frac{d}{dt} \int_{r_{oci}}^{r_{oco}} B_{o\Phi} dr \quad (4.3)$$

$$E_{iz} = \frac{d}{dt} \int_{r_{oci}}^{r_{oco}} B_{o\Phi} dr + \frac{d}{dt} \int_{r_{ici}}^{r_{ico}} B_{i\Phi} dr \quad (4.4)$$

$$V_o = N_o \int_0^l E_{oz} dz = N_o^2 P_m \cdot \frac{d}{dz} \left(\frac{N_i}{N_o} i_i - i_o \right) \quad (4.5)$$

$$V_i = N_i \int_0^l E_{iz} dz = N_i^2 P_m \cdot \frac{d}{dt} (i_i - \frac{N_o}{N_i} i_o) + N_i^2 P_l \cdot \frac{d}{dt} i_i \quad (4.6)$$

Where $P_m = l \frac{\mu_o\mu_r}{2\pi} \ln(\frac{r_{oco}}{r_{oci}})$ and $P_{leak} = l \frac{\mu_o\mu_r}{2\pi} \ln(\frac{r_{ico}}{r_{ici}})$

Therefore, the magnetic coupling circuit model can be represented in Fig 4.4.

As shown in Fig 4.4, the magnetic flux of the inner cores is determined solely by the current flowing through the inner winding. On the other hand, the magnetic flux in the outer cores is determined by the magnetizing current, after canceling out the currents in both windings in the opposite direction.

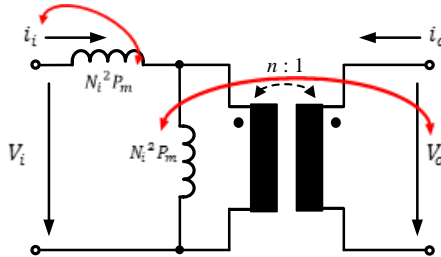


Figure 4.4: Equivalent circuit model

Terminal voltage and line currents are directly measurable in practice and system control variables. It is convenient to think that the mutual flux is driven by the voltage on the outer winding, and the leakage flux is driven by the line current on the inner winding. DAB DC/DC converter operation is of a non-resonant type. Hence the analysis of the ICWT operation for SST applications is based on a magnetic circuit model only, and the capacitive coupling will be considered as a parasitic effect. The amplified leakage inductance of the transformer by the inner cores plays a role as a series inductance in the filter network, as it lags the load current, and enables zero-voltage switching (ZVS).

Magnetic flux on inner and outer cores : The essential feature of the ICWT is that the magnetic flux of both the inner and outer cores are independent. This also means the mutual and leakage magnetic flux are independent in concentric and infinitely long geometry. The independently and symmetrically formed magnetic field makes the transformer's properties simple and predictable even with inductor integration.

The leakage inductance of the transformer is simplified in Eq 4.7 with only the magnetic flux inside the inner core due to the high permeability of the magnetic material when compared to air.

$$L_l = N_i^2 \frac{\mu_o \mu_r}{2\pi} \ln \frac{r_{ic.o}}{r_{ic.i}} \text{ referred to inner winding} \quad (4.7)$$

The power transfer of the single phase DAB operation can be calculated using the power flow equation with the fundamental frequency components and shows good agreement. However, accurate calculation of magnetic flux density is a fundamental task of transformer design in order to calculate the core loss and saturation limits, which is the critical design constraints of the magnetics design. The equation for line current which corresponds to the magnetic flux in the inner cores is calculated in a piece-wise fashion in Chapter 1.

The peak magnetic flux density of the outer cores is simply determined by the integration of the induced voltage on the outer winding over one half period. It should be noted that the magnetic flux density in the outer cores is dependent on the voltage on the LV side only, as is shown in the equivalent circuit model in Fig 4.4. Specifically, nanocrystalline material has very low specific loss at the given operating frequency of 20kHz. The dimension of the outer cores is determined not by loss and heat limitations, but the saturation flux density. Therefore, it is important to know the flux variation during DAB DC/DC conversion. The peak magnetic flux density in the outer cores is given in Eq 4.8. The dimension has to be selected by a specific margin considering the buck-boost conversion ratio, k , during transient operation.

$$B_{oc_peak} = \frac{V_2}{4f_s N_o A_c} = \frac{kV_1}{4f_s N_i A_c} \text{ at } \omega t = \theta_{ps} \quad (4.8)$$

The peak magnetic flux in the inner cores has two distinct regions of operation with buck-

boost conversion ratio k ; hence, the peak value is represented as a function of the control variable θ_{ps} with k . The ratio between the inner radius r_{ic_i} and the outer radius r_{ic_o} of the inner cores is set by $\sqrt{e} \cong 1.65$, which will be discussed in the following section. The magnetic flux density near the inner surface of the inner cores is greater than that near outer surface under the given condition as shown in Fig 4.6. Therefore the saturation limit has to be considered with the inner radius of the inner cores.

Boost mode : $k \geq 1$

$$\mu_o\mu_r \frac{V_1 N_i}{4\omega L_{leak} \pi r_{ic_i}} ((k-1)\pi + 2\theta_{ps}) \text{ at } \omega t = \theta_{ps} \quad (4.9)$$

Buck mode : $k < 1$

$$\mu_o\mu_r \frac{V_1 N_i}{4\omega L_{leak} \pi r_{ic_i}} ((1-k)\pi + 2k\theta_{ps}) \text{ at } \omega t = \pi \quad (4.10)$$

Where $V_1 = \frac{V_{MVDC}}{2}$ and $V_2 = \frac{V_{LVDC}}{2}$ are in a half bridge configuration.

In order to verify the accuracy of the calculation results in two dimensional approximation, a simplified three-dimensional geometry of the laboratory prototype is used for FEM transient simulation as shown in Fig 4.5. The specifications of the operating condition and the cores are shown in Table 4.1.

Table 4.1: Operating condition

Freq.	Turns ratio	MVDC	LVDC	Modulation scheme
20 kHz	n = 15	3kVDC	200VDC	Phase-shift

Table 4.2: Specification of the outer cores and inner cores

Outer cores					Inner cores			
Transformer					Inductor			
ID	OD	HT	Stacking factor	μ_r	ID	OD	HT	μ_r
36mm	55mm	25mm	0.8	30000	14.7mm	26.9mm	11.2mm	300

The transient behavior of the laboratory prototype under a different conversion ratio k is shown in Fig 4.7. The magnetic field density in the inner cores is following the current in the inner winding. On the other hand, the magnetic flux density in the outer cores is determined by a time integration of the voltage on the outer winding as explained in the previous section. In the case of $k > 1$ in Fig 4.7(c), the maximum magnetic flux density in the inner and outer

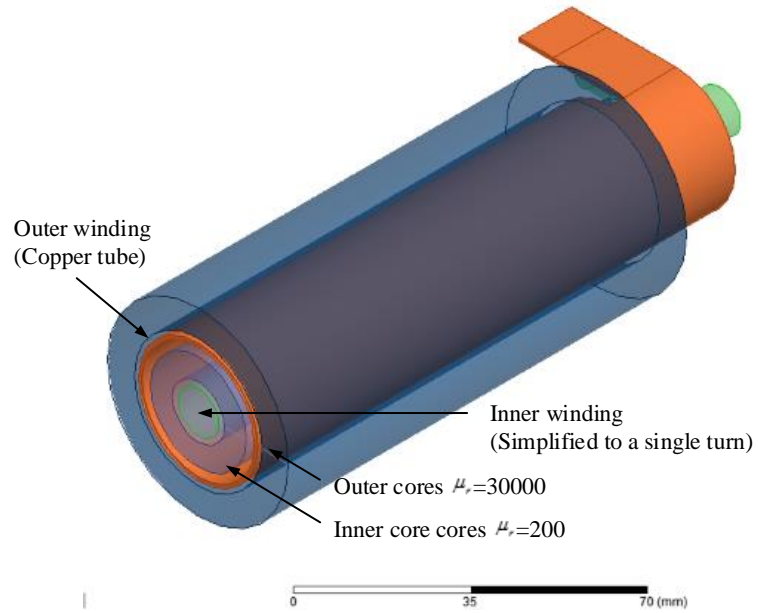
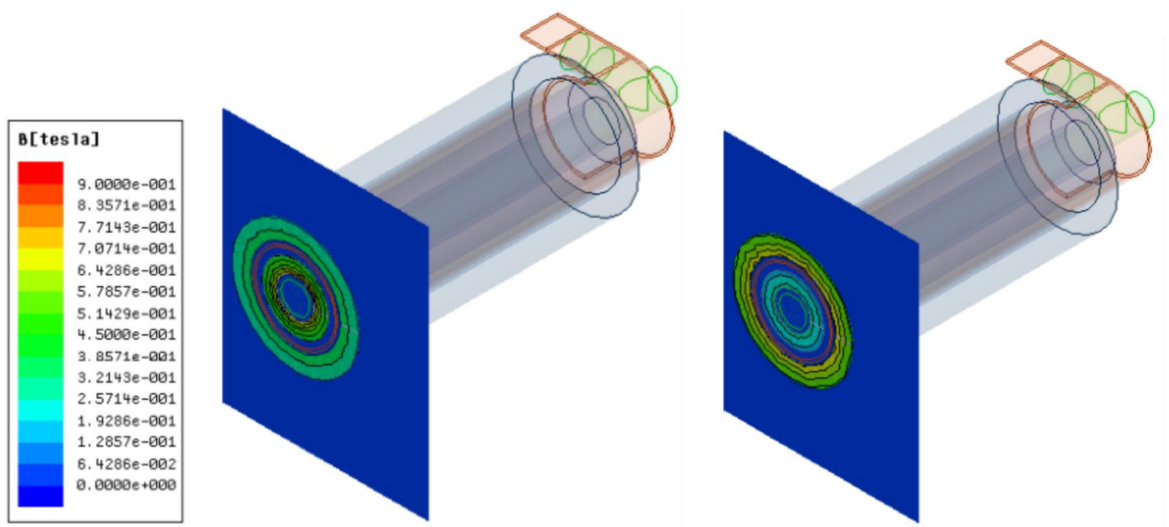


Figure 4.5: One quarter of a simplified model for 3D FEM transient solution

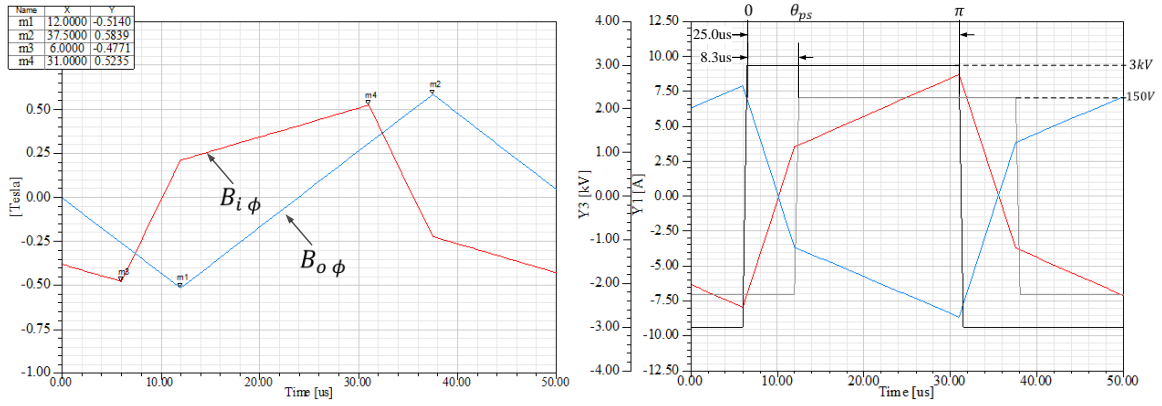
cores is at $\omega t = \pi$. On the other hand, the maximum B-field in the inner cores is at $\omega t = \pi$ and the maximum B-field in the outer cores is at $\omega t = \theta_{ps}$ in case of $k < 1$ as shown in Fig 4.7(a).



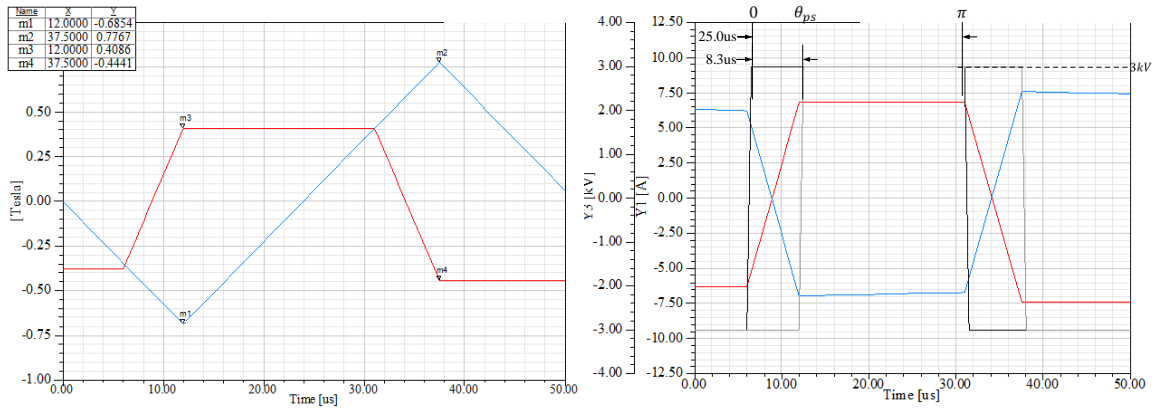
(a) Peak B-field in inner cores at 8.3us ($\omega t = \pi$)

(b) Peak B-field in outer cores at 33.3us ($\omega t = \pi + \theta_{ps}$)

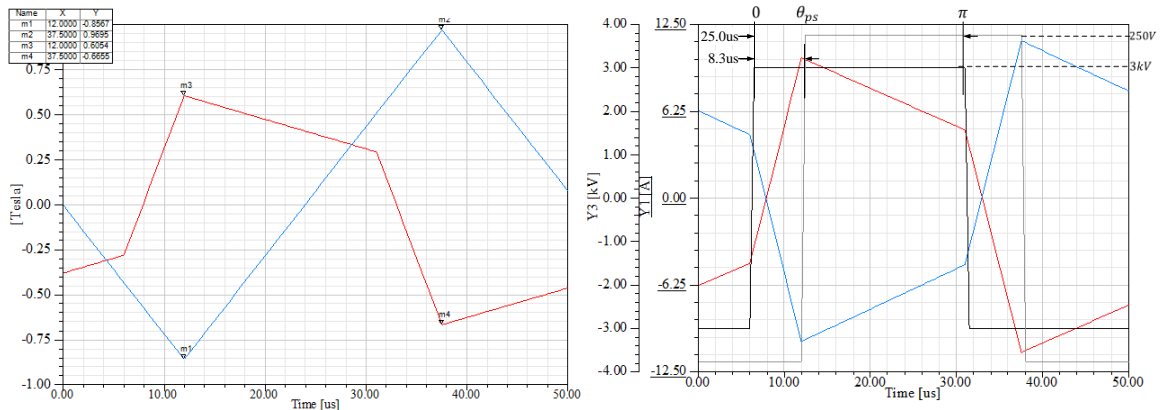
Figure 4.6: Peak magnetic field density in single-phase DAB DC/DC converter operation (3kV/150V DAB DC/DC conversion at, $\theta_{ps} = \pi/4$, $k = 0.75$)



(a) $k = 0.75$



(b) $k = 1.00$



(c) $k = 1.25$

Figure 4.7: Transient waveforms of an ICWT in a single-phase DAB DC/DC conversion at $\theta_{ps} = \pi/4$

4.2 Selection of materials and dimensions of cores

4.2.1 Selection of core material

Two different high frequency magnetic cores are used for the ICWT, and the inner and outer cores have to be carefully selected based on their functionality and operating conditions. Broadly speaking, magnetic core materials for power transformers are categorized by saturation-limited and loss-limited. The operation mechanism and environment of the inner and outer cores are different, so proper methods for each core have to be applied in order to select the correct materials.

Inner core selection in commercial off-the-shelf magnetic cores: Inner core selection has more restrictions than that of the outer cores. First, the inner core has to function as a circuit element which requires a certain value of inductance. In order to meet this requirement, there are two approaches using constant low permeability materials, or high permeability materials with a gap that can be adjusted mechanically to achieve the inductance value as seen in Fig 4.8. However, the inner cores are thermally isolated and a high electrical field can be formed between the inner and outer winding. Hence, mechanical and thermal properties are significant criteria when selecting inner cores. High permeability cores with a gap have the advantage of flexibility in the selection of materials. Ferrite can be considered to be one of the most popular core materials for high frequency power electronics applications, however ferrite has a low Curie temperature, around $200C^{\circ}$, and unstable mechanical and electrical properties at temperature. Nanocrystalline material has a very high relative permeability, which helps stabilize the inductance with a gap, and a high Curie temperature of above $600C^{\circ}$. The specific loss is also very low, so it is one of the best materials with an air gap. However, the air-gap structure can generate more parasitics and losses, and is also vulnerable to electric breakdown or corona discharge under high electric stress and heat congestion. In order to deal with these issues, good manufacturing processes and mechanical efforts are required, which are typically not available in college facilities.

In the case of a low permeability material, powder composite cores can be considered. Powder composite cores are made of fine particles of magnetic material with a distributed airgap. There are a variety of powder composite cores, such as Magnetics Molypermalloy Powder (MPP), High Flux, Cool Mu, and XFlux (Magnetics inc.). High flux, Cool Mu and XFlux have an advantage in size due to their high saturation flux density. However the powder composite cores are loss-limited materials at 20kHz. Hence, the saturation magnetic flux density is not a considerable factor, especially under pure AC conditions.

MPP cores have a variety of advantages as an inner core for ICWT applications. First, MPP cores have the lowest specific loss among commercially available powder composite cores, even though the specific loss is still higher when compared to other high frequency materials, such as

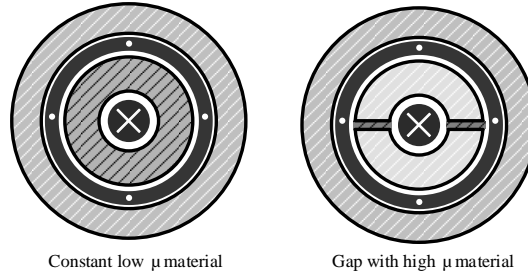


Figure 4.8: Inductor integration in coaxial winding transformer

nanocrystallin and ferrite. The constant and linear electrical and mechanical material properties with temperature and frequency make the system more reliable and predictable. The variation in the permeability of MPP cores is in the range of 3% up to $200C^\circ$ and 4% up to 0.4T flux density with a Curie temperature of $460C^\circ$. The very simple construction and assembly without advanced facilities is another significant advantage. Accordingly, MPP has a large selection of permeabilities in the range of 4 to 300 with a variety of dimensions off the shelf

Both methods work, but there are always trade-offs. If system efficiency is the primary concern and a precise mechanical process is available, the air-gap structure would be preferred. Otherwise, low constant permeability material can be used with much less mechanical effort and lower cost, without needing a professional manufacturing process. Therefore, the low constant permeability structure with MPP cores was selected for the ICWT prototype.

Outer core selection: Outer cores magnetically couple the inner and outer windings as a function of the isolation step up-down transformer. One of the main restrictions in choosing the outer core material of an ICWT is the permeability of the material. A very low number of turns, usually a single turn of copper tube, require a high permeability to limit the magnetizing current to a low level. Ferrite material is one of most common high frequency materials for ranges up to hundreds of kilohertz. However, the relative permeability of the ferrite core is around 1,000 to 3,000, which is not high enough to suppress the magnetizing current for medium voltage applications with a low number of turns. There are specialized ferrite materials with a relative permeability higher than 5,000, however they are very weak at temperature and frequency so they are not proper for a power transformer. The low saturation magnetic flux density is another considerable disadvantage of ferrite material for the proposed SST application. The specific loss at an operating frequency of 20kHz is low enough, hence the saturation flux density can be fully leveraged at the given frequency. However the low saturation magnetic flux density limits the size reduction.

Nanocrystalline cores are metallic tape-wound. The relative permeability of nanocrystalline

material is more than 10,000, and typically over 30,000. Even though the permeability of nanocrystalline is not linear and is affected by operating frequency, it is high enough to sustain good magnetic coupling and suppress magnetizing current at an acceptable level at the operating frequency of power electronics applications. The high saturation flux density, 1.2 T, and very low specific loss allow not only small size, but high efficiency at 20kHz. Nanocrystalline is a saturation limited material at 20kHz. It is selected as an outer core of the ICWT prototype and is customized by MKmagnetics for this SST application.

4.2.2 Dimension optimization of the cores

Parameter comparisons for inner cores: There are many factors in the design of inductors and transformers. All concerns have to be considered at the same time for proper integration. There are more restrictions when selecting inner cores with MPP material off-the-shelf, accordingly the inner core is designed first. Afterwards, the outer cores can be selected based on those fixed parameters.

The magnetic flux density is assumed to be uniform inside the cores by averaging the flux density of the cross sectional area in Eq 4.11.

$$B_{ac} = \mu_o \mu_r \frac{N_i l \ln(r_o/r_i)}{2\pi(r_o - r_i)} \quad (4.11)$$

The volume is the overall volume, and the loss calculation is based on the Steinmetz equation at the same operating frequency under sinusoidal voltage excitation. The plot in Fig 4.9 is generalized by the value at the point in minimal size with the fixed inductance value. The volume of the toroid core is minimized to the point where the ratio between the inner and outer radius is \sqrt{e} , 1.65, with a constant inductance value at the critical point of the volume

$$\frac{2\pi^2 L r_i^2 \left(2 \ln \left(\frac{r_o}{r_i} \right) - 1 \right)}{\mu_o \mu_r N_i^2 \ln \left(\frac{r_o}{r_i} \right)^2} = 0 \quad (4.12)$$

There is a large reduction in total weight of cores with a small ratio r_o/r_i , which means material cost is reduced as well. However, the total volume and size of the transformer is exponentially increased with greater length due to the large portion of the hollow area with a ratio r_o/r_i smaller than \sqrt{e} . The weight of the cores is reduced, however the amount of copper required will be increased with the increased length. The large ratio r_o/r_i with short length increases the weight and volume because the magnetic flux density decreases with the radius. More material is required to achieve the fixed inductance value. The calculation error in two dimensional approximation will increase due to the increase of the edge effect. The deviation of the volume curve is not large around the optimized point so the selection can be made around

the critical point, 1.5 ~ 1.7, at the designer's discretion. In the case of core loss, it is very stable with constant inductance considering the typical value of α is nearly 2. These formulas can be applied to any concentric dimension for inductor design.

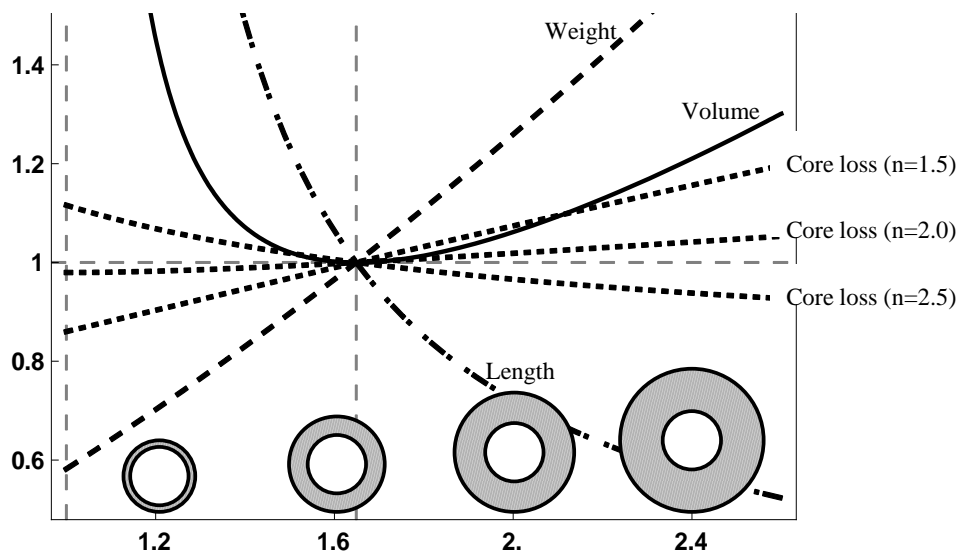


Figure 4.9: Volume, Weight, Length and loss comparison with respect to the ratio r_o/r_i

Table 4.3: Equations

Length	Weight	Volume	Loss
$\frac{2\pi L}{\mu_o\mu_r N_i^2 \ln(r_o/r_i)}$	density $\cdot \frac{2\pi^2 L(r_o^2 - r_i^2)}{\mu_o\mu_r N_i^2 \ln(r_o/r_i)}$	$\frac{2\pi^2 L r_o^2}{\mu_o\mu_r N_i^2 \ln(r_o/r_i)}$	Weight $\cdot K \cdot (B_{ac})^2$

Selection of the commercially available MPP cores for prototype : The power transfer of the DAB operation is determined by:

$$P_o = \frac{dV^2(1 - \theta_{ps}/\pi)\theta_{ps}}{\omega L_{sc}} \quad (4.13)$$

The given preliminary test condition for 12kV SiC Mosfet-based SST prototype 2 was 6kVDC/400VDC at 10kVA. The required inductance with a phase shift of $\pi/4$ is around 4mH referred to HV winding which is the inner winding of the ICWT. The commercially available MPP cores with a relative permeability from 14 to 500 are investigated at a frequency of 20

kHz. Considering the fill factor of 0.1 for insulation and multi strands, the commercially available inner diameter of 14.7 mm and an outer diameter of 26.9mm with ratio r_o/r_i around 1.8 is selected. The specific losses with relative permeability at magnetic flux density 0.1 T are compared on the basis of the coefficients on the datasheets provided by the manufacturer in Table 4.4. As a higher permeability material is used, higher loss, and smaller size are achieved to meet the same inductance value in Table shown 4.5. The coefficients are based on Eq 4.14.

$$Loss[mW/cm^3] = K \cdot (freq[kHz])^\beta \cdot (B_{ac}[T])^\alpha \quad (4.14)$$

Table 4.4: Coefficients of specific loss of MPP cores on datasheets

μ_r	14	26	60	125	147,160,160	200, 300	500
K	115.9	70.83	357.1	53.05	52.16	37.97	181
α	2.50	2.34	2.05	2.06	2.00	2.09	2.13
β	1.87	1.65	1.12	1.56	1.57	1.68	1.47
Loss[mW/cm ³] @20kHz, 0.1T	99.31	45.39	91.19	49.46	57.54	47.33	109.7

Table 4.5: Loss and size comparison (Sinusoidal excitation, line current =3.33 [A_{rms}])

	MPP cores, Di=14.7mm, Do=26.9mm, 15 turns, inductance: 4mH at 20kHz						
μ_r	26	125	147	160	173	200	300
Length [m]	5.52	1.15	0.98	0.90	0.83	0.72	0.48
Volume [m^3]	$3.10 \cdot 10^{-3}$	$6.52 \cdot 10^{-4}$	$5.55 \cdot 10^{-4}$	$5.09 \cdot 10^{-4}$	$4.71 \cdot 10^{-4}$	$4.08 \cdot 10^{-4}$	$2.72 \cdot 10^{-4}$
B_{ac} [T]	0.036	0.175	0.206	0.224	0.242	0.280	0.420
Core Loss[W] @20kHz	9.4	71.6	94.7	103.1	111.5	116.3	181.0

There is a trade-off between size and efficiency at discretion of the designer. Size reduction has been given more weight for this application, and a relative permeability of 300 is chosen with around 2% loss of the system from the inductor.

Outer dimension: The nanocrystalline for the outer cores is a saturation-limited material at the given specifications. Accordingly, the dimensions of the outer cores are determined with the length and outer diameters of the inner cores. The major concern of the outer cores is the saturation flux density which can be calculated by Faradays law of induction.

$$\int v \cdot dt = B_{ac} \cdot N \cdot A_c \quad (4.15)$$

The inner radius of the outer core can be slightly larger than the outer core, and the outer radius is determined by the cross sectional area to limit the magnetic flux density under the saturation limit. Considering transient operation up to a buck-boost conversion ratio $k = 1.3$, maximum magnetic flux density is chosen to be around 0.8T.

4.3 Proposed loss formula for ICWT for phase-modular single phase DAB DC/DC converters

4.3.1 Cores properties

Steinmetz's equation with the manufacturer-provided coefficients are a simple and reliable method for the sinusoidal excitation without DC components. However, the DAB DC/DC converter operation has large number of high frequency components even though it is a purely AC operation in steady state. Therefore, the coefficients are revised with square wave voltage excitation with *Yokogawa WT3000 precision power analyzer* with a 0.02% degree of power accuracy.

Nanocrystalline - High performance 0.0007" Nanocrystalline cores (ID:3.6mm, OD:5.5mm, HT:2.5mm) are customized by Mkmagnetics in Fig 4.10. The outer cores operate at a fixed frequency during single-phase DAB DC/DC operation with phase-shift modulation. The revised coefficients with square wave voltage excitation are measured by converters in the form of *Steinmetz's equation*.

Table 4.6: Coefficients of specific loss of 0.0007" Nanocrystalline

K_o	n_o	m_o
$2.626 \cdot 10^{-6}$	2.053	1.461

$$Loss\ on\ outer\ cores, P_{s\ oc}[mW/cm^3] = K_o \cdot B_o[T]^{n_o} \cdot f[Hz]^{m_o} \quad (4.16)$$

The permeability of the outer core without an air gap has a direct relationship with the magnetizing inductance. The inductance with frequency is measured by an *Agilent 4294A precision impedance analyzer*. High permeability materials lose the magnetic characteristics easily at high frequency as does the nanocrystalline core material. The magnetizing inductance

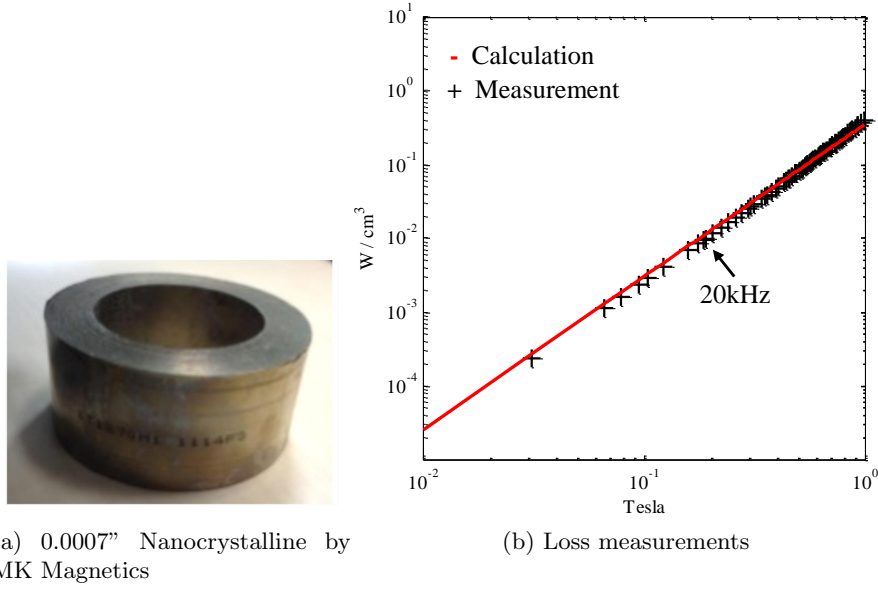


Figure 4.10: Outer cores

and current are not circuit elements, but parasitic elements for single-phase DAB operation. The inductance is high enough to not affect steady state operation at the switching frequency of 20kHz of the prototype even though it is cut down to almost one half at 20kHz. On the other hand, the magnetizing current helps to nullify parasitic capacitances and expand the soft-switching region while increasing line current and rating of power devices.

MPP powder type cores MPP cores (*Magneticsinc.*) with different relative permeabilities in the range of interest, $r = 160, 200, 300$, are chosen and measured. The revised coefficients are calculated by measurement in the form of *Steinmetz's equation*.

$$\text{Loss on inner cores, } P_{s\ ic} [mW/cm^3] = K_o \cdot B_i [T]^{n_i} \cdot f [Hz]^{m_i} \quad (4.17)$$

The measurement results and the calculation results with the coefficients provided on the datasheets shows considerable difference as seen in Table 4.7. According to datasheet, the specific loss [mW/cm^3] of those three models are close, however the specific loss measured by square wave voltage excitation is nearly inversely proportional and the total loss for the same inductance, which is the same capacity of magnetic energy, are similar each other. In order to increase the power density, the cores with high relative permeability are preferred, however the limitation is set by efficiency requirements and temperature rise due to reduction of surface area in order to dissipate heat.

Table 4.7: Specific loss of MPP cores at 20kHz, 0.1T (ID: 14.7mm, OD:26.9mm, HT: 11.2mm))

	C055929A2		C055927A2		C055925A2	
	Datasheet	Measure	Datasheet	Measure	Datasheet	Measure
μ_r	160	160	200	200	300	300
K_i	52.16	2.2650e-05	37.97	1.2261e-05	37.97	1.2681e-05
n_i	2.00	1.9801	2.09	2.0710	2.09	2.1063
m_i	1.57	1.6648	1.68	1.3435	1.68	1.3092
Loss [mW/cm ³]	57.54	101.35	47.33	62.50	47.33	42.45

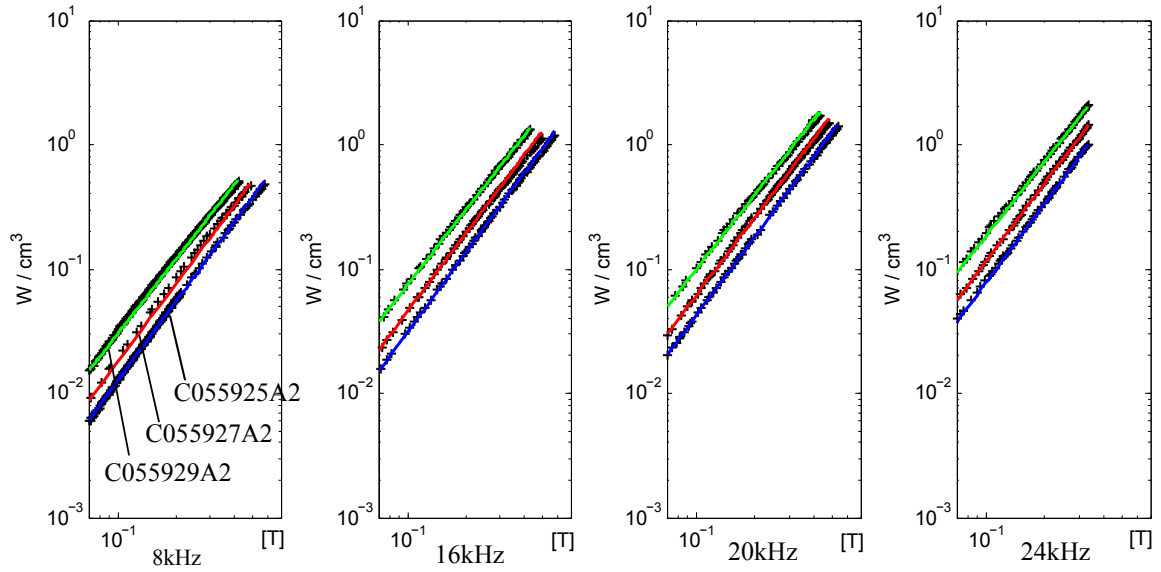


Figure 4.11: Specific loss measurement of MPP cores

The specific losses with magnetic flux densities are plotted in Fig 4.11. It is obvious that nanocrystalline material is superior to MPP cores with respect to loss. However, the stability of the material property of MPP cores is superior to that of Nanocrystalline cores. Therefore, the high permeability and low specific loss of nanocrystalline make it suitable for the outer cores of ICWT, the high electrical and mechanical stability of MPP cores make it suitable for the inner cores of the ICWT. The outer core, nanocrystalline, is saturation limited due to the low specific loss and the inner cores, MPP cores, are loss-limited at 20kHz. Considering loss balance, the magnetic flux density 0.7T~0.9T of outer core and 0.2T~0.4T of inner core are at the proper

design point.

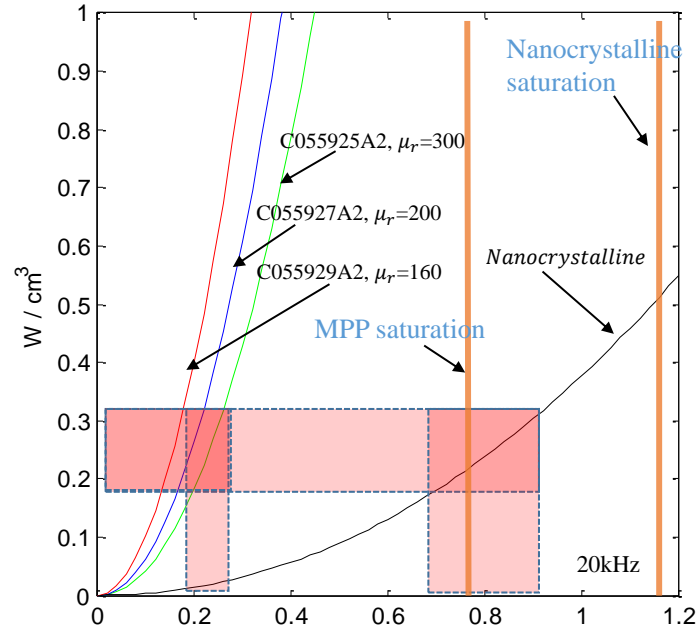


Figure 4.12: Specific losses vs magnetic flux density at 20kHz

4.3.2 Loss characteristics with DAB DC/DC conversion operation

Nominal operating condition of DAB DC/DC converter stage of SST applications

The nominal operating condition of the DC/DC converter has to be considered for transformer design because the power electronics application has to be designed most efficiently not at the maximum ratings, but at the nominal operating condition. This can be represented by a fractional load k_s . Maximum efficiency occurs when the load-loss under the fractional load condition is the same as the no-load loss, which is considered to be the same as core loss.

$$k_s^2 \cdot P_{load} = P_{no-load} \quad (4.18)$$

A typical value of k_s for nominal operating conditions of distribution transformers is around 0.4~0.5. The transformer should be designed at the nominal condition most efficiently with respect to loss and size.

The principles for steady-state operation of a single-phase DAB DC/DC converter were discussed in the previous chapter. The upper limit of the buck-boost conversion ration k is set

by the saturation point of the outer core and the maximum load is limited by the saturation of the inner cores. Soft-switching has to be used inside the two boundaries. Typically, the ‘ k ’ is constrained in unity to defend high voltage power devices in maximum soft-switching range with phase-shift modulation in steady state operation. The phase-shift of 30° of the single phase DAB DC/DC converter gives a fractional load of 0.55 when k is unity and the harmonic components are low.

Proposed loss formula for ICWT for phase-modular single phase DAB DC/DC converter

As explained in previous sections, the magnetic flux of the inner and outer cores are independent allow for accurate separation of the calculation for losses. Therefore, the magnetic flux density of the outer cores can be represented by the electromotive force on the outer winding driven by a fixed frequency square wave voltage excitation, and the magnetic flux density of the inner cores is represented by the magnetomotive force on the inner winding driven by a line current.

The most trusted approach in dealing with a loss of the non-sinusoidal flux waveform is the Modified Steinmetz equation (MSE) and the General Steinmetz Equation (GSE). The magnetization in ferro- and ferrimagnetic material is proven to be non-uniform and separated by domain walls. The local change of the domain walls is different from the external field change and the operating frequency of the application can be seen as quasi-static compared to the velocity of the local magnetization. Therefore, those two theories replaces the variable operating frequency of *Steinmetz’s equation* by the rate of the change of magnetic induction dB/dt as a source of magnetic loss. Both approaches are a mathematical implementation based on the classic Steinmetz equation rather than a physical approach.

For piece-wisely symmetric and linear current by square voltage excitation, dB/dt is constant and a function of frequency. The specific energy loss is extracted by the empirical parameters in Table 4.4 and in Table 4.6

$$w_{loss} = K \cdot B^n \cdot f^{m-1} \quad (4.19)$$

The steady-state operation of the DAB DC/DC converter at $k = 1$ with phase-shift modulation, the simple piece-wisely linear waveform in the inner and outer cores, is represented by one closed equation. The magnetic flux density in the outer cores of the ICWT is determined by the square wave voltage on the outer winding. Hence the electromotive force is triangular at a fixed frequency which is the same as the measurement conditions in Chapter 4.3. The specific power loss in the outer core $P_{s\ o.c}$ is represented in Eq 4.20.

$$P_{s\ o.c} = K_o \cdot B_o^{n_o} \cdot f^{n_o} = K'_o \cdot B_o^{n_o} \quad (4.20)$$

In the case of the inner cores, the change of magnetic induction dB/dt during one cycle for the inner core is identical with square voltage excitation, besides the idling time, with no change of magnetic field which does not generate loss in Fig 4.13. Therefore, the power loss can be converted with effective frequency, f' , by simply averaging the losses. The specific loss of the inner core $P_{s\ i-c}$ is represented by averaging the switching period T_s by Eq 4.21.

$$P_{s\ i-c} = w_{loss} \cdot f_s = K_i \cdot B_i^{n_i} \cdot f'^{m_i-1} \cdot f_s, \quad (T' = 2 \cdot T_s \cdot \frac{\theta_{ps}}{2\pi}, f' = f_s \cdot \frac{\pi}{\theta_{ps}}) \quad (4.21)$$

The total core loss of the ICWT can be represented by the control variable θ_{ps} and the magnitude of the square wave voltage on the outer winding V_o in the case of $k = 1$,

$$P_{loss} = K_o \cdot 4^{-n_o} \cdot \left(\frac{V_o}{A_{c_o} f_s}\right)^{n_o} \cdot vol_i + K_i \cdot 2^{-n_i} \cdot \theta_{ps} \cdot \pi^{-1+m_i-n_i} \cdot \left(\frac{\theta_{ps} V_o}{A_{c_i} f_s}\right)^{n_i} \cdot \left(\frac{f_s}{\theta_{ps}}\right)^{m_i} \cdot vol_o \quad (4.22)$$

where vol_i and vol_o are the volumes of the material used for inner and outer cores respectively. The coefficients measured from the square wave voltage excitation are in Table 4.8 and the comparison between calculation and measurement with a laboratory prototype is shown in Fig 4.13 (b) and shows a good agreement. The derived loss equation by Eq 4.22 provides a simple means of analyzing the loss performance, with only one control variable and DC capacitance voltage at $k = 1$. The detailed study and specific solution for SST applications will be discussed in chapter 5.

Table 4.8: Loss coefficients of inner and outer cores

f_s	K_o	n_o	K_i	n_i	m_i
20kHz	0.357	2.069	2.62610^{-6}	2.053	1.461

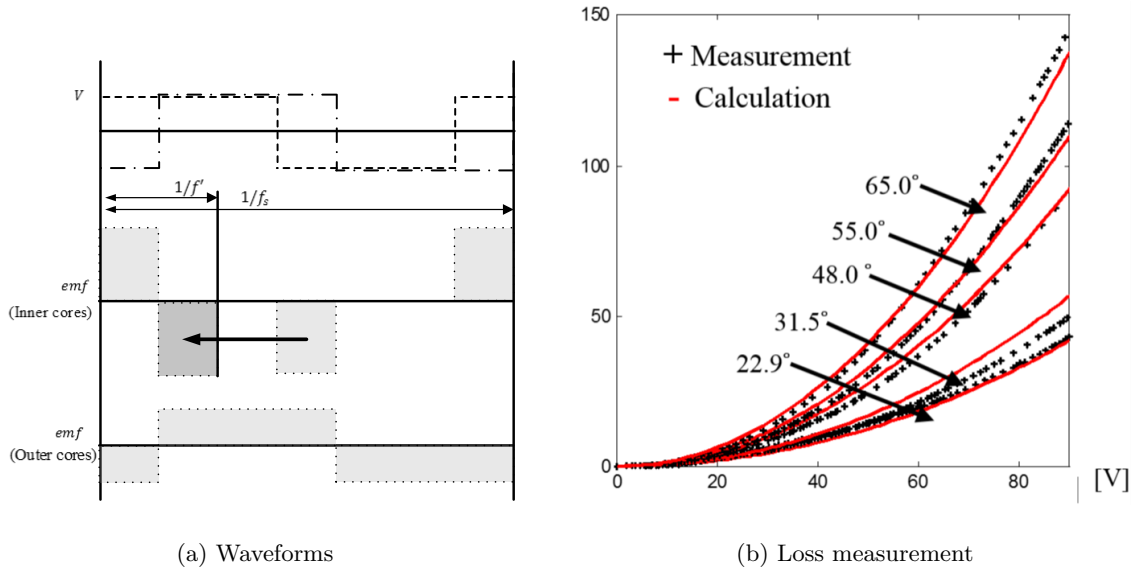


Figure 4.13: DAB DC/DC converter at $k = 1$ with phase-shift modulation

4.4 High frequency effect on a multi-tubular conductor with harmonics components

Nominal load condition of the distribution transformer is around 40~50% of the maximum power rating, and the transformer is designed to be most efficient at this power rating. The phase shift angle of 30° gives around 55% percent of the maximum power capacity. The trapezoidal current waveform is the sum of harmonics components of multiple switching frequencies, hence the harmonic components of the trapezoidal current waveform at 30° with peak current $I_m = 0.98$, which makes the total rms current 1A, are shown in Table 4.9 on the basis of coefficients of the Fourier series in Eq 4.23.

Table 4.9: Fourier series quantities of trapezoidal waveform with phase shift 30° at 20kHz, 1Arms

Harmonic order	1 20kHz	3 60kHz	5 100kHz	7 140kHz	9 180kHz
Magnitude	1.232	0.374	0.184	0.094	0.042

$$a_k = -\frac{4I_m(k\pi\cos(\frac{k\pi}{2}) - 12\sin(\frac{k\pi}{12})\sin(\frac{k\pi}{2}))}{k^2\pi^2} \quad (4.23)$$

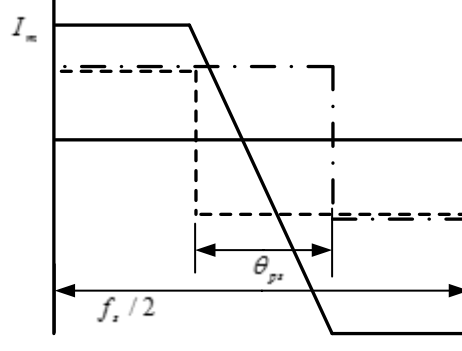


Figure 4.14: trapezoidal current waveform

As the harmonic order increases, the magnitude of the corresponding current decreases. Hence only the first few terms of the series are of interest. The 11th order harmonic components is already less 1% of the total current, hence the harmonic components at frequencies over 180kHz are ignorable. The thickness of commercially available copper tubes is multiple or division of 0.125", hence AC resistance of several thickness of copper tube at an inner diameter of 1.25" (31.75mm) are investigated. The overall AC resistance of the copper tube under nominal operation condition is calculated by Eq 80.

$$R_{ac} = \frac{\sum_2^k a_k^2 \cdot R_{ac k}}{I_{rms}^2} \quad (4.24)$$

The AC resistance at the fundamental frequency is typically used for calculation, however the harmonic components increases the AC resistance to almost double that of the fundamental frequency, as shown in Fig 4.16. The overall AC resistance is calculated by considering up to the 9th harmonic components in Table 4.10. The single turn of copper with thickness 0.125"/4 (0.79mm) has the lowest AC resistance at nominal operations condition which is consistent with the minimum AC resistance from the analytical solution in the previous chapter. The AC resistances approximately converges from thickness 0.125"/4 (0.40mm).

The proximity effect is typically even more serious problem than eddy effect with high frequency operation, especially with non-linear waveforms. . The AC resistance of second turn

Table 4.10: AC resistance [$\mu\Omega/m$] with thickness and frequency

		1 20kHz	3 60kHz	5 100kHz	7 140kHz	9 180kHz
	Magnitude	1.232	0.374	0.184	0.094	0.042
The first layer	0.125"/16	1054.6	1080.2	1129.7	1200.4	1288.4
	0.125"/8	547.6	718.0	951.6	1169.4	1352.8
	0.125"/4	412.8	784.4	1012.8	1198.4	1360.0
	0.125"/2	449.3	781.8	1011.7	1198.6	1360.2
The second layer	0.125"/16	1078.6	1293.2	1708.8	2300.0	3033.7
	0.125"/8	732.4	2139.6	4004.2	5646.5	6917.0
	0.125"/4	1506.3	4055.7	5123.4	5883.0	6568.1
	0.125"/2	2239.8	3607.5	4660.5	5516.4	6252.3

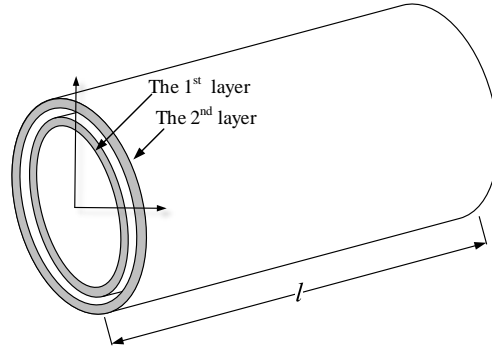


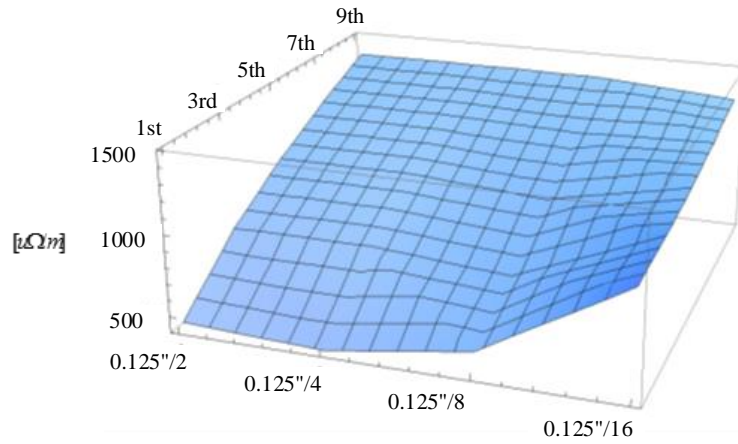
Figure 4.15: Copper tubes

of copper tube is already double at 0.125"/4 and almost 5 times of that of single turn above 0.125"/2 (1.59mm). The AC resistance of the second turn at thickness 0.125"/16 is higher than 0.125"/16, however the difference comes from the change of the cross-sectional area of the copper. It is noted that the AC resistance of the first and second turns are almost the same, which means there is almost no eddy or proximity effect at the fundamental frequency 20kHz. Therefore, multiple turns of copper tube should not be used unless the thickness of the copper tube is less than 0.125"/16. The increase of resistance due to proximity effect is significant up to five times with one another.

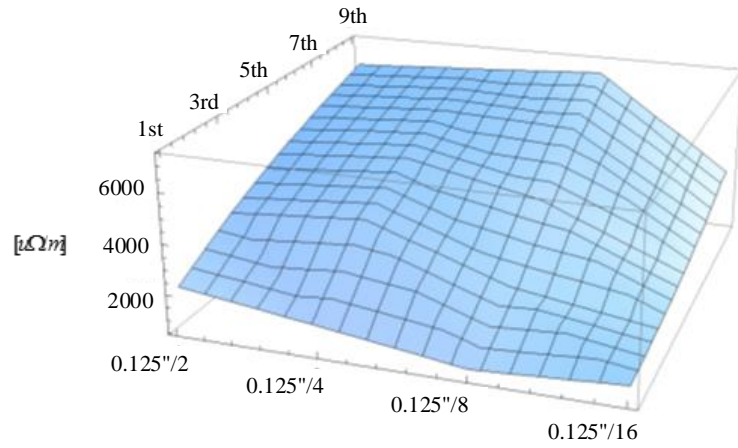
The 3D CAD model of the ICWT prototype is shown in Fig 5.4. The AC resistance at 20kHz sinusoidal excitation is 915 $\mu\Omega$. ($D_i:1.15"$, $D_o:1.25"$).

Table 4.11: AC resistance [$\mu\Omega/m$] with thickness of trapezoidal current waveform with DAB DC/DC operation phase shift 30° at 20kHz

	0.125"/16	0.125"/8	0.125"/4	0.125"/2	0.125" 3/4
The first layer	1802.9	975.6	783.5	838.5	836.4
The second layer	1902.5	1608.6	3090.6	4121.8	3753.5



(a) The first layer



(b) The second layer

Figure 4.16: AC resistance of the multiple of copper tubes

4.5 Insulation strategies for MV-MF ICWT prototype

The voltage rating of the SiC based SST application prototype is underrated a half scale 6kVDC-200VDC due to the limitation of the power device and facilities. The highest voltage of the prototype is 6kV, hence the rated withstand voltage requirement for 7.2kV according to the IEC international standard in shown Table 4.12. As discussed in the previous chapter, insulation oil or epoxy resin encapsulation is required at the given medium voltage range to reduce the size of the transformer.

Table 4.12: Rated withstand voltages IEC60076-3

Highest voltage for equipment	Rated short duration power frequency withstand voltage	Rated lightning withstand voltage
7.2kV	20kV	60kV

Winding method of MV-MF ICWT for 6kVDC-200VDC SST application : Two different winding methods in concentric and longitudinal in Fig. 4.17 and the static electric field distribution is investigated at 60kVDC in Fig 4.18. The wires can be arranged with bobbins as done for the first CWT prototype, however the wires on HV side of ICWT prototype are randomly wound for preliminary tests. The specifications of the windings are in Table ??.

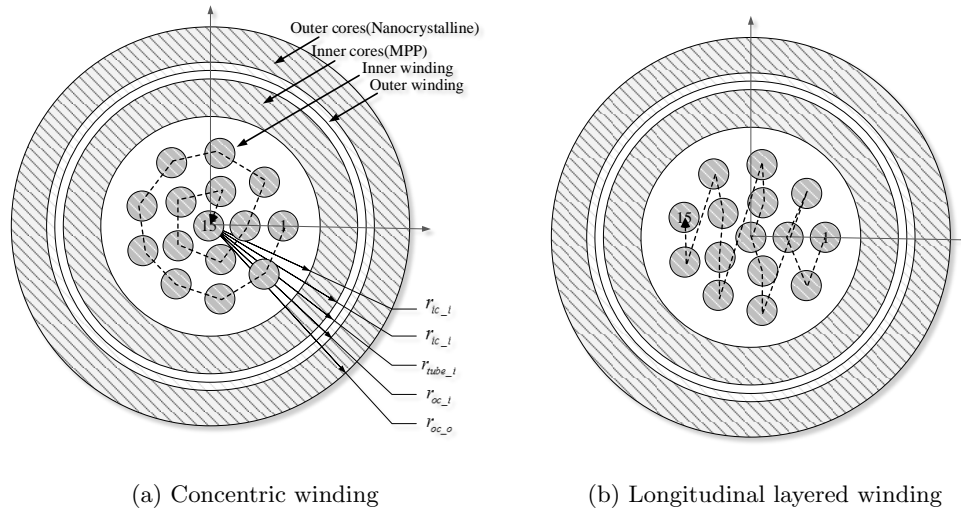
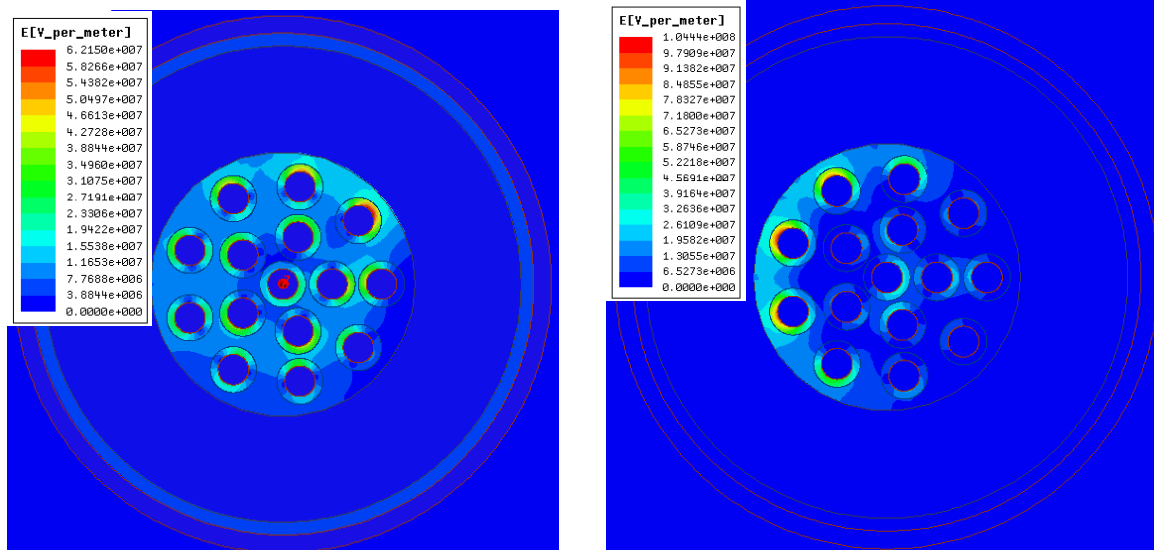


Figure 4.17: Winding arrangement



(a) Concentric winding

(b) Longitudinal layered winding

Figure 4.18: E-field distribution in 2D (Excitation : $V_1=60\text{kV}, V_2=V_3=0$, insulation medium : epoxy resin)

Table 4.13: Electric stress at power frequency

Inter-turn insulation		Interlayer insulation		Main insulation (Inter winding insulation)
Turn 1 and 2	Turn 1 and 8	layer 1-2	layer 2-3	Turn 17 and copper tube
200V	1.6kV	1.6kV	1.0kV	3kVDC+1.6kVAC

Table 4.14: Specifications of MV-MF CWT prototype

r_1	r_2	r_3	N_1	N_2	N_3	$r_{tube\ i}$	$r_{tube\ o}$	$r_{ic\ i}$	$r_{ic\ o}$	$r_{oc\ i}$	$r_{oc\ o}$	D_c	D_o
0	2.8	5.6	1	5	9	13.72	14.46	14.7	26.9	36.0	55.0	1.73	2.62

Table 4.15: Specifications of the windings and insulation materials

HV Side	Type	Litz 35/32	
	Guage	17AWG	
	Strands	MW77-C (Thermal class H 180°C)	
	Insulation material and thickness	0.0175" PFA JACKET	
		Relative permittivity	$\epsilon_r = 2.1$
		Dielectric strength	$\sim 80\text{MV/m}$
		Continuous service temperature	$260C^\circ$
	Outer diameter	0.102"	
DC resistance	$9.9 \cdot 10^{-3}\Omega/m$		
LV Side	Type	Two copper tubes connected by plates	
	Dimension	Length of body 300mm each	

Chapter 5

ICWT PROTOTYPE IMPLEMENTATION AND EXPERIMENT RESULTS

While the first CWT prototype in chapter 3 was built with an emphasis on verification of the feasibility to operate with the 15kV DAB DC/DC converter, the ICWT has been built with the emphasis on verification of the functionality with inductor integration and size reduction. Even though the switching test was conducted with the SiC-based 6kVDC/400VDC stage of SST without an advanced insulation method, epoxy resin casting is considered in the future. Load tests were conducted at 200VDC/200VDC DAB operation with 1:1 turns ratio by replacing the HV winding with 4 of AWG7 Litz wires in parallel. The assembly and configuration of the ICWT prototype for the SiC-based 20kHz 6kVDC/400VDC stages of the solid state transformer are shown in Fig 5.1 and in Fig 5.18.

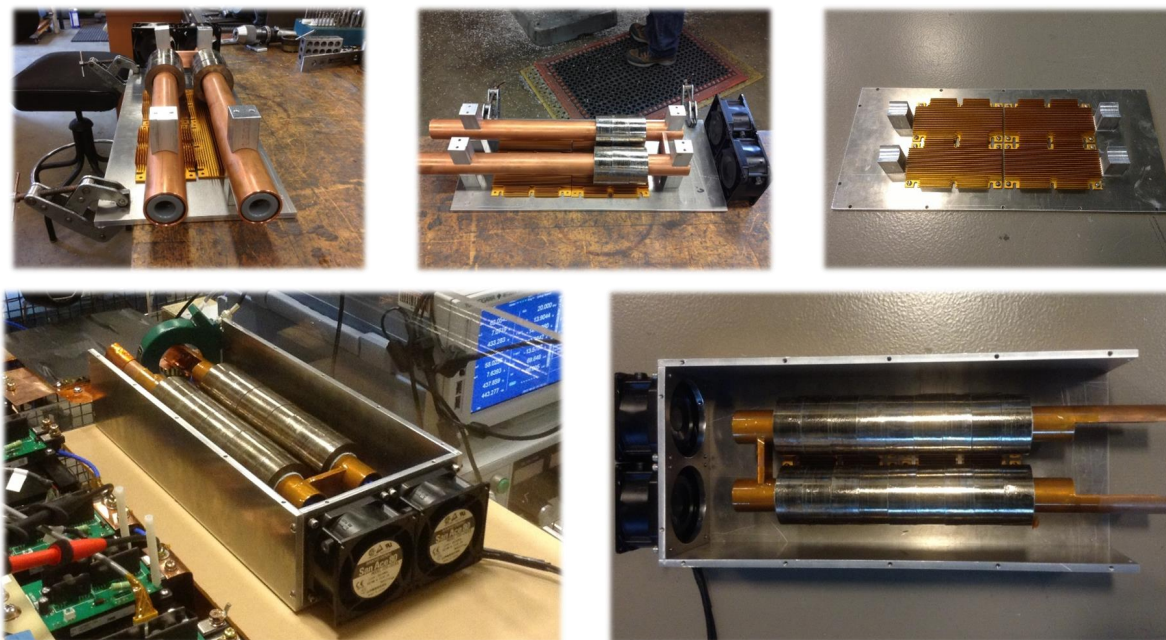


Figure 5.1: ICWT prototype with aluminum case and heatsinks- Machine shop built assembly

5.1 Loss Characteristics of the ICWT prototype

5.1.1 Eddy and proximity effects in real geometry and consideration on the auxiliary parts

LV winding - tubular copper

The low voltage winding is constructed using two tubular conductors and connecting copper. In order to reduce flux congestion near connecting areas of the CWT prototype, connecting copper is machined to fit the surface of the tubular conductor shown in Fig 5.2. The dimension of the LV winding is given in Table 5.1. The thickness of the tubular copper is oversized above 1.56δ due to limited selection commercially available. The design method used is the same as that for the CWT in chapter 3. The effective resistance with frequency in real geometry is plotted with a red region which is the frequency range of interest for the operation of Lab. prototype A in Fig 5.3.

The effective resistance is $306\mu\Omega$ at 20kHz, and the harmonic components can be considered with each effective resistance at the given frequency. The loss generated by LV winding of ICWT is often ignorable comparing to other losses of ICWT, due to the low number of turns, good space utilization, and high immunity to eddy and proximity effect.

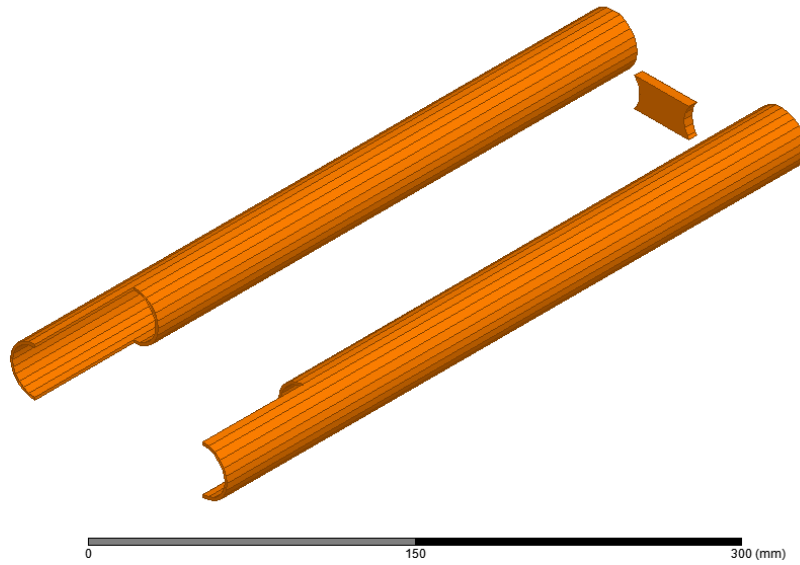


Figure 5.2: Tubular copper and connecting copper for LV winding of ICWT

Table 5.1: Specifications of LV winding [mm]

$r_{tube\ i}$	$r_{tube\ o}$	Thick. of tubes	Thick. of a conductor	length of tube
13.72	14.46	0.74	5.00	300.00

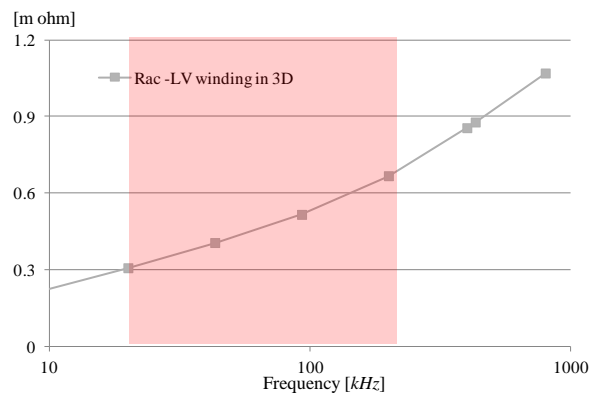
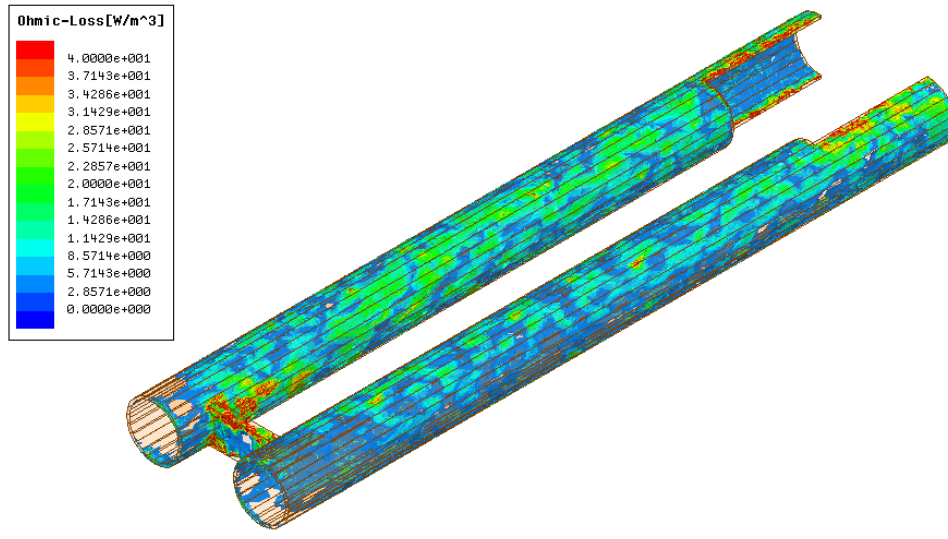
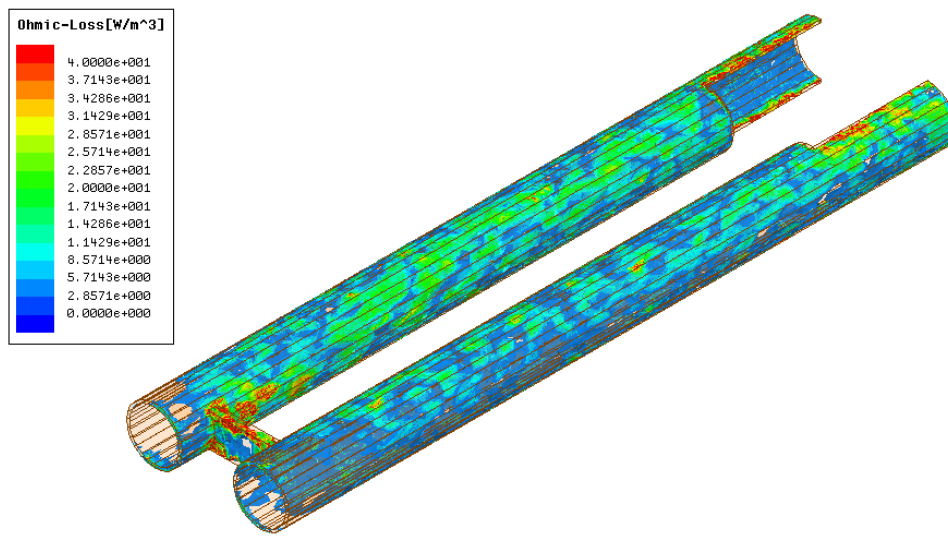


Figure 5.3: Effective resistance on LV windings



(a) 20kHz, 1Arms



(b) 200kHz, 1Arms

Figure 5.4: Current density on LV winding of the ICWT prototype in 3D

HV winding - Litz wire

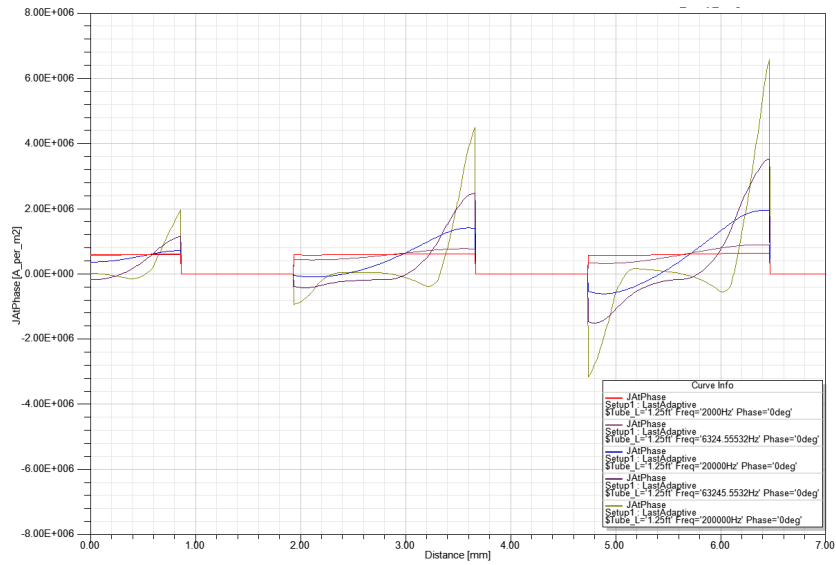
The amount of AC current that solid copper handles is limited regardless of the cross sectional area, at a certain frequency. Therefore, multi-strands wire is typically used to increase the surface area of copper for high frequency applications. High frequency Litz wire consists of very fine enamel-insulated strands. The number of strands ranges from two to several thousand with insulation. As explained in chapter 3, the conductors in parallel connections have to switch their location in order to balance out the effect of the fields on each conductor. In case of Litz wire, the strands have to change their location from the core to the outside regularly, otherwise, there is no effective difference between a solid conductor and the divided conductors in a parallel connection no matter how small they are. Therefore, the method to twist strands is also an important factor for the Litz wire.

As matter of fact, the two dimensional approach cannot represent the change in location of the strands. However, a sense of the high frequency effect on the Litz wire can be gained by assuming the switch of location of each conductor is evenly distributed inside outer diameter, and current is evenly shared on each strand. Actually, this assumption is true for most commercially available twisted Litz wires with carefully prescribed patterns. Under the given assumption, the effective resistances of three different cases have been investigated using 2D FEM in Fig. 5.6. Three case, single conductor in Fig. 5.6 (a), 65 strands of 32AWG magnet wire in Fig. 5.6 (b), and 65 strands of 32AWG magnet wire with secondary winding and cores in Fig. 5.6 (c) are investigated by finite element analysis in 2D.

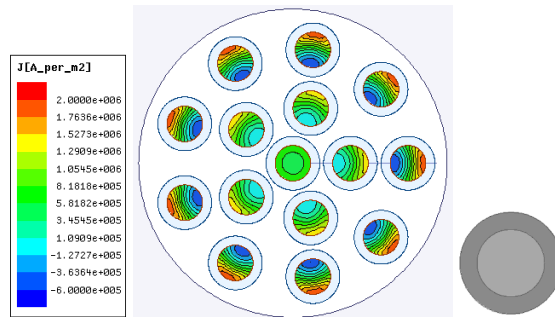
The single conductor shows current congestions on the surface above the skin effect corner frequency, 4kHz, due to skin and proximity effects as seen in Fig 5.5. However, we should consider that the fill factor of the Litz wire is generally around $0.5 \sim 0.6$ due to the insulation, gap, and the increase of length by twisting the strands. This means that DC resistance of Litz wire can be double of the solid copper wire with the same outer diameter. The effective resistance of the Litz wire exceeds the solid copper wire's above the skin depth corner frequency of the strands again due to proximity effect. Hence, the proper operating frequency using Litz wire is approximately between the skin depth corner frequencies of the outer diameter of a wire and the diameter of a strand. It is around 4kHz to 4MHz for the Litz wire used for HV winding of ICWT prototype, which covers the considerable harmonic components of the operation. Unnecessary use of Litz wire without careful consideration of the high frequency effect can result in loss of size and increased cost. Another considerable aspects of the coaxial winding configurations is that the external field does not affect the field distribution in window area and loss of inner winding as shown in Fig 5.7. The loss increase on coppers due to the air gap or inductance integration is often significant.

The aluminum case and heat sinks also have losses due to the induced current from the

eddy effects. The configuration of the ICWT is electrically and magnetically shielded effectively. Nonetheless the auxiliary losses are sometimes considerable in practice. The 3D FEM simulation is conducted with excitation on the simulation with a net current of 50A on both windings in opposite directions and a 1A magnetizing current as shown in Fig 5.8. The case, connection, and heatsinks are all made of Aluminum, which has lower conductivity than copper. The induced current is mostly congested in the metal connection parts, which are used as a heat path to the case and heatsinks, The additional loss due to the auxiliary parts with a line current of 100Arms with 3Arms magnetizing current is around 7W at 20kHz. This calculation is based on phasor analysis and the signal is assumed to be sinusoidal. Hence the total loss is expected around 14 W at 20kVA for maximum power transfer of a single-phase DAB DC./DC converter when considering harmonic components.

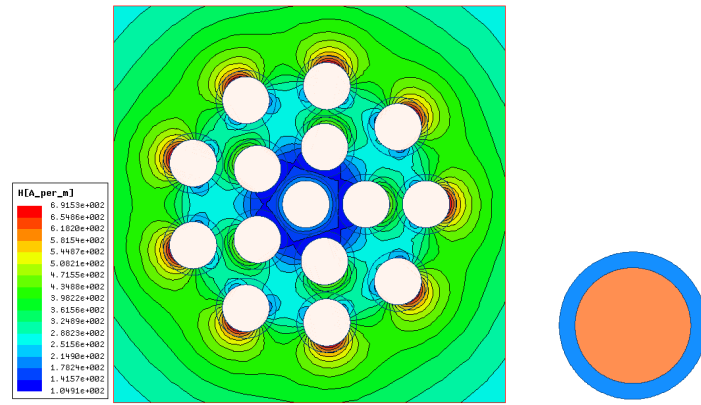


(a) Current density on solid coppers with frequency

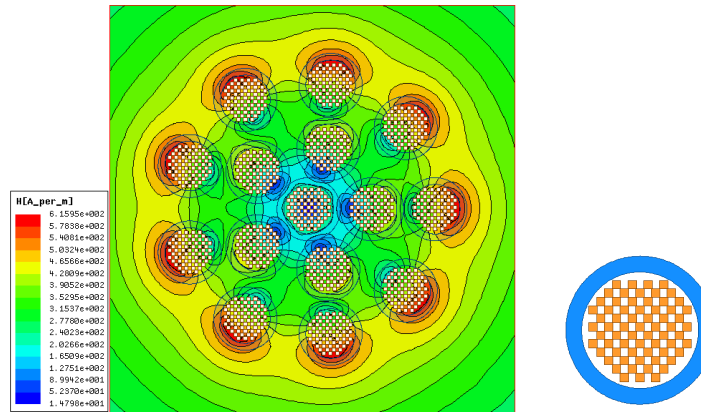


(b) Single conductor

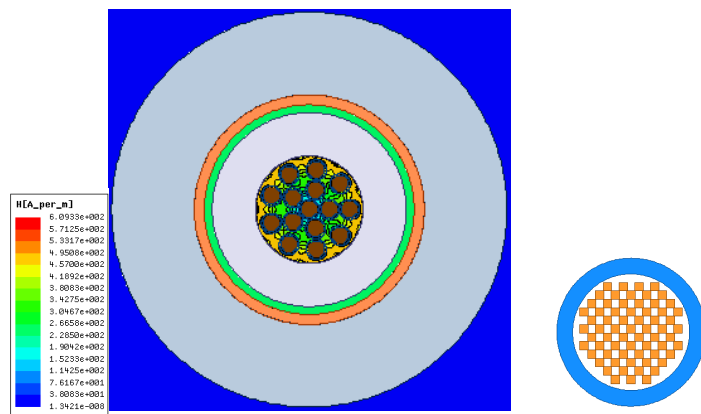
Figure 5.5: Current density distribution on the HV winding (Excitation : inner winding - 1Arms, outer winding 1Arms)



(a) Solid coppers (Excitation : HV winding 1Arms)



(b) Litz wire (Excitation : HV winding 1Arms)



(c) Litz wire with LV winding and cores (Excitation : HV winding 1Arms, LV winding -1Arms)

Figure 5.6: H-field distribution at 10kHz

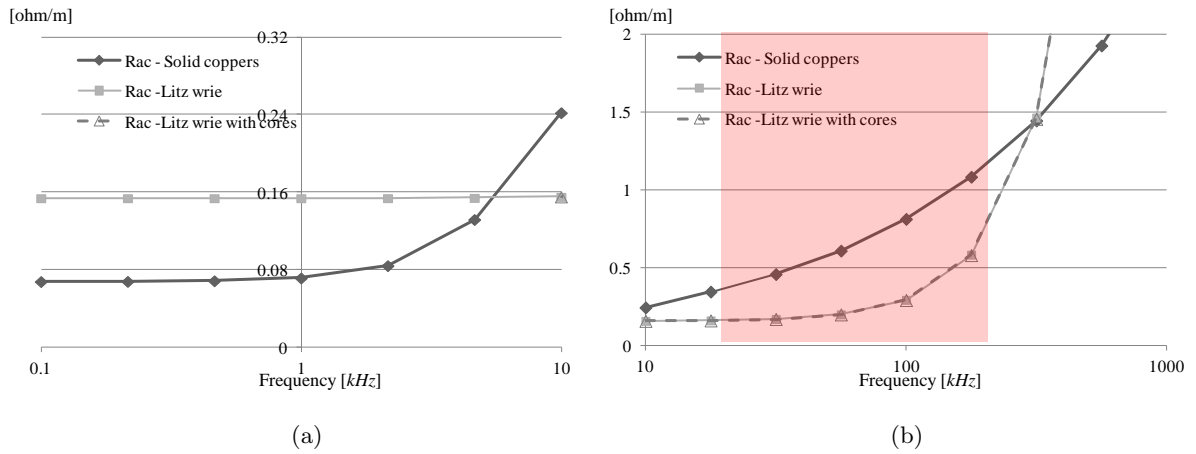


Figure 5.7: Effective resistance on HV windings

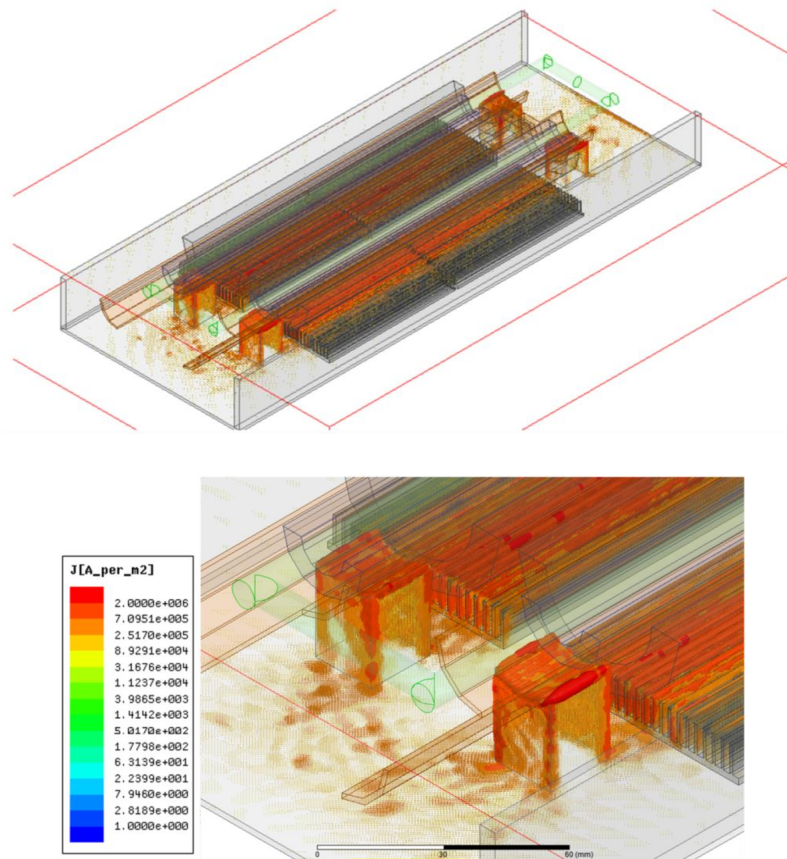


Figure 5.8: Eddy current in an aluminum case (Excitation : HV winding 3.33Arms, LV winding:51.0A with magnetizing current at 20kHz)

5.1.2 Inner and outer core losses

The diameter and size of the inductor are selected with a fixed required inductance and number of turns with the system requirements in chapter 4. Therefore, the size of the outer cores can be determined by the ratio $r_{oc.o}/r_{oc.i}$ 'm' while considering losses in both the inner and outer cores shown in Fig 5.12. The lower limit of m is around 1.3 due to the outer core saturation shown in Fig 5.13 and the control variable θ_{ps} is limited to around $\pi/3$ due to the inner core saturation. The selected value of m is around 1.5 bringing the buck-boost conversion ratio up to 1.3 for the prototype. The expected maximum efficiency is around 98%. at $\theta_{ps} \cong \pi/6$ without factoring in copper loss, which is not considerable at 10kVA operation.

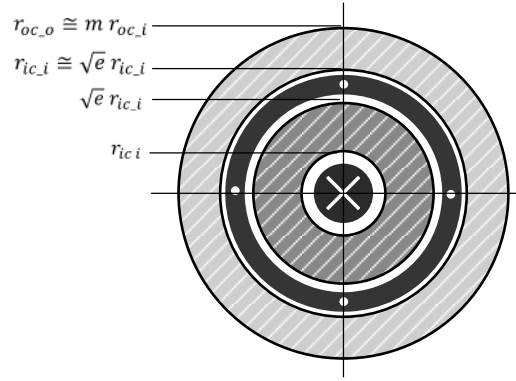


Figure 5.9: Configurations with ratio $r_{oc.o}/r_{oc.i}$, m

The best efficiency, around 97% of the ICWT, is achieved at a phase shift of around $\pi/6$ with copper loss, when the loss from the inner and outer cores is almost balanced. The loss from the outer cores is constant, as long as the operating frequency and DC-link voltage is fixed. However, the loss from the inner core is affected by the phase shift, which is the load. The loss from the inner core takes over the larger portion of the power loss at a phase shift of approximately $\pi/6$.

Resistive load tests with the solid-state transformer prototype have been conducted. The hot spot temperature settles at around $170C^\circ$ after 70 minutes of operation at 6.5kVA, without an active cooling method in a dry-type shown in Fig 5.22. The upper temperature limit of wire insulation material, PFA (Perfluoroalkoxy), is $260C^\circ$, and the Curie temperature of the magnetic cores is more than $400 C^\circ$. Loss, real power transfer, and efficiency during load conditions have been plotted based on the core loss equation. Considering the loss contour and

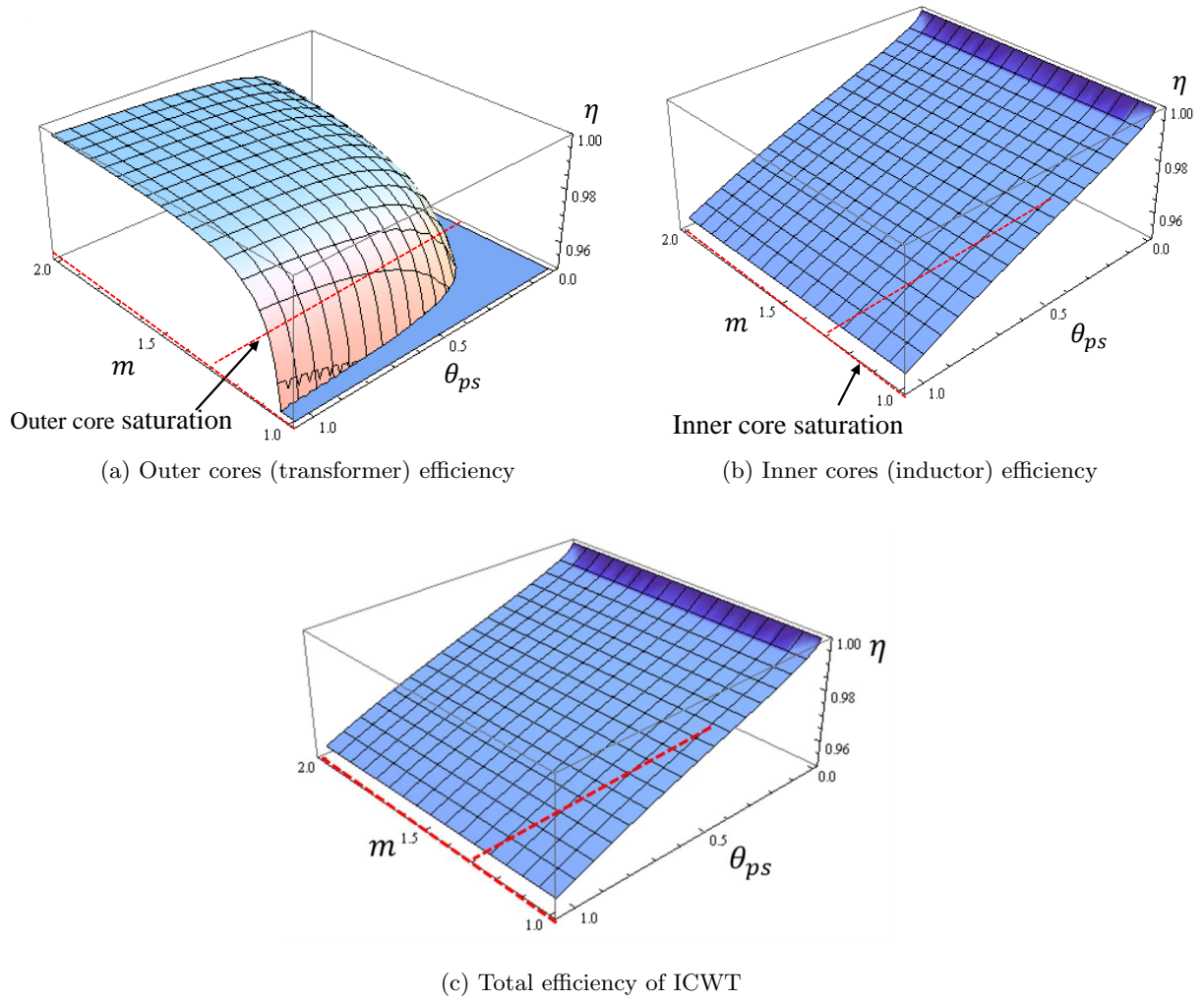


Figure 5.10: Efficiency of the ICWT laboratory prototype with m and load condition

hot-spot temperature of 170 degree, the operating region without active cooling is indicated with a light blue color, and the restricted region with the inner core saturation is indicated with red in Fig 5.24. The comparison with the results from the equation and measurements is shown in Fig ?? and is in good agreement.

5.1.3 Operation region of ICWT prototype with SiC-based 6kVDC/400VDC DAB DC/DC converter

The operation region of the laboratory prototype is determined by the soft-switching boundaries, inner and outer core saturation boundaries, efficiency requirement, and, eventually, ther-

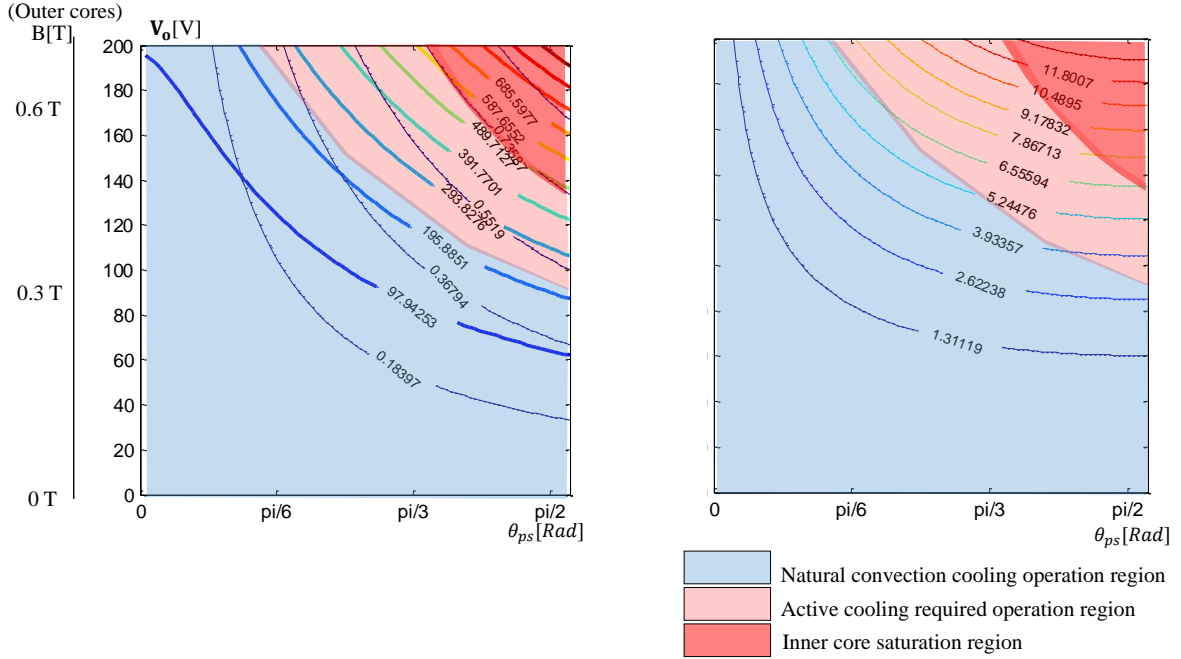


Figure 5.11: Loss and real power transfer vs. load

mal limits by the hot-spot temperature. The saturation of magnetic materials and soft-switching boundaries are critical limits which cannot be compromised without a change of characteristics in the materials. The operating limit of the ICWT has combined with the plot of P_o/P_b with load and buck-boost conversion ratio k in Fig 5.17. The saturation of the outer cores is determined by the DC voltage on LV side due to the very low impact of leakage inductance on the LV winding as shown in the proposed equivalent circuit model. Hence, the saturation boundary of the outer cores is a function of k and the upper side of the boundary in the blue region has to be restricted. The limit of the ICWT prototype for the given operating conditions is around $k = 1.3$. The saturation of the inner cores are load-dependent, which means that the boundary is set by the phase-shift θ_{ps} in the x -axis, and the right side of the boundary condition has to be restricted in the red region to avoid saturation of the inner cores. It is also not a desirable operation region with respect to operation of the DAB DC/DC converter. The rate of power transfer is not effective when compared to the high portion of the harmonic components. The dotted line represents P_o/T_{VA} . Thermal limits have to be included under load conditions. The thermal limit is a relatively flexible restraint that has many variables such as the cooling method and test environment that can still cause changes after completion of the mechanical assembly. Setting the thermal limit also requires collecting data and measurements.

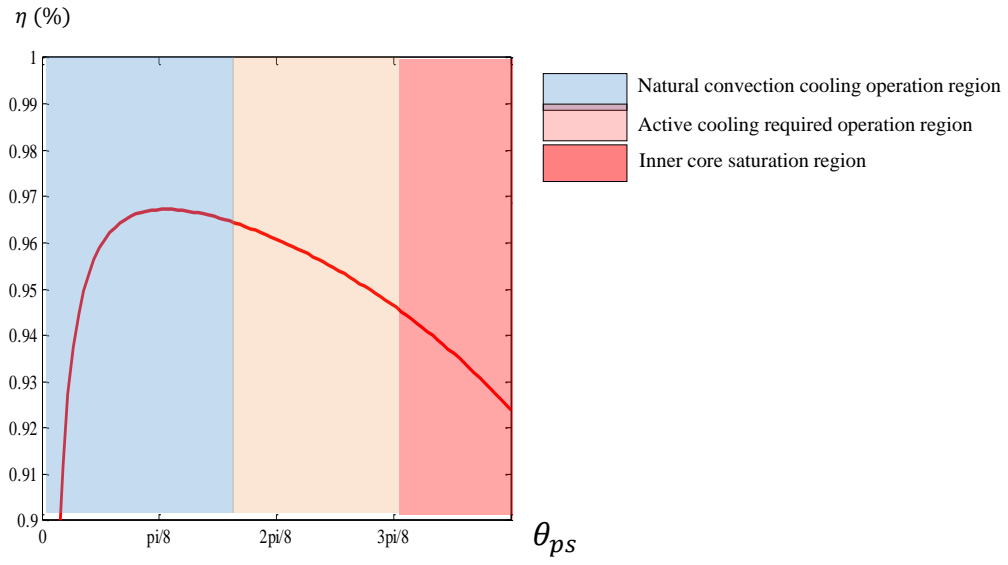


Figure 5.12: Efficiency vs. load ($\eta = \frac{P_{in} - P_{loss}}{P_{in}}$)

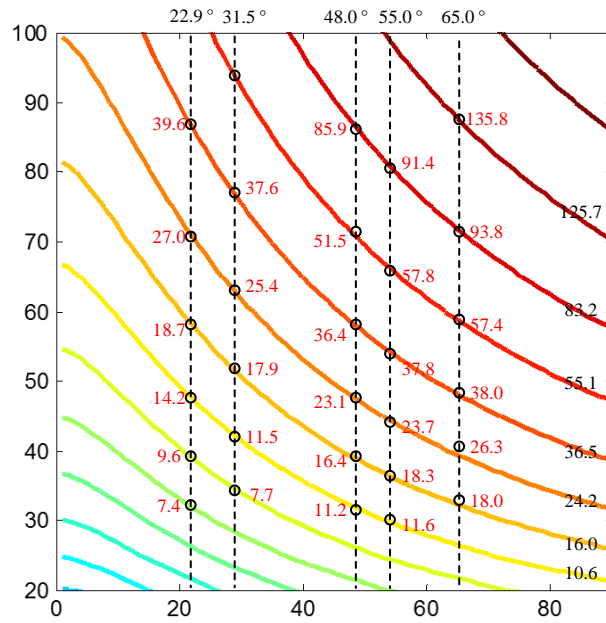


Figure 5.13: Loss measurements from ICWT Prototype with C055927A2 and comparison with analytical solution (turns ratio 1:1)

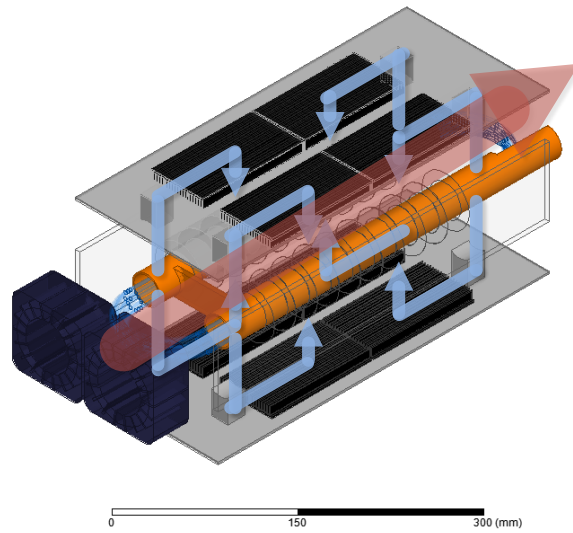
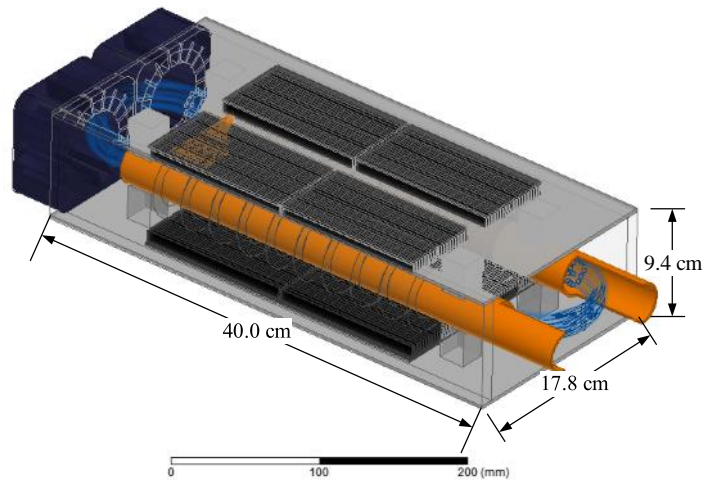
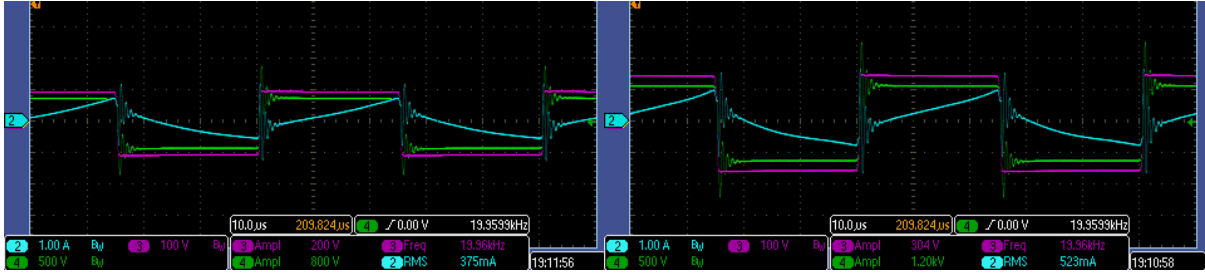
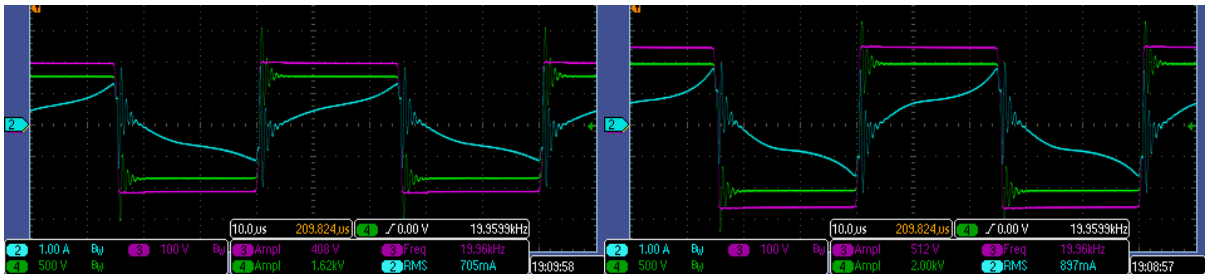


Figure 5.14: Heat pathes from hot-spot to the case and heatsink



(a) LVDC=200V

(b) LVDC=300V



(c) LVDC=400V

(d) LVDC=500V

Figure 5.15: Waveforms of open-circuit tests (turns ratio 4:1)

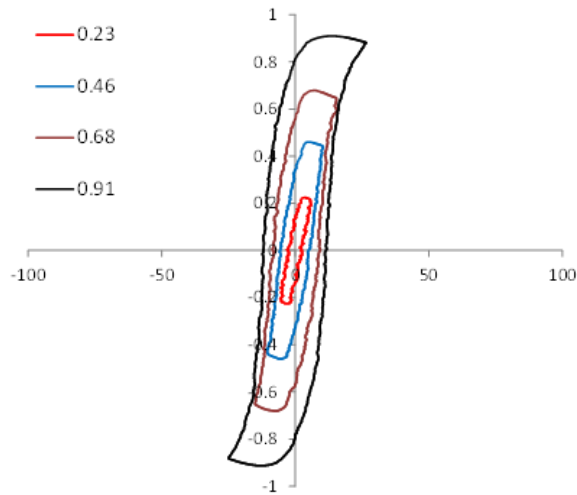


Figure 5.16: B-H curve at 20kHz

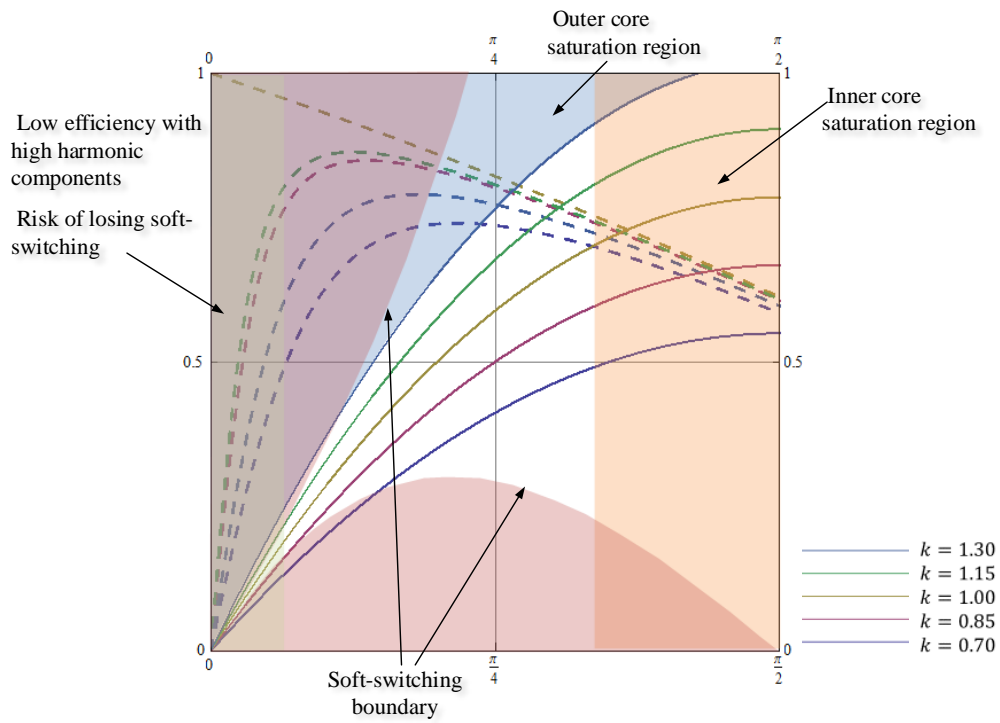


Figure 5.17: Nominal operation region of the laboratory prototype, SiC based single-phase DAB 6kVDC/400VDC converter and ICWT with C055925A2

5.2 ICWT with SiC-based 6kVDC/400VDC DAB DC/DC stage of SST

5.2.1 The switching response of the ICWT with 15kV SiC MOSFET under DAB operation

For the operation and switching tests with a 20kHz 12kV SiC-based DAB 6kVDC/400VDC converter stage at 6kVDC-400VDC, the ICWT prototype is preliminarily built in the laboratory as shown in Fig 5.18. The series inductance of $3.85mH$ is achieved with MPP powder cores C055925A2 ($\mu_r = 300$), considering nominal power transfer 10kVA under soft-switching conditions. The machine shop-built ICWT prototype assembly with an aluminum case and heatsinks are shown in Fig 4.2 (b). The heat of the transformer is congested in the center of the copper tube because the inner cores are lossy and the lamination of the outer cores interrupt the heat dissipation to the surface. Metal connections between LV winding, which is copper tubes, and the aluminum cases play a role as a mechanical support and heat path to the heatsinks mounted on the aluminum case. Two fans are installed in case temperatures exceed nominal operating conditions during a load test. Insulation oil or epoxy encapsulation are not used for preliminary load tests.

400VDC is supplied on the LV side of the 12kV SiC-based DAB 6kVDC/400Vdc converter in half bridge configurations to step up to 6kVDC. The voltage excitation to MV-MF transformer is one half of the DC voltage, 200Vpeak on the LV side and 3kVpeak on the HV side, respectively.

The proposed lumped-element equivalent circuit model with inductive and capacitive coupling is represented with three capacitance values and two inductance values. The large DC-link capacitors and magnetizing inductance at switching are negligible at the frequency range of interest. The high frequency response from the inner winding shows only a capacitive response. On the other hand, the high frequency response from the outer winding shows only an inductive response of L_{sc} in Fig 5.19.

The frequency responses of the prototype with a turns ratio of 15:1 are measured with an *Agilent 4294A precision impedance analyzer*. The measurable frequencies are simply two values because the inner winding is wound randomly. Hence, the capacitance C_b and C_c is almost the same.

$$\begin{aligned} f_1 &= \frac{1}{2\pi\sqrt{L_{oc\ MV'}C_{eff\ MV}}} \cong \frac{1}{2\pi\sqrt{L_{oc\ LV'}C_{eff\ LV}}} \\ f_2 &= \frac{1}{2\pi\sqrt{L_{sc\ MV'}C_{eff\ MV}}} \cong \frac{1}{2\pi\sqrt{L_{sc\ LV'}C_{eff\ LV}}} \end{aligned} \quad (5.1)$$

Where $L_{oc\ MV} = n^2 P_m^2 + n^2 P_1^2$, $L_{oc\ LV} = P_m^2$, $L_{sc\ LV} = P_1^2$, $L_{sc\ MV} = n^2 L_{sc\ LV}$, $C_{eff\ LV} = n^2 C_{eff\ LV}$.

The switching response of the 15kV SiC MOSFET in DAB operation with the ICWT prototype is shown in Fig 5.10. Considering that the effective capacitance of the transformer to the differential voltage on medium voltage side is $85pF$ and the negative point of the DC-link capacitors are earth-grounded during test, and an approximately 1.5A current damp is shown at dV/dt 10kV/us at switching on the MV side. There is also a slight ringing at 2MHz at switching on the LV side. This is due to the parasitics on the wires and devices.

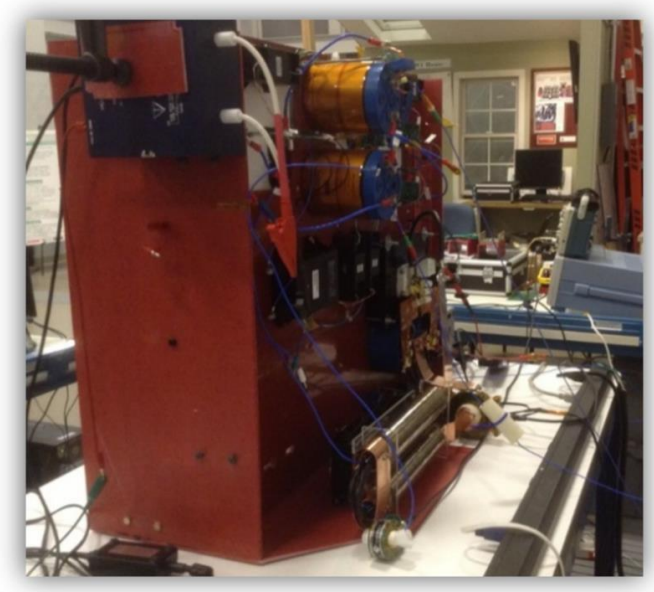


Figure 5.18: The SiC-based 6kVDC/400VDC DAB DC/DC stage of SST with an inductor (3.8mH) integrated coaxial winding transformer

Table 5.2: Specifications of inner and outer cores

	Material	A [mm]	B [mm]	C [mm]	μ_r	The number of cores
Inner cores	MPP(C055925A2)	26.9	14.7	11.2	300	46
Outer core	Nanocrystalline	55.0	36.0	25.0	$\sim 30,000$	20

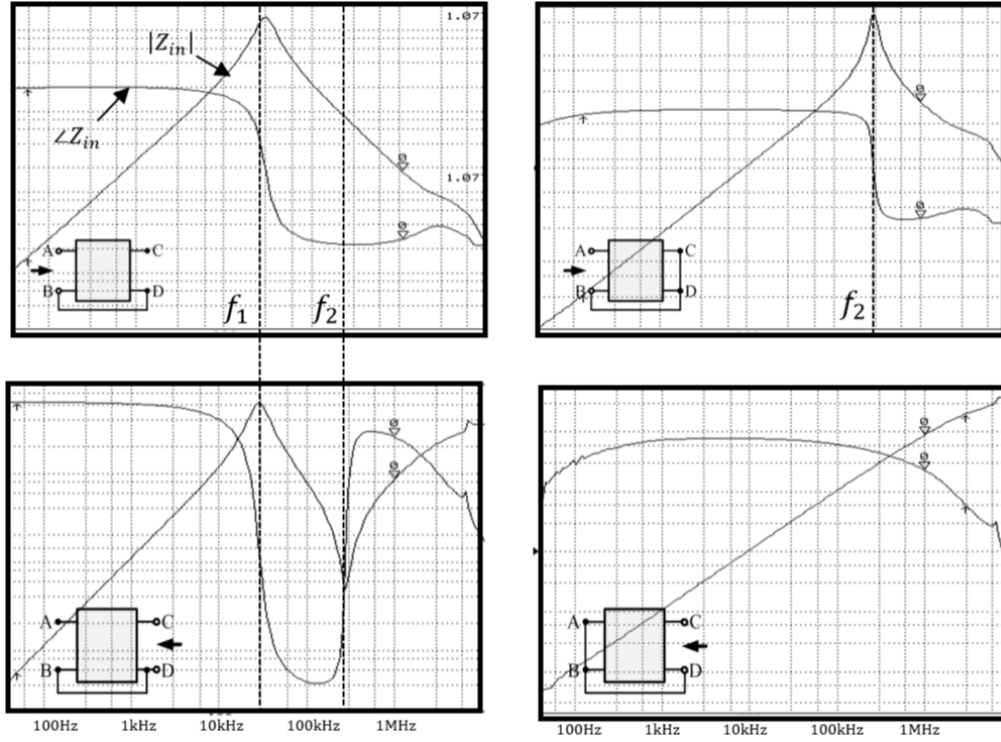


Figure 5.19: Impedance plot (turns ratio 15:1)

Table 5.3: Parasitic elements

C_{eff1}	C_{eff2}	C_{eff3}	C_a	C_b	C_c	L_{ocMV}	L_{ocLV}	L_{scMV}
193pF	85pF	85pF	-11.5pF	96.5pF	96.5pF	408mH	1.8mH	3.85mH

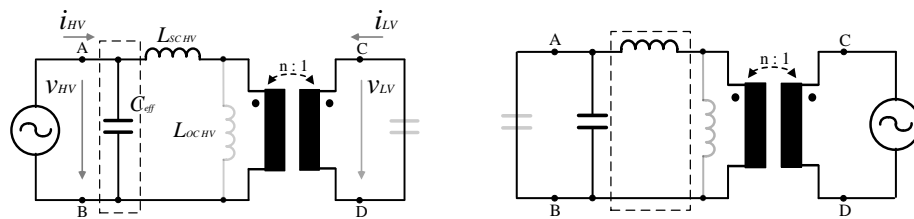
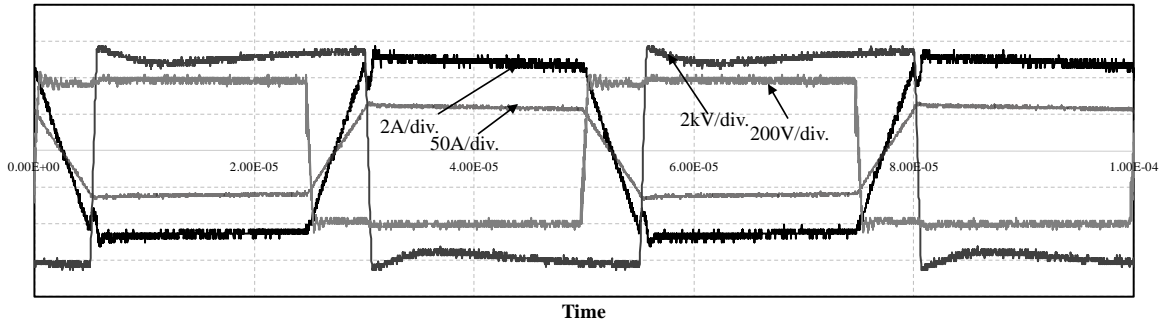
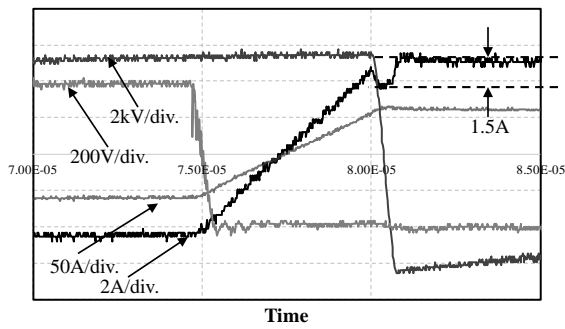


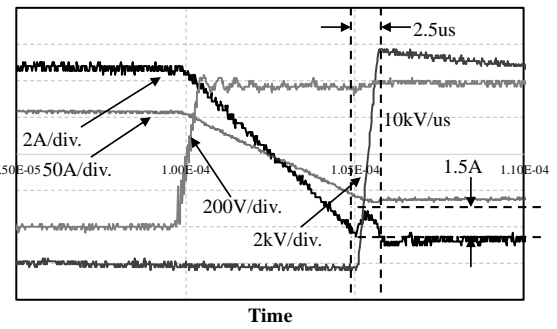
Figure 5.20: Equivalent lumped circuit model of high frequency switching response



(a) DAB 6kVDC/400VDC operation



(b) switching response



(c) switching response

Figure 5.21: Waveforms of DAB 6kVDC/400VDC operation with the ICWT prototype

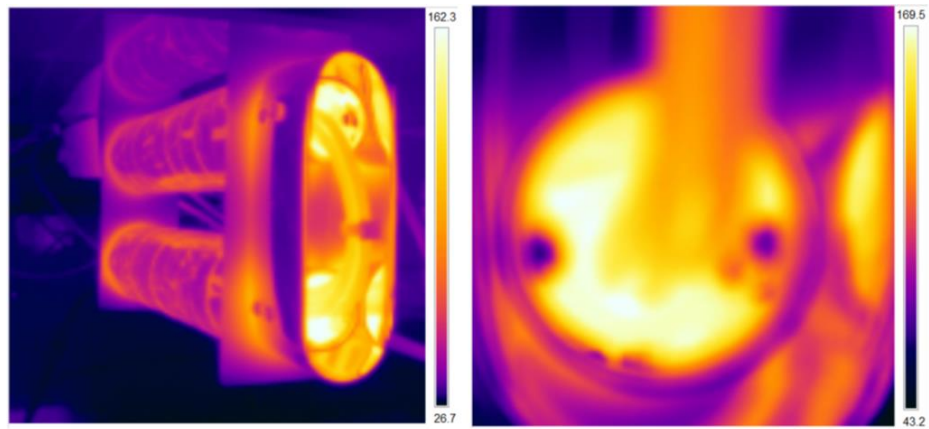


Figure 5.22: Heat distribution at 6.5kW power transfer without an active cooling method after 60 minute operation

5.3 Loss and temperature measurement of ICWT under operation at 10kVA

The temperature change under heavy load conditions has to be investigated to verify the reliability and define the power rating of the transformer. Operating test over 10kVA for longer than an hour are still risky using the developing 15kV SiC power devices, and an accurate measurement at 6kV is not available. A 1200V IGBT-based DAB DC/DC converter has been built for the load test and an accurate measurement of efficiency and loss. NI CompactRIO real-time controller and *Labview FPGA* are used for phase-shifted PWM modulation at 20kHz. Only one turn on each winding, a turns ratio of 1:1, is used to connect both DC terminals on both sides and the transformer is loaded up to 11kVA by circulating real power shown in Fig 5.23. The tests are conducted at a voltage of 200VDC at 11kVA load conditions for 60 minutes until the temperature settled down.

The machine shop built assembly with a forced-air cooling method is shown in Fig 5.1. In order to conduct the operation test at 11kVA, which is closer to the rating of SST applications, the laboratory prototype is built using C055925A2 ($/\mu_r = 200$). The case and heatsinks are installed to dissipate heat.

10.1kW of power is transferred for 60 minutes with a total loss 360W. The case was open, without the lid, and the fans were not active during the test. The hot spot temperature settled down at 125°C after 60 minutes of operation without an active cooling method in Fig ??, and the overall efficiency of transformer, 96.4%, was achieved at 10.9kVA, with a 10.1kW power transfer.

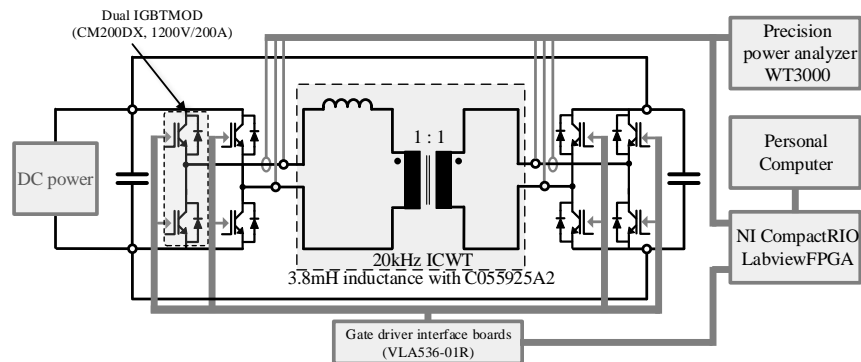
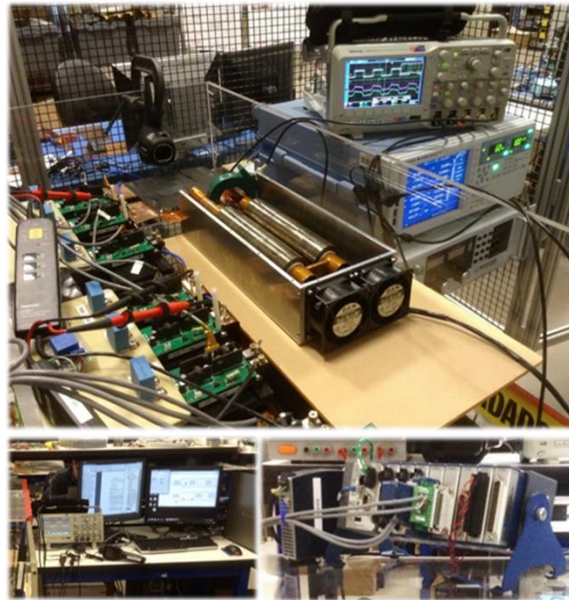


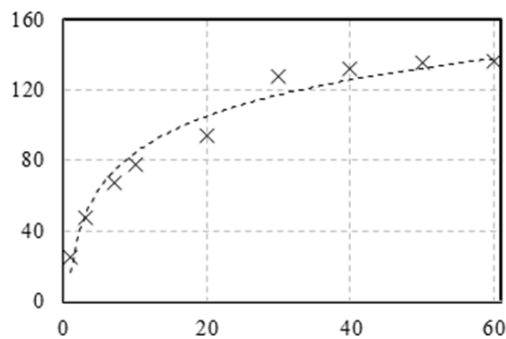
Figure 5.23: The configuration of the test set-up, 1200V IGBT-based DAB DC/DC converter for load-test

Table 5.4: Specifications of the single phase DAB DC/DC converter for loss measurement

Freq.	VA	Connection	Turns ratio	DC : DC	Modulation scheme
20 kHz	11kVA	Single-phase	1:1	200V : 200V	Phase-shift



(a) 1200V IGBT-based DAB DC/DC converter with ICWT prototype



(b) The hot-spot temperature of ICWT with C055925A2 for 60 minutes at 11kVA, 10kW and total transformer loss of 360W

Figure 5.24: 1200V IGBT-based DAB DC/DC converter test set-up using NI Crio and Lab-viewFAPGA

Table 5.5: ICWT with 2.7mH inductance integration (efficiency η)

Inner cores	μ_r	L_{sc}	kVA	Power [W]	Est. maximum η	Power density
C055927A2	200	2.7mH	24.5kVA	18.5kW	96.5%	2.8 kVA/dm ³

Table 5.6: ICWT with 4.0mH inductance integration (efficiency η)

Inner cores	μ_r	L_{sc}	kVA	Power [W]	Est. maximum η	Power density
C055925A2	300	4.0mH	16.5kVA	12.5kW	96.5%	1.9 kVA/dm ³

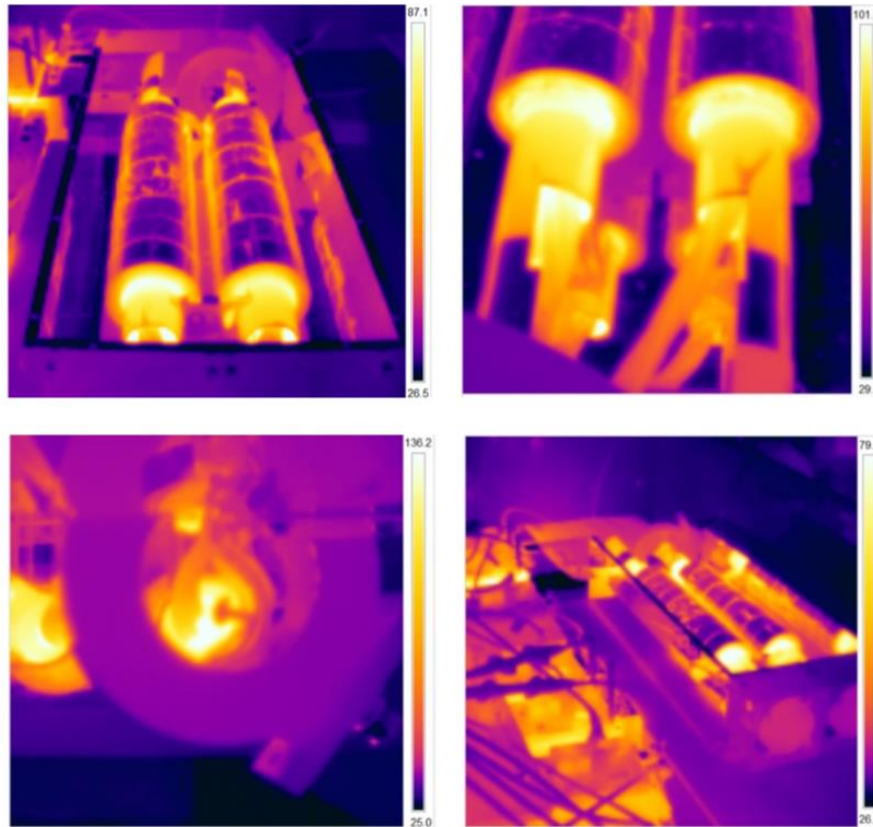


Figure 5.25: Thermal images of ICWT with C055925A2 ($\mu_r = 200$) at 10.9kVA, 10.1kW and total transformer loss of 360W

5.4 Summary

The performance of an inductor-integrated coaxial winding transformer (ICWT) has been proposed and analyzed with respect to high frequency response and loss for the high-frequency DC/DC conversion stages of the solid state transformer application. The essential benefit of the ICWT is that the transformer and inductor bodies are integrated, resulting in both size and copper loss reduction. Nonetheless, the operation mechanism is thoroughly separated and analyzed in a combined form with a high degree of accuracy. The homogeneous flux distribution prevents loss and heat congestion. A simple and accurate lumped-element equivalent circuit is introduced in order to understand the magnetic and electric coupling. This includes common-mode voltages to predict the high frequency switching response of converter operation. The loss behavior of an inductor-integrated coaxial winding transformer (ICWT) is also interpreted with the control variable and system parameters of DAB DC/DC converter operation in one closed form. The concept and feasibility of the ICWT has been proven by operational tests at the SiC based 20kHz 6kVDC/400VDC stages under soft-switching conditions.

Medium voltage insulation is an important concern for this design. The insulation level is estimated and determined by FEM simulation and the simplified DC and AC insulation tests are conducted for the CWT prototype to verify the feasibility of the approach. However, the final design has to be verified by iterative tests statistically, due to the variations of the insulation characteristics in practice. In the case of using an insulation medium with high permittivity, the parasitic capacitance values are increased by a factor of the relative permittivity of the insulation medium. The impact of the leakage current during switching on the HV winding also has to be considered.

Chapter 6

PROPOSED THREE-PORT AND THREE-PHASE DAB CONVERTER IN Y_{yd} CONFIGURATION

6.1 Winding types and considerations on three-phase system

As is commonly known, three-phase AC systems allow for higher power density with a lower VA rating on components than with single-phase systems. Therefore, most electric power transmission and distribution system used today, especially those in high-power applications, are of three phase configurations.

Conceptually, the same principles can be applied to three-phase DAB DC/DC converter operations. The existing three phase DAB DC/DC configurations already developed, which are mostly for low voltage applications, are based on a $Wye - wye$ (Yy) connection. However, a Yy connection of three phase systems is rarely used in medium voltage levels because of the serious problems caused by third-harmonic components. The third-harmonic components of each phase in a three phase system are in phase, and are added in the neutral point of the Wye connection of the transformer. This voltage induced on the neutral point of the Wye connection is connected to ground, and can be grounded to the tank of the transformer, through air can be larger than the fundamental voltage itself. The third harmonic components cause the greatest amount of distortion in both the current and voltage on the AC line.

Third-harmonic components always exist due to the nonlinearity of both the core and switching mode converters. Therefore, a $Delta$ connection is always used in conjunction with a Wye

connection in order to provide a path for the circulating current, unless the neutral point is solidly grounded. Therefore, most distribution transformers are in connection Yd11 when used medium voltage levels because the delta connection inherently provides a path for the third-harmonic component to circulate through the *Delta* connection.

One solid-state-transformer application, the Transformer-less Intelligent Power Substation (TIPS) application, has suggested the use of a phase modular medium-voltage three-phase three-port dual active bridge DC/DC converter in a Yyd connection, as shown in Fig. 6.1. The proposed configuration is suitable for a high power, high step up/down ratio three-phase DAB DC/DC converter application which requires a parallel combination of converters that share the high current on the low voltage side. One of the converters on the LV side is connected in a delta connection in order to avoid the problem of third-harmonics.

The important features and requirements of the proposed topology are:

1. Soft-switching during buck-boost operation has to be achieved across a wide range for all devices.
2. The three-port inductance network is integrated with the isolation transformer.
3. The power flow of the three port inductance network occurs between the LV and HV sides in the same direction (port 1 \leftrightarrow port 2, and port 1 \leftrightarrow port 3).
4. The circulating current between ports 2 and 3 through the DC-link on the LV side has to be minimized.

The amount of power and current flow shared in port 2 and port 3 is in balance.

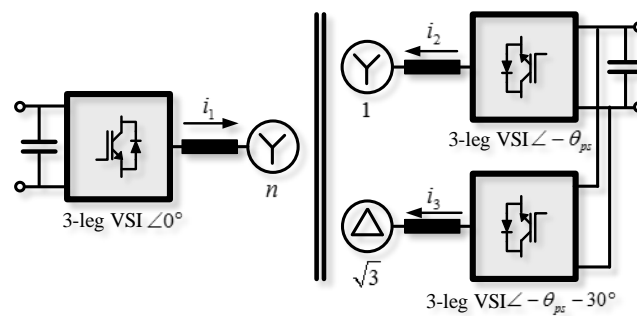


Figure 6.1: One line diagram of a three-port three-phase bidirectional isolated DAB DC/DC converter in Yyd connection

In order to understand and control the proposed three-phase, three-port DAB DC/DC converter topology, the steady-state operation principle has been studied and compared with other existing topologies at the end of this chapter.

6.2 Three-phase DAB converter topology - Yd connection

It is also possible to connect using only a Yd connection for three-phase DAB DC/DC converter operation. The steady-state operation and soft-switching region is investigated in this chapter and compared with other configurations.

6.2.1 Steady state lossless operation Yd connection

The method used to derive the inductance current and design parameters is the same as that used for single-phase DC/DC converter applications.

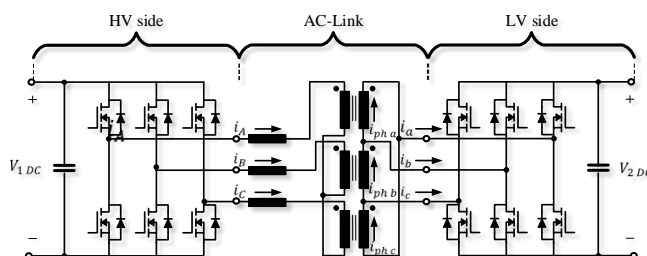


Figure 6.2: Three phase DAB in Yd connection

Five modes of operation with phase-shift modulation are identified for each operating regions of $0 \leq \theta_{ps} < \pi/3$ and $\pi/3 \leq \theta_{ps} < \pi/2$ (Appendix A). It should be noted that the line current has to be used to define the soft-switching region and VA rating of the power devices, and the phase current has to be used to determine VA rating of the transformer. The line current is the subtraction of the two connected phase currents as seen in Fig 6.3.

The amount of power transfer with phase-shift modulation in a three-phase Yd connection is given as :

$$\begin{cases} P_o Yy = \frac{kV_{1DC}^2(\pi - 6\theta_{ps})}{6\omega L_s \pi}, & \text{for } \frac{\pi}{6} \leq \theta_{ps} < \frac{\pi}{3} + \frac{\pi}{6} \\ = -\frac{kV_{1DC}^2(2\pi^2 - 12\pi + 9\theta_{ps}^2)}{6\omega L_s \pi}, & \text{for } \frac{\pi}{3} + \frac{\pi}{6} \leq \theta_{ps} < \frac{\pi}{2} + \frac{\pi}{6} \end{cases} \quad (6.1)$$

The inductance current $i_{L1 rms}$ for the phase-shift modulations are given by:

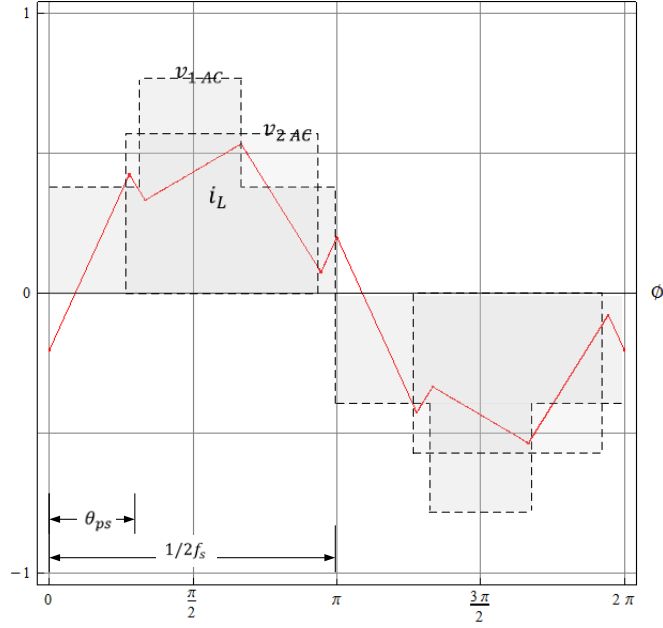


Figure 6.3: Waveforms in Yd connection

$$\begin{cases} i_{A rms} = \frac{V_{1DC} \sqrt{5(1-3k+3k^2)\pi^2 - 27k\pi\theta_{ps} + 81k\theta_{ps}^2}}{9\sqrt{3}\pi\omega L_s}, & \text{for } \frac{\pi}{6} \leq \theta_{ps} < \frac{\pi}{3} + \frac{\pi}{6} \\ = \frac{V_{1DC} \sqrt{(5-12k+15k^2)\pi^3 - 54k\pi^2\theta_{ps} + 162k\pi\theta_{ps}^2 - 81k\theta_{ps}^3}}{9\sqrt{3}\pi\omega L_s}, & \text{for } \frac{\pi}{3} + \frac{\pi}{6} \leq \theta_{ps} < \frac{\pi}{2} + \frac{\pi}{6} \end{cases} \quad (6.2)$$

where $i_{L1 rms} = i_{A rms} = n i_{ph a rms}$, $i_a = i_{ph a} - i_{ph c}$,
 $v_{1 Yd rms}$ and $v_{2 Yd rms}$ are represented by:

$$v_{1 Yd rms} = \frac{\sqrt{2}}{3} V_{1 DC}, \quad v_{2 Yd rms} = n \frac{2}{3} V_{2 DC} \quad (6.3)$$

Hence, the power rating of the transformer is:

$$T_{VA Yd} = \frac{v_{1 rms} \cdot i_{1 rms} + v_{2 rms} \cdot i_{2 rms}}{2} = \frac{(1 + \sqrt{2}k)v_{1 rms} \cdot i_{1 rms}}{2} \quad (6.4)$$

the line inductance can be chosen arbitrarily. Different base numbers are used with respect to the maximum power transfer in order to generalize and compare the different converter topologies. As is the case with conventional approach in sinusoidal form, each frequency component of the current waveform is shifted by $\frac{\pi}{6}$ in phase while the magnitude is scaled by factor

of $\sqrt{3}$.

Hence, the scaling factor for the three-phase DAB DC/DC converter in a Yd connection, in order to match the maximum power transfer from the single-phase DAB DC/DC converter is :

$$\begin{cases} P_{o \text{ single phase}}|_{k'=k, \theta_{ps}=\frac{\pi}{2}} = \frac{k\pi V_{1DC}^2}{2\omega L_s \pi} \\ P_{o \text{ Yd}}|_{k'=\frac{k}{\sqrt{3}}, \theta_{ps}=\frac{\pi}{2}+\frac{\pi}{6}} = \frac{7k\pi V_{1DC}^2}{36\omega L_s \pi} \end{cases}, \frac{P_{s \text{ single phase}}|_{\theta_{ps}=\frac{\pi}{2}}}{P_{o \text{ Yd}}|_{\theta_{ps}=\frac{\pi}{2}}} = \frac{3\sqrt{3}}{4} \quad (6.5)$$

The line inductance per phase in a three-phase Yd connection is scaled by a factor of $\frac{3\sqrt{3}}{4}$ in order to achieve the same maximum power transfer. Hence, the base numbers used for three-phase DAB DC/DC converter in a Yy connection are:

$$V_b = V_{1DC}, I_b = \frac{3\sqrt{3}}{4} \frac{V_b}{\omega L}, P_b = V_b I_b \quad (6.6)$$

Circulating current in three-phase Wye-Delta connection: Harmonic current, which does not contribute to the power flow, is always a significant issue in active control. A conventional technique used to mitigate harmonics is phase shifting. In the proposed topology of the TIPS application, the high frequency link dc-dc converter has a three level inverter in a Wye connection on the HV side and a paralleled two level inverter on the the LV side in Wye and Delta connection as shown in Fig 6.6. The three phase output from the DC link is generated by a three phase voltage.

In order to understand its operation, the simplest six-step mode of operation is considered, which has a phase shift of $\frac{2}{3}\pi$ between phases.

The fundamental and harmonic components of the phase-neutral point voltage is:

$$v_{an} = V_{dc} \frac{2}{\pi} \left(\cos(\omega t) + \frac{1}{5} \cos(5\omega t) - \frac{1}{7} \cos(7\omega t) - \frac{1}{11} \cos(11\omega t) \dots \right) \quad (6.7)$$

The fundamental and harmonic components of the phase-phase voltage is

$$v_{ab} = \sqrt{3} V_{dc} \frac{2}{\pi} \left(\cos(\omega t + \frac{\pi}{6}) - \frac{1}{5} \cos(5\omega t + \frac{\pi}{6}) - \frac{1}{7} \cos(7\omega t + \frac{\pi}{6}) - \frac{1}{11} \cos(11\omega t) \dots \right) \quad (6.8)$$

The difference between the fundamental components of the phase-neutral point voltage, v_{an} , and phase-phase voltage, v_{ab} , is that v_{ab} is $\sqrt{3}$ times v_{an} with a phase shift of $\frac{\pi}{6}$.

The fundamental and harmonic components of the phase-phase voltage with phase shift is $\frac{\pi}{6}$

$$v_{ab} = \sqrt{3} V_{dc} \frac{2}{\pi} \left(\cos(\omega t) - \frac{1}{5} \cos(5\omega t) + \frac{1}{7} \cos(7\omega t) - \frac{1}{11} \cos(11\omega t) \dots \right) \quad (6.9)$$

Therefore, the 5th and 7th elements of the magnetizing current are mitigated, and the fun-

damental components of the induced current that flow on the windings are cancelled out. This is done by using a turns ratio of $\sqrt{3} : 1$ and a phase shift of 30° between the Yd connections.

6.2.2 Soft switching scheme three phase Yd connection

The line current during turn-on has to be less than zero to meet the requirements for soft-switching, therefore the lagging bridge, in the case of positive power transfer in a *Delta* connection, has to be calculated by subtracting phase currents in phase 'a' and 'c'.

For the leading bridge: $i_{L A1}[0] \leq 0$,

$$\begin{cases} k \leq \frac{\sqrt{3}}{2}, & \text{for } \frac{\pi}{6} \leq \theta_{ps} < \frac{\pi}{3} + \frac{\pi}{6} \\ k \leq \frac{3\sqrt{3}}{8}, & \text{for } \frac{\pi}{3} + \frac{\pi}{6} \leq \theta_{ps} < \frac{\pi}{2} + \frac{\pi}{6} \end{cases} \quad (6.10)$$

For the lagging bridge: $i_{L a1}[\theta_{ps}] - i_{L a3}[\theta_{ps}] \geq 0$,

$$\begin{cases} k \leq \frac{\sqrt{3}\pi}{2(2\pi-3\theta_{ps})}, & \text{for } \frac{\pi}{6} \leq \theta_{ps} < \frac{\pi}{3} + \frac{\pi}{6} \\ k \leq \frac{3\sqrt{3}(2\pi-3\theta_{ps})}{8\pi}, & \text{for } \frac{\pi}{3} + \frac{\pi}{6} \leq \theta_{ps} < \frac{\pi}{2} + \frac{\pi}{6} \end{cases} \quad (6.11)$$

The Fig 6.4 shows the line current waveforms at different load conditions. Note that there is a phase difference, 30° , between windings in *Wye* and *Delta* connections. The no-load condition occurs at phase shift $\theta_{ps} = 30^\circ$, and circulating current exits without power transfer as seen in Fig 6.4 (a). The Fig 6.5 (a) shows theoretically achievable real power transfer and the soft switching boundaries for the leading and lagging bridges with the phase shift θ_{ps} and k under steady-state operation. The average value of the VA ratings on both sides is typically considered to be the VA rating of the transformer shown in Fig 6.5 (b). The design parameters can be chosen based on the required power rating of the application and controllability under soft-switching.

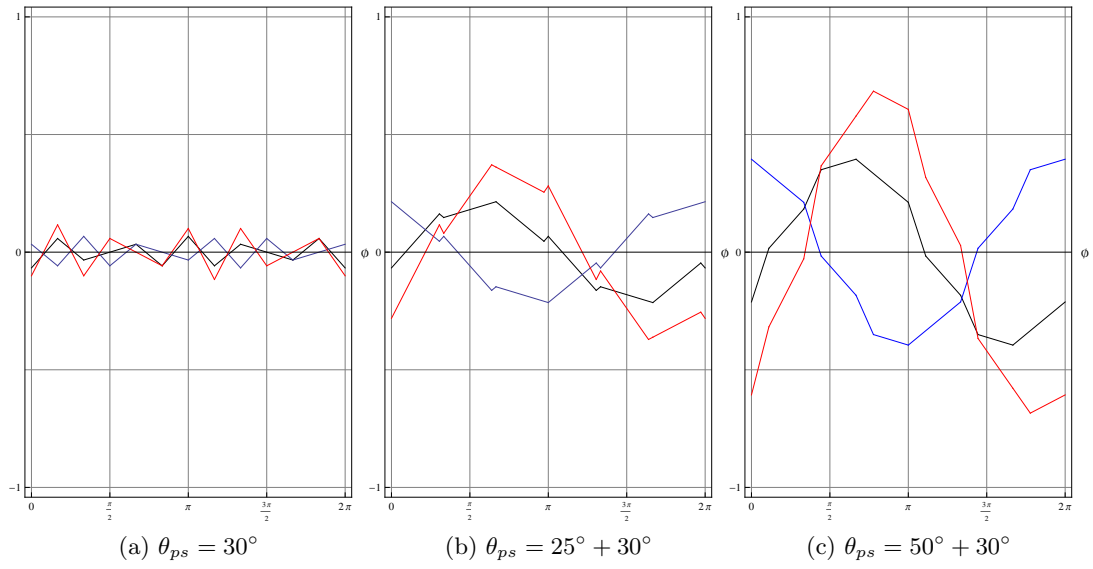


Figure 6.4: Line current waveforms ($k = 1/\sqrt{3}$)

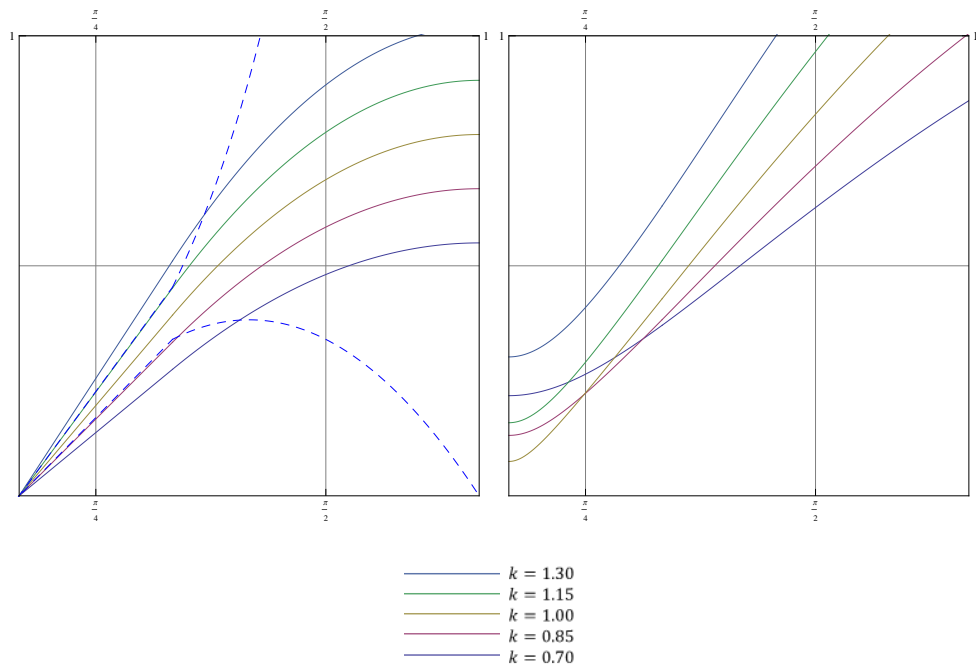


Figure 6.5: Real and average apparent power with θ_{ps} and k (Red line : Soft swathing boundary)

6.3 Proposed three-port three-phase bidirectional and isolated dc/dc converter in Yyd connection

All three phases of the three-phase AC system are theoretically the same, with only their phase shifted $2\pi/3$ from each other under balanced load conditions. It is customary to use a one-line diagram analysis to represent the interconnected three phase system in a more readable and efficient manner for circuit analysis. The three-port, three-phase DAB DC/DC converter can be also simplified using a one-line diagram with three independent voltage sources and three lumped inductances in *Wye* or *Delta* type equivalent circuit.

6.3.1 Power flow analysis using network calculations and impedance model

A port network is used for circuit analysis, with the terminals carrying equal and opposite currents. The three port system is represented by an impedance or admittance model when the system is a lossless, linear electrical circuit. The three-phase converter connected, three-winding AC-link transformers can be shown as a 3-port system with a 3×3 impedance model. The effect of the capacitances and resistances of the power conversion system are considered a parasitic effect; hence, the impedance model can be seen as purely inductance model for steady-state analysis.

Actively controlled converters at each winding can be seen as independent voltage sources and the three-winding transformer in the AC-link section can be represented by an inductive filter, 3×3 impedance model.

$$\begin{bmatrix} L_{11} & L_{12} & L_{13} \\ L_{21} & L_{22} & L_{23} \\ L_{31} & L_{32} & L_{33} \end{bmatrix} d/dt \begin{bmatrix} i_1 \\ i_2 \\ i_3 \end{bmatrix} = \begin{bmatrix} v_1 \\ v_2 \\ v_3 \end{bmatrix} \quad (6.12)$$

In order to represent the proposed topology in Fig 6.6 with a one-line diagram convention for lumped element circuit analysis, the inductance matrix needs to be simplified by a *Wye* or *Delta*-type equivalent circuit as in Fig 6.7.

It is helpful to understand the system's behavior with fundamental frequency components first. This has a dominant impact on system performance. By using the delta-type equivalent circuit model, the power flow of the multi-port system can be divided into three independent two port systems. The relationship between voltage, current, and power flow is simplified with phasor vector notation as shown in Fig 6.8. The real and reactive power is represented in harmonic form by:

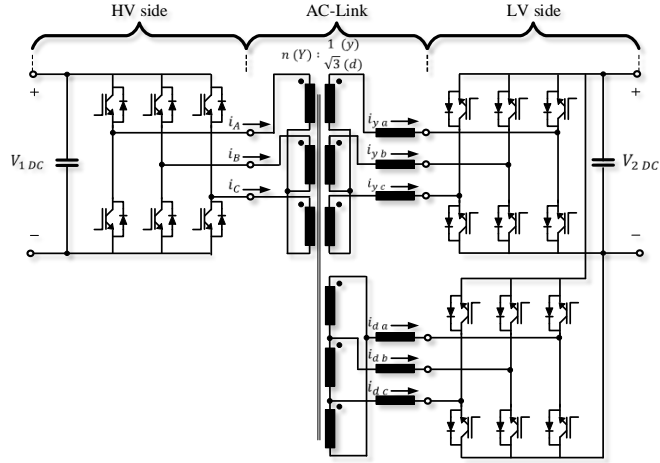


Figure 6.6: Proposed three-port three-phase bidirectional and isolated dc/dc converter in Yyd connection.)

$$\begin{cases} P_{ij} = \frac{V_i V_j \sin \theta_{ij}}{\omega L_{ij}} \\ Q_{ij} = \frac{V_i (V_i - V_j \cos \theta_{ij})}{\omega L_{ij}} \end{cases} \quad (6.13)$$

Two important concepts of dual-active bridge operation illustrated in the phasor diagram. The bidirectional power flow between any two ports is equally possible, and the direction is determined by the phase shift. The line current always lags v_1 and leads v_2 when the magnitude of the voltage vectors are the same. This is an important design parameter to determine the soft switching region of the DAB operation for high frequency switching. Therefore, the full controllability over the entire switching region is achieved when the system parameter ' k ' is unity. In other words, the turns ratio of the transformer is the same as the conversion ratio of the system.

The proposed topology seen in Fig 6.6 is an isolated three phase DAB DC/DC configuration in Yyd connection with the minimum number of power devices. The high step up/down ratio of the distribution line transformer and size reduction are achieved using the high frequency AC-link transformer. The necessary galvanic isolation in medium-voltage level, and the third harmonic issue are taken care of by the AC-link transformer in a Yyd connection. As investigated with the fundamental frequency model, the direction of the power flow is determined by active switching of the converters.

Steady-state operation in three phase Yy connection (port 1 ↔ port 2): The operation between port 1 and 2 is identical to the conventional three-phase DAB DC/DC converter

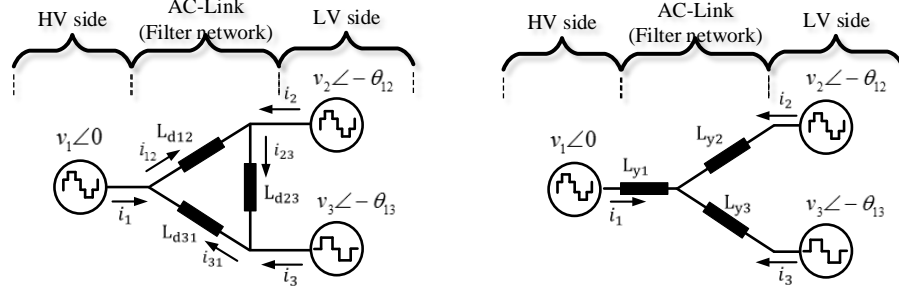


Figure 6.7: Simplified *Wye*-type (left) and *Delta*-type (right) primary-referred equivalent circuit of three port system)

operation, and is actively controlled by switching delay, phase-shift θ_{ps} , of both bridges. The amount of power transfer is determined by L_{d12} and ' k '. The scaling factor of the inductance value refers to the inductance required for a single phase DAB operation to transfer the same amount of real power, and is approximately 0.77 in three-phase DAB operation in both Yy and Yd configurations.

Steady-state operation in three phase Yd connection (port 1 \leftrightarrow port 3 and port 2 \leftrightarrow port 3): The phase shift and turns ratio of the winding in delta connection has to be adjusted to balance the power flow to both bridges on the LV side. The three-phase transformer winding inherently generates a magnitude change along with a phase displacement of $\sqrt{3}\angle\pi/6$ (Yd11) in phasor notation; hence, the mismatch has to be compensated for by active switching of the bridge and turns ratio of the windings. Therefore, the phase shift angle between port 1 and port 3 has another $\pi/6$ on top of the phase shift angle between port 1 and port 2 with a turns ratio of $N_1 : N_2 : N_3 = n : 1 : \sqrt{3}$. The constant phase displacement of $\pi/6$ between them does not transfer real power between port 2 and port 3. However, high harmonic circulating current always exists due to the mismatch of both voltage waveforms, and it has to be minimized with high impedance.

Therefore, the desirable one-line circuit model of the proposed topology is shown in Fig. 3.20 with a high inductance value of L_{d23} .

6.3.2 Steady state lossless operation - Three phase in Yyd connection

The eight modes for line current i_1 are identified and extracted in Appendix A.

$$i_1 = i_{12} - i_{31} \quad (6.14)$$

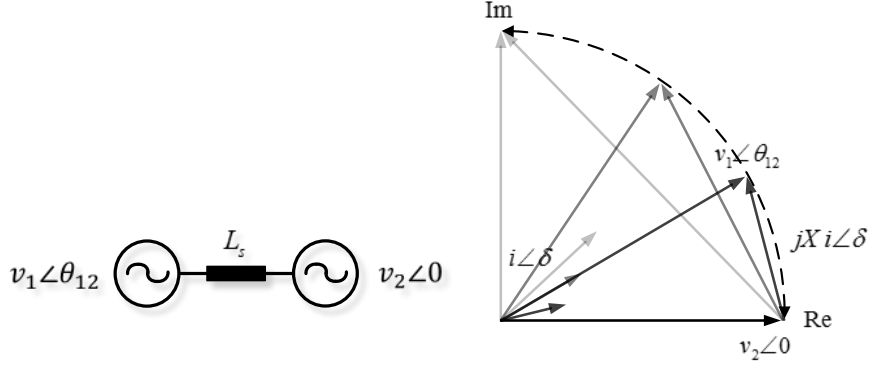


Figure 6.8: One line diagram of DAB operation and vector notation for voltage and current in phasor form)

where i_{23} is a circulating current which does not contribute to the power flow. The minimum rms value of i_{23} between the bridges on the LV side can be achieved with a phase difference of $\pi/6$, which is consistent with the conventional approach for fundamental frequencies.

$$\frac{di_{23}}{d\theta_{ps}} = \frac{-27\pi + 162\theta_{ps}}{18\sqrt{3}\sqrt{5\pi^2 - 27\pi\theta_{ps} + 81\theta_{ps}^2}} = 0, \quad \theta_{ps} = \frac{\pi}{6} \quad (6.15)$$

Assuming that i_{23} is small enough with high impedance between ports 2 and 3, the amount of power transferred with phase-shift modulation in a three phase Yd connection is simplified by:

$$P_o Y_{yd} = P_o Y_y |_{k=k', \theta_{ps}=\theta'_{ps}} P_o Y_{yd} |_{k=\frac{k'}{\sqrt{2}}, \theta_{ps}=\theta'_{ps} + \frac{\pi}{6}} (L_{d12} \cong L_{d32} = L_s [p.u]) \quad (6.16)$$

$$\left\{ \begin{array}{ll} P_o Y_{yd} = \frac{kV_{1DC}^2 (2(2+\sqrt{3})\pi - 3\theta_{ps})\theta_{ps}}{6\pi\omega L_s}, & \text{for } 0 \leq \theta_{ps} < \frac{\pi}{6} \\ = -\frac{kV_{1DC}^2 (\sqrt{3}\pi^2 - 12(4+3\sqrt{3})\pi\theta_{ps} + 36(1+\sqrt{3})\theta_{ps}^2)}{72\pi\omega L_s}, & \text{for } \frac{\pi}{6} \leq \theta_{ps} < \frac{\pi}{3} \\ = -\frac{kV_{1DC}^2 ((4+\sqrt{3})\pi^2 - 36(2+\sqrt{3})\pi\theta_{ps} + 36(2+\sqrt{3})\theta_{ps}^2)}{72\pi L_s}, & \text{for } \frac{\pi}{3} \leq \theta_{ps} < \frac{\pi}{2} \end{array} \right. \quad (6.17)$$

the inductance current $i_{L1 rms}$ for phase-shift modulation is given by:

$$\left\{ \begin{array}{l} i_{A1} =, \text{ for } 0 \leq \theta_{ps} < \frac{\pi}{6} \\ i_{A1} =, \text{ for } \frac{\pi}{6} \leq \theta_{ps} < \frac{\pi}{3} \\ i_{A1} =, \text{ for } \frac{\pi}{3} \leq \theta_{ps} < \frac{\pi}{2} \end{array} \right. \quad (6.18)$$

$v_1 Y_{d rms}$ and $v_2 Y_{d rms}$ is represented by:

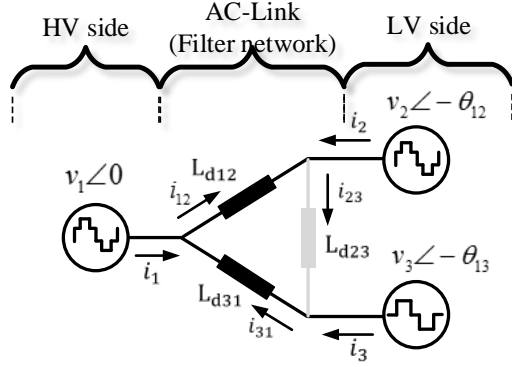


Figure 6.9: One line diagram Proposed three-port three-phase bidirectional and isolated dc/dc converter in Yd connection)

$$v_1 Yd_{rms} =, \quad (6.19)$$

Hence, the power rating of the transformer is:

$$T_{VA Yd} = \frac{v_1_{rms} \cdot i_1_{rms} + v_2_{rms} \cdot i_2_{rms} + v_3_{rms} \cdot i_3_{rms}}{3} \quad (6.20)$$

6.3.3 Soft switching scheme Three phase Yd connection

In the proposed topology, the soft-switching boundaries have to be considered for each bridge independently. The soft-switching region of the leading bridge is determined by the sum of the phase-currents on both windings in *Wye* and *Delta* connections on the LV side. The same boundary criteria can be applied to the lagging bridges on the LV side of the *Wye – Wye* and *Wye – Delta* sides respectively. All three criteria have to be met in order to achieve zero-voltage switching on all devices.

To meet this operating condition for each bridge the following is shown,

For the leading bridge:

$$\left\{ \begin{array}{l} \text{for } 0 \leq \theta_{ps} < \frac{\pi}{3} \\ \text{for } \frac{\pi}{3} \leq \theta_{ps} < \frac{\pi}{2} \end{array} \right. \quad (6.21)$$

For the lagging bridge:

Bridge in wye connection:

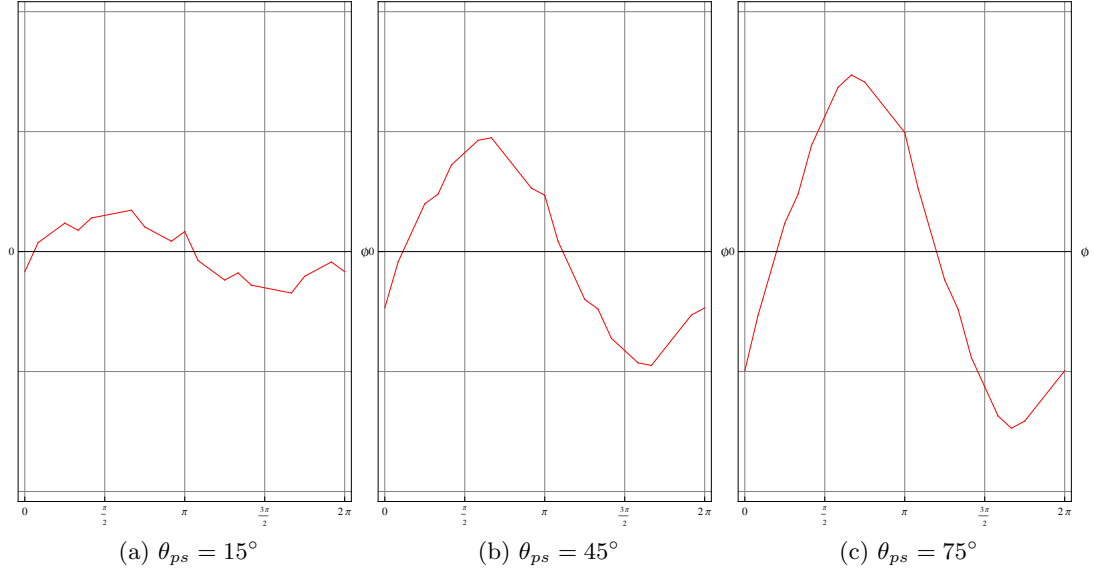


Figure 6.10: Line current waveforms in winding 1

$$\begin{cases} k \leq \frac{6\pi}{7(\pi-2\theta_{ps})}, & \text{for } 0 \leq \theta_{ps} < \frac{\pi}{3} \\ k \leq \frac{27(\pi-2\theta_{ps})}{14\pi}, & \text{for } \frac{\pi}{3} \leq \theta_{ps} < \frac{\pi}{2} \end{cases} \quad (6.22)$$

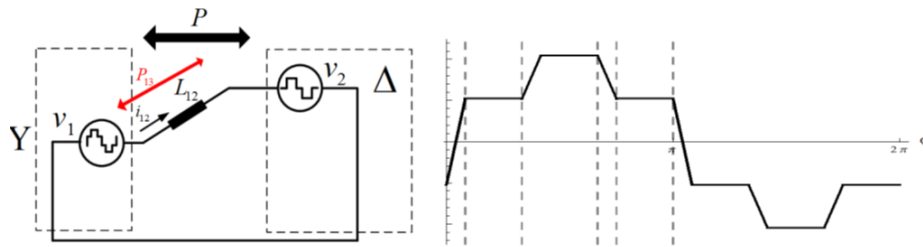
Bridge in *Delta* connection:

For the lagging bridge: $i_{L a1}[\theta_{ps}] - i_{L a3}[\theta_{ps}] \geq 0$,

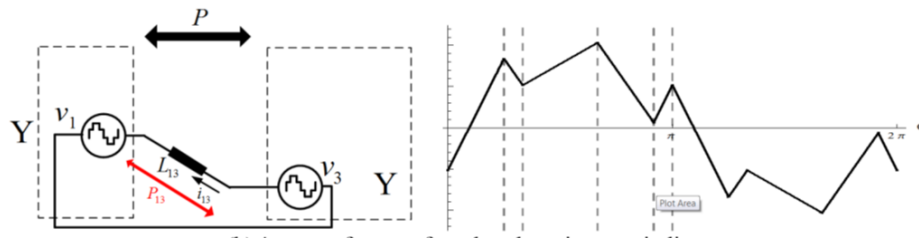
$$\begin{cases} k \leq \frac{\sqrt{3}\pi}{2(2\pi-3\theta_{ps})}, & \text{for } 0 \leq \theta_{ps} < \frac{\pi}{3} \\ k \leq \frac{3\sqrt{3}(2\pi-3\theta_{ps})}{8\pi}, & \text{for } \frac{\pi}{3} \leq \theta_{ps} < \frac{\pi}{2} \end{cases} \quad (6.23)$$

The real and apparent power transfer, with the soft switching boundaries of the three-phase DAB DC/DC converter in *Yy* connection is shown in Fig 3.22 in the same manner as for single-phase DAB applications.

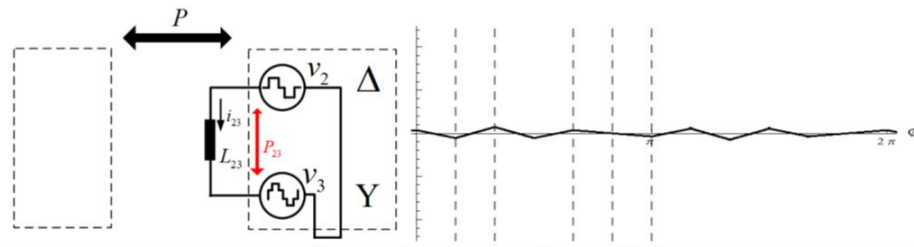
Harmonic current that does not contribute to power flow is always a significant issue in active control. A convention technique to mitigate harmonics is phase shifting. In the proposed topology of the TIPS application, the high frequency link DC/DC converter has a three level inverter in *Wye* connection on the HV side and a paralleled two level inverter on the LV side in a *Wye* and *Delta* connection as shown in Fig 1.4. The three phase output from the DC link is generated by three phase voltage



(a) i_{12} waveforms referred to the primary winding



(b) i_{13} waveforms referred to the primary winding



(c) i_{23} waveforms referred to the primary winding

Figure 6.11: Current waveforms referred to the primary winding

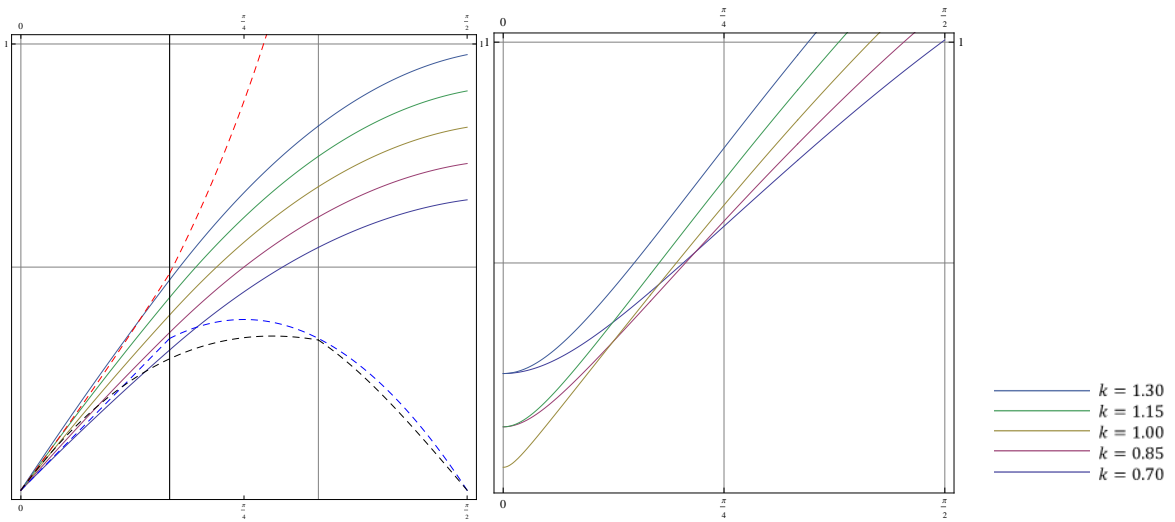


Figure 6.12: Real and average apparent power with θ_{ps} and k (Red line : Soft swathing boundary)

6.4 Proposed inductor integrated three-winding planar transformer for the proposed topology

The proposed geometry and design method for the AC-link transformer allows us to integrate a large number of bulky inductors that are required for the proposed topology to the transformer without additional connections and unanticipated parasitic effects. The proposed transformer considerably simplifies the equivalent leakage inductance circuit model and power flow analysis. This configuration is suitable for high power and high step up/down ratio DC/DC converter applications which requires series and/or parallel combinations of converters. The experimental and FEM simulation results from prototypes are presented, and they validate the theoretical considerations and feasibility of the proposed approach for isolated DC/DC converter applications such as the solid-state transformer (SST).

6.4.1 Modeling concept : inductance matrix of a three winding planar transformer and geometrical analysis

A three winding shell-type planar transformer is one of the most suitable transformers for the three port phase modular DAB converter applications. The leakage magnetic flux of the transformer is fairly high and predictable which allows it to be used for series inductance integration. The difference of leakage terminal inductances between windings can be utilized to adjust the circulating current and power flow between the ports for each winding arrangement. The simplified terminal leakage inductance model is used, and the analytical solution for the steady state operation of the proposed converter in Yd connection is provided.

6.4.2 Winding arrangement and inductance calculation

The magnetic behavior of a three winding transformer is represented by a 3×3 inductance matrix. However, it is complex and hard to convert to an equivalent circuit model useful for circuit analysis.

$$\begin{bmatrix} L_{11} & L_{12} & L_{13} \\ L_{21} & L_{22} & L_{23} \\ L_{31} & L_{32} & L_{33} \end{bmatrix} \quad (6.24)$$

In order to build a simple and reliable equivalent circuit model, terminal leakage inductances $L_{t\ ij}$ are meaningful and measurable parameters. The terminal leakage inductances are easily measured for two windings at a time by shorting the relevant winding, and opening the last winding (unused) as shown in Fig 6.6.

$$L_{t\ ij} = L_{ii} - \frac{L_{ij}^2}{L_{jj}}, \quad (L_{ii} = N_i^2 P_{ii}, \quad L_{1ij} = N_i N_j P_{ij}) \quad (6.25)$$

In order to efficiently guide the magnetic flux path, the geometry of the cores needs to be symmetric and shielded by a high permeability material. Due to the symmetry of the geometry and high permeability of the magnetic cores, the leakage magnetic field intensity is confined in the window area and becomes proportional and uniform. Therefore, the terminal leakage inductance is proportional to the factor of $\frac{l \cdot d}{h}$ and is naturally amplified by the planar shape of the window. The terminal leakage permeance is calculated from the trapezoidal magnetic flux distribution with geometric.

$$\begin{cases} p_{t\ 12} = \frac{\mu_0 l}{3h} \cdot (3d_{12} + d_1 + d_2) \\ p_{t\ 13} = \frac{\mu_0 l}{3h} \cdot (3d_{13} + d_1 + d_3) \\ p_{t\ 23} = \frac{\mu_0 l}{3h} \cdot (3d_{12} + 3d_{13} + 3d_1 + d_2 + d_3) \end{cases} \quad (6.26)$$

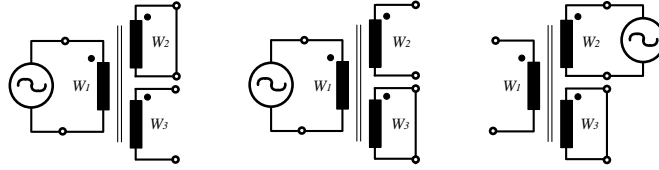


Figure 6.13: Terminal leakage inductances measurements

Even though the terminal leakage inductances are not equivalent to the inductance elements of the leakage equivalent circuit model, the magnetic field distribution in the window and the terminal leakage inductances give an insight to understanding the magnetic coupling between windings. Since the permeance $P_{t\ 13}$ is greater than the sum of $P_{t\ 12}$ and $P_{t\ 13}$, port 2 and port 3 have to be assigned to the windings on both ends of the window area so that the interaction between ports 2 and 3 is mitigated. The symmetric arrangement also gives the similar permeances between ports 1 and 2, and between ports 1 and 3. This winding arrangement is beneficial for balancing current sharing on the two bridges in parallel.

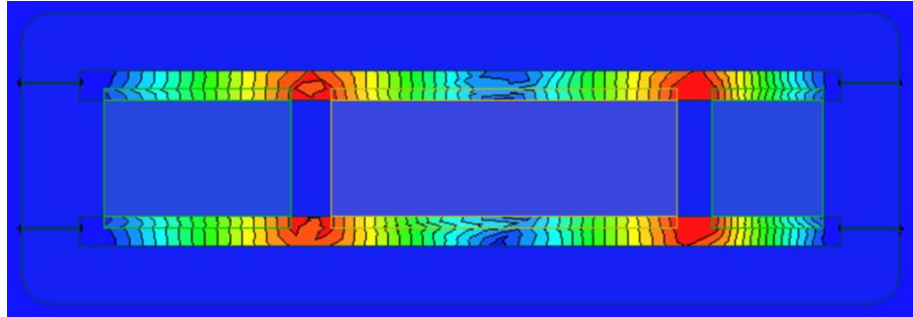
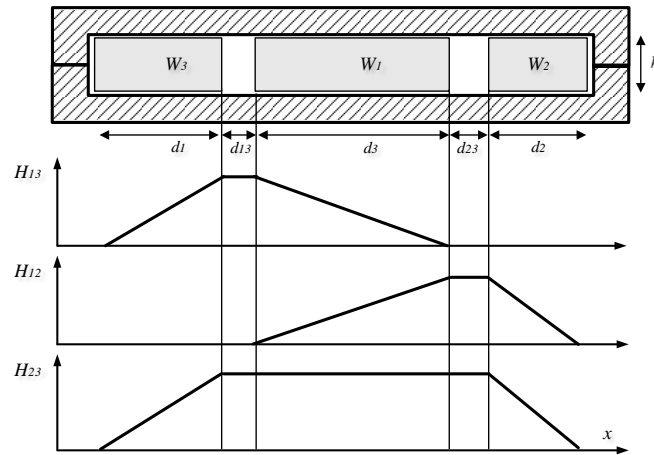


Figure 6.14: Leakage magnetic field intensity distribution in planar window area

6.4.3 FEM transient simulation results and comparison with analytical solution

The 5.5kVA three winding planar transformer has been built with a width/height ratio of 21.7 in order to achieve two series inductances of $10mH$ on ports 2 and 3. This is designed for a laboratory prototype of 5.5kV to 400V DC/DC stage of the topology, SST application. Six pairs of nanocrystalline magnetic cores are customized and litz wires are applied to reduce eddy and proximity effects at high frequencies shown in Table 4.10. The bobbin is made of Teflon with holes for each individual wire to support medium voltage.

The results from the calculation, FEM magnetostatic solution and measurements are shown in Table 5.5. The 3D FEM transient solution with proposed specifications shown in Table 6.1 verifies the steady-state operation principles. The terminal leakage measurement results from the laboratory prototype are shown in Table 3.3. The measured values of L_{t12} and L_{t13} , which are used as circuit elements, are slightly smaller than the calculated results, but within

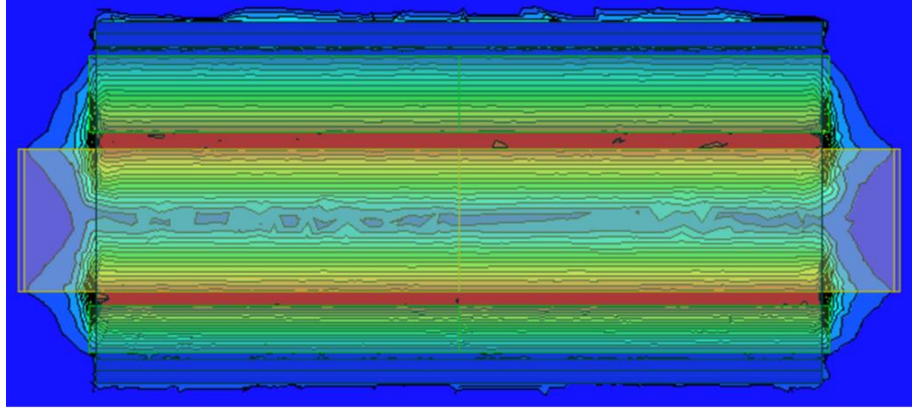
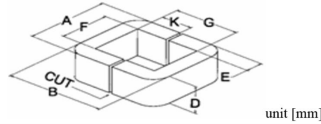


Figure 6.15: H-field distribution - Top view

Table 6.1: Dimensions of the proposed planar transformer

		A	F	B	G	E	D		
		150	130	26	6	10	50		
N_1	N_2	N_3	d_1	d_2	d_3	d_{12}	d_{23}	l	h
4	55	8	19	59	32	6	7	600	6



reasonable error. $L_{t\ 23}$ shows more than 40% error. This is not critical in practice, so long as it is much larger than the other terminal leakage inductances because $L_{t\ 23}$ is not a circuit element for the simplified equivalent circuit. The mismatch between the measurement and the calculation on the basis of the simplified equivalent circuit is not avoidable, and does not affect the system operation considerably. However, more study will be needed to form a solid conclusion. The line current waveforms on the three-dimensional geometry of the prototype, three-winding inductance integrated planar transformer, are extracted by exciting a voltage waveform on each winding in the Yd connection in Fig 6.18. There is a slight mismatch with the analytical solution because the equivalent model is simplified with terminal leakage inductance and the circulating current is ignored. Nonetheless, the error is within an acceptable range considering the errors from the imperfection of manufacturing processes, the measurement, and the benefit of the simple lumped circuit equivalent circuit, when used in place of an impedance matrix is large. The magnetizing flux on the cores is sinusoidal with low harmonic components. This characteristic could help for three-phase transformer design in the future.

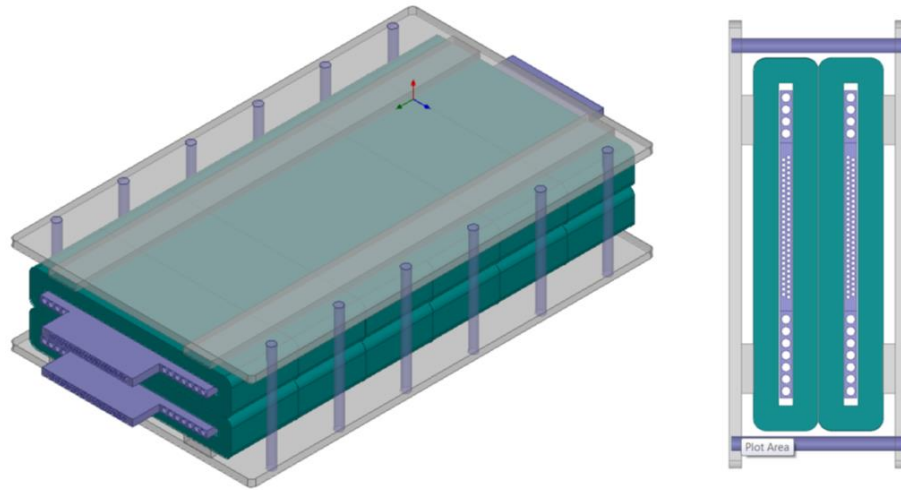


Figure 6.16: Inductance integrated planar MV-MF transformer

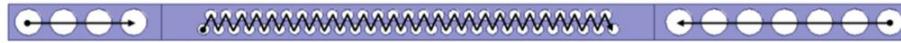


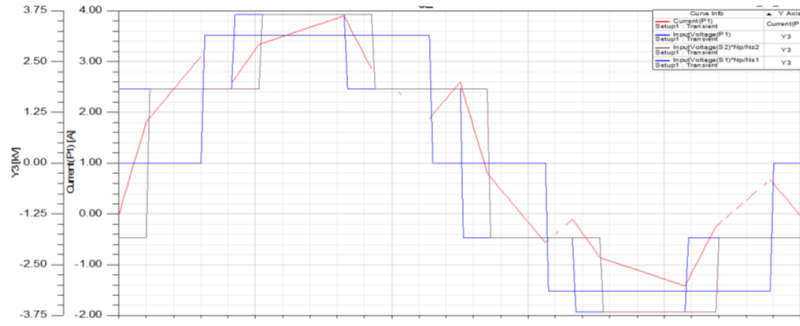
Figure 6.17: Winding arrangement

Table 6.2: Specifications

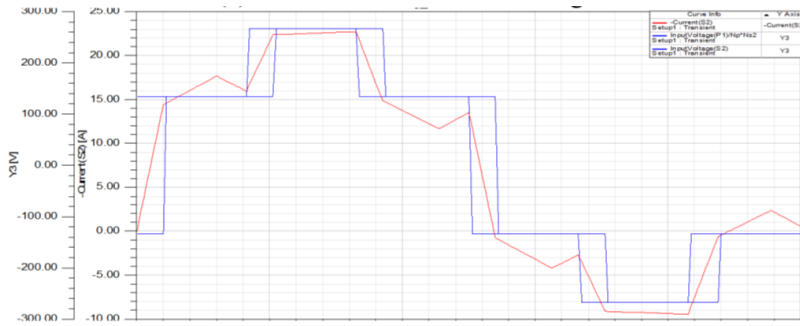
Freq.	V_{dc1}	V_{dc2}	kVA_{phase}	$V_{phase\ rms}$	$i_{phase\ rms}$	$N_1 : N_2 : N_3$
10kHz	5500V	400V	5.5kVA	2.6kV	2.1 Arms	55:7:4

Table 6.3: Terminal leakage inductances

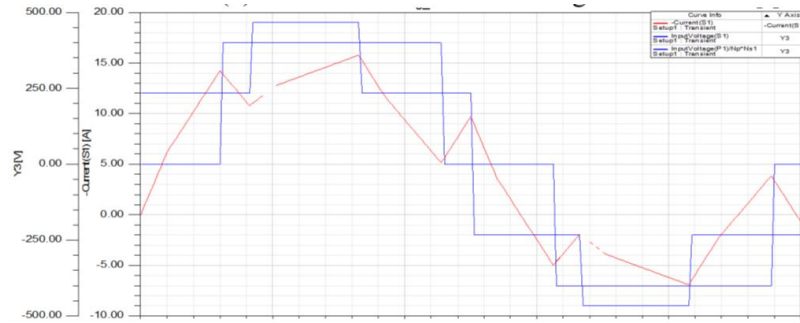
	$P_{t\ 12}[uH]$	$p_{t\ 23}[uH]$	$p_{t\ 23}[uH]$	$L_{t12}[mH]$	$L_{t13}[mH]$	$L_{t23}[mH]$
Calculation	4.02	4.69	12.3	12.2	14.2	37.2
3D FEM	4.82	5.58	12.9	14.6	1639	39.0
Measurement	.	.	.	@10Hz:11.3 @10kHz:10.5	@10Hz:12.5 @10kHz:11.8	23.3



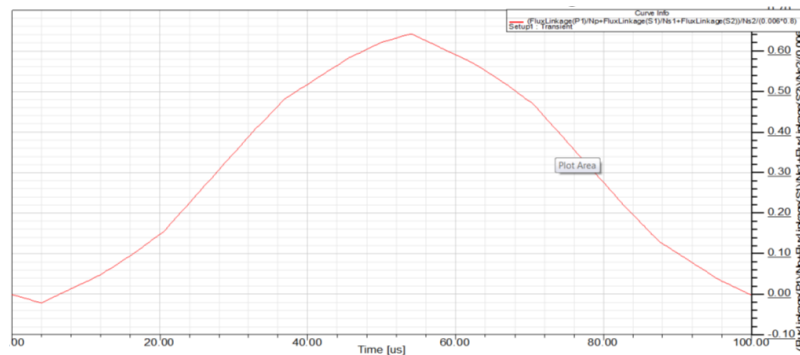
(a) Current waveform on winding 1



(b) Current waveform on winding 2



(c) Current waveform on winding 3



(d) Magnetic field intensity on the core cross section [T]

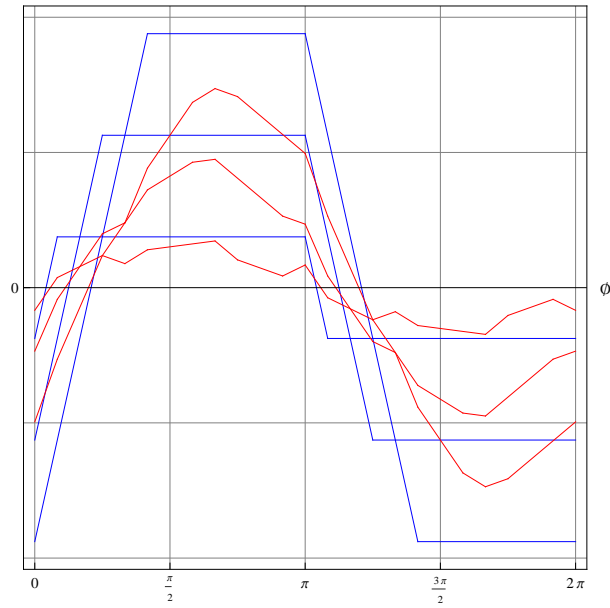


Figure 6.19: Current waveforms on HV side of single-phase DAB (blue, topology 2) and phase current waveforms on HV side of three-phase DAB in Yyd connection (red, topology 3) - the same DC-link voltages and line inductance are applied

6.5 Comparison and implementation of laboratory prototype

VA rating and current waveforms: With respect to VA ratings and harmonics while ignoring system complexity and cost, the three-phase DAB converter in Yy connection shows the greatest performance of the topologies. The circulating current in the Yd connection makes a difference under light load conditions. However, all three phase topologies shows almost identical performance under heavy load conditions. The single-phase DAB DC/DC converter has a high VA ratings over the entire operation range greater than the other three-phase topologies. The current waveforms of the single-phase DAB DC/DC converter and the three phase DAB DC/DC converter in Yyd connection are shown and compared. There is a considerable difference in the harmonic components in the current waveforms between topology 2 and topology 3 on the HV side. The VA rating on the HV side of the proposed topology at $k = 1$, $\theta_{ps} = \frac{\pi}{4}$ is approximately 12% less than topology 1 in exchange for additional switches.

Soft-switching region : The Soft-switching region of the high power DC/DC converter is of considerable interest when defining the possible operating range and controllability of the application. The leading bridge on the HV side is determined by the line current, which is the sum of the phase current of both bridges on the LV side. The lagging bridges on the LV side in *Wye* and *Delta* connection have different boundaries and operation has to remain inside the inner boundary of both to have soft-switching on all three bridges.

The single-phase DAB DC/DC converter is obviously the worst case with respect to VA ratings. However, the single-phase topology is superior to the others in terms of the simplicity of the system and the low cost with a minimum number of devices. The performance of the topology 3 is in the middle of the three-phase DAB in a Yy connection and Yd connection. Nonetheless, topology 3 shows fairly good performance, close to a Yy connection, and superior to topology 1. The third harmonics problems are nonexistent in analysis under ideal conditions. However, switch-mode non-linear operation is vulnerable to third harmonics issues, and a Yyd connection is highly recommended, except for a few special cases for three phase applications in medium voltage levels whose reliability is of a critical concern.

Proposed inductor integrated three-winding planar transformer: In this chapter, the inductor-integrated three winding planar transformer has been designed for the phase modular three-port bidirectional dc/dc converter in a Yyd connection on the basis of the analytical solution to the steady-state operation. The power flow characteristics of the converter operation are analyzed using the terminal leakage inductance model. The terminal leakage inductance model has been simplified with only two measurable and calculable inductances with the proposed core shape and winding arrangement. The complex power flow analysis and system behavior of a multi-port converter with inductor-integrated transformers has been significantly simplified and therefore the system configuration becomes simple and reliable. The operation

principle, with a comprehensive analysis of the converter and isolation transformer, is presented and verified the experimental results.

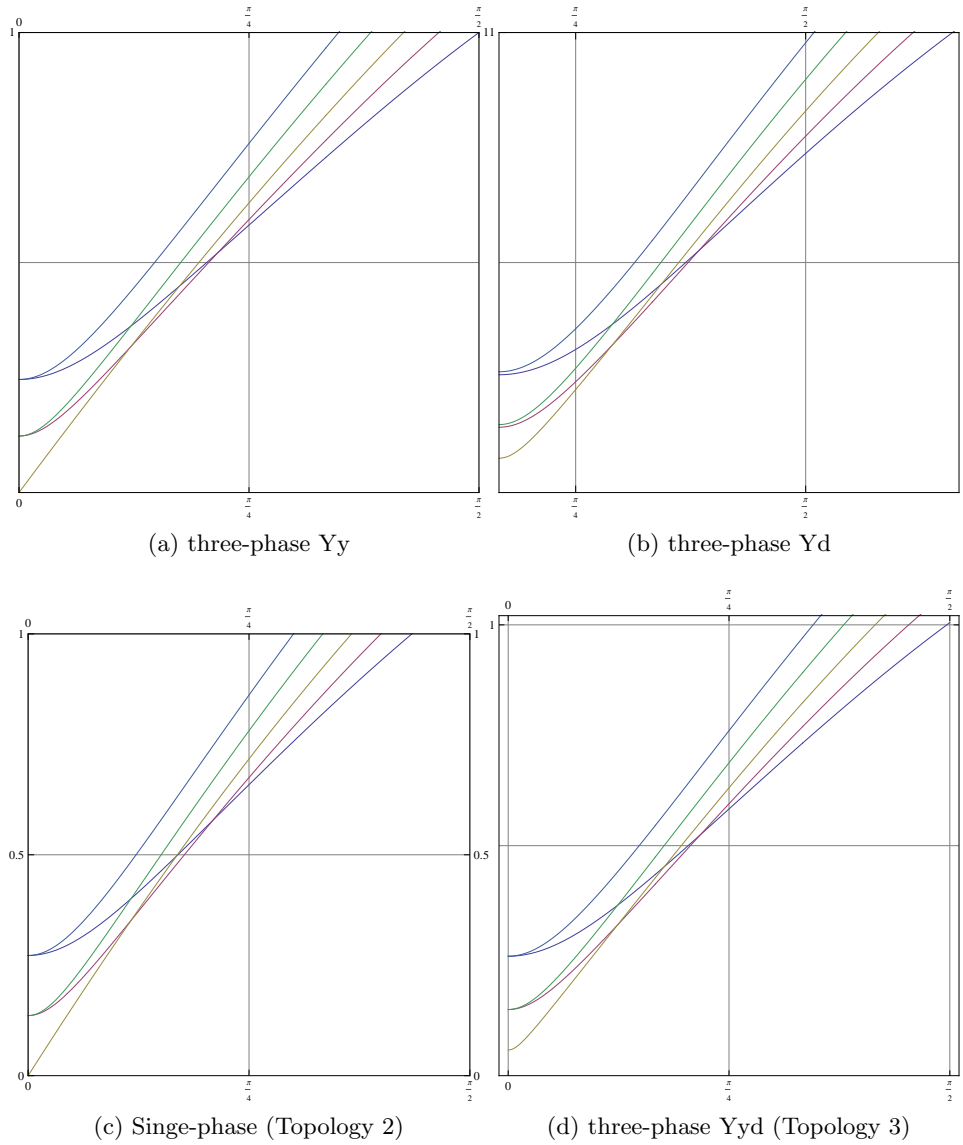
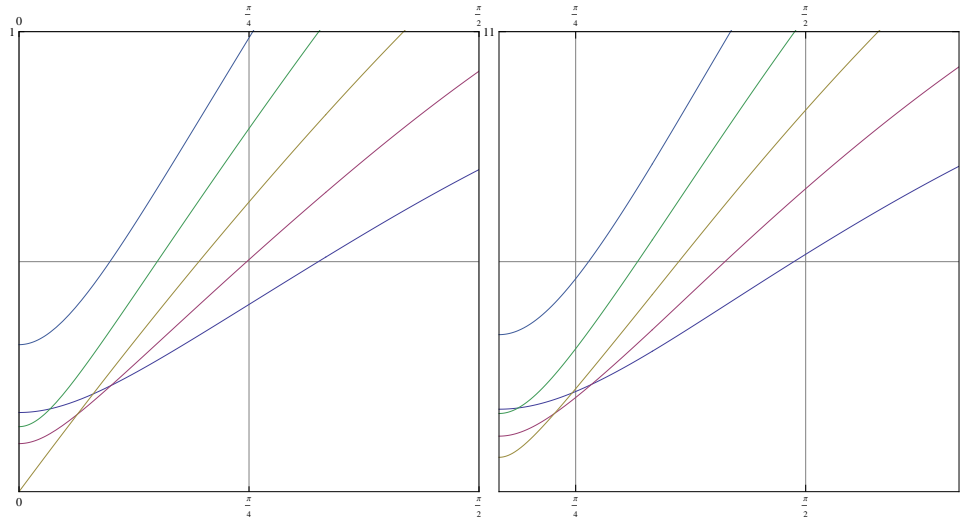
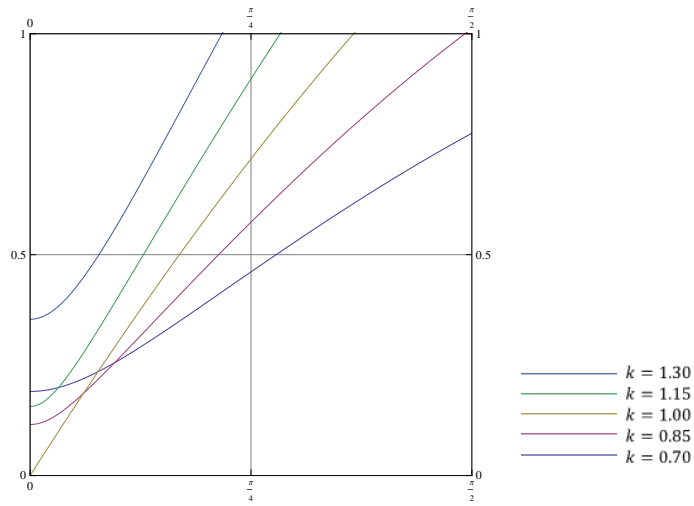


Figure 6.20: VA rating on HV side



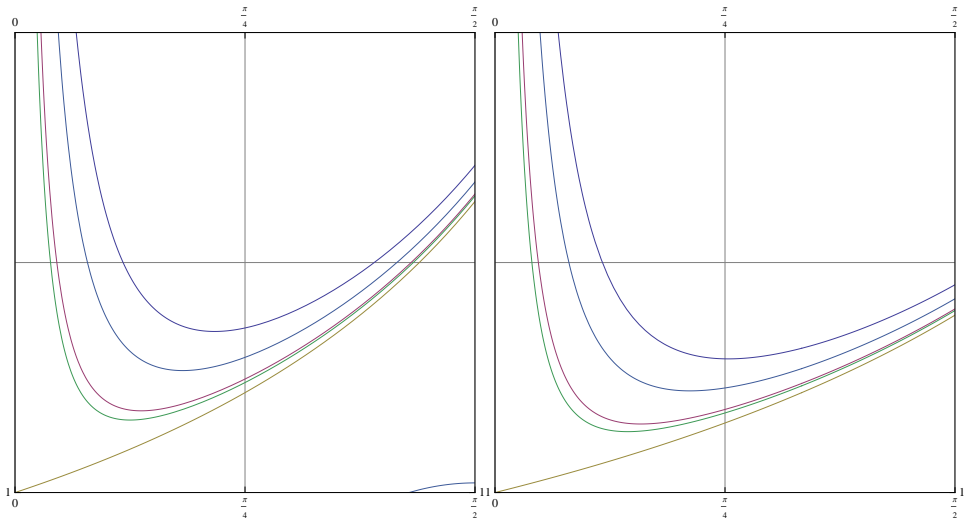
(a) three-phase Yy and Yyd

(b) three-phase Yd and Yyd



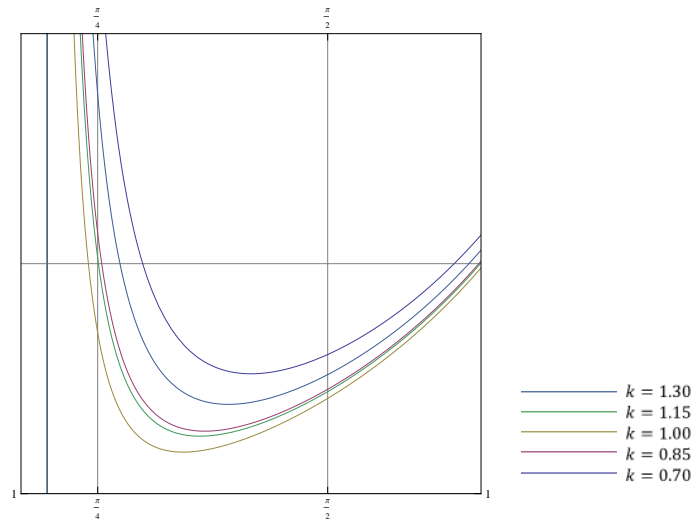
(c) Single-phase (Topology 2)

Figure 6.21: VA rating on LV side



(a) Single-phase (Topology 2)

(b) three-phase Yy



(c) three-phase Yd

Figure 6.22: Ratio between real and average apparent power (T/P)

6.6 Prototype implementation and experiment results

Experiments have been conducted to validate the operating principle at a low power rating. The required series inductances are integrated as a leakage inductance of the transformer without connecting external inductors. An NI Compact RIO real-time controller and Labview FPGA are used for phase-shifted PWM modulation at 10kHz with a dead time of $1.5\mu s$.

The core loss coefficients are extracted via square wave voltage excitation by an open circuit test and loss has been determined by a short circuit test. The total loss is estimated at around 2.2% of the kVA rating on the basis of the open and short circuit measurements. The turn ratio of the three winding isolation transformer is $1 : 1 : \sqrt{3}(YY\Delta)$. The DC-links are connected in parallel at 300V and the bidirectional operation is monitored with different phase shift angles without any power flow from power source but the losses. The duty ratio is fixed at 0.5 and as additional phase shift of 30° is applied to the winding in *Delta* connection. The measured steady-state voltage and current waveforms at phase shifts of 10° , 20° , 30° are shown in Fig. 6.25.

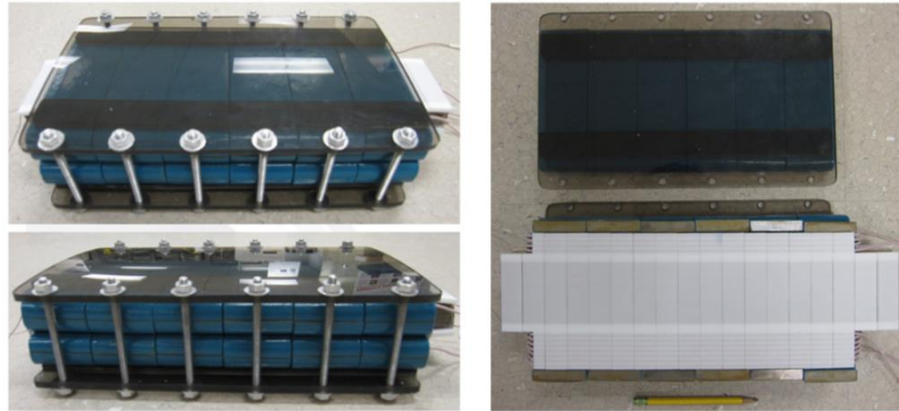
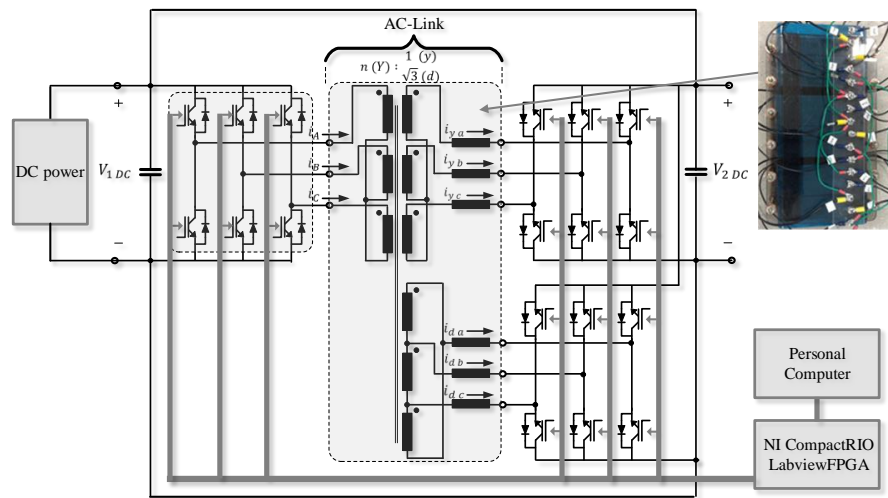


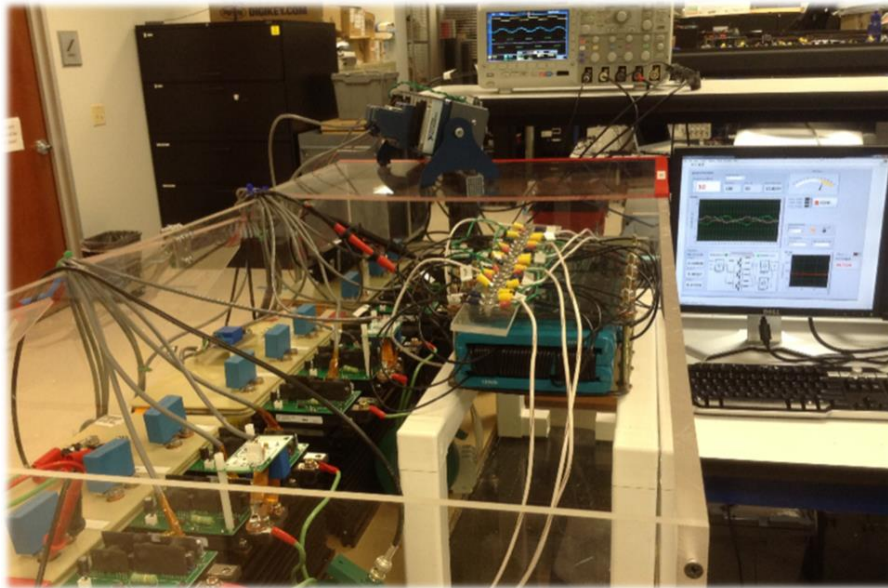
Figure 6.23: Prototype of MV-HF series inductance integrated planar transformer

Table 6.4: Ratings and losses

kVA_{phase}	B_{ac}	Phase shift	Est. core loss on the basis of open circuit test	Est. current loss on the basis of short circuit test	Estimated total loss
5.5kVA	0.28T	20°	40W	78W	118W

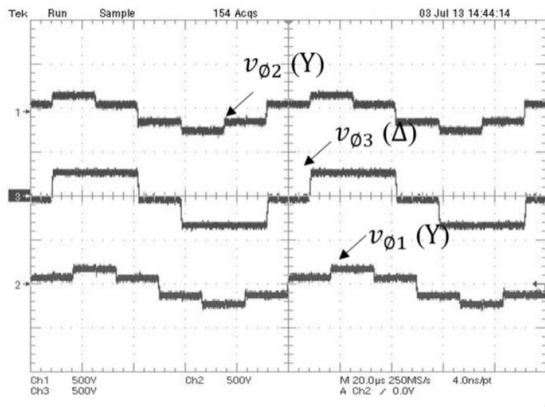


(a) Configuration of proposed three-port three-phase dual active bridge DC/DC converter Yd configuration

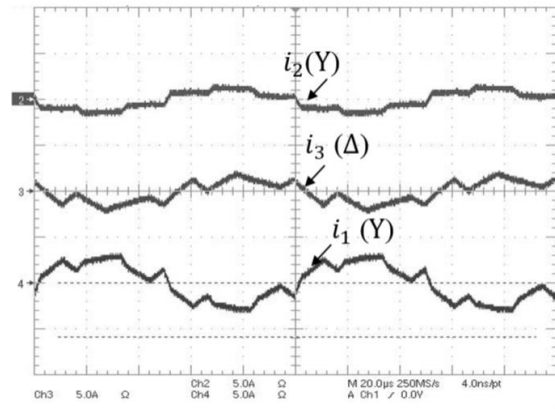


(b) 1200V IGBT based three-port three-phase DAB DC/DC converter with NI Compact Rio and LabviewFPGA

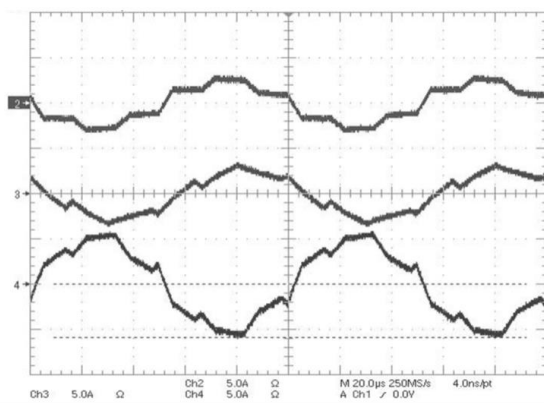
Figure 6.24: Laboratory prototype



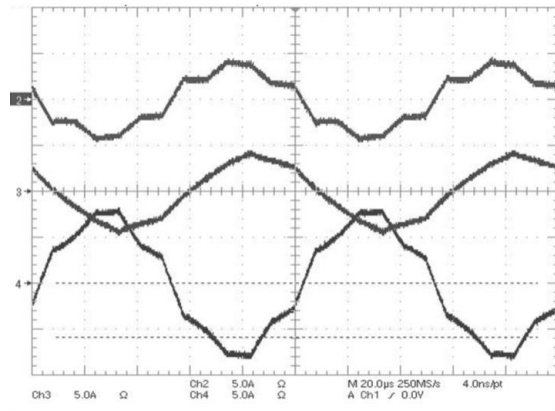
(a) Voltage waveforms on each winding with $\theta_{ps} = 30^\circ$



(b) Line current waveform with $\theta_{ps} = 10^\circ$



(c) Line current waveform with $\theta_{ps} = 20^\circ$



(d) Line current waveform with $\theta_{ps} = 30^\circ$

Figure 6.25: Waveforms (500V Div, 5A/Div, 20 μ s/Div)

Chapter 7

Conclusions

7.1 Summary and conclusion

The main goal of this thesis was to understand operating and system characteristics of the MV-MF DC/DC conversion stage, and design suitable, optimized magnetic components for these specific applications. This thesis contains comprehensive design considerations for medium-voltage and medium frequency AC-link transformers for SST applications operating with different types of high-power dual-active bridge DC/DC converters.

This study can be categorized by the development of two major aspects, isolated high-power DAB DC/DC converters (chapters 2 and 6) and AC-link transformers, (chapters 3, 4, and 5) for SST applications. There is an emphasis on developing and designing magnetic components, however neither focus can be carried out and optimized without a thorough understanding of the other.

The following topologies were studied and implemented, including the newly proposed three-port three-phase DAB converter in Y_{vd} connection for SST applications:

1. Single-phase DAB DC/DC converter (SST Lab. prototype A)
2. Proposed three-port three-phase DAB DC/DC in Y_{vd} connection (SST Lab. prototype B)

The single-phase DAB DC/DC converter in a half bridge configuration is considered superior to other high power DC/DC converters in terms of its simplicity and controllability. During the development phase of the laboratory prototype, more weight was put on system reliability and reduction of voltage stress on devices on the MV side for mature Silicon-based low voltage devices. This was done instead of using complex configurations and control strategies. Hence, the prototype was built at 12kVDC/400V, which one half of the given specification 12kVDC/400V, to be within a practically applicable range for the test facilities used.

The proposed three-port three-phase DAB DC/DC converter in Yyd connection has attractive features for high power applications, such as low device and component stresses and low harmonic components. This configuration was introduced based on the three-phase concept to reduce the VA rating of the power devices and filter components. Since most distribution transformers include a *Delta* connection at medium voltage to avoid third harmonics issues in three-phase AC systems, the *Delta* connection is one option that has to be discussed for distribution voltage level power electronics applications. The overall performance advantages and disadvantages are still being researched.

The following AC-link transformers were studied and implemented in this thesis, including the newly proposed inductor-integrated coaxial winding transformer and inductor-integrated three winding low-profile planar transformer

1. A MV-MF coaxial winding transformer
2. An inductor-integrated coaxial winding transformer (ICWT)
3. An inductor-integrated three winding low-profile planar transformer

The inductor-integrated three winding planar transformer was designed for the phase modular three-port bidirectional DC/DC converter in a Yyd connection. A three winding low-profile planar transformer is one of the best suited transformers for three port phase modular DAB converter applications. The leakage magnetic flux of the transformer is both high and predictable, which allows it to be used for series inductance integration. The difference of leakage terminal inductances between windings can be utilized to adjust the circulating current and power between the ports for each winding arrangement. The simplified terminal leakage inductance model is used, and the analytical solution for the steady state operation of the proposed converter in a Yyd connection is provided. The operating principle, with a comprehensive analysis of the converter and isolation transformer, was presented, and verified the experimental results that were obtained. The 1200V IGBT-based DAB DC/DC converter set up was extended to three bridges and used for verification of the proposed three-port three-phase DAB DC/DC in Yyd connection.

The first CWT prototype was built with an emphasis on verification of the feasibility of operation with a 15kV SiC based DAB DC/DC converter. The parasitic inductance and capacitance elements for the CWT were derived by analytical calculation and verified using both FEM simulation and measured results. The equivalent circuit model for a coaxial winding transformer was proposed in order to expect the response from high dV/dt pulse switching. The skin and proximity effects of the copper tube on the LV winding was also reviewed in detail for optimization.

The insulation of the CWT prototype was designed by investigating electric stress using FEM, and tested in pulse switching conditions of up to 10kVDC and 6kVAC. There was no sign of insulation failure in the laboratory tests; however, insulation oil may have to be considered in order to meet international standards. With respect to the insulation level, further study and tests in qualified facilities will be required. Even though a load test was not available due to the limitation of the laboratory capacity, the CWT prototype is expected to achieve an overall efficiency 99.5% at 50kVA based on open and short circuit tests and computer-aided analysis.

The coaxial winding power transformer is suitable for high frequency applications with good electric and magnetic shielding. The simple and concentric configuration without gaps generates low parasitics and is strong against skin and proximity effects. The evenly distributed magnetic field and losses help avoid heat congestion and high hot-spot temperatures. The highly predictable leakage inductance inside the transformer can be utilized for special purposes, such as inductor integration.

One of the key advantages of resonant/non-resonant high power DC/DC converters comes from their ability to utilize the transformer without requiring external inductors to transfer power, while still achieving zero-voltage switching. The accurate and analyzable inductor-integrated coaxial winding transformer (ICWT) was introduced as a solution. The operating mechanism and concepts of the ICWT were introduced and verified. The analytical design approach for the single-phase DAB DC/DC converter, which included selection of the core material, size optimizations, and an accurate loss formula, was discussed and verified with measured results.

The ICWT prototype was built, and the feasibility of the new concept was verified by experimentation. Medium-voltage switching and operation tests were implemented on a 12kV SiC-based single-phase 6kVDC/400VDC conversion stage of the SST application at power transfer of 7kVA. A 1200V IGBT-based DAB DC/DC converter was built for the load test, and provided an accurate measurement of efficiency over wide operating range. A NI Compact RIO real-time controller and a *Labview FPGA* were used for phase-shifted modulation at 20kHz. The hot-spot temperature settled down at 125°C after 60 minutes of operation without an active cooling method and the overall efficiency of ICWT, 96.4%, was achieved at 10.9kVA, with a 10.1kW real power transfer.

The ICWT prototype was designed with an emphasis on size reduction, rather than efficiency. The majority of the total losses were due to loss from the inner cores (powder-type, inductor), which are not as efficient as the outer cores (Nanocrystalline, transformer). Note that the ICWT is a physical combination of a transformer and an inductor, and the overall efficiency comes from both of these components. The efficiency is analytically designed and maximized by the proposed loss equation. Therefore, the efficiency can be improved upon by evenly scaling up the geometry, without introducing considerable problems, while still remaining under optimized

conditions.

Insulation oil or epoxy encapsulation were not used for the preliminary load tests, however an insulation material is necessary in this size in order to avoid electric breakdown at a medium voltage level. These insulation materials have high thermal conductivity and will help to better dissipate heat outside. On the other hand, this will increase parasitic capacitances due to the high permittivity of the insulation materials. The capacitance coupling of the AC-link side is generally not desirable, unless it is utilized as a circuit element, e.g. it can reduce the soft switching region of the DAB DC/DC converter.

Two of the main issues in practical use of the compact MV-MF transformer are the heat and parasitic capacitance on the windings. This high voltage in a small space necessarily generates an intensive electric field in small space, which results in a high possibility of electric breakdown and high parasitic capacitances. Different winding methods, insulation materials, and advance cooling could be used in regards to these issues for future research.

REFERENCES

- [1] Xu She; Alex Huang, Burgos, R. "Review of Solid-State Transformer Technologies and Their Application in Power Distribution Systems", Emerging and Selected Topics in Power Electronics, IEEE Journal of, On page(s): 186 - 198 Volume: 1, Issue: 3, Sept. 2013
- [2] J.W. Kolar, G.I. Ortiz, "Solid State Transformer Concepts in Traction and Smart Grid Applications", IEEE Power Electronics Society
- [3] G. Ortiz, M. LEibL, J. W. Kolar and O. Apeldoorn, "Medium Frequency Transformers for Solid-State-Transformer Application Design and Experimental Verification", IEEE, 2013
- [4] Seunghun Baek, Subhashish Bhattacharya, "Analytical modeling of a MV-HF resonant coaxial type power transformer for a solid state transformer application", ECCE 2011.
- [5] Uwe Drogenik, ABB Corporate Research, CH-5405 Dattwil, Switzerland, "A 150kW Medium Frequency Transformer Optimized for Maximum Power Density", CIPS 2012, March, 6-8, 2012, Nuremberg/Germany
- [6] G. Ortiz, J. Biela, D. Bortis and J. W. Kolar, "1 Megawatt, 20kHz, Isolated, Bidirectional 12kV to 1.2kV DC-DC convert for Renewable Energy Applications", The 2010 International Power Electronics Conference
- [7] Gabriel Ortiz, Dominik Bortis, Student member; IEEE, Jurgen Biela, Member, IEEE, and Johann W. Kolar, Senior Member, IEEE, "Optimal Design of a 3.5-kV/11-kW DC-DC Convert for Charging Capacitor Banks of Power Modulators", IEEE Transactions on Plasma Science, Vol 38, No. 10, October 2010
- [8] Michael Steiner, Harry Reinold, "Medium Frequency Topology in Railway Applications", 2007.
- [9] G. Ortiz, J. Biela and J. W. Kolar, "Optimized Design of Medium Frequency Transformers with High Isolation Requirements", IEEE 2010
- [10] Gangyao Wang, Seunghun Baek, Joseph Elliott, Arun Kadavelugu, Fei Wang, Xu She, Sumit Dutta, Y. Liu, Tiefu Zhao, W. Yao, R. Gould, Subhashish Bhattacharya, Alex Huang, "Design and Hardware Implementation of Gen-1 Silicon Based Solid State Transformer", Applied Power Electronics Conference and Exposition (APEC), 2011 26th Annual IEEE
- [11] Xu She, Huang, A.Q., Tiefu Zhao, Gangyao Wang, "Coupling Effect Reduction of a Voltage-Balancing Controller in Single-Phase Cascaded Multilevel Converters", Power Electronics, IEEE Transactions on Volume: 27, 2012
- [12] Subhashish Bhattacharya, Tiefu Zhao, Gangyao Wang, Sumit Dutta, Seunghun Baek, Yu Du, Babak Parkhideh, Xiaohu Zhou, Alex Huang, "Design and Development of Generation-I Silicon based Solid State Transformer", Applied Power Electronics Conference and Exposition (APEC), 2010 25th Annual IEEE

- [13] Fei Wang, Xu She, Gangyao Wang, Huang, A, Burgos, R, "Parallel operation of solid state transformer", Energy Conversion Congress and Exposition (ECCE), 2012 IEEE
- [14] Sachin Madhusoodhanan, Kamalesh Hatua, S. Bhattacharya, "Control Technique for 15 kV SiC IGBT based Active Front End Converter of a 13.8 kV Grid Tied 100 kVA Transformerless Intelligent Power Substation", Energy Conversion Congress and Exposition (ECCE), 2013 IEEE
- [15] Dhaval Patel, Arun Kadavelugu, Sachin Madhusoodhanan, Kamalesh Hatua, Scott Leslie, Sei-Hyung Ryu, David Grider, Anant Agarwal, S. Bhattacharya. "15 kV SiC IGBT Based Three-Phase Three-Level Modular-Leg Power Converter", Energy Conversion Congress and Exposition (ECCE), 2013 IEEE
- [16] F. Krismer, S. Round, J. W. Kolar, "Performance Optimization a High Current Dual Active Bridge with a Wide Operating Voltage Range", Power Electronics Specialists Conference, 2006. PESC '06. 37th IEEE
- [17] Haihua Zhou, Ashwin M. Khambadkone, "Hybrid Modulation for Dual-Active-Bridge Bidirectional Converter With Extended Power Range for Ultra capacitor Application", IEEE Transactions on Industry Applications, Vol. 45, No. 4, July/August 2009
- [18] German G. Oggier, Guillermo O. Garcia, and Alejandro R. Oliva, "Modulation Strategy to Operate the Dual Active Bridge DC-DC Converter Under Soft Switching in the Whole Operating Range",
- [19] Hauke van Hoek, Marus Neubert, Rik W. De Doncker, "Enhanced Modulation Strategy for a Three-Phase Dual Active Bridge-Boosting Efficiency of an Electric Vehicle Converter", IEEE Transaction on Power Electronics, Vol.28, No. 12, December 2013
- [20] Mustansir H. Kheraluwala, Randal W. Gascoigne, Deepakraj M. Divan, Eric D. Baumann, Performance Characterization of a High-Power Dual Active Bridge dc-to-dc Converter, IEEE transactions on industry applications, VOL. 28, NO. 6, NOVEMBER / DECEMBER 1992.
- [21] Bruno Cogitore, Jean-pierre Keradec, Jean Barbaroux, "The Two Winding Transformer: An Experimental Method to Obtain a wide Frequency Range Equivalent Circuit", IEEE Transactions on instrumentation and measurement, Vol 40, No. 2, April 1994.
- [22] Francois BLACHE, Jean-pierre Keradec, Bruno Cogitore, "Stray Capacitances of Two Winding Transformers:Equivalent Circuit, Measurements, Calculation and Lowering", IEEE, 1994.
- [23] Eric Laveuve, Jean-pierre Keradec, Michel Bensoam, Electrostatic of Wound Components: Analytical Results, Simulation and Experimental Validation of the Parasitic Capacitance, IEEE, 1991.
- [24] Juergen Biela and Johann W. Kolar, "Using Transformer Parasitics for Resonant Converters-A Review of the Calculation of the Stray Capacitance of Transformers", IEEE Transactions on industry applications, Vol 44, No. 1, January/February 2008.

- [25] Mark S. Rauls, Donald W. Novotny, Deepakraj M. Divan Robert R. Bacon, and Randal W. Gascoigne, “Multiturn High-Frequency Coaxial Winding Power Transformers”, IEEE Transactions on Industry Applications, Vol. 31, No. 1, January/February 1995
- [26] Mustansir H. Kheraluwala, Donald W. Novotny, and Deepakraj M. Divan, “Coaxial Wound Transformers for High-Power High-Frequency Applications”, IEEE Transactions on Power Electronics, Vol. 7, No. 1, January 1992
- [27] J. Biela, D. Bortis, J. W. Kolar, “Design Procedure for Compact Pulse Transformers with Rectangular Pulse Shape and Fast Rise Times”, IEEE transactions on Dielectrics and Electrical Insulation Vol.18, No.4;August 2011.
- [28] Bernardo Cougo and Johann W. Kolar, “Integration of Leakage Inductance in Tape Wound Core Transformers for Dual Active Bridge Converters”, CIPS 2012, March, 6-8,2012, Nuremberg/Germany
- [29] M. Albach, Th. Durbaum, A.Brockmeyer, “Calculating Core Losses in Transformers for Arbitrary Magnetizing Currents A Comparison of Different Approaches”, IEEE, 1996
- [30] Irma Villar, Alfred Rufer, Unai Viscarret, Frederic Zurkinden and Ion Etxeberria-Otadui, “Analysis of Empirical Core Loss Evaluation Methods For Non-Sinusoidally Fed Medium Frequency Power Transformers”, IEEE, 2008
- [31] Kapil Venkatachalam, Charles R. Sullivanm, Tarek Abdallah, and Hernan Tacca, “Accurate Prediction of Ferrite Core Loss with Nonsinusoidal Waveforms Using Only Steinmetz Parameters”, IEEE, 2002
- [32] V. Joseph Thottuvelil, Thomas G. Wilson, Harry A. Owen, JR., “High-Frequency Measurement Techniques for Magnetic Cores”, IEEE Transactions on Power Electronics Vol.5, No.1, January 1990
- [33] Keith W. Klontz, Deepakraj M. Divan, and Donald W. Novotny, “An Actively Cooled 120-kW Coaxial Winding Transformer for Fast Charging Electric Vehicles”, IEEE Transactions on Industry Applications, Vol. 31, No. 6, November/December 1995
- [34] Jurgen Reinert, Ansgar Brockmeyer, Rik W. A. A. De Doncker, “Calculation of Losses in Ferro- and Ferrimagnetic Materials Based on the Modified Steinmetz Equation”, IEEE Transactions on Industry Applications, Vol. 37, No. 4, July/August 2001
- [35] Jieli Li, T. Abdallah, C. R. Sullivan, “Improved Calculation of Core Loss with Nonsinusoidal Waveforms”, IEEE Industry Application Society Annual Meeting, Oct 2001, pp. 2203-2210
- [36] Giorgio Bertotti, “General Properties of Power Losses in Soft Ferromagnetic Material”, IEEE Transaction on Magnetism, Vol. 24, No. 1, January 1988 IEEE Transaction on Power Electronics, Vol. 26, No. 4, April 2011
- [37] Florian Krismer, Johann W. kolar, “Accurate Power Loss Model Derivation of a High-Current Dual Active Bridge Converter for an Automotive Application”, IEEE Transaction on Industrial Electronics, Vol. 57, No. 3, March 2010

- [38] Gabriel Ortiz, Hirofumi Uemura, Dominik Bortis, Johann Walter Kolar, Oscar Apeldoorn, “Modeling of Soft-Switching Losses of IGBTs in High-Power High-Efficiency Dual-Active-Bridge DC/DC Converters”, *IEEE Transaction on Electron Devices*, Vol. 60, No. 2, February 2013
- [39] Jordi Events, Jeroen Van Den Keybus, Florian Krismer, Johan Driesen, and Johann W. Kolar, “Switching Control Strategy for Full ZVS Soft-Switching Operation of a Dual Active Bridge AC/DC Converter”, *IEEE* 2012
- [40] Hauke van Hoek, Markus Neubert, Albert Kroeber and Rik W. De Doncker, “Comparison of a Single-Phase and a Three-Phase Dual Active Bridge with Low-Voltage, High-Current Output”
- [41] Luca Dalessandro Fabiana da Silveira Cavalcante, and Johann W. Kolar, Self-Capacitance of High-Voltage Transformers, *IEEE Transactions on power electronics*, VOL. 22, NO. 5, September 2007
- [42] Mark S. Rauls, Donald W. Novotny, Deepakraj M. Divan, Design Considerations for High-Frequency Coaxial Winding Power Transformers, *IEEE Transactions on industry applications*, Vol 29, No. 2, 1993.
- [43] Mustansir H, Kheraluwala, Donald W. Novotny, Deepakraj M. Divan, Eric D. Baumann, Coaxially Wound Transformers for High-Frequency Application, *IEEE Transactions on industry applications*, Vol 28, No. 6, 1992.
- [44] Antonio Massarini and Marian K. Kazimierczuk, Self-Capacitance of Inductors, *IEEE Transactions on power electronics*, Vol 12, No. 4, July 1997.
- [45] Vedran Boras, Slavko Vujevic, Dino Lovric, Definition and Computation of Cylindrical Conductor Internal Impedance for Large Parameters, *ICECom*, 2010 Conference Proceedings, Sept. 2010.
- [46] Hurbert Bristol Dwight, Skin Effect and Proximity Effect in Tubular Conductors, *Transactions A.I.E.E.*, New York, N.Y., February 15-17,1922. 6
- [47] Francisco De Leon, Dual Three-Winding Transformer Equivalent Circuit Matching Leakage Measurements, *IEEE Transactions on Power Delivery*,2009
- [48] Xavier Margueron and Jean-Pierre Keradec, Design of Equivalent Circuits and Characterization Strategy for n-port Coupled Inductors, *IEEE Transactions on Industry Applications*,2007
- [49] Rik W. A. A. De Deonker, Deepakraj M. Divan, Mustansir H. Kheraluwala, A three-phase soft-switched high-power-density dc/dc converter for high-power applications, *IEEE transactions on industry applications*, VOL. 27, NO. 1, JANUARY/FEBRUARY 1991
- [50] Luca Dalessandro, Fabiana da Silveira Cavalcante, and Johann W. Kolar, Self-Capacitance of High-Voltage Transformers, *IEEE*.

- [51] Hua Bai, Chris, “MiEliminate Reactive Power and Increase System Efficiency of Isolated Bidirectional Dual-Active-Bridge DCDC Converters Using Novel Dual-Phase-Shift Control”, *IEEE transactions on power electronics*, VOL. 23, NO. 6, NOVEMBER 2008
- [52] C. Zhao S.D. Round J.W. Kolar, “Full-order averaging modelling of zero-voltage-switching phase-shift bidirectional DCDC converters”, *IET Power Electron.*, 2010, Vol. 3, Iss. 3, pp. 400410
- [53] G. Eason, B. Noble, and I.N. Sneddon, “On certain integrals of Lipschitz-Hankel type involving products of Bessel functions,” *Phil. Trans. Roy. Soc. London*, vol. A247, pp. 529-551, April 1955.
- [54] McLyman, Colonel William T., “Transformer and inductor design handbook”, 1932
- [55] K. Hatua, S. Dutta, A. Tripathi, Seunghun Baek, G. Karimi, S. Madhusoodhanan, S. Bhattacharya , “Transformer less Intelligent Power Substation: Connects 13.8 kV and 480 V Grid using 15kV SiC-IGBTs, ECCE2011
- [56] Yaow-Ming Chen, Yuan-Chuan Liu, Feng-Yu Wu , “Multi-Input DC/DC Converter Based on the Multiwinding Transformer for Renewable Energy Applications”, *IEEE transactions on industry applications*, vol. 38, no. 4, 2002
- [57] C. Zhao, Simon D. Round, Johann W. Kolar “An Isolated Three-Port Management”, *IEEE transactions on power electronics*, vol. 23, no. 5, 2008
- [58] Rik W. A. A. De Doncker, Deepakraj M. Divan, and Mustansir H. Kheraluwala, “A Three-phase Soft-Switched High-Power-Density dc /dc Converter for High-Power Applications”. *IEEE transactions on industry applications*, vol. 27, no. 1,1991
- [59] Francisco de Len, Juan A. Martinez, “Dual Three-Winding Transformer Equivalent Circuit Matching Leakage Measurements”, *IEEE transactions on power delivery*, vol. 24, no. 1, january 2009
- [60] Seunghun Baek, Dutta, S. ; Bhattacharya, “Characterization of a three-phase dual active bridge DC/DC converter in wye-delta connection for a high frequency and high power applications”, *ECCE, 2011 IEEE*, 17-22 Sept. 2011
- [61] Hanna Plesko, Jurgen Biela, Jorma Luomi, Johann W. Kolar, “Novel Concepts for Integrating the Electric Drive and auxiliary DCDC Converter for Hybrid Vehicles”, *IEEE transactions on power electronics*, vol. 23, no. 6, november 2008

APPENDICES

Appendix A

Classification of transformers - international standard IEC 60076

IEC (International Electrotechnical Commission) 60076 is one of the most referenced international standards to three phase and single phase power transformers. The terminology and classification of the power transformer is briefly summarized in this chapter.

Scope

- Single-phase transformers with rated power more than 1 kVA and three-phase transformers more than 5 kVA.
- Any winding has rated voltage higher than 1kV

Glossary - IEC 60076-1

Power transformer : a static piece of apparatus with two or more windings which, by electromagnetic induction, transforms a system of alternating voltage and current into another system of voltage and current usually of different values and at the same frequency for the purpose of transmitting electrical power

dry-type transformer : a transformer in which the magnetic circuit and windings are not immersed in an insulating liquid: transformer in a ventilated enclosure cooled by the circulation of the external air A supply voltage of which the waveshape is approximately sinusoidal.

Rating : those numerical values assigned to the quantities which define the operation of the transformer in the conditions specified in this part of IEC 60076 and on which the manufacturer's guarantees and the tests are based HV winding : The winding having the highest rated voltage

LV winding: The winding having the lowest rated voltage

No-load loss : the active power absorbed when a rated voltage (tapping voltage) at a rated frequency is applied to the terminals of one of the windings, the other winding or windings being opencircuited

No-load current: The r.m.s. value of the current flowing through a line terminal of a winding when rated voltage is applied at a rated frequency to that winding, the other winding or windings

Type of cooling medium	Air	A
Type of circulation	Natural	N
	Forced	F

Class C1	Class C2
The transformer is suitable for operation at ambient temperature not below 5°C but may be exposed during transport and storage to ambient temperatures down to 25°C.	The transformer is suitable for operation, transport and storage at ambient temperatures down to 25°C

being open-circuited

Load loss : The absorbed active power at a rated frequency and reference temperature, associated with a pair of windings when rated current is flowing through the line terminals of one of the windings, and the terminals of the other winding are shortcircuited. Further windings, if existing, are open-circuited

Total losses: the sum of the no-load loss and the load loss

Temperature rise: The difference between the temperature of the part under consideration and the temperature of the external cooling medium

Preferred values of rated power : ...100, 125, 160, 200, 250, 315, 400, 500, 630, 800, 1 000, etc..

Classification of dry-type transformers - IEC 60076-11

Normal temperature-rise limits : The maximum temperature occurring in any part of the winding insulation system is called the hot-spot temperature.

The temperature of the core, metallic parts and adjacent materials shall not reach a value that will cause damage to any part of the transformer.

Cooling method

Climate class

Environmental classes: Environmental conditions for dry-type transformers are identified in terms of humidity, condensation, pollution and ambient temperature.

Fire behavior classes: Two fire behavior classes are defined

Class E0	Class E1	Class E2
No condensation occurs on the transformers and pollution is negligible. This is commonly achieved in a clean, dry indoor installation.	Occasional condensation can occur on the transformer (for example, when the transformer is de-energized). Limited pollution is possible.	Frequent condensation or heavy pollution or combination of both. Special tests according to the procedure of Clause 26 shall confirm the conformity of E1 or E2 class transformers.

Class F0	Class F1
There is no special fire risk to consider. Except for the characteristics inherent in the design of the transformer, no special measures are taken to limit flammability.	Transformers subject to a fire hazard. Restricted flammability is required. The emission of toxic substances and opaque smokes shall be minimised.

IEC vector group

- D or d: Delta winding, also called a mesh winding..
- Y or y: Wye winding, (also called a star).
- Z or z: Zigzag winding, or interconnected star winding.
- N (uppercase): indicates that a system neutral is connected to the high-voltage side.
- n (lowercase): indicates that a system neutral is connected to the low-voltage side.
- Digit: Phase displacement, rotation counterclockwise. The number is multiple of 30 degree lag for LV winding using HV winding as the reference.

Appendix B

Steady state lossless operation with phase shift modulation Yy connection

Region For $0 \leq \theta_{ps} < \pi/3$:

Six modes of operation with phase-shift modulation are identified for each operating regions.

Mode 1 : $0 \leq \theta < \theta_{ps}$, ($v_{1 AC} = \frac{1}{3}V_{1 DC}$, $v_{2 AC} = -\frac{1}{3}kV_{1 DC}$)

$$i_{L1 1}[\theta] = \frac{V_{1 DC}(1+k)}{3\omega L_s} \cdot \theta + i_{L1 1}[0],$$

Mode 2 : $\theta_{ps} \leq \theta < \frac{\pi}{3}$, ($v_{1 AC} = \frac{1}{3}V_{1 DC}$, $v_{2 AC} = \frac{1}{3}kV_{1 DC}$)

$$i_{L1 2}[\theta] = \frac{V_{1 DC}(1-k)}{3\omega L_s} \cdot (\theta - \theta_{ps}) + i_{L1 2}[\theta_{ps}],$$

Mode 3 : $\frac{\pi}{3} \leq \theta < \frac{\pi}{3} + \theta_{ps}$, ($v_{1 AC} = \frac{2}{3}V_{1 DC}$, $v_{2 AC} = \frac{1}{3}kV_{1 DC}$)

$$i_{L1 3}[\theta] = \frac{V_{1 DC}(2-k)}{3\omega L_s} \cdot (\theta - \frac{\pi}{3}) + i_{L1 3}[\frac{\pi}{3}],$$

Mode 4 : $\frac{\pi}{3} + \theta_{ps} \leq \theta < \frac{2\pi}{3}$, ($v_{1 AC} = \frac{2}{3}V_{1 DC}$, $v_{2 AC} = \frac{2}{3}kV_{1 DC}$)

$$i_{L1 4}[\theta] = \frac{V_{1 DC}(2-2k)}{3\omega L_s} \cdot (\theta - \theta_{ps} - \frac{2\pi}{3}) + i_{L1 4}[\frac{\pi}{3} + \theta_{ps}],$$

Mode 5 : $\frac{2\pi}{3} \leq \theta < \frac{2\pi}{3} + \theta_{ps}$, ($v_{1 AC} = \frac{1}{3}V_{1 DC}$, $v_{2 AC} = \frac{2}{3}kV_{1 DC}$)

$$i_{L1 5}[\theta] = \frac{V_{1 DC}(1-2k)}{3\omega L_s} \cdot (\theta - \frac{2\pi}{3}) + i_{L1 5}[\frac{2\pi}{3}],$$

Mode 6 : $\frac{2\pi}{3} + \theta_{ps} \leq \theta < \pi$, ($v_{1 AC} = \frac{1}{3}V_{1 DC}$, $v_{2 AC} = \frac{1}{3}kV_{1 DC}$)

$$i_{L1 6}[\theta] = \frac{V_{1 DC}(1-k)}{3\omega L_s} \cdot (\theta - \theta_{ps} - \frac{2\pi}{3}) + i_{L1 6}[\frac{2\pi}{3} + \theta_{ps}],$$

Where the $k = n \cdot G$, conversion ratio $G = \frac{V_2 DC}{V_1 DC}$

From the symmetry condition, the initial inductance current values are obtained.

$$\begin{aligned} i_{L1\ 1}[0] &= -\frac{2\pi V_1 DC - 2\pi k V_1 DC + 3k V_1 DC \phi}{9L\omega}, & i_{L1\ 2}[\theta_{ps}] &= -\frac{2\pi V_1 DC}{9L\omega} + \frac{2\pi k V_1 DC}{9L\omega} + \frac{V_1 DC \phi}{3L\omega}, \\ i_{L1\ 3}\left[\frac{\pi}{3}\right] &= -\frac{2\pi V_1 DC}{9L\omega} + \frac{\pi k V_1 DC}{9L\omega} + \frac{k V_1 DC \phi}{3L\omega}, & i_{L1\ 4}\left[\frac{\pi}{3} + \theta_{ps}\right] &= -\frac{\pi V_1 DC}{9L\omega} + \frac{\pi k V_1 DC}{9L\omega} + \frac{2V_1 DC \phi}{3L\omega}, \\ i_{L1\ 5}\left[\frac{2\pi}{3}\right] &= \frac{\pi V_1 DC}{9L\omega} - \frac{\pi k V_1 DC}{9L\omega} + \frac{2k V_1 DC \phi}{3L\omega}, & i_{L1\ 6}\left[\frac{2\pi}{3} + \theta_{ps}\right] &= \frac{\pi V_1 DC}{9L\omega} - \frac{\pi k V_1 DC}{9L\omega} + \frac{V_1 DC \phi}{3L\omega} \end{aligned}$$

Region For $\pi/3 \leq \theta_{ps} < \pi/2$:

Mode 1 : $0 \leq \theta < \theta_{ps} - \frac{\pi}{3}$, ($v_{1 AC} = \frac{1}{3}V_1 DC$, $v_{2 AC} = -\frac{2}{3}kV_1 DC$)

$$i_{L1\ 1}[\theta] = \frac{V_1 DC(1+2k)}{3\omega L_s} \cdot \theta + i_{L1\ 1}[0],$$

Mode 2 : $\theta_{ps} - \frac{\pi}{3} \leq \theta < \frac{\pi}{3}$, ($v_{1 AC} = \frac{1}{3}V_1 DC$, $v_{2 AC} = -\frac{1}{3}kV_1 DC$)

$$i_{L1\ 2}[\theta] = \frac{V_1 DC(1+k)}{3\omega L_s} \cdot (\theta - \theta_{ps} + \frac{\pi}{3}) + i_{L1\ 2}[\theta_{ps} - \frac{\pi}{6}],$$

Mode 3 : $\frac{\pi}{3} \leq \theta < \theta_{ps}$, ($v_{1 AC} = \frac{2}{3}V_1 DC$, $v_{2 AC} = -\frac{1}{3}kV_1 DC$)

$$i_{L1\ 3}[\theta] = \frac{V_1 DC(2+k)}{3\omega L_s} \cdot (\theta - \frac{\pi}{3}) + i_{L1\ 3}[\frac{\pi}{3}],$$

Mode 4 : $\theta_{ps} \leq \theta < \frac{2\pi}{3}$, ($v_{1 AC} = \frac{2}{3}V_1 DC$, $v_{2 AC} = \frac{1}{3}kV_1 DC$)

$$i_{L1\ 4}[\theta] = \frac{V_1 DC(2-k)}{3\omega L_s} \cdot (\theta - \theta_{ps}) + i_{L1\ 4}[\theta_{ps}],$$

Mode 5 : $\frac{2\pi}{3} \leq \theta < \theta_{ps} + \frac{\pi}{3}$, ($v_{1 AC} = \frac{1}{3}V_1 DC$, $v_{2 AC} = \frac{1}{3}kV_1 DC$)

$$i_{L1\ 5}[\theta] = \frac{V_1 DC(1-k)}{3\omega L_s} \cdot (\theta - \frac{2\pi}{3}) + i_{L1\ 5}\left[\frac{2\pi}{3}\right],$$

Mode 6 : $\theta_{ps} + \frac{\pi}{3} \leq \theta < \pi$, ($v_{1 AC} = \frac{1}{3}V_1 DC$, $v_{2 AC} = \frac{2}{3}kV_1 DC$)

$$i_{L1\ 6}[\theta] = \frac{V_1 DC(1-2k)}{3\omega L_s} \cdot (\theta - \theta_{ps} - \frac{\pi}{3}) + i_{L1\ 6}\left[\theta_{ps} + \frac{\pi}{3}\right],$$

$$\begin{aligned}
i_{L11}[0] &= \frac{V_{1DC}((-2+3k)\pi - 6k\theta_{ps})}{9L\omega}, & i_{L12}[\theta_{ps} - \frac{\pi}{6}] &= \frac{V_{1DC}((-3+k)\pi + 3\theta_{ps})}{9L\omega}, \\
i_{L13}\left[\frac{\pi}{3}\right] &= -\frac{2\pi V_{1DC}((-1+3k)\pi - 3k\theta_{ps})}{9L\omega}, & i_{L14}[\theta_{ps}] &= \frac{V_{1DC}((-3+2k)\pi + 6\theta_{ps})}{9L\omega}, \\
i_{L15}\left[\frac{2\pi}{3}\right] &= \frac{V_{1DC}(\pi + 3k\theta_{ps})}{9L\omega}, & i_{L16}\left[\theta_{ps} + \frac{\pi}{3}\right] &= \frac{V_{1DC}(k\pi + 3\theta_{ps})}{9L\omega}
\end{aligned}$$

Steady state lossless operation with phase shift modulation Yd connection

Region For $\leq \theta_{ps} < \pi/3$:

Six modes of operation with phase-shift modulation are identified for each operating regions.

Mode 1 : $0 \leq \theta < \theta_{ps}$, ($v_{1AC} = \frac{1}{3}V_{1DC}$, $v_{2AC} = 0$)

$$i_{L11}[\theta] = \frac{V_{1DC}}{9\omega L_s} \cdot \theta + i_{L11}[0],$$

Mode 2 : $\theta_{ps} \leq \theta < \frac{\pi}{3}$, ($v_{1AC} = \frac{1}{3}V_{1DC}$, $v_{2AC} = kV_{1DC}$)

$$i_{L12}[\theta] = \frac{V_{1DC}(1-3k)}{3\omega L_s} \cdot (\theta - \theta_{ps}) + i_{L12}[\theta_{ps}],$$

Mode 3 : $\frac{\pi}{3} \leq \theta < \frac{2\pi}{3}$, ($v_{1AC} = \frac{2}{3}V_{1DC}$, $v_{2AC} = kV_{1DC}$)

$$i_{L13}[\theta] = \frac{V_{1DC}(2-3k)}{3\omega L_s} \cdot (\theta - \frac{\pi}{3}) + i_{L13}\left[\frac{\pi}{3}\right],$$

Mode 4 : $\frac{2\pi}{3} \leq \theta < \frac{2\pi}{3} + \theta_{ps}$, ($v_{1AC} = \frac{1}{3}V_{1DC}$, $v_{2AC} = kV_{1DC}$)

$$i_{L14}[\theta] = \frac{V_{1DC}(1-3k)}{3\omega L_s} \cdot (\theta - \frac{2\pi}{3}) + i_{L14}\left[\frac{2\pi}{3}\right],$$

Mode 5 : $\frac{2\pi}{3} + \theta_{ps} \leq \theta < \pi$, ($v_{1AC} = \frac{1}{3}V_{1DC}$, $v_{2AC} = 0$)

$$i_{L15}[\theta] = \frac{V_{1DC}}{3\omega L_s} \cdot (\theta - \theta_{ps} - \frac{2\pi}{3}) + i_{L15}\left[\frac{2\pi}{3} + \theta_{ps}\right],$$

Where the $k = n \cdot G$, conversion ratio $G = \frac{V_{2DC}}{V_{1DC}}$

From the symmetry condition, the initial inductance current values are obtained.

$$\begin{aligned}
i_{L11}[0] &= \frac{(-2+3k)\pi V_{1DC}}{9L\omega}, & i_{L12}[\theta_{ps}] &= \frac{(-2+3k)\pi V_{1DC}}{9L\omega} + \frac{V_{1DC}\theta_{ps}}{3L\omega}, \\
i_{L13}\left[\frac{\pi}{3}\right] &= -\frac{V_{1DC}(\pi-9k\theta_{ps})}{9L\omega}, & i_{L14}\left[\frac{2\pi}{3}\right] &= \frac{V_{1DC}(\pi-3k\pi+9k\theta_{ps})}{9L\omega}, \\
i_{L15}\left[\frac{2\pi}{3}+\theta_{ps}\right] &= -\frac{V_{1DC}(\pi-3k\pi+3\theta_{ps})}{9L\omega}
\end{aligned}$$

Region For $\pi/3 \leq \theta_{ps} < \pi/2$:

Mode 1 : $0 \leq \theta < \theta_{ps} - \frac{\pi}{3}$, ($v_{1AC} = \frac{1}{3}V_{1DC}$, $v_{2AC} = -kV_{1DC}$)

$$i_{L11}[\theta] = \frac{V_{1DC}(1+3k)}{3\omega L_s} \cdot \theta + i_{L11}[0],$$

Mode 2 : $\theta_{ps} - \frac{\pi}{3} \leq \theta < \frac{\pi}{3}$, ($v_{1AC} = \frac{1}{3}V_{1DC}$, $v_{2AC} = 0$)

$$i_{L12}[\theta] = \frac{V_{1DC}}{3\omega L_s} \cdot (\theta - \theta_{ps} + \frac{\pi}{3}) + i_{L12}[\theta_{ps} - \frac{\pi}{3}],$$

Mode 3 : $\frac{\pi}{3} \leq \theta < \theta_{ps}$, ($v_{1AC} = \frac{2}{3}V_{1DC}$, $v_{2AC} = 0$)

$$i_{L13}[\theta] = \frac{2V_{1DC}}{3\omega L_s} \cdot (\theta - \frac{\pi}{3}) + i_{L13}[\frac{\pi}{3}],$$

Mode 4 : $\theta_{ps} \leq \theta < \frac{2\pi}{3}$, ($v_{1AC} = \frac{2}{3}V_{1DC}$, $v_{2AC} = kV_{1DC}$)

$$i_{L14}[\theta] = \frac{V_{1DC}(2-3k)}{3\omega L_s} \cdot (\theta - \theta_{ps}) + i_{L14}[\theta_{ps}],$$

Mode 5 : $\frac{2\pi}{3} \leq \theta < \pi$, ($v_{1AC} = \frac{1}{3}V_{1DC}$, $v_{2AC} = kV_{1DC}$)

$$i_{L15}[\theta] = \frac{V_{1DC}(1-3k)}{3\omega L_s} \cdot (\theta - \frac{2\pi}{3}) + i_{L15}\left[\frac{2\pi}{3}\right],$$

Where the $k = n \cdot G$, conversion ratio $G = \frac{V_{2DC}}{V_{1DC}}$

From the symmetry condition, the initial inductance current values are obtained.

$$\begin{aligned}
i_{L11}[0] &= \frac{6kV_{1DC}\pi - 2\pi V_{1DC} - 9kV_{1DC}\theta_{ps}}{9L\omega}, & i_{L12}\left[\theta_{ps} - \frac{\pi}{3}\right] &= \frac{kV_{1DC}\pi - \pi V_{1DC} + V_{1DC}\theta_{ps}}{3L\omega}, \\
i_{L13}\left[\frac{\pi}{3}\right] &= \frac{\pi(3kV_{1DC} - V_{1DC})}{9L\omega}, & i_{L14}[\theta_{ps}] &= \frac{kV_{1DC}\pi - \pi V_{1DC} + 2V_{1DC}\theta_{ps}}{3L\omega}, \\
i_{L15}\left[\frac{2\pi}{3}\right] &= \frac{-3kV_{1DC}\pi + \pi V_{1DC} + 9kV_{1DC}\theta_{ps}}{9L\omega}
\end{aligned}$$